
UNIVERSIDADE TÉCNICA DE LISBOA
INSTITUTO SUPERIOR TÉCNICO

# Development and Experimental Study of a Detector Module for Positron Emission Mammography

**Catarina Moreira Figueira Ortigão**
(Mestre)

Dissertação para obtenção do Grau de Doutor em Física

**Orientador:** Doutor João Manuel Coelho dos Santos Varela
**Co-Orientador:** Doutor Luís Filipe dos Santos Garcia Peralta

**Júri:**

**Presidente:** Reitor da Universidade Técnica de Lisboa

**Vogais:** Doutor Stefaan Tavernier
Doutor Sérgio Eduardo de Campos Costa Ramos
Doutor João Manuel Coelho dos Santos Varela
Doutor Luís Filipe dos Santos Garcia Peralta
Doutor Pedro Jorge da Silva Rodrigues

**Outubro de 2009**

# Abstract

The ClearPEM detector was developed by the Portuguese PET Consortium under the framework of the Crystal Clear Collaboration for early stage breast cancer detection. The scanner relies on a modular design in which $\gamma$-ray detector modules are readout by low-noise ASICs. FPGAs then extract the information for energy and timing measurements required for the selection of events in coincidence. The baseline detector module comprises avalanche photodiodes arrays (APDs) to collect the light from $2\times2\times20$ mm$^3$ LYSO:Ce crystals, assembled on a matrix of $4\times8$ crystals, individually encased in $BaSO_4$. Double readout architecture is provided by two APDs, one at each end of the crystal matrix, endeavouring depth-of-interaction (DOI) capability.

In the scope of this thesis, experimental tests were performed in order to characterize the baseline detector module, considering light yield, energy resolution, inter-crystal crosstalk and DOI resolution. 80 detector modules (42% of the total) were measured and average results were obtained with 13–14% energy resolution at 662 keV and a typical DOI resolution of 2.2 mm FWHM. Long-term stability of the detector modules was also appraised, showing a severe degradation in DOI resolution (30% in one year). This degradation was studied and identified to be caused by a aging effect of the optical interface used between the crystal and the APD.

Due to pixelized disposal and detector compactness, inter-crystal crosstalk needs to be assess as it can generate false triggering in channels adjacent to the main event. The degree of crosstalk has critical implications on the specifications of the front-end electronics. Dedicated studies have shown that within the detector module the average crosstalk is small (3 to 7%).

In order to improve the detection sensitivity and spatial resolution of the scanner, the detector module was revised. Permanent optical solutions like Meltmount and Histomount were tested in terms of performance and mechanical properties. Modules assembled with Histomount have shown a superior light collection (20–30% improvement) and DOI resolution (5.5–6%/mm), in comparison with the baseline detector module. Different crystal dimensions and crystal coatings were also compared. Exploratory experimental work was carried out with new crystal matrices, with $2.2\times2.2\times30$ mm$^3$ LYSO:Ce crystals wrapped in a specular reflector (78% packing fraction). Based on these studies, all ClearPEM production detector modules were re-assembled with Histomount coupling medium.

The ClearPEM scanner has two detector planar heads comprising 8 supermodules, in a total of 192 detector modules. The integration of the supermodules was performed successfully and performance test results were in good agreement with the obtained for individual detector modules. In late 2008, the ClearPEM scanner was transfered to IPO Hospital facilities for clinical trials. Characterization of the scanner performance showed a spatial resolution of 1.3–1.6 mm, 15.9% energy resolution at 511 keV and time resolution of 5.2 ns FWHM, in fully agreement with the initial performance requisites.

Key-words: Positron Emission Tomography, Detector Module, Avalanche Photodiodes, Scintillation Crystals, Optical Couplings, Crosstalk.

# Resumo

O detector ClearPEM é um tomógrafo desenvolvido pelo consórcio português PET–Mamografia, no âmbito da colaboração internacional Crystal Clear e do CERN, para a detecção precoce de cancro da mama. O protótipo é baseado em módulos detectores constituídos por cristais cintiladores de LYSO:Ce com 2×2×20 $mm^3$, dispostos numa matriz de $BaSO_4$ de 4×8 cristais, lidos individualmente, por fotodíodos de avalanche pixelizados, possibilitando a determinação da coordenada longitudinal da interacção do fotão no cristal (DOI). Os módulos detectores são lidos por um sistema de electrónica rápida e de baixo ruído, que extrai a informação em tempo e de energia, necessária à selecção de fotões em coincidência.

No âmbito desta tese, foram realizados estudos experimentais de caracterização do módulo detector, considerando a colecção de luz, a resolução em energia, a distribuição do sinal principal entre canais adjacentes (*crosstalk*) e resolução DOI. 80 módulos (42% do total) foram medidos com resultados médios de 13–14% de resolução em energia a 662 keV e uma resolução DOI de 2.2 mm FWHM acompanhada por uma assimetria de colecção de luz de 4 %/mm. Estudos de estabilidade ao longo do tempo mostram uma degradação de cerca de 30% na resolução DOI no período de um ano. A causa desta degradação foi identificada, sendo devido ao envelhecimento do acoplamento óptico utilizado, Rhodorsil Paste 7 grease.

Sendo o módulo detector bastante compacto e pixelizado, o crosstalk entre canais foi considerado como sendo um parâmetro de relevância, uma vez que influencia as especificações da electrónica integrada de frontend (ASIC). Estudos dedicados demonstraram que o *crosstalk* no módulo detector é baixo (3 a 7%).

Com o objectivo de melhorar a sensibilidade de detecção e resolução espacial do tomógrafo, o módulo detector foi revisto. Neste sentido, os acoplamentos ópticos Meltmount e Histomount foram testados em termos de desempenho e propriedades mecânicas. Verificou-se que os módulos montados com Histomount colectavam mais luz (20–30% superior) e obtinham 5.5–6%/mm de assimetria de colecção de luz, em comparação com o módulo de produção. Foram ainda exploradas outras alterações ao módulo, como a utilização de cristais de diferentes dimensões e um novo reflector, realizando-se testes com uma nova matriz de cristais de LYSO:Ce com 2.2×2.2×30 $mm^3$, revestidos por um reflector especular (fracção de empacotamento 78%). Com base nos resultados obtidos neste trabalho, todos os módulos do detector ClearPEM foram remontados com o acoplamento Histomount.

O tomógrafo ClearPEM possui duas cabeças detectoras constituídas por 8 supermódulos, num total de 192 módulos. Procedeu-se à integração dos supermódulos e os resultados dos testes de desempenho estão de acordo com os obtidos com os módulos detectores medidos individualmente. No final de 2008, o detector ClearPEM foi transferido para o IPO-Porto para ensaios clínicos. O desempenho do detector caracteriza-se por 1.3–1.6 mm de resolução espacial, com resolução em energia de 15.9% para 511 keV e resolução temporal de 5.2 ns FWHM, cumprindo os requisitos iniciais do detector.

Palavras-chave: Tomografia por Emissão de Positrões, Módulo Detector, Fotodíodos de Avalanche, Cristais de Cintilação, Acoplamentos Ópticos, Crosstalk.

# List of Publications

The work developed throughout this thesis was subject to publication in the following journals and presentation in conferences.

## Publications in Journals

- R. Bugalho, C. S. Ferreira, M. Frade, M. Ferreira, R. Moura, C. Ortigão, J. F. Pinheiro, P. Rodrigues, I. Rolo, J. C. Silva, R. Silva, A. Trindade, J Varela, *Experimental Characterization of the Clear–PEM Scanner Spectrometric Performance*, accepted for publication in Journal of Instrumentation, JINST 004P 0709, 2009.

- E. Albuquerque, V. Bexiga, R. Bugalho, B. Carriço, C. S. Ferreira, M. Ferreira, J. Godinho, F. Gonçalves, C. Leong, P. Lousã, P. Machado, R. Moura, P. Neves, C. Ortigão, F. Piedade, J. F. Pinheiro, J. Rego, A. Rivetti, P. Rodrigues, J. C. Silva, M. M. Silva, I. C. Teixeira, J. P. Teixeira, A. Trindade, J. Varela, *Experimental characterization of the 192 channel Clear–PEM frontend ASIC coupled to a multipixel APD readout of LYSO:Ce crystals*, Nucl. Instrum. and Methods in Physics Research A, Vol. 598, pp. 802–814, 2009.

- P. Amaral, B. Carriço, M. Ferreira, R. Moura, C. Ortigão, P. Rodrigues, J. C. Silva, A. Trindade, J. Varela, *Performance and Quality-Control of Clear–PEM Detector Modules*, Nucl. Instrum. and Methods in Physics Research A, Vol 580, pp. 1123–1126, 2007.

- M. C. Abreu, P. Amaral, B. Carriço, M. Ferreira, J. Luyten, R. Moura, C. Ortigão, P. Rato, J. Varela, *Characterization and quality control of avalanche photodiode arrays for the Clear–PEM detector modules*, Nucl. Instrum. and Methods in Physics Research A, Vol. 576, pp. 19-22, 2007.

- J. Varela, *Clear–PEM: a PET imaging system dedicated to breast diagnostics. Nucl. Instrum. and Methods in Physics Research A, vol. 571, pp. 81Ű4, 2007.*

- *P. Amaral, P. Bruyndonckx, B. Carriço, M. Ferreira, J. Luyten, R. Moura, C. Ortigão, P. Rodrigues, J. C. Silva, A. Trindade, J. Varela, Long-term Stability of*

*the Clear–PEM detector modules, Nucl. Instrum. and Methods in Physics Research A, Vol. 571, pp. 488-492, 2007.*

- *M. C. Abreu, J. D. Aguiar, F. G. Almeida, P. Almeida, P. Bento, B. Carriço, M. Ferreira, N. C. Ferreira, F. Gonçalves, C. Leong, F. Lopes, P. Lousã, M. V. Martins, N. Matela, P. R. Mendes, R. Moura, J. Nobre, N. Oliveira, C. Ortigão, L. Peralta, R. Pereira, J. Rego, R. Ribeiro, P. Rodrigues, J. Sampaio, A. I. Santos, L. Silva, J. C. Silva P. Sousa, I. C. Teixeira, J. P. Teixeira, A. Trindade, J. Varela, Design and evaluation of the Clear–PEM scanner for positron emission mammography, IEEE Transactions on Nuclear Science 53 (1): 71–77 Part 1, 2006.*

- *M. C. Abreu, P. Almeida, F. Balau, N. C. Ferreira, S. Fetal, F. Fraga, M. Martins, N. Matela, R. Moura, C. Ortigão, L. Peralta, P. Rato, R. Ribeiro, P. Rodrigues, A. I. Santos, A. Trindade, J. Varela, Clear–PEM: A dedicated pet camera for improved breast cancer detection, Radiation Protection Dosimetry 116 (1-4): 208–210, 2005.*

- *R. Ribeiro, M. C. Abreu, P. Almeida, F. Balau, P. Bordalo, N. C. Ferreira, S. Fetal, F. Fraga, P. Lecoq, M. Martins, N. Matela, R. Moura, C. Ortigão, L. Peralta, S. Ramos, P. Rato, P. Rodrigues, A. I. Santos, A. Trindade, J. Varela, Breast imaging with a dedicated PEM, Nuclear Instruments and Methods in Physics Research A 527 (1-2): 87–91, 2004.*

# Publications in Conference Proceedings

- E. Albuquerque, F. G. Almeida, P. Almeida, E. Auffray, J. Barbosa, A. L. Bastos, V. Bexiga, R. Bugalho, S. Carmona, B. Carriço, C. S. Ferreira, N. C. Ferreira, M. Ferreira, M. Frade, J. Godinho, F. Gonçalves, C. Guerreiro, P. Lecoq, C. Leong, P. Lousã, P. Machado, M. V. Martins, N. Matela, R. Moura, J. Neves, P. Neves, N. Oliveira, C. Ortigão, F. Piedade, J. F. Pinheiro, P. Relvas, A. Rivetti, P. Rodrigues, I. Rolo, J. Sampaio, A. I. Santos, J. Santos, M. M. Silva, S. Tavernier, I. C. Teixeira, J. P. Teixeira, R. Silva, J. C. Silva, A. Trindade, J. Varela, *Characterization of the Clear–PEM Breast Imaging Scanner Performance*, Nuclear Science Symposium Conference Record NSS-MIC 2009, 2009.

- E. Albuquerque, F. G. Almeida, P. Almeida, E. Auffray, J. Barbosa, A. L. Bastos, V. Bexiga, R. Bugalho, S. Carmona, B. Carriço, C. S. Ferreira, N. C. Ferreira, M. Ferreira, M. Frade, J. Godinho, F. Gonçalves, C. Guerreiro, P. Lecoq, C. Leong, P. Lousã, P. Machado, M. V. Martins, N. Matela, R. Moura, J. Neves, P. Neves, N. Oliveira, C. Ortigão, F. Piedade, J. F. Pinheiro, P. Relvas, A. Rivetti, P. Rodrigues, I. Rolo, J. Sampaio, A. I. Santos, J. Santos, M. M. Silva, S. Tavernier, I. C. Teixeira, J. P. Teixeira, R. Silva, J. C. Silva, A. Trindade, J. Varela, *The Clear–PEM Imaging Scanner for Positron Emission Mammography*, 14th International Conference on Emerging Nuclear Energy Systems, 2009.

- E. Albuquerque, F. G. Almeida, P. Almeida, S. Augusto, V. Bexiga, R. Bugalho, S. Carmona, B. Carriço, C. S. Ferreira, N. C. Ferreira, M. Ferreira, J. Godinho,

F. Gonçalves, C. Guerreiro, C. Leong, P. Lousã, P. Machado, M. V. Martins, N. Matela, R. Moura, P. Neves, N. Oliveira, C. Ortigão, F. Piedade, J. F. Pinheiro, J. Rego, P. Relvas, A. Rivetti, P. Rodrigues, D. N. Sá, J. Sampaio, A. I. Santos, M. M. Silva, I. C. Teixeira, J. P. Teixeira, J. C. Silva, A. Trindade, J. Varela, *An overview of the Clear-PEM breast imaging scanner*, Nuclear Science Symposium Conference Record NSS-MIC 2008, pp. 5616–5618, 2008.

- E. Albuquerque, F. G. Almeida, P. Almeida, S. Augusto, V. Bexiga, R. Bugalho, S. Carmona, B. Carriço, C. S. Ferreira, N. C. Ferreira, M. Ferreira, J. Godinho, F. Gonçalves, C. Guerreiro, C. Leong, P. Lousã, P. Machado, M. V. Martins, N. Matela, R. Moura, P. Neves, N. Oliveira, C. Ortigão, F. Piedade, J. F. Pinheiro, J. Rego, P. Relvas, A. Rivetti, P. Rodrigues, D. N. Sá, J. Sampaio, A. I. Santos, M. M. Silva, I. C. Teixeira, J. P. Teixeira, J. C. Silva, A. Trindade, J. Varela, *Performance Evaluation of a Highly Integrated APD/ASIC Double-Readout Supermodule with 768 channels for ClearPEM*, IEEE Nuclear Science Symposium Conference NSS-MIC, 2008.

- M. C. Abreu, J. D. Aguiar, E. Albuquerque, F. G. Almeida, P. Almeida, P. Amaral, P. Bento, R. Bugalho, B. Carriço, H. Cordeiro, M. Ferreira, N. C. Ferreira, F. Goncalves, C. Leong, F. Lopes, P. Lousã, M. V. Martins, N. Matela, P. R. Mendes, R. Moura, J. Nobre, N. Oliveira, C. Ortigão, L. Peralta, J. Rego, R. Ribeiro, P. Rodrigues, A. I. Santos, J. C. Silva, M. M. Silva, I. C. Teixeira, J. P. Teixeira, A. Trindade, J. Varela, *First experimental results with the Clear–PEM detector*, Nuclear Science Symposium Conference Record, 2005 IEEE, Vol. 3 (2005), 5 pp.

- B. Carriço, M.C. Abreu, P. Mendes, R. Moura, C. Ortigão, L. Peralta, R. Ribeiro, P. Rodrigues, A. Trindade, J. Varela, *Quality control for Clear–PEM detector modules*, proceedings of the $11^{th}$ IPEM Annual Scientific Conference, 2005.

- A. Trindade, P. Almeida, N. C. Ferreira, M. V. Martins, N. Matela, R. Moura, N. Oliveira, C. Ortigão, P. Rodrigues, J. Varela, *Breast cancer imaging studies by Monte Carlo simulation with Clear–PEM*. IEEE NSS–MIC Conference 2005, Conference Records, Puerto Rico, USA, 2005.

- A. I. Santos, P. Almeida, M. V. Martins, N. Matela, N. Oliveira, N. C. Ferreira, J. D. Aguiar, F. G. Almeida, F. Lopes, J. Sampaio, P. Bento, F. Gonçalves, C. Leong, P. Lousã, L. Silva, I. C. Teixeira, J. P. Teixeira, M. C. Abreu, B. Carriço, P. R. Mendes, R. Pereira, P. Sousa, M. Ferreira, R. Moura, C. Ortigao, L. Peralta, R. Ribeiro, P. Rodrigues, J. C. Silva, A. Trindade, J. Varela, *Design and evaluation of the Clear–PEM detector for positron emission mammography*, Nuclear Science Symposium Conference Record, 2004 IEEE, Vol. 6 (2004), pp. 3805-3809 Vol. 6.

- A. Trindade, P. Almeida, F. Balau, N. Ferreira, S. Fetal, F. Fraga, M. Martins, N. Matela, P. Mendes, P. Mendes, R. Moura, C. Ortigao, L. Peralta, R. Ribeiro, P. Rodrigues, J. Varela, *Clear–PEM: Monte Carlo performance and image reconstruction studies*. IEEE NSS–MIC Conference 2003, Conference Records, Portland, USA, 2003.

# Contents

# List of Tables

# List of Figures

# List of Acronyms and Abbreviations

| | |
|---|---|
| ADC | Analog to Digital Converter |
| APD | Avalanche PhotoDiode |
| ASIC | Application Specific Integrated Circuit |
| CERN | European Organization for Nuclear Research |
| CFD | Constant Fraction Discriminator |
| CMS | Compact Muon Solenoid |
| CPU | Central Processing Unit |
| CT | Computed Tomography |
| DAE | Data Acquisition Electronics |
| DAQ | Data Acquisition |
| DOI | Depth–Of–Interaction |
| ENC | Equivalent Noise Charge |
| FDG | $^{18}$F–Fluoro–Deoxy–Glucose |
| FIFO | First In–First Out |
| FOV | Field–Of–View |
| FPGA | Field Programmable Gate Array |
| FWHM | Full Width at Half Maximum |
| HAL | Hardware Access Library |
| HV | High Voltage |
| LMF | List Mode File |
| LV | Low Voltage |
| LSO:Ce | Ceruim–doped Lutetium Oxyorthosilicate |
| LYSO:Ce | Cerium–doped Lutetium and Yttrium Oxyorthosilicate |
| MRI | Magnetic Resonance Imaging |
| PCB | Printed Circuit Board |
| PCI | Peripheral Component Interconnect |
| PEM | Positron Emission Mammography |
| PET | Positron Emission Tomography |
| PMT | PhotoMultiPlier |
| RMS | Root Mean Square |
| SNR | Signal–to–Noise Ratio |
| STIR | Software for Tomographic Image Reconstruction |
| TDC | Time to Digital Converter |
| US | Ultra–Sound |
| USB | Universal Serial Bus |
| VME | VERSA Module Eurocard |

# Introduction

Positron Emission Tomography (PET) is a well established nuclear medicine imaging technique, widely use in Oncology, Cardiology and Neurology, to detect cancer tumors and search for metastases, heart disease and certain brain disorders. It produces a image or map of functional processes in the body, by the injection of a short-lived radioactive tracer isotope, which decays by emitting a positron, that also has been chemically incorporated into a biologically active molecule, into the blood stream. As the radioisotope undergoes $\beta^+$ decay, it emits a positron which annihilates with an electron of the medium, producing a pair of photons moving in opposite directions that are detected by the scanner to create the image.

Cancer is a leading cause of death worldwide: it accounted for 7.9 million deaths (around 13% of all deaths) in 2007. Lung, stomach, liver, colon and breast cancer cause the most cancer deaths each year [WHO2008]. Breast cancer is the second leading cause of cancer deaths in women today after lung cancer, and is the most common cancer among women, excluding nonmelanoma skin cancers. According to the American Cancer Society, about 1.3 million women will be diagnosed with breast cancer annualluy worldwide [Imaginis2008]. About one-third of the cancer burden could be decreased if cases were detected and treated early.

Motivated by these facts and numbers, the Portuguese PET–Mammography Consortium, within the framework of the international Crystal Clear Collaboration at CERN, has been developing, building and testing the ClearPEM detector, a compact high-resolution scanner for breast cancer detection, exploiting state-of-the-art technology and knowledge transfer from high energy particles detectors to medical imaging, improving the detection of early stage breast cancer, comparatively to actual screening techniques.

Breast cancer detection with PET requires good time and energy resolution, to minimize random events from outside the field-of-view as 99% of the injected dose is located outside the FOV, and reduce scattered events in the object, high sensitivity, to have less injected dose or faster exams, and spatial resolution down to 2 mm. In order to accomplish these requirements, the detector module must be compact and with high-Z scintillation crystals to improve the detection efficiency of the 511 keV photons. To achieve a desirable spatial resolution after reconstruction, pixelized crystals are required in a 1:1 coupling scheme

readout, and the detectors must be able to measure the depth-of-interaction of the incoming photons to avoid parallax effect.

The PET-Mammography consortium comprises several national institutions, with well defined responsibilities, where LIP – Laboratório de Instrumentação e Física Experimental de Partículas is responsible for the detector design, simulation studies, experimental tests, integration and co-responsible for the development of the data acquisition electronics, operation and image correction reconstruction software. In order to perform experimental tests with radioactive sources, a new working area was needed and TagusLIP laboratory was born to address this necessity.

After five years working in the ClearPEM project, it was inevitable the wish of telling a story. This thesis focuses on the evolution of the ClearPEM detector module along this period, as it was meant to be on the year of 2004, at the start-up of the TagusLIP laboratory, to its present stand, assembled in the detector heads of the prototype in preclinical phase, evolving through all experimental tests, driven achievements and major conclusions that conduced to the actual and revised detector module.

This journey begins with a brief introduction of the ClearPEM project, its main goals and motivations (**Chapter 1**), followed by the description of the TagusLIP laboratory, its purposes and main equipment, including a environmental radiation evaluation according to law requisites of safety for personnel working with radioactive material, and also the explanation of the discrete electronic setups, specially developed for APD (Avalanche Photo Diodes) readout, with which substantial experimental tests were performed, before the ClearPEM front-end ASIC has been available (**Chapter 2**).

Thus said, it is time to characterize the baseline ClearPEM detector module, with a insight view of all its components and mechanical assembly, primary studies and first proof-of-principle results (**Chapter 3**). As the detector module is a key element to the full ClearPEM scanner performance, exhaustive dedicated testbenchs were accomplished to characterize light collection, energy resolution, DOI (depth of interaction) resolution, APD response and long-term stability.

Also the study of crosstalk and its main contributors within the detector module had required special attention (**Chapter 4**), as the degree of crosstalk has critical implications on the specifications of the front-end electronics, which has 12 288 channels, as a result of the 1:1 crystal-pixel APD coupling scheme, that enable the DOI measurement capability. Evaluation of the electrical and optical crosstalk on S8550 APD was also performed.

**Chapter 5** presents the experimental efforts and results that led to a revised detector module, which improves the light collection and detection sensitivity of the ClearPEM scanner. Optimization of the optical coupling media led to a improved light collection stability with direct consequences in the performance of the detector module. Studies of the detector module packing fraction and detection efficiency with a new LYSO crystal matrix were explored.

The integration of the detector modules in supermodule arrangement into the ClearPEM detector heads is described in **Chapter 6**. The validation of the supermodules (each unit is a set of twelve detector modules) was performed before the final assembly. The tests of the supermodules allowed to assess the performance of the detector modules in their final working environment, combining instrumentation effects introduced by the frontend electronics readout and the processing of the data flow by the data acquisition electronics and trigger system. After validation, the supermodules were inserted in the ClearPEM detector heads and the performance characterized in terms of energy resolution, DOI resolution, light collection, linearity and time resolution. A preliminary evaluation of the system sensitivity is also presented.

Finally, the story ends with **Summary and Conclusions**.

Chapter 1

# Breast Cancer Detection with PET

## Contents

## 1.1 Positron Emission Tomography (PET)

Positron emission tomography (PET) is an imaging technique that measures metabolic activity of the cells of body tissues and is used mostly by oncologists, in the detection of cancer and the evaluation of cancer treatment, by neurologists and neurosurgeons, in monitoring and surgery of the brain and nervous system, and by cardiologists, in the diagnosis of heart diseases.

PET is actually a combination of nuclear medicine and biochemical analysis and differs from other nuclear medicine examinations in that PET images provide information about the function and metabolism within body tissues, whereas other types of nuclear medicine procedures detect the amount of a radioactive substance collected in body tissue in a certain location to examine the tissue's function. PET may detect biochemical changes in an organ or tissue that can identify the onset of a disease process before anatomical changes related to the disease can be detected with other imaging processes such as computed tomography (CT) or magnetic resonance imaging (MRI)[HSVU2008].

To provide images of the body, PET uses a radiopharmaceutical (radionuclide or radioactive tracer) which decays by positron emission and that is administered to the patient either into the blood stream or inhaled as a gas. Positrons are emitted by the breakdown of the radionuclide, through a $\beta^+$ decay process. The positron annihilates with an electron of the medium, producing a pair of 511 keV photons emitted at 180 degrees that are then detected by the scanner in temporal coincidence ($\leq$ 20 ns). Dedicated hardware and software analyze the reconstructed energy and time of the 511 keV photon pair and use the information to create an image map of the organ or tissue in observance. The amount of the radionuclide collected in the tissue affects how brightly the tissue appears on the image, and indicates the level of organ or tissue function.

Originally, PET procedures were performed in dedicated PET centers, because the equipment to make the radiopharmaceuticals, including a cyclotron and a radiochemistry laboratory, had to be available in addition to the PET scanner [Muehllehner2006]. Now, the radiopharmaceuticals are produced in synchrotrons by dedicated companies and are sent to PET centers, only when a PET scan is required.

The radiopharmaceuticals used in PET scanners include in the composition radionuclides that decay by positron emission bounded to chemical substances such as glucose, carbon, or oxygen used naturally by the particular organ or tissue during its metabolic process. The most commonly used positron emitting tracer in the field of oncology is the glucose analogue ($^{18}$F)fluoro-2-deoxy-D-glucose ($^{18}$F-FDG), which is taken up like glucose but is not metabolized through the entire mitocondrial Krebs cycle. Instead, it becomes metabolically trapped within the cell and allows the detection of metabolic alterations within cells. High concentration of $^{18}$F-FDG in an organ or tissue typically indicates abnormal metabolism or cell proliferation, a distinguishing mark of malignant tumours and cancer metastases [Schilling2008].

In general, PET scanners may be used to evaluate organs and/or tissues for the presence of disease or abnormal conditions and other radiopharmaceuticals may be applied for PET scanning, depending on the purpose of the scan [Smith1999]. PET may also be used in conjunction with anatomical diagnostic techniques such as computed tomography (CT) or magnetic resonance imaging (MRI) to provide more definitive information about malignant tumors and other lesions. An example of typical images obtained with mutimodality PET/CT is shown in Fig. 1.1.

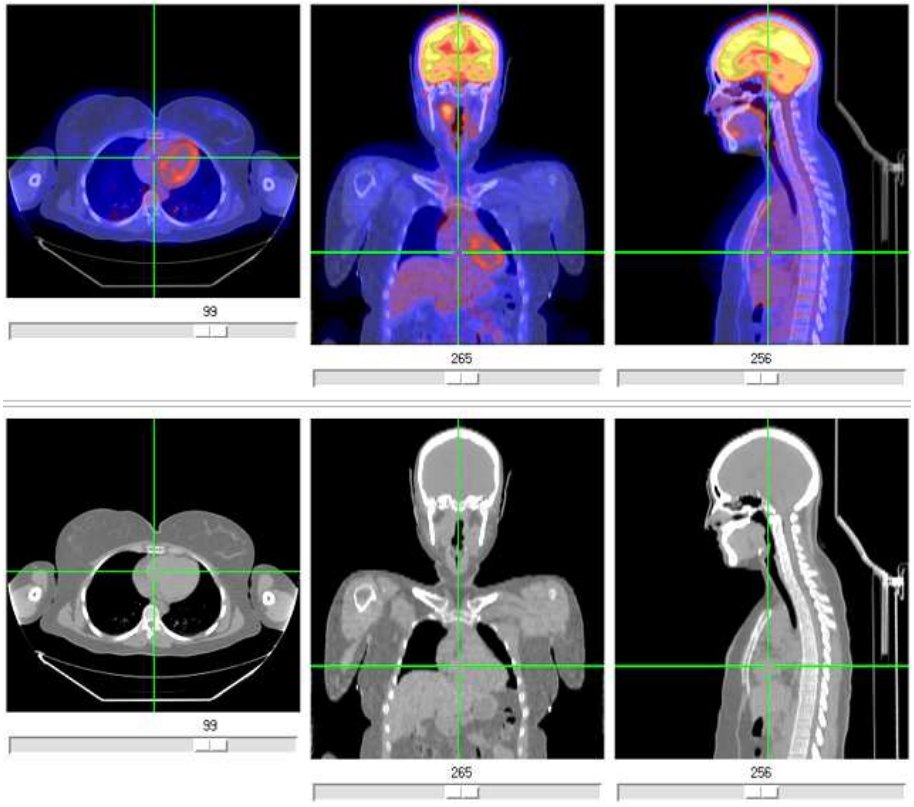


Figure 1.1: Typical multimodality PET/CT scan.

## 1.2 Positron Emission Mammography (PEM)

Breast cancer is the second leading cause of cancer deaths in women today (after lung cancer) and is the most common cancer among women, excluding nonmelanoma skin cancers. According to the American Cancer Society, about 1.3 million women will be diagnosed with breast cancer annually worldwide [Imaginis2008]. About one-third of the cancer mortality could be decreased if cases were detected and treated in an early stage.

One of the major goals of breast imaging is to detect small cancer lesions so that treatment may be initiated when the clinical outcome is most favourable. Once a cancer has been detected, it is useful to demonstrate the extent of the lesion for surgical planning and to identify other foci of tumor in the breast. These tasks are not reliably performed even with the best tools currently in general use (mammography and ultrasound). A

key reason for the limited efficacy of conventional imaging is the limitation to anatomic depictions. With the addition of functional imaging, however, it is possible that mammographically occult disease may be better characterized, benign lesions may be recognized as such, and unsuspected tumors may be detected [Levine2003].

PET instruments customized for breast applications, commonly known as Positron Emission Mammography (PEM), have been shown to exhibit superior technical characteristics for imaging small lesions in the breast [Levine2003]. Compared with whole-body PET, PEM scanners can better image small breast lesions and provide more accurate localization. Images obtained with a commercial PEM scanner are shown in Figs 1.2 and 1.3. Preliminary results from clinical trials with the Naviscan PEM scanner, indicate a sensitivity (defined as the number of detected lesions over the total number of lesions) of 92% (decreasing down to 88% for lesions smaller than 5 mm) and a specificity (defined as the number of true positive lesions over the total number of detected lesions) of 93%. In comparison whole-body PET, when applied to breast cancer detection, show a sensitivity of 80% and a specificity of 76%. In a study with this PEM scanner, 250 patients with breast cancer were scanned. Of 124 malignant lesions imaged, PEM detected 114 for an overall sensitivity rate of 92 percent. Eighteen percent were ductal carcinoma in situ (DCIS), a noninvasive cancer confined to the ducts of the breast; 82 percent were invasive cancer. PEM successfully detected cancer in about: 100 percent of fatty breasts; 96 percent of dense breasts; 91 percent of extremely dense breasts; 93 percent of women both with and without a history of hormone replacement therapy; 88 percent of pre-menopausal women; 95 percent of post-menopausal women.

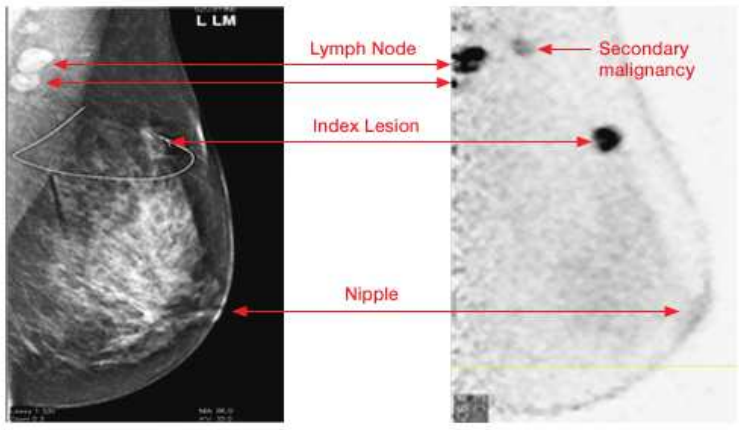


Figure 1.2: Clinical case of a breast imaged with X-ray mammography (*left*) and the Naviscan PEM scanner (*right*). The mammography scan found an index lesion but missed the secondary malignancy detected with PEM. A metastasized cancer lesion was also identified with PEM.

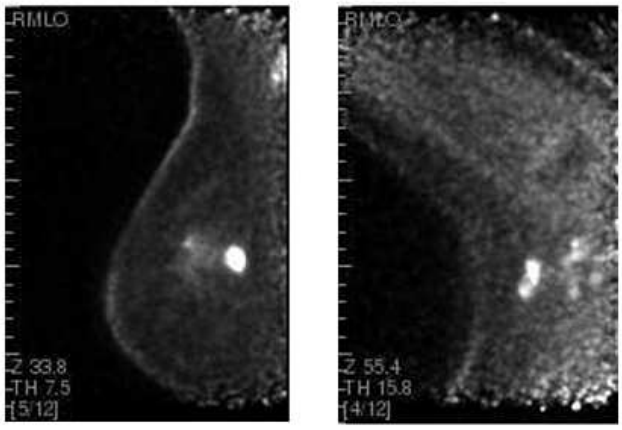


(a) (b)

Figure 1.3: Clinical case of a breast and axilla region imaged with the Naviscan PEM scanner. (right) Intraductal carcinoma at 2:00 right breast with intraductal extension. (left) The right axilla has also numerous lymph nodes showing FDG uptake consistent with metastatic disease.

The guiding principal behind PEM instrumentation is that a camera whose Field-Of-View (FOV) is restricted to a single breast will have significantly higher performance and lower cost than a conventional PET camera. By placing the detectors close to the breast, the PEM geometry is able to subtend more solid angle around the breast than a conventional PET camera. In addition, it provides reduced attenuation and higher coincident count rates for image production as the 511 keV photons emitted in the breast have to pass through at most one attenuation length ($\sim$10 cm) of tissue in the PEM geometry, but may have to travel through as much as four attenuation lengths of tissue in a conventional PET camera [Moses2003].

## 1.3 The ClearPEM Scanner

### 1.3.1 Motivation and General Design Principles

Several designs for PET cameras have been optimized to image the breast since 1994, when the first feasibility study had been reported by Thompson *et al* [Thompson1994]. An ideally breast imaging technique should be able to detect and diagnose primary tumors, determine the extent of the disease to regional lymph nodes as well as detect tumor recurrences and follow-up of patients after surgery, chemotherapy and/or external radiotherapy [Trindade2007].

Under this context, the Portuguese PET–Mammography Consortium, within the framework of the international Crystal Clear Collaboration at CERN, has been developing,

building and testing the ClearPEM detector, a compact high-resolution scanner for early breast cancer detection, exploiting state-of-the-art technology and knowledge transfer from high energy particles detectors to medical imaging, in order to avoid some of limitations found in the first generation of PEM scanners [Rodrigues2007].

The ClearPEM scanner was developed based on three main guidelines [Abreu2006]: low background, minimizing the fraction of random coincidences under a high flux of single photons (up to 10 MHz); high sensitivity; and spatial resolution down to 2 mm. The first requirement arises from the fact that in this type of exams 99% of the injected dose is located outside the FOV. As a result, the scanner must cope with a large single photon rate which imposes the use of fast radiation sensors and readout electronics, capable of achieving high-resolution time measurements. The second prerequisite, the high sensitivity, intends less injected dose or faster exams. In order to accomplish this requirement, the ClearPEM imaging system uses high-Z scintillation crystals to improve the detection efficiency of the 511 keV photons and exploits both photoelectric and Compton interactions in the detector improving substantially the detection sensitivity. In the case of Compton events, the reconstruction of the scattering topology is required in order to not degrade the spatial resolution. The trigger and data acquisition system is able to process and acquire two-hit interactions in the detector head, corresponding to Compton diffusion followed by photoelectric absorption, which are reconstructed using the energy and coordinates of the measured hits. Finally, in order to achieve the required 2 mm spatial resolution after reconstruction, the detectors must be able to measure the depth-of-interaction of the incoming photons [Varela2007].

Due to the small lesion dimensions in the early stage of the disease, detection techniques require a large sensitivity and high resolution, with the aim to increase the signal over background significance. The point source sensitivity of a PET scanner can be defined in first approximation as [Rodrigues2007]:

$$\eta_p = \Omega_{solid\ angle} \times \xi^2_{packing\ fraction} \times \varepsilon^2_{detector\ efficiency} \tag{1.1}$$

where $\Omega_{solid\ angle}$ stands for the subtended solid angle at the symmetry center of the system, $\xi_{detector\ efficiency}$ is the scintillator sensitivity for 511 keV photons and $\varepsilon_{packing\ fraction}$ is the ratio between the actual scintillator volume and the ideal scintillator material volume. In order to compensate the larger ring diameter, PET scanners are usually equipped with multiple rings of detector elements, having a direct impact in the final cost of the system.

The reconstructed spatial resolution in millimetres ($\Gamma$) measured at full width half maximum can be described as [Dezenzo1993, Lecomte2004]:

$$\Gamma = a\sqrt{(d/2)^2 + b^2 + 0.0022D^2 + r^2} \tag{1.2}$$

where $d$ is the crystal cross-section, $b$ is the contribution to the spatial resolution introduced by the different scintillation light readout schemes, $D$ is the diameter of the detector ring used to describe the contribution from annihilation photon noncollinearity

and $r$ is the effect of the positron range in tissue before annihilation. The factor $1.1 < a < 1.3$ depends on the algorithm used to reconstruct the image and typically takes value of $a = 1.2$ when using filtered backprojection reconstruction with a ramp filter [Lecomte2004]. Positrons emitted from the $\beta^+$ decay of the tracer radioisotopes used in PET undergo an energy loss mechanism, mainly due to the ionization of the atoms of the medium, before they annihilate in two 511 keV photons. In-flight annihilation is largely suppressed and the cross-section only becomes significant when the positron has loss most of its initial kinetic energy. Due to the thermal or orbital movement of the electrons of the medium, the rest energy of the electron-positron system is not zero. In this case, the annihilation will not produce photons exactly with 511 keV energy and the corresponding angular distribution will show some spread from the expected back-to-back emission. For a ring with 80 cm diameter, the contribution from noncollinearity reaches 2.1 mm, but is almost negligible ($\leq$ 0.33 mm) in a small dedicated scanner for rats and mice imaging (D $\leq$ 15 cm) [Lecomte2004]. To be economic viable, blocks of crystal material are made either by cutting a solid piece of scintillator part-way through to various depths and coupling this to four photomultipliers, or by coupling individual crystals to a glass light guide which has a similar pattern of cuts [Thompson2005]. When combined, these factors contribute to a spatial resolution between 5 mm to 8 mm. A 1:1 coupling between the scintillator and the readout element could bring $b$ to 0, but increasing even more the cost of a whole-body PET [Rodrigues2007].

Even assuming a small dedicated scanner, to achieve a good reconstructed image resolution, the intrinsic detector resolution must be kept as low as possible and this concept was explored on the development of the ClearPEM detector module, with a 1:1 coupling scheme. The position accuracy can be scale down to the size of individual crystals (Chapter 3), to obtain a spatial resolution only limited to the crystal size, and be improved by special crystal surface treatment and assembly (Chapters 3 and 5). In the same way, inter-crystal crosstalk has to be small as it has important implications in the data acquisition scheme (Chapter 4), allowing to have $b \approx 0$. Sensitivity also played a central role on the development of the ClearPEM system. The detector heads close to the object provide a large angular coverage and the double readout for depth-of-interaction measurement minimize the so-called parallax effect. In spite of the significant development, optimization of packing fraction and detector efficient of the detector module in terms of new high-Z stopping power crystals, with adequate thickness to improve photoelectric interaction probability, as well as new optical coupling materials and reflectors, is a continuous work (Chapter 5).

### 1.3.2 ClearPEM Detector Layout

The Clear-PEM scanner has two parallel detector heads each one comprising 96 detector modules. The baseline detector module, which design was carried out at LIP in the scope of this thesis, with double readout has avalanche photodiodes arrays (APDs) that collect the light from 2×2×20 mm$^3$ LYSO:Ce crystals which are assembled on a 4×8 matrix, individually encased in $BaSO_4$. Double readout architecture in a 1:1 scheme is provided by two Hamamastu S8850 APDs, one at each end of the crystal matrix, endeavouring

depth-of-interaction (DOI) capability (see a detailed explanation and characterization of the detector module in Chapter 3). Twelve detector modules are mechanically fixed and electrically connected to top and bottom front-end electronics boards forming a supermodule - Fig. 1.4. Eight supermodules are mounted in a detector head, covering a 16.5×14.5 $cm^2$ field-of-view [Abreu2006] - Fig. 1.5.

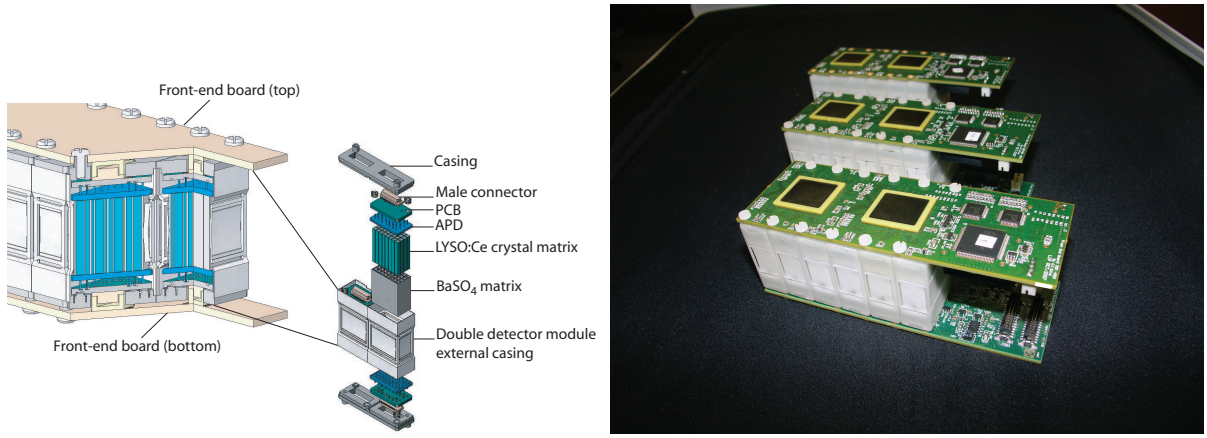


Figure 1.4: A cut-side view of a supermodule with a exploded detector module (*left*) and photograph of ClearPEM supermodules (*right*).

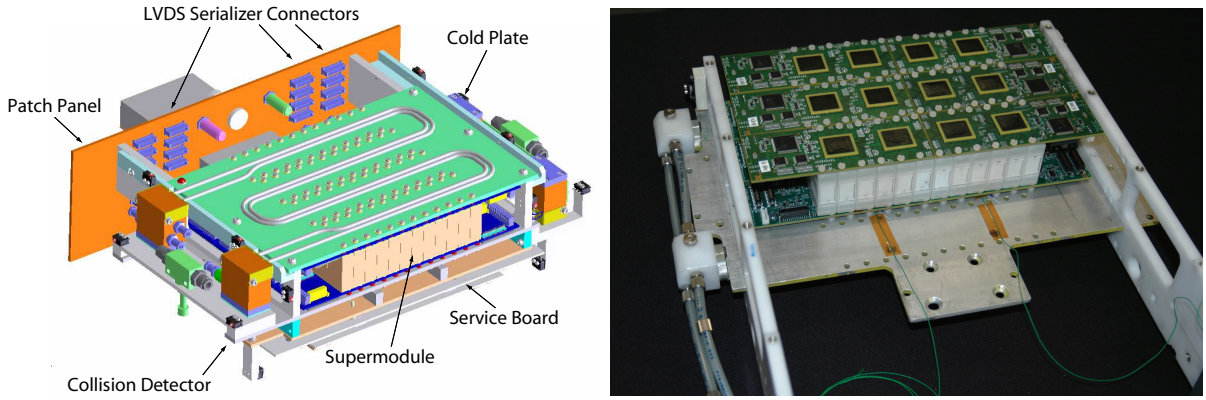


Figure 1.5: Schematic view of a ClearPEM detector head, where main components are pointed out (*left*) and photograph of the detector heads (*right*).

The detection heads are mounted on a robotized mechanical system, enabling the exam of both breasts - Fig. 1.6 (*left*), as well as the axillary lymph nodes - Fig. 1.6 (*right*). It is necessary to examine the axillary lymph nodes in staging the disease, because though breast cancer has the potential to spread to other regions of the body first, it most commonly spreads primary to the axillary lymph nodes, known as regional spread. From there, the breast cancer can metastasize systematically to other areas of the body (such as the bone, liver, lung, or brain). The system is used in conjunction with a examination table that makes possible the exam to be performed with the patient in prone position, with the breast well separated from the body. Configurable openings in the examination

table allow the exam of both breasts with the detector heads positioned in each side of the breast (standard exam).

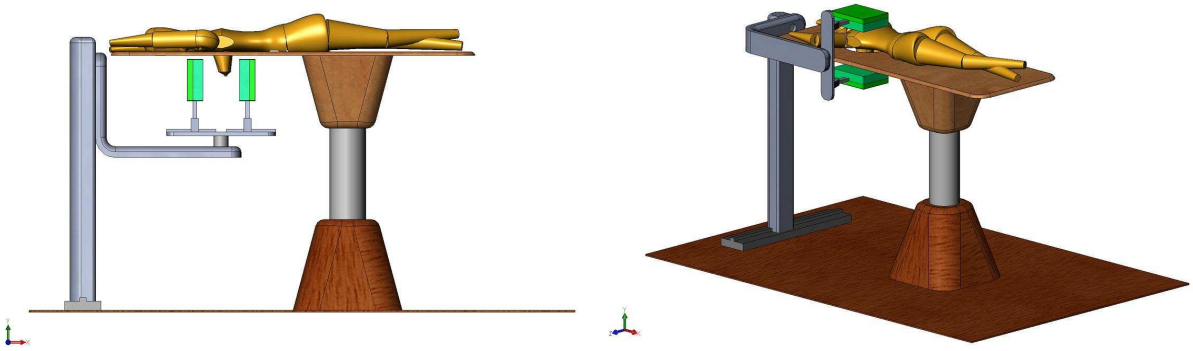

Figure 1.6: Clear-PEM scanner conceptual drawings showing the breast (*left*) and axilla (*right*) examination configurations.

During the exam, the detector heads can rotate around the detector main axis, collecting data at several angular orientations as required for tomographic image reconstruction. The examinations of the breast region close to the chest and of the axilla region are performed in a front-back configuration. One detector head is facing the breast (complementary exam) or the axilla region under the scanner table and the other is positioned against the patient back. Since the area of interest will be imaged across the body, the attenuation is expected to be higher and, in this case, attenuation corrections may be mandatory and small angle image reconstruction techniques have to be developed. The position of the detector heads, as well as their separation, can be adjusted to fit the anatomical region under analysis, minimizing the contribution of the annihilation noncollinearity photon emission to less than 0.2 mm, for a reference detector heads separation distance of 10 cm [Rodrigues2007].

### 1.3.3 ClearPEM Electronics and Data Acquisition System

In the ClearPEM scanner, the electronic system functionality is partitioned into front-end electronics, coupled to the detector heads, and a off-detector trigger and data acquisition electronics [Albuquerque2006]. The front-end electronic block is responsible for analogue signal detection, directly connected to the top or bottom of a crystal plane. Amplifiers and multiplexer integrated circuits (ASIC) and the free-sampling analogue to digital converters (ADCs) are the main components of the front-end electronics. After serialization, digital signal cables connect the front-end blocks to the off-detector electronics which are housed in a standard crate system. Accepted data is sent to a host computer for a second level of event filtering before image reconstruction [Abreu2006].

#### 1.3.3.1 Front-End Electronics

The front-end electronics system, physically located on the detector heads, performs signal amplification, channel selection and analog multiplexing, analog to digital conversion and

parallel-to-serial translation. The front-end electronics development has been centered on the design of a low noise amplifier, due to the initial reduced charge at the amplifier input, and multiplexer VLSI ASIC. The front-end chip needs to amplify this charge by about three orders of magnitude, while complying with the low-power dissipation requirements, compatible with a compact cooling system. A cooling system is required since the LYSO:Ce light yield and APD gain are inversely dependent on the temperature. The collected charge at the input is constrained by the S8550 APD gain, crystal-APD pixel size mismatch, and to the fact that in each crystal the light is split by two photosensors. The need to readout 12 288 channels placed in a very constrained space demands that the front-end ASIC, developed by INESC-ID and INFN-Torino for this project, has an unprecedent level of integration - Fig. 1.7. This chip performs the readout of one side of six modules (total of 192 APD pixel channels), amplification, sampling and storage in analogue memories and the selection of two active channels (192:2 multiplexing) above a common threshold - Fig. 1.8.

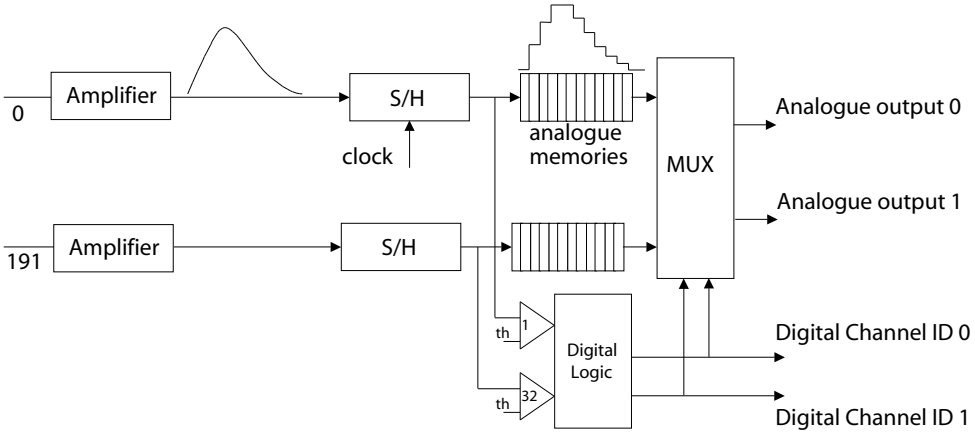


Figure 1.7: ASIC functional scheme.

Power and cabling constrains required that some form of multiplexing and zero suppression should be implemented in the chip, keeping to a minimum the number of output channels. The number of output channels in a scanner based on crystals with small cross-section has to be chosen adequately in order to avoid significant losses of information, that could compromise the detection sensitivity of two photon events in coincidence. Monte Carlo results show that in the case of ClearPEM about 53% of all coincidences will have two or more crystal hits in a given detector head per event. Therefore, the number of output channels for the front-end ASIC should be 2, still allowing for the readout of multi-Compton interactions (more than 2) in the scanner if the event is readout by two different ASIC regions ("Trigger Cell"). If three or more channels are found active, i.e. two channels are already transmitting two dataframes and a request is made to transmit a third, an error code is produced indicating the occurrence of an overflow condition. The operates in data-driven synchronous mode, such that the output samples have fixed latency relative to the input pulse. No dedicated trigger signal is generated by the front-end system, otherwise it would require sophisticated discriminators. Instead, the trigger information is extracted from the main data flow in the off-detector system. Each analogue

dataframe is composed of 10 samples and stored in analogue memories. The pre-samples are used by the off-detector electronic system for pedestal estimation and correction on an event-by-event basis.

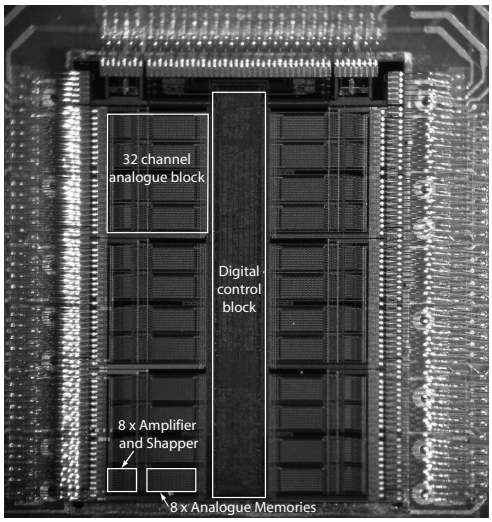


Figure 1.8: Photograph of a bare die.

The analogue samples are digitized in the front-end by 10-bit sampling ADCs. The digital data are serialized in low-voltage differential signaling (LVDS) bit streams and transmitted to the off-detector system. The transmission of 10-sample dataframes per detector pulse to the trigger and data acquisition system represents a more flexible way to adapt the trigger algorithms [Albuquerque2006].

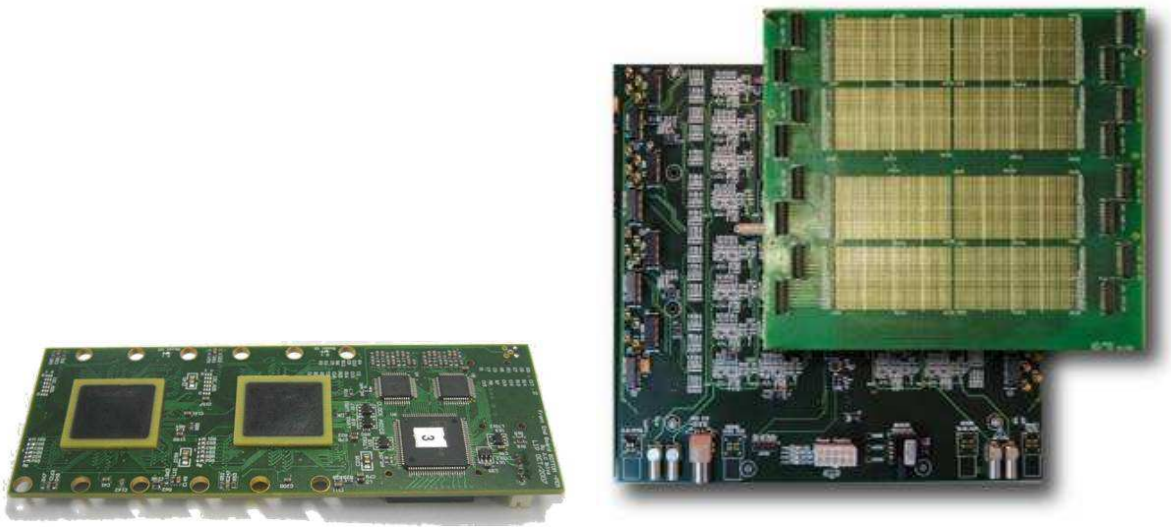

Figure 1.9: Photographs of a Front-End Board (*left*) and Service Board (*right*).

In Fig. 1.9 it is shown a Front-End Board (FEB) with bonded ASICs (left) and the Service Board (right) developed at LIP, which distributes the LV voltage lines to the

front-end chips, ADCs and the HV bias voltages to the APDs. The Service Board provides also temperature measurements to the software monitoring system, which is essential to control the APDs gain. The Service Board is also responsible for the fanout of clock, synchronization, test and reset lines to the front-end boards.

The cooling system, designed and built by INEGI, is based on a computer controllable flux of cold water, capable of keep a constant temperature, up to 0.1% r.m.s around the target temperature. The target temperature can be set bewteen 10 °C and 20 °C. The estimated power dissipation per detector head is 60 W. Water is carried by thin aluminium tubes to cool the dissipation plates. In the patient port the dissipation plate is built in graphite, in order to minimize the amount of non sensitive material placed in the path of the photons.

#### 1.3.3.2 Data Acquisition Electronics

The off-detector DAQ system, developed by INOV/INESC-ID under LIP coordination, is housed in a 6U crate with two dedicated buses (Trigger and Data) implemented in CompactPCI backplanes (Fig. 1.10). Two types of electronic boards were developed and produced: Data Acquisition Boards (DAQ Boards) and the Trigger and Data Concentrator Board (TGR/DCC Board) equipped with 4 and 2 million gates Xilinx Virtex II FPGAs, respectively - Fig. 1.11. DAQ Boards perform the initial phase of data reduction/selection (pipeline data storage, parallel algorithmic processing to extract the amplitude and time of the detector hits) and transmit the potentially interesting events to the TGR/DCC Board which performs the trigger candidate selection. The energy, time extraction algorithms and their impact on trigger performance are discussed in more detail in [Rodrigues2007].

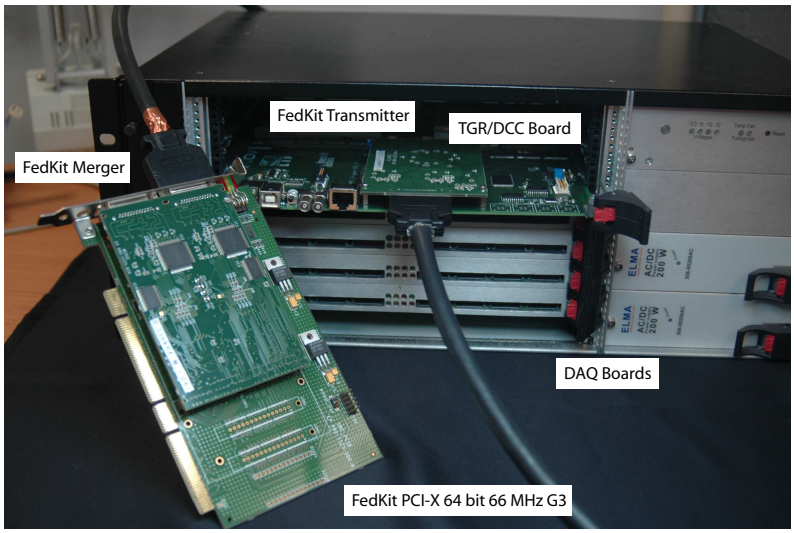


Figure 1.10: ClearPEM off-detector data acquisition electronics.

Two types of coincidence triggers operate simultaneously in the TGR/DCC Board: coincidence trigger in which candidate hits with timetags less than the coincidence window are accepted and random coincidence trigger in which timetags before comparison are

randomized. At each trigger, complete dataframes of the identified detector hits are transmitted to the Acquisition servers (Acquisition Manager) via a fast data link with a throughput of 400 Mbyte/s (Fig. 1.10). The S–Link64 is a FIFO-like interface standard, originally developed at CERN, for generic data readout with a maximum throughput of 800 MByte/s. The standard defines a hardware, link specifications and a common 64–bit words data format. The format encapsulates the detectors specific raw-data in a common envelope, consisting of a header, trailer and generic payload. Several research and commercial boards were developed upon this standard. For the ClearPEM scanner, the CMS (Compact Muon Solenoid experiment at CERN) implementation named FEDkit was adopted after some adaptations performed by LIP [Bugalho2008].

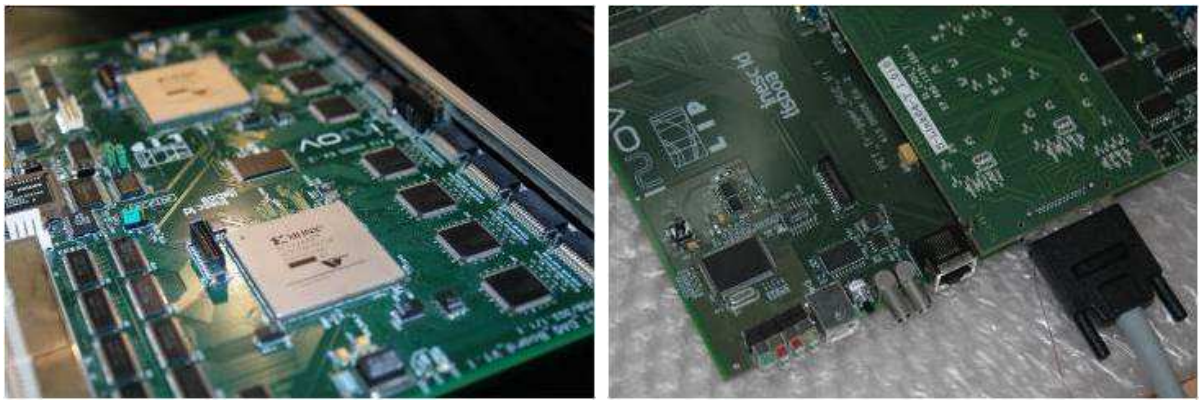

Figure 1.11: 6U DAQ Board (*left*) and 6U TGR/DCC Board (*right*).

Both type of boards possess a Built-In-Self-Test [Leong2005] which is used from the early phase of component testing up to the level of system testing after the final detector electronics integration. FPGAs firmware was developed and bit-level comparisons between FPGA VHDL testbenches against a C++ high-level FPGA simulation performed. Front-end dataframes were generated from Geant4 simulations and used as test vectors for the VHDL testbench and C++ FPGA simulations. For each front-end dataframe features like, pulse peak search, pedestal computation, energy and time extraction and trigger candidates selection were evaluated. A perfect match at bit-level between the outputs of the energy and time extraction algorithms was accomplished.

#### 1.3.3.3 Control System

The ClearPEM control system, developed by IBILI and LIP, is divided into three sub-systems namely, the Acquisition Manager, the Acquisition Tool and the Service Manager. Each sub-system runs in dedicated servers interconnected through a private Gigabit LAN switch. The Acquisition Tool runs on a single-CPU dual-core computer that is physical located in the control room of the ClearPEM scanner at the Hospital (Fig. 1.12). The Acquisition and Service Manager servers are placed in a rack together with the High and Low Voltage units, that in the Hospital are located also in a technical room (Fig. 1.13). The Acquisition Tool is the front application available for the technician or medical doctor who wants to perform a patient examination with the ClearPEM scanner [Trindade2007].

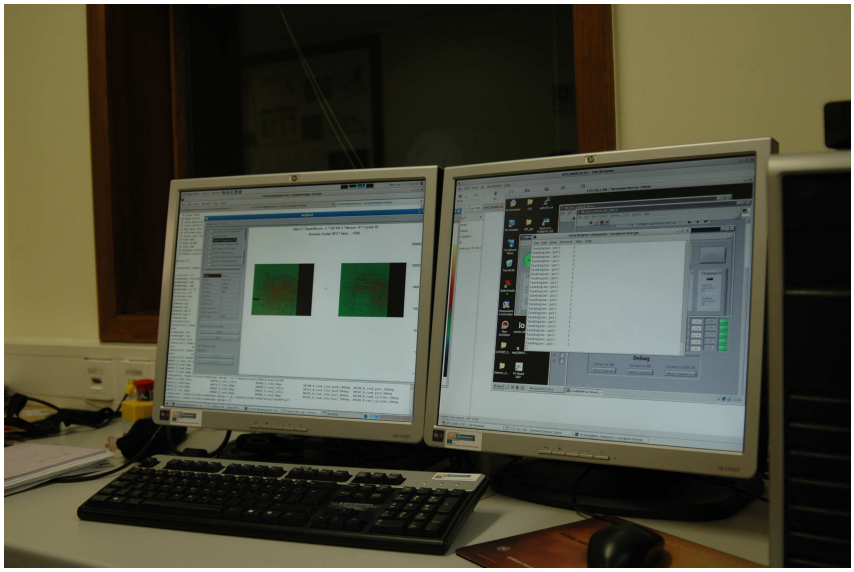

Figure 1.12: Photograph of the Acquisition Tool at IPO–Porto.

After each exam, the scanner operator can perform the image reconstruction through the Acquisition Tool application. Several algorithms specifically developed by IBEB to deal with data acquired with the ClearPEM scanner are available to be used. The reconstructed images can then be displayed using the visualization tool that allows to visualize, manipulate and analyze the imaging data sets obtained with the scanner. Image correction techniques, developed at LIP, that allow to correct Compton scattering in the breast, random coincidences and photon attenuation are also available [Ferreira2009].

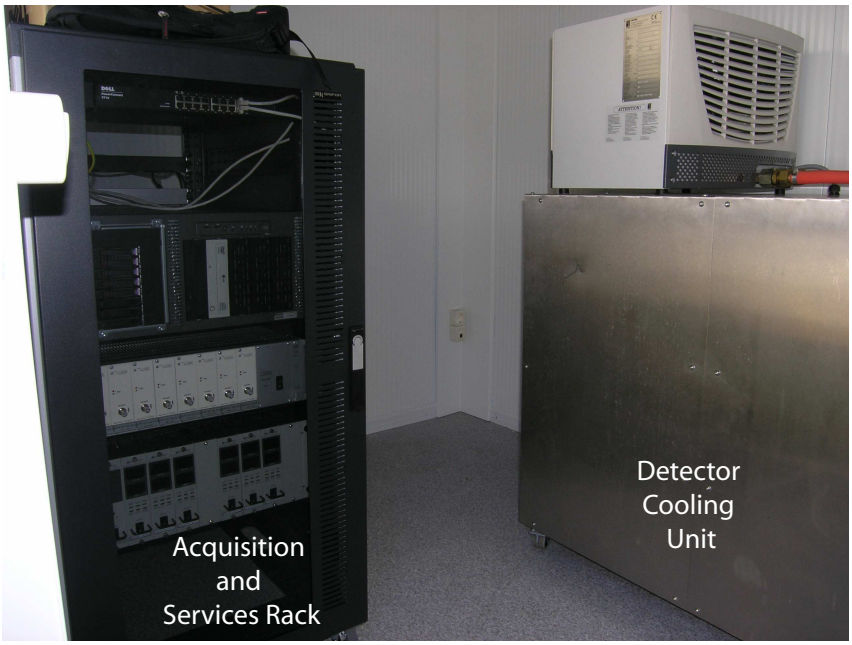


Figure 1.13: Photograph of the rack in the technical room at IPO–Porto.

### 1.3.4 Detector Integration Status

The ClearPEM scanner integration was concluded in 2008. Due to logistics-related time constraints, only 75% of the total number of crystal matrices were initially assembled. The remaining 25% will be inserted in the end of 2009, during an upgrade intervention. The two detector planar heads comprising 16 supermodules, were assembled successfully and validation tests followed (Chapter 6) at IPO–Porto. In Fig. 1.14 it can be seen the two detector heads assembled for a demonstration exercise at TagusLIP (Chapter 2) before the final deployment at IPO–Porto and on Fig. 1.15 a picture of the ClearPEM scanner with the examination table, integrated in the robotic system, at the IPO–Porto Hospital facilities, where pre-clinical trials have started in May 2009.

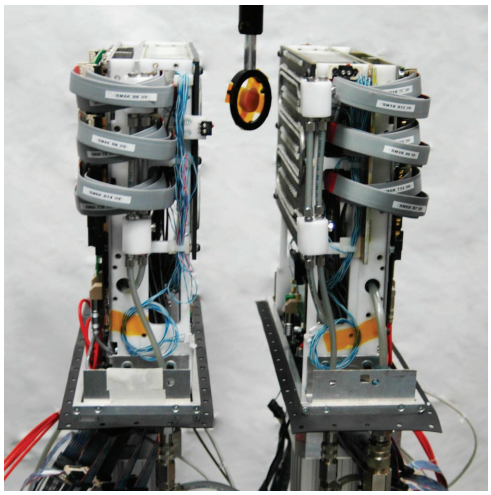

Figure 1.14: Photograph of the Clear-PEM detector heads during the integration phase at TagusLIP.

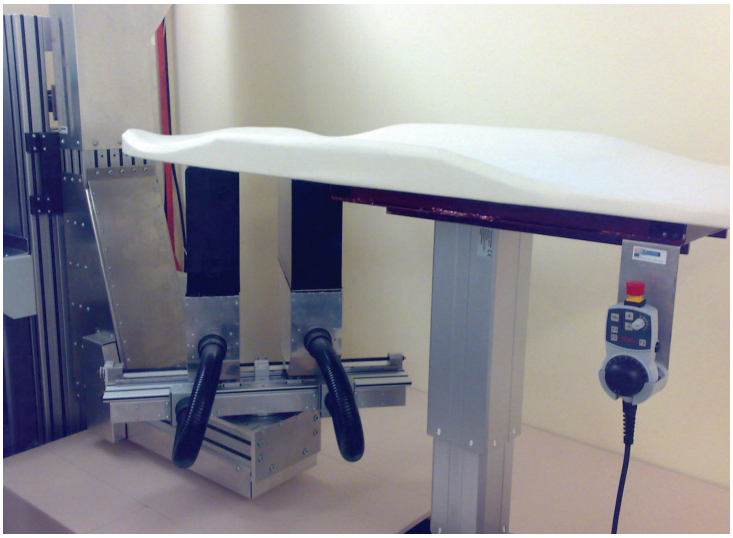

Figure 1.15: Photograph of the Clear-PEM scanner at the IPO–Porto Hospital.

Chapter 2

# Experimental Environment

## Contents

## 2.1 Introduction

The PET-Mammography consortium comprises several national institutions, with well defined responsibilities, where LIP – Laboratório de Instrumentação e Física Experimental de Partículas is responsible for the ClearPEM detector design, simulation studies, experimental tests, integration and is also co-responsible for the development of the data acquisition electronics, operation and image reconstruction software.

To accomplish these responsibilities a dedicated working area was needed, where handling sealed and unsealed radioactive sources would be possible, in order to study the performance of the ClearPEM detector modules (Chapters 3, 4 and 5) validate the main concepts and proof-of-principle results as well as measure the combined performance of the ClearPEM scanner (Chapter 6). More over, experimental tests concerning the quality control of the detector module main components and the design of specific electronic processing boards were also foreseen and taken into account on the requisites for the new working area.

In late 2004, after a period of infrastructural construction and equipment, TagusLIP was a newly laboratory with 100 $m^2$ area created and approved by portuguese governmental regulations on radiation safety, based on a dedicated report elaborated by independent experts from Nuclear and Technological Institute (Instituto Tecnológico e Nuclear – ITN), which was evaluated by the Direcção-Geral de Saúde from the Ministry of Health. The ground floor of the laboratory consists of an open space with work benches for computing and electronics, an area of toilets, a depository and a hot laboratory. The ground floor has a capacity of 6 to 8 people to work in the existing open space. The top floor has two offices equipped with workstations with capacity for 5 people. In 2008, the lab was upgraded with an additional 200 $m^2$ area, giving room for more workplaces (5 to 7 people), electronic workshop and a hangar for integration of PET systems.

In this chapter an overview of the concepts regarding radiation protection and measurement is given, together with the experimental work carried out in this thesis concerning the validation of the radiological protection schemes implemented in TagusLIP. The discrete electronics setups and commissioning, performed as a preparatory work for the detector module characterization, are also described.

## 2.2 The TagusLIP Laboratory

### 2.2.1 The Hot Lab

The Hot Lab, or the "bunker" (Fig. 2.1), is an area devoted to nuclear testing and is isolated from the rest of the laboratory technical areas, according to the main guiding principles on protecting workers and the environment from the risk of exposure. It has an area of 14 $m^2$ with 30 cm thick concrete walls, washable floor and rounded corners, with facilities to manage and store both sealed and unsealed radioactive sources. Inside

Figure 2.1: Top view of the hot lab with 30 cm thick concrete walls (*left*) and entrance to the bunker (*right*) where is visible the environmental radiation monitor.

the bunker a shower for rapid cleansing if liquid radioactive source spreads over a person was installed.

### 2.2.2 Primary Radiation Barriers


Figure 2.2: L-block table shielding for handling high-energy radionuclides(*left*) and wall made of lead bricks for primary protection(*right*).

For handling doses of high-energy radionuclides, radiation block protectors, made of lead with 5 cm thickness, were bought to Biodex Medical Systems, Inc.. Barriers in "L"

configuration are designed for receiving and preparing unit doses of radionuclides like FDG, providing a protected area for safe handling of the 511 keV nuclides. The front wall and the base of the unit are constructed of steel with built-in lead shielding. A 10 cm thick lead glass window provide a protected viewing area - Fig. 2.2 (*left*). Several lead blocks was also purchased to build up primary protective walls - Fig. 2.2 (*right*).

## 2.3 Radiation Protection and Measurement

Humans benefit from the use of X/$\gamma$-rays, radioisotopes, fissionable materials in medicine, industry and many research areas. However, these gains entails the exposure of people to radiation in the procurement and routine use of sources, as well as exposures from accidents that may occur. Since any radiation exposure presumably involves some risk to the individual involved, the levels of exposure allowed should be worth the result that is achieved.

As experience and knowledge have been gained through the years, basic ideas and concepts behind radiation protection and dosimetry have continually evolved. On a world scale, the recommendations of the International Commission on Radiological Protection (ICRP) have played a major role in establishing criteria at many facilities that deal with radiation [Turner2007].

Radiation Dosimetry attempts to quantitatively relate specific measurements made in a radiation field of health and medical physics that is focused on the calculation of internal and external absorbed doses in matter and tissue resulting from the exposure to ionizing radiation.

The primary physical quantity in Radiation Dosimetry is the absorbed dose. It is defined as the energy absorbed per unit mass from any kind of ionising radiation in any target. *Absorbed dose*, or simply *dose*, is reported in Gray (Gy) for matter or Sieverts (Sv) for biological tissue, where 1 Gy or 1 Sv is equal to 1 joule per kilogram. Non-SI units are still prevalent as well, where, by definition, 1 Gy = 100 rad and 1 Sv = 100 rem. The distinction between *absorbed dose* (D) and *equivalent dose* (H) is based upon the biological effects of the radiation in question and the tissue and organism irradiated. For different types of radiation, the same absorbed dose may have very different biological consequences. Therefore, *radiation weighting factors* ($\mathrm{w}_R$) and *tissue weighting factors* ($\mathrm{w}_T$) have been established, which compare the relative biological effects of various types of radiation and the susceptibility of different organs. It follows that:

$$D = \frac{1\ J}{kg} \equiv 1Gy \tag{2.1}$$

The absorbed dose is treated as a point function, having a value at every position in an irradiated object. The equivalent dose $\mathrm{H}_{T,R}$ in a tissue or organ, T, due to radiation, R, is given by the average absorbed dose, $\mathrm{D}_{T,R}$, in T from R, wighted by the factor $\mathrm{w}_R$:

$$H_{T,R} = \mathrm{w}_R D_{T,R} \qquad (Sv) \tag{2.2}$$

When radiation consists of components with different $w_R$, then the equivalent dose in T is given by summing all contributions:

$$H_T = \sum_R w_R D_{T,R} \qquad (Sv) \tag{2.3}$$

With dose expressed in Gy and equivalent dose in Sv. Values of $w_R$ specified by the ICRP are shown in Tab. 2.1.

| Radiation | $w_R$ |
|---|---|
| Photons, all energies | 1 |
| Electrons and muons, all energies (except Auger electrons) | 1 |
| Neutrons, energy $<$ 10 keV | 5 |
| 10 keV to 100 keV | 10 |
| $>$ 100 keV to 2 MeV | 20 |
| $>$ 2 MeV to 20 MeV | 10 |
| $>$ 20 MeV | 5 |
| Protons, other than recoil protons, energy $>$ 2 Mev | 5 |
| *alpha*–particles, fission fragments, heavy nuclei | 20 |

Table 2.1: Radiation weighting factors, $w_R$, from ICRP [Leo1994].

Effects of ionizing radiation, whereby the probability of their occurrence, but not their severity is a function of the dose without the existence of a threshold value. Non-stochastic effects, or deterministic radiation effects, are those in which the severity of the effect varies with the dose and for which a threshold value exists. In the dose range relevant for radiation protection purposes, inheritable damage, cancer and leukemia belong to stochastic radiation damages. The probability that stochastic radiation damage will occur differs widely for the irradiated individual organs or tissues. The International Commission on Radiological Protection (Publication 103, 2007) indicates a value of 5.5 % per sievert for cancer and 0.2 % per sievert for heritable effects after exposure to radiation at low dose rate.

Since different tissues of the body respond differently to radiation, the probability for stochastic effects that result from a given equivalent dose will generally depend upon the particular tissue or organ irradiated. To take that differences into account, it was defined, as already said, a weighting factor for tissues, $w_T$. The equivalent dose $H_T$, weighted by $w_T$, gives a quantity that is intended to correlate with the overall detriment to an individual, independently of T.

The risk for all stochastic effects for an irradiated individual is represented by the *effective dose*, E, defined as the sum of the weighted equivalent doses over all tissues:

$$E = \sum_T w_T H_T \qquad (Sv) \tag{2.4}$$

Values of $w_T$ specified by the ICRP are shown in Tab. 2.2. The data refer to a reference population of equal number of both sexes and a wide range of ages. In the definition of

effective dose, they apply to workers, of the whole population and to either sexes. The $w_T$ are based on rounded values of the organ's contribution to the total detriment.

| Tissue or organ | $w_T$ |
|---|---|
| Gonads | 0.20 |
| Bone marrow (red) | 0.12 |
| Colon | 0.12 |
| Lung | 0.12 |
| Stomach | 0.12 |
| Bladder | 0.05 |
| Breast | 0.05 |
| Liver | 0.05 |
| Esophagus | 0.05 |
| Thyroid | 0.05 |
| Skin | 0.01 |
| Bone Surface | 0.01 |
| Remainder | 0.01 |

Table 2.2: Tissue weighting factors, $w_T$, specified by ICRP, which add to unity when summed all tissues [Turner2007].

The risk of stochastic effects is dependent only on the value of the effective dose, whether or not the body is irradiated uniformly. In case of whole-body irradiation, since the tissue weighting factors sum to unity, the effective dose is equal to the equivalent dose:

$$E = \sum_T w_T H_T = H_T \sum_T w_T = H_T \tag{2.5}$$

The ICRP has defined other dosimetric quantities that apply to the exposure of groups or population to radiation. The *collective equivalent dose* and the *collective effective dose* are obtained by multiplying the average value of these quantities in a population or group by the number of people therein.

Under the ICRP recommendations, the system of radiation protection is based on three factors: the justification of the practice, the optimization of the protection and individual dose limits [Wrixon2008].

Different permissible exposure criteria are usually applied to different groups of people. Certain levels are permitted for people who work with radiation. These guidelines are referred as "occupational" or "on-site" radiation-protection standards. Other levels, often ten times less than the allowable occupational values apply to members of the general public. These are referred as "non-occupational" or "off-site" guides. In Tab. 2.3 the ICRP limits are presented for occupational and public to exposure. Lower values are applied for occupationally exposed pregnant women and apprentices.

| | Occupational Exposure | Public Exposure |
|---|---|---|
| Effective Dose | | |
| Annual | 50 mSv | 1 mSv (higher if need, provided 5-y average $\leq$ 1mSv) |
| Cumulative | 100 mSv in 5 y | – |
| Equivalent Dose | | |
| Annual | 150 mSv lens of eye; 500 mSv skin, hands, feet | 15 mSv lens of eye; 50 mSv skin, hands, feet |

Table 2.3: Occupational and public radiation exposure limits, established by ICRP.

An essential facet of the application of maximum permissible exposure levels to radiation protection practices is the ALARA (As Low As Reasonably Achievable) philosophy. The ALARA concept stands for the principle that exposures should always be kept as low as feasible. The maximum permissible levels are not to be considered "acceptable" but, instead, they represent the levels that should not be exceeded.

The International Commission on Radiation Units and Measurements (ICRU) has addressed the relationship between practical radiation-protection measurements and assessment of compliance with the limits set forward by the ICRP. The basic organ and tissue doses specified in the limits are essentially unmeasurable, but can be estimated from measurements made at appropriate locations in tissue-equivalent phantoms and from simulations. Accordingly, the ICRU has introduced three operational quantities for practical measurements under well defined conditions with explicitly stated approximations. Two quantities are defined for area monitoring that link an external radiation field to the effective dose equivalent and the dose equivalent to the skin and to the lens of the eye. A third quantity concerns to individual monitoring:

- The *ambient dose equivalent*, H*(10), at the point of interest in the actual radiation field is the dose equivalent which would be generated in the associated oriented and expanded radiation field at a depth of 10 mm on the radius of the ICRU sphere which is oriented opposite to the direction of incident radiation. An oriented and expanded radiation field is an idealized radiation field which is expanded and in which the radiation is additionally oriented in one direction.

- The *directional dose equivalent*, H'(d, $\Omega$), at the point of interest in the actual radiation field is the dose equivalent which would be generated in the associated expanded radiation field at a depth, d, typically of 0.07 mm (H'(0.07, $\Omega$)), on the radius of the ICRU sphere which is oriented in the fixed direction $\Omega$. An expanded radiation field is an idealized radiation field in which the particle flux density and the energy and direction distribution of the radiation show the same values at all points of a sufficient volume as the actual radiation field at the point of interest.

- The *personal dose equivalent*, Hp(d), is the dose equivalent in soft tissue, at an appropriate depth, d, below a specified point on the body.

The ICRU has defined a number of measurable, operational quantities which overestimate E under nearly all circumstances. For penetrating external radiation, the principal radiation hazard at particle accelerators, the ambient dose equivalent H*(10) is the most important quantity. Its exact relation to effective dose is determined by calculation. H*(10) can be calculated in a similar way as E when the radiation field is specified with sufficient precision.

In this context, personnel exposure and environmental radiation at TagusLIP is measured and monitorized continually.

### 2.3.1 Personnel Dosimeters

For real time monitoring of the personal dose and dose rate, TagusLIP is equipped with the Dosicard System, from Canberra, which consists of electronic dosimeters (badges) and a computerized data handling system for real time measurements and triggering of audible and visual alarm systems. The data acquisition and processing system enables the corresponding dosimetric information to be exploited independently or as part of a network.


Figure 2.3: The Dosicard and the LCB badge reader. The badge has three touch buttons that allow programming and display setup on the LCD screen of the current dose, dose rate and cumulative doses per day/month/quarter/year and five years.

The badge has the size of a credit-card ($89 \times 57 \times 8$ mm$^3$) and weights 60 g - Fig. 2.3. It is enclosed in a transparent plastic envelope provided with a clip enabling it to be clipped onto the breast pocket of the laboratory coat, for example. Dosicard features a silicon detector to estimate the equivalent dose received by an operator, analog and digital circuitry with a microcontroller that controls measurements, triggers alarms and ensures the transfer of information between the badge and an external data acquisition and processing system. The silicon detector measures the Hp(10) deep dose equivalent, the operational quantity defined in ICRU39. The detector's energy response was normalized to unit for $^{137}$Cs in accordance with specification requirements. The overall variation

in response is ± 15% in the 60 keV to 1.25 MeV energy range and ± 30% from 50 keV to 60 keV and from 1.25 MeV to 2 MeV. The dose equivalente range is 1 $\mu$Sv to 10 $\mu$Sv and it can be displayed either in Sv or in rem (1 Sv = 100 rem).

The Dosicards can be connected to any PC via the LCB badge reader, with the DoseManager software. This program enables transfers of the user personal data (name, ID number, company, professional training, medical aptitude, etc) into the badge memory and retrieval of the stored data. It also allows data base operations for detailed dose history and dosimetry monitoring.

### 2.3.2 Environmental Dosimeters

TagusLIP has a working environmental radiation control system, that have been purchased to MED Nuklear-Medizintechnik, Dresden. The stationary dose rate measurement system ALMO consists in one NaI(Tl) detector and two Geiger-Muller (G-M) counter tubes, connected to the measuring electronics and the display unit via special probe cables. The alarm monitor detects automatically which channel corresponds to each detector, performing an auto calibration based, by default, on $^{137}$Cs measurements.

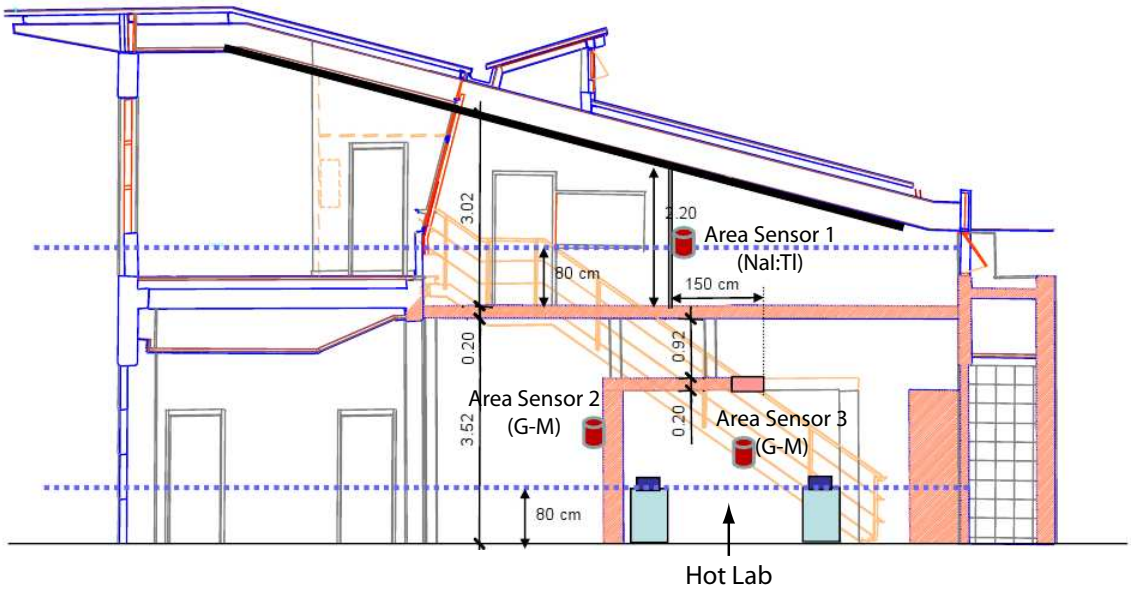


Figure 2.4: TagusLIP laboratory plan with environmental dosimeters marked in dark red (not to scale), surrounding the hot lab.

One of G-M detectors is positioned at head-level inside the bunker, the other G-M tube is placed outside of the bunker concrete wall that is closer to the open space office area, and the NaI(Tl) detector is above the bunker ceiling, on the wall of the first-floor offices, covering the main areas where workers are. In Fig. 2.4 it can be seen the three detectors on the laboratory plan.


Figure 2.5: Monitor for the Almo environmental radiation control.

Measuring electronics and display unit are integrated into a plastic desktop case - Fig. 2.5. The front panel includes a large LC display presenting the measured results. On the LC display, the current dose rate data of the three connected detectors are shown in the selected unit of measure. For each detector, the alarm threshold parameters can be defined as needed. This setting is made on the menu level and when it is exceeded, a visual and acoustic warning is triggered.

The system is also controlled and monitorized in a PC via the ALMO software, developed to display the measuring data of the three detectors graphically, to store the data and make them available for further processing.

### 2.3.3 Survey Meter

TagusLIP laboratory also has a survey meter to monitor radiation levels where radioactive materials or other radiation sources are present. This type of portable unit is useful for detecting small quantities of radioactivity from minor spills and waste receptacles, for instance. The external pancake probe is used to check hands, clothing, floors, furniture, equipment, and package surfaces for contamination. According to the probe chosen, the survey meter is suitable for different radiation detection.

Figure 2.6: Survey Meter with Pancake GM Probe, suitable for $\alpha$, $\beta$ and $\gamma$ survey.

The Survey Meter is a portable equipment (0.5 kg) to monitor levels of radiation which measures the rate of counts. It is an analog device, small size (2.1 $dm^3$) which measures the level of radiation in $min^{-1}$ (cpm). A second scale allows reading dose rate in units of mR/h using a implicit conversion factor of 1mR/h = 3.3 Kcpm. The model chosen was the portable 14C Survey Meter with Pancake G-M Probe 44-9, specific for $\alpha$, $\beta$ and $\gamma$ survey - Fig. 2.6. It has a cylindrical probe type (pancake) that contains a halogen. It works with high voltage of about 0.9 kV, adequate for a Geiger-Muller detector in which the energy deposited by radiation results in an electric discharge collected by an anode. The active area of the probe is 15 $cm^2$. The probe is connected by a connector to the counter inside a aluminum box. Inside the box, there is also a Geiger-Muller tube that is activated only when the measure counts more than 106 cpm. The detector is energy dependent, over responding by a factor of six in the 60 keV – 100 keV range when normalized to $^{137}$Cs. For background readings, the unit's built-in energy-compensated G-M detector handles counts up to 2 R/hr. The time response of the Survey Meter depends on the position of the button «F/S» (fast/slow). The survey meter in the F-position acquires 90% of the final value of measuring in 4s. In the S-position it takes 22s to get the final value of measurement. In practice, the F-position is used to put rapidly the Survey Meter in the value region of interest and then it is changed to the S-position in order to acquire the value with greater precision.

### 2.3.4 Dose Calibrator

Figure 2.7: Atom100 Dose calibrator.

A dose calibrator must be capable of measuring with great accuracy the activity of a radioisotope known. Its main application is to measure the dose and characterize the activity of radiation sources, for example in the quantification of the system sensitivity in PET scanners. This system was used to measure the activity of a $^{22}$Na source, employed in the sensitivity assessment of the ClearPEM detector and results will be shown in Chapter

6. The existing equipment in TagusLIP, an Atomlab 100 from Biodex Medical Systems, Inc. - Fig. 2.7, is composed of two parts: a display unit and the detector itself. The detector consists of an ionization chamber, for detection of radiation and a electrometer, to measure the ion current. The camera has a height of 26 cm and an aperture diameter of 6.4 cm and it has a large range of activities measuring: from 0.01 $\mu$Ci to 9999mCi for $^{99m}$Tc.

The Atom100 Dose Calibrator provides accurate radionuclide activity measurements. Moreover, the unit is simple to operate and it has 13 isotope selection keys, ten are pre-programmed for the most commonly used radionuclides ($^{57}$Co, $^{137}$Cs, $^{131}$I, $^{133}$Cn, $^{67}$Ga, $^{133}$Xe, $^{123}$I, $^{201}$Tl, $^{99}$Mo, $^{99m}$Tc), and three are to be defined by the user. There are 88 isotope-specific dial values listed in the manual and any key can be reprogrammed by the user for a desired isotope.

The activity is displayed on a LED readout in either Curie or Becquerel units. Background correction and zero adjustment are performed at the touch of a button and range selection is automatic. Activity measurements are performed by a microprocessor controlled electrometer located within the detector assembly of the ionization chamber. This chamber is shielded with 0.64 cm lead to protect both the user from the source to be measured, and the dose calibrator from radiation environment. The detector has a geometry close to $4\pi$ allowing measuring the activity of a source regardless of their shape or size, provided that the source lies inside the cavity. To enter the source in this cavity the equipment has a structure of plastic, adjusted to the inside measures of the chamber, with a latch for easy access. This piece of plastic is prepared to halt syringes and to prevent any contamination in the chamber during the process of measurement.

The response of the ionization chambers is characterized by the manufacture using isotopes calibrated by the National Institute of Standards and Technology (NIST), yielding an answer in energy well known, used to determine very precisely the values of calibration of various isotopes. Each chamber is also calibrated with a tracer of the NIST and the result recorded in the memory of the detector. The detector communicates with the display unit through a serial port. This unit contains the controls and the display allowing the measurements.

### 2.3.5 Radiation Survey at TagusLIP

To estimate the annual dose received by a typical TagusLIP researcher a case study was conducted. The study consider all experimental work done by one person, beginning by an interview to have a detailed description of the daily routine in order to determine the time exposure to radioactive sources. A qualitative analysis of the record of his/her personal dosimeter and identification of possible peaks, its correlation with unusual activities involving radioactive sources were also taken into account. In Fig. 2.8 it can be seen records of a personal dose summary and daily registration of a personal dosimeter along four months. This badge was only used to perform radiation dosimetry measurements, so it shows mainly background activity.

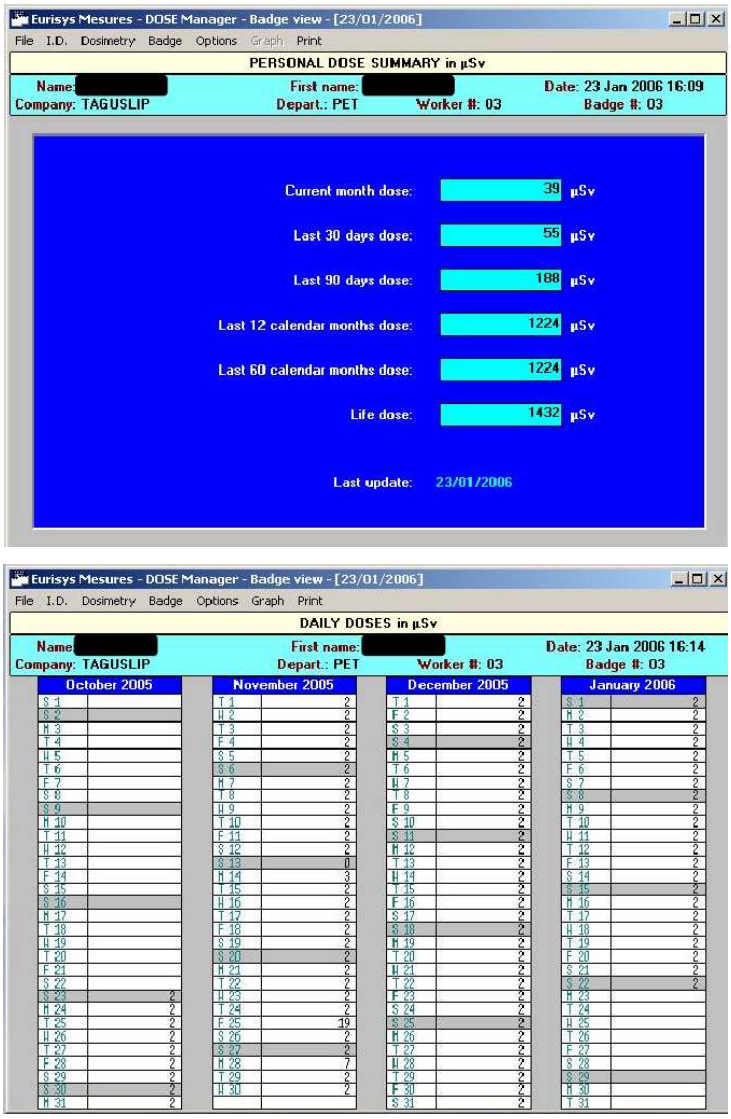


Figure 2.8: Dose Manager badge view: personal dose summary (*top*) and daily registry (*bottom*).

For everyday tests the sources handled are essential sealed point sources of $^{137}$Cs and $^{22}$Na with activities between 1$\mu$Ci to 100$\mu$Ci. The workers' exposure is mainly due to the source positioning in the support of the experimental apparatus, transportation and storage of the radioactive sources. It is performed several times throughout the day, everyday in periods of data acquisition and occasionally in periods of data analysis. In order to experimentally measure the dose received by a research worker from operating a source of $^{137}$Cs with activity of 10 $\mu$Ci, a wire was tightened from the bunker ceiling to the floor, marking the positions of some typical regions of the human body: face, chest, abdomen and pelvis (Fig. 2.9). The hands region was considered to be at 1 cm of the source, placed behind the primary barrier of lead. Counting rates and equivalent dose rates were acquired with the survey meter and the personal dosimeter in each position marked.

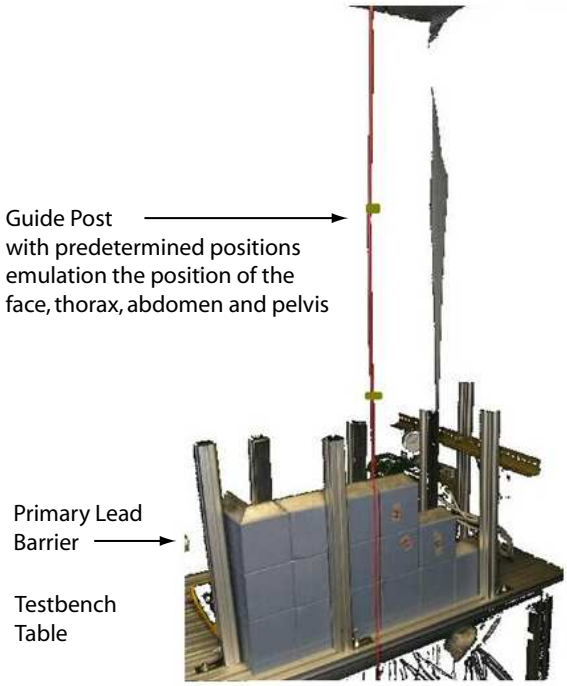


Figure 2.9: Experimental setup used to estimate the typical dose exposure of body regions.

These measurements were then used to estimate the dose exposure for one worker carrying a set of typical experiments with a constrained academic radioactive sources ($^{137}$Cs with 100 $\mu$Ci), and the annual dose considering the same routine procedures along one year (4 experiments per day, 4 days a week, along 45 weeks). In Tab. 2.4 it can be seen the summary of these results. As can be observed the one-year dose is well within the maximum values referred by the actual legislation of 15 mSv per year. As for the

| | H'$_p$(10) | | |
|---|---|---|---|
| Timeline | Hands | Head | Trunk |
| One experiment | 15.5 ($\mu$Sv) | 0.095 ($\mu$Sv) | 0.083 ($\mu$Sv) |
| One year | 11.16 (mSv/year) | 0.07 (mSv/year) | 0.06 (mSv/year) |

Table 2.4: Estimated dose exposure of one worker per experiment and per year, for different parts of the body.

environmental background radiation, measured by the area detectors, it is read directly on the alarm panel located at the entrance of the bunker, with all the radioactive sources enclosed in the safe container. The results are shown in Tab. 2.5. The background equivalent dose rate will be given by the average of the values recorded by the three area sensors and it has the value of $\mathrm{H'}_P(10)_{background} = 0.497 \pm 0.006$ $\mu$Sv/h. This value is in line with the typical range of the annual background radiation. According to the [Amsler2008] an equivalent dose rate received by absorption of background radiation varies between 0.05

| Detector | NaI(Tl) | G-M (inside bunker) | G-M (outside bunker) |
|---|---|---|---|
| H'$_p$(10) ($\mu$Sv/h) | 0.49 ± 0.01 | 0.50 ± 0.01 | 0.50 ± 0.01 |

Table 2.5: Equivalent dose rates for background radiation at TagusLIP.

$\mu$Sv/h and 0.46 $\mu$Sv/h and, in some cases, up to 5.7 $\mu$Sv/h. It is also natural that in the vicinity of the radioactive sources enclosed in the safe container, background dose rate is higher than the typical reference. For comparison, the Nuclear Medicine department at IPO–Porto, where the ClearPEM scanner was installed, shows in low-level regions dose measurements between 0.10 $\mu$Sv/h and 0.40 $\mu$Sv/h, scaling up to 1–2 mSv/h in hot areas such as radiotracer storage and patient holding rooms.

For intercalibration of the environmental detectors, the correlation between the dose measured and the distance of the source from the detector was studied. A $^{137}$Cs (10 $\mu$Ci) source was placed near each detector at distances of 0 cm, 1 cm, 5 cm and 10 cm. For each distance, the dose rate was measured on the alarm panel. During each measurement, or source placement, there was a 30 s wait time for sensors stabilization before considering the dose rate value. In Fig. 2.10 it is shown the registration chart obtained through the Almo software. It can been seen that the NaI:Tl detector has a higher sensitivity than the G-M tubes, registering a much higher dose. This is due to the fact that the absorption efficiency of the NaI:Tl crystal is much larger than the Geiger-Muller tube, resulting in greater intrinsic detection efficiency of radiation.

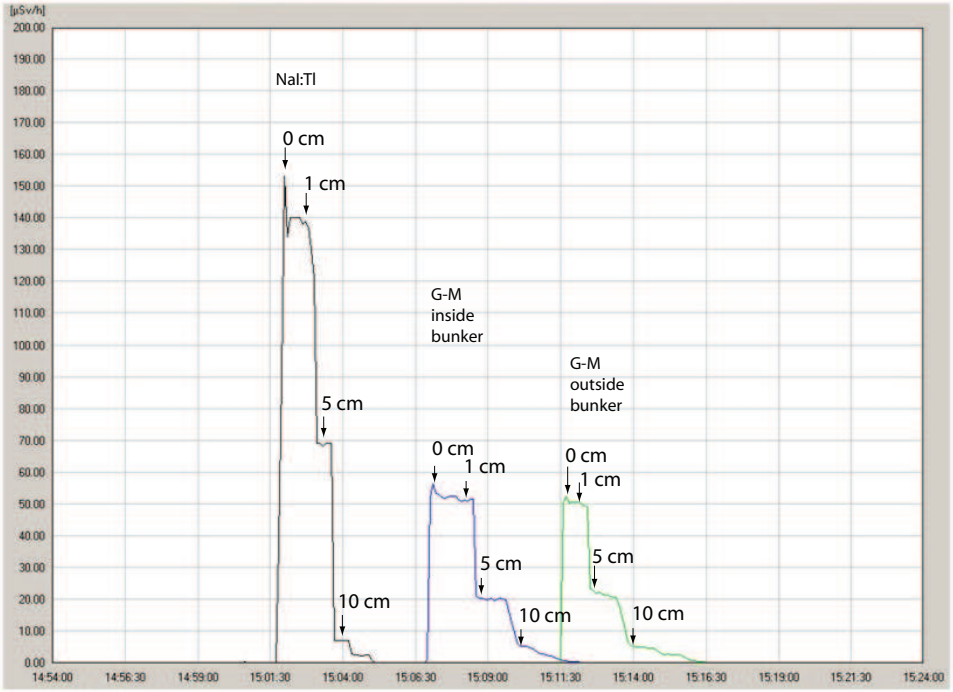


Figure 2.10: Registration chart of the area sensors for each source-detector distance.

The measurements done in this context showed that the area detectors can effectively

monitor the activity in the laboratory and Almo3 software enables the access to the registration charts and data base. Moreover, the annual dose for TagusLIP workers are far below from the established maximum acceptable values. This evaluation was performed previously to the acquisition of $^{68}$Ge sources with 18.5 MBq (0.5 mCi) and 37 MBq (1.0 mCi), used in ClearPEM detector calibration and normalization and for Compton and attenuation correction studies, respectively. Although the ALARA principle is being followed, further studies may be considered for the next experimental generation. Preliminary measurements performed with the TagusLIP personal dosimeters at IPO-Porto show that a typical worker involved in the commissioning and clinical tests of the ClearPEM scanner receive a daily dose in the order of 4 to 6 $\mu$Sv.

## 2.4 TagusLIP Main Equipment

### 2.4.1 General Equipment

TagusLIP has a robust computer infrastructure autonomous from the main LIP Computer Centre. It includes a gigabit network with several Windows and Linux workstations, dedicated servers for internal and external network resource management and high capacity for data storage. All workers can access to their own areas from any computer of the network by NFS (Network File System) and Kerberos V plus LDAP (Lightweight Directory Access Protocol) distributed authentication. A tape backup unit ensures daily data backup to magnetic tapes. All the equipment is protected from voltage transients and power failures by UPS (Uninterruptable Power Supply) systems.

Figure 2.11: Photographs of general TagusLIP equipment: Robot (*left*) and oven (*right*).

Several laboratory equipment has been purchased, like oscilloscopes and low voltage power supplies, high precision balance and multimeters, microscope and arbitrary pulse generators, according to the necessities of the activities being performed at TagusLIP, namely PCB design, firmware development, detector assembly, among all experimental and quality control tests. It would be tedious and uninteresting to list all the equipment existing in the laboratory so, as an illustrative example, it can be seen in Fig. 2.11 the

robot, used to glue APD arrays to PCB-APD, and the oven, used to accelerate the gluing process.

### 2.4.2 VME and NIM Standard Modules

There have been three major data acquisition standards used in modern nuclear physics. The first to be introduced was the NIM standard and was used to provide power to the electronics. CAMAC went further and allowed data transfer on the crates backplane. The current standard is VME, expanded on CAMAC by providing more options and a faster bus speed. In TagusLIP there are NIM and VME standards coexisting.

The NIM standard is the first crate standard widely accepted by physicists. It provided a way to organize and distribute power to the electronic setups. The power is distributed by a series of connectors on the back of the crate and a low voltage power supply is either behind the crate or sat in the crate along side the other modules. Typical voltages distributed are +/-6V, +/-12V, and +/-24V, although many custom power supplies have been built for NIM crates. NIM crates have 12 slots and are often used for small setups with only a handful of detectors because their low overhead makes setup easy. They are often used in larger experiments for setup and to handle logic signals and analog electronics. Some of the most often used modules are amplifiers, gate and delay generators, discriminators, high voltage modules, and linear fan-in fan-out units. One of the main disadvantage with the NIM standard is the channel density. Because NIM modules use knobs and switches on the front panel to adjust parameters that take considerable space, the number of channels per module is low [Hoagland2004].

VME offered a rear backplane for fast and efficient data transfer. The VME bus is industry standard used in physics, meaning that there is a larger variety of crates and modules commercially available. VME is currently used in most large-scale experiments and also very popular in smaller scale experiments. The fast bus also mean that more data may be transferred (up to 320 MB/s) and channel density can be increased. This made VME a very attractive alternative. VME crates can have slots up to 21 modules, being the first one reserved for the crate controller. The VME backplane has two 3-row connectors per module for data and power distribution. VME also offers options to incorporate other crates into VME setups which allows experimenters to use modules and crates they already have.

Although avoiding an exhaustive description of all VME and NIM modules existing at TagusLIP, some of these modules prevail on importance for being part of the experimental data taken electronic chains. On Fig. 2.12 the VME and NIM racks existing in TagusLIP are shown. As examples of the most relevant NIM modules, TagusLIP counts with 8 Channel Constant Fraction Discriminator, 4-8 Logic Fan-in Fan-Out, Quad Scaler And Preset Counter or Timer, 4 channel programmable HV Power Supply, Triple 4-Fold Logic Unit, 8 channel Leading Edge Discriminator. These modules are described here briefly. Additional information on these or other NIM and VME modules can be seen in the CAEN and ISEG websites [Caen2008, Iseg2008].

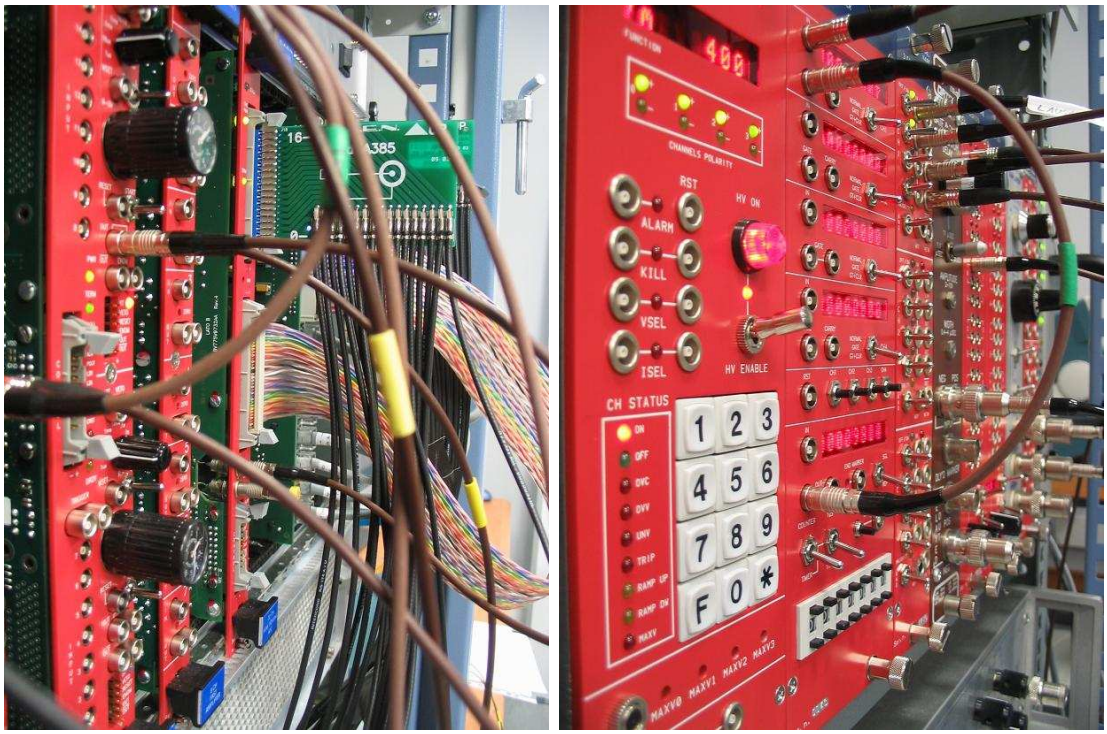


Figure 2.12: VME and NIM modules at TagusLIP used for readout of discrete electronic setups.

The 8 Channel Constant Fraction Discriminator is the Mod. N842 from CAEN. The module accepts 8 negative inputs and produces 2×8 NIM outputs (NIM outputs are provided with a fan-out of two), plus 8 negated NIM outputs, on front panel LEMO 00 connectors. The constant fraction delay is defined by a delay line network of 20 ns with 5 taps. The timing stage of the discriminator produces an output pulse whose width is adjustable in a range from 16.5 ns to 273 ns. Moreover, in order to protect against multiple pulsing, it is possible to program a dead time during which the discriminator is inhibited from retriggering.

The 4-8 Logic Fan-in Fan-out (Mod. N454 from CAEN) is a single width NIM unit housing 4 independent Fan In-Fan Out sections. Each section accepts 4 input NIM signals and performs on these the logic OR function. The result of the function is available as 4 normal and 2 complementary NIM signals on 6 front panel connectors. The unit can be programmed, via a front panel switch, to work as 4 OR sections (4 inputs / 4 outputs) or 2 OR sections (8 inputs / 8 outputs).

The Quad Scaler And Preset Counter or Timer (Mod. N1145 from CAEN) is a double unit NIM module that includes four independent 8-digit up-counters plus a fifth 7-digit down-counter that can be used either as a preset counter or timer. The counters can have different operating modes and can be variously interconnected, making the module a flexible tool for applications involving time, frequency and ratio measurements. All counters can accept either TTL or NIM inputs and all control and output signals are

standard NIM. The maximum input frequency is 250 MHz and the minimum pulse width is 2 ns for the up-counters, and respectively 80 MHz and 3 ns for the down-counter. All input and output connectors as well as all the control switches are located on the front panel.

The Programmable High Voltage Power Supply (Mod. N470 from CAEN) is a double width NIM unit housing 4 independent HV channels, with output voltage ranges from 0 to ± 8kV (1 to 3 mA), with a precision voltage of ± 1 V. The range selection is automatic, as the output voltage is set, and the current resolution is 1 $\mu$A. The output polarity is independently selectable for each channel and it is possible to control several operating parameters on each channel (two levels of presettable high voltage, two levels of current limit, Ramp-up, Ramp-down). All these parameters can be programmed and monitored either in remote mode, via High Speed CAENET (either using the V288 VME controller or the A1303 PCI Bus controller), or in local mode, via front panel alphanumeric keypad and two 8-character displays. In addition some LEDs display the status of the selected channel. The Front panel trimmers allow the setting of maximum voltage limits, and the two current and voltage limits can be selected via two external NIM/TTL signals.

The VHR high voltage module, Mod. NHQ 224M from ISEG, is a NIM module with two channels of high voltage from 0 to 4 kV. This unit offers high precision voltage (±10 mV) and current resolution with high stability, essential to sensing and radiation detection units where low noise and high stability are paramount, such as APD based systems. The module has manual controls on the front panel and can be controlled with these if remote control of the module is not needed. An RS–232 interface provides the user with full functionality of the module allowing to control and operate from a standard PC.

The Triple 4-Fold Logic Unit/Majority with VETO (Mod. N405 from CAEN) is a one unit wide NIM module housing three independent sections that can be used either as logic unit or majority. The two modes are selectable via internal switches. Each section accepts 4 input signals, a VETO input and provides 4 outputs (2 normal and 1 complementary, shaped, plus 1 linear). The linear output provides a signal whose width is equal to the time during which the input signals satisfy the conditions programmed via the front panel lever switches. The shaped output widths can be set via front panel trimmers in the range 6 ns to 800 ns.

As examples of the most relevant VME modules, TagusLIP counts with 32 Channel Multievent Peak Sensing ADC, Dual Timer, Quad Linear Fan-in Fan-out, 8 Channel Fast Amplifier, VME–USB2.0 and VME–PCI Optical Link Bridges.

The 32 Channel Multievent Peak Sensing ADC, Model V785 from CAEN, is a 1-unit wide VME 6U module housing 32 Peak Sensing Analog-to-Digital Conversion channels. Each channel is able to detect and convert the peak value of the positive analog signals (with risetime bigger than 50 ns) fed to the relevant connectors. Input voltage range is from 0 to 4 V. The outputs of the peak detector electronics are multiplexed and subsequently converted by two fast 12-bit ADCs (the total readout time for digitalization for all channels is 5.7 $\mu$s). The integral non linearity is ±0.1 of full scale range (FSR), measured

from 2% to 97% of FSR; the differential non linearity is ±1.5% of FSR, measured from 3% to 100% of FSR. The ADCs use a sliding scale technique to reduce the differential non-linearity. This technique consists in adding a known value to the analog level to be converted, thus spanning different ADC conversion regions with the same analog value. The known level is then digitally subtracted after the conversion and the final value is sent to the threshold comparator. If the sliding scale is enabled, it reduces slightly the dynamic range of the ADC: the 12-bit digital output is valid from 0 to 3840, while the values from 3841 to 4095 are not correct. Programmable zero suppression, multievent buffer memory, trigger counter and test features complete the flexibility of the unit. A 16 channel flat cable to LEMO input adapter (Mod. A385 from CAEN) is available for the Mod. V785 (one 32 ch. V785 requires two A385 boards). The board supports the live insertion that allows inserting or removing them into the crate without switching it off.

The Dual Timer (Model V993 from CAEN) is a 1-unit VME module housing two identical triggered pulse generators. The module produces NIM/TTL (NIM/TTL selection is performed via an on-board switch) and ECL pulses whose width ranges from 50 ns to 10 s when triggered. Output pulses are provided normal and negated. Timers can be re-triggered with the pulse end marker signal, a short pulse occurring at the end of each output pulse. The coarse adjustment of the output width is provided via a 9-position rotary switch and the fine adjustment can be performed via either a rotary handle or by providing an external voltage. The trigger START can be provided via either an external signal (NIM, TTL or ECL) or manually via a front panel switch. The module features also VETO and RESET input signals. RESET is also available on a front panel switch.

VME–USB2.0 (Mod. V1718) and VME-PCI Optical Link (Mod. VX2718) Bridges are a 1-unit wide 6U VME master module which can be operated from the USB port of a standard PC and a 1-unit wide 6U VME64X master module, which can be controlled by a standard PC equipped with a PCI controller card (Mod. A2818 from CAEN), respectively. The connection between the VX2718 and the PCI controller card takes place through an optical fiber cable. These boards can operate as VME System Controller acting as Bus Arbiter in Singlemaster or Multimaster systems (when plugged in the slot 1). The VME bus activity can be monitored in detail, both locally (through a LED display) and remotely. The front panel of both modules includes 5 TTL/NIM programmable outputs on LEMO 00 connectors and two programmable TTL/NIM inputs (on LEMO 00 connectors). The I/Os can be programmed in order to implement functions like Timer, Counter, Pulse generator and I/O register. The sustained data rate on the USB is up to 30 MByte/s and up to 70 MByte/s on the optical link. The modules are equipped with a 128KB memory buffer in a way that the activity on the VME bus is not slowed down by the transfer rate on the USB port or when several VX2718s share the same PCI bus.

The Quad Linear Fan-in Fan-out (Mod. V925 from CAEN) is a 1-unit VME module which houses three 4 In / 4 Out and one 3 In / 3 Out sections. one Discriminator channel is also featured. Each Fan-in Fan-out section produces on all its output connectors, the sum of the signals fed to the inputs, eventually inverted. Fan-in Fan-out inputs are bipolar, while the output can be either inverting or non inverting by a jumper selectable

independently for each section. Both input and output signals are DC coupled. Maximum input amplitude is ś1.6 V. Moreover each Fan-in Fan-out section features a screwdriver trimmer which allows the DC offset adjustment. The module has also one discriminator channel, which has one DC coupled input (polarity is selectable by one jumper), the threshold is screwdriver adjustable and monitorable via test point and the output is NIM standard, its width is screwdriver adjustable as well. Front panel LEDs allow to monitor all the mode, gain and polarity adjustments performed via internal jumpers.

The 8 Channel Fast Amplifier (Mod. V975 from CAEN) is an 8 channel fast rise time amplifier housed in a 1-unit VME module. Each channel features a fixed voltage gain of 10. Channels are bipolar, non-inverting and can be cascaded in order to obtain larger gain values. Input bandwidth is 250 MHz for signals up to 50 mVpp and decreases for larger ones (up to 110 MHz at 400 mVpp). Each channel is provided with three LEMO 00 connectors, one for the input and two bridged for the output. The board features a $\pm 2$ V output dynamics. Screw-trimmers (one per channel) allow the offset calibration which operates over a $\pm 25$ mV range.

## 2.5 The Experimental Setups

The main experimental setups implemented for the characterization studies described in the next chapters of this thesis (APDs, crystal matrices and fully assembled detector modules) are based in two different discrete electronics systems. These systems are generally characterized by a modest number of readout channels and their use was mainly dictated by the fact that the final ClearPEM front-end ASIC was only available in late 2007.

In the following sections a description of two setups is provided as well as the validation conducted previously the beginning of the actual studies.

### 2.5.1 Discrete Electronics for Single Readout

This electronic chain was developed by the Inter-University Institute For High Energies (IIHE) group, from the Vrije Universiteit Brussel (VUB), and it was acquired by LIP in the context of the Crystal Clear Collaboration, from which both institutes are members. It was designed for tests with Hamamatsu 32 channel APD arrays and it is compatible with standard NIM and CAMAC modules.

The basic readout principles is that whenever a signal appears at any of the 32 channels, there will be a negative NIM gate signal, which trigger all the ADC channels. The discriminator, together with logic gates and TTL-NIM signal level converter, provide strobe for the ADC. The strobe output on the board is terminated with a 50-ohm resistor to ground. In order to meet the requirements of the peak sensing ADC, the analog signal is delayed by long twisted pair flat cable before input to ADC [Jiangui2004].

The amplifier chain electronics is partitioned into three main boards. The APD array,

Cremat preamplifiers and 1st stage op-amp are on the first board. Zero-pole, 2nd stage op-amp, discriminator, logic and TTL-NIM conversion are on the second board. Twisted pair signal receiver and shaper are on the third board. Analog signal is carried from the second board to the third board by twisted pair flat cable, the digital strobe goes directly from the second board to the peak sensing ADC. To trigger the ADC module whenever any channel has an analog signal, a NIM standard fast negative logic signal with a leading edge preceding the peak of the analog signal by at least 80 ns is also generated.

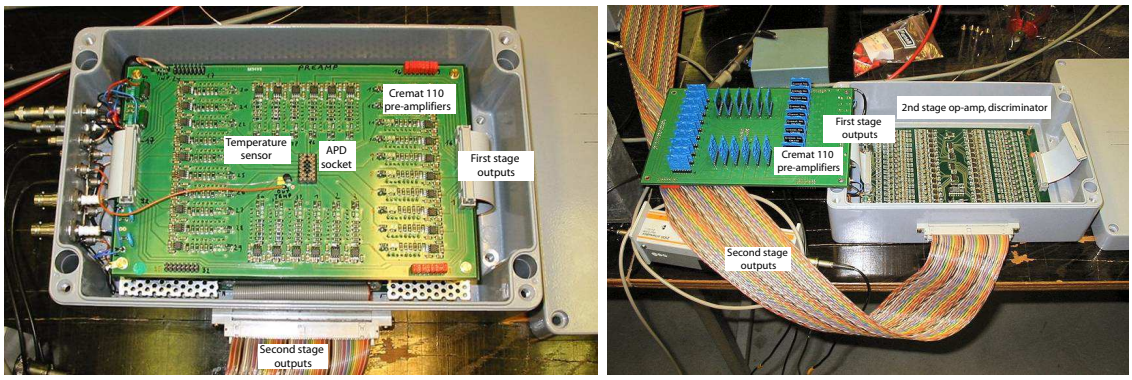


Figure 2.13: Photographs of 2 boards of the "Brussels" Electronics (the third, twisted pair signal receiver and shaperboard, is not shown).

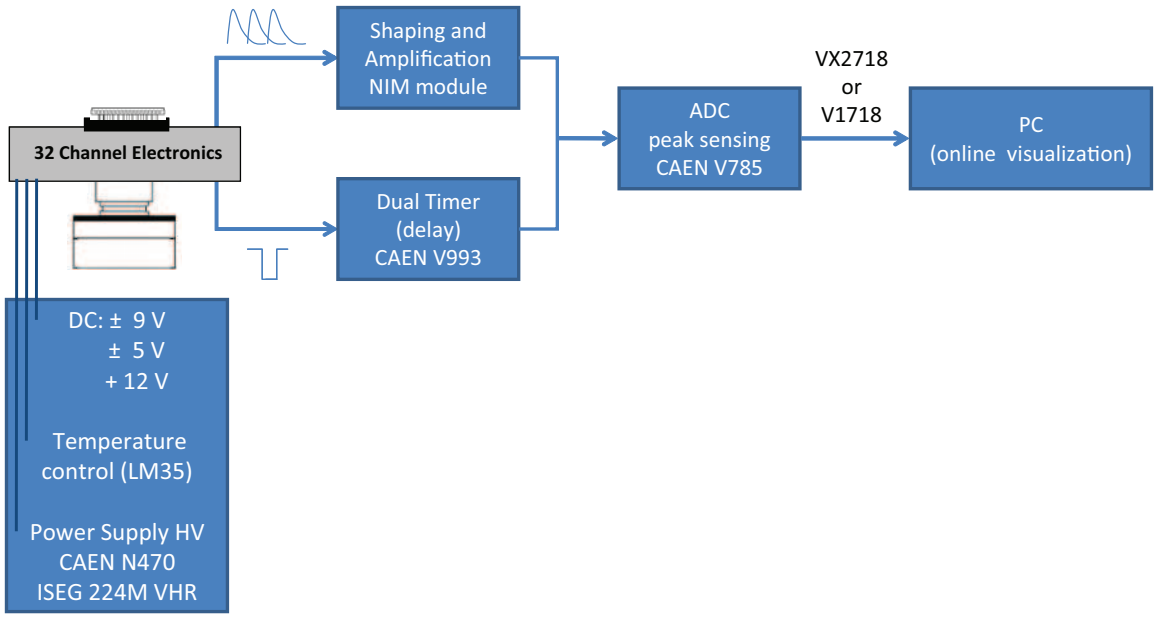


Figure 2.14: 32 channel discrete electronics for single readout scheme.

A schematic diagram of the setup for single readout using this electronic amplifier chain is shown in Fig. 2.14. A single Hamamastu S8550 APD is placed in the discrete electronics chain to collect the signal from the radioactive source, using 2-stage amplification, shaping and trigger. Signals are readout by a peak sensing CAEN V785 VME ADC, data is

collected on a dedicated computer for online visualization and analyzed shortly after. The dedicated software to control the experimental runs and monitorized the data taken is based on HAL (Hardware Access Library, CMS) and ROOT, An Object Oriented Framework For Large Scale Data Analysis [Brun1997].

### 2.5.2 Discrete Electronics for Double Readout

To fully explore the detector module performance another discrete electronics was acquired and adapted from the original purpose to the Laboratoire de Physique des Hautes Energies (LPHE) at the "Ecole Polytechnique Federale de Lausanne". The "Lausanne" analogue electronics provide low-noise amplification of 32 APD pixel inputs. Each pixel APD is connected to a charge sensitive pre-amplifier, after which are feed into differential-integrator shapers. The shaped output pulse passes through level discriminators, producing digital signals that are analyzed by a trigger logic. Two sets of 32 output channels are available: slow outputs after the differential-integrator shaper/amplifiers and fast lines available after the amplification and the differential shaper stage [Mosset2006].

Originally, the "Lausanne" analogue processing electronics was developed with the aim of performing the signal readout of a complete 32 crystal matrix read at one of its ends by a Hamamatsu S8550 multi-pixel APD. In order to collect data from a double readout module, a group of 16 channels was connected to one APD and the second group to the opposite APD. The 32-channel positive signals are coupled to CR–110 Cremat low-noise charge pre-amplifiers with an internal gain of 1.4 V/pC [Rodrigues2007]. Due to the low amplitude of the output signal pulse is sent through a differential-integrator shaper for amplification and pulse shaping needs before it reaches the ADC module.

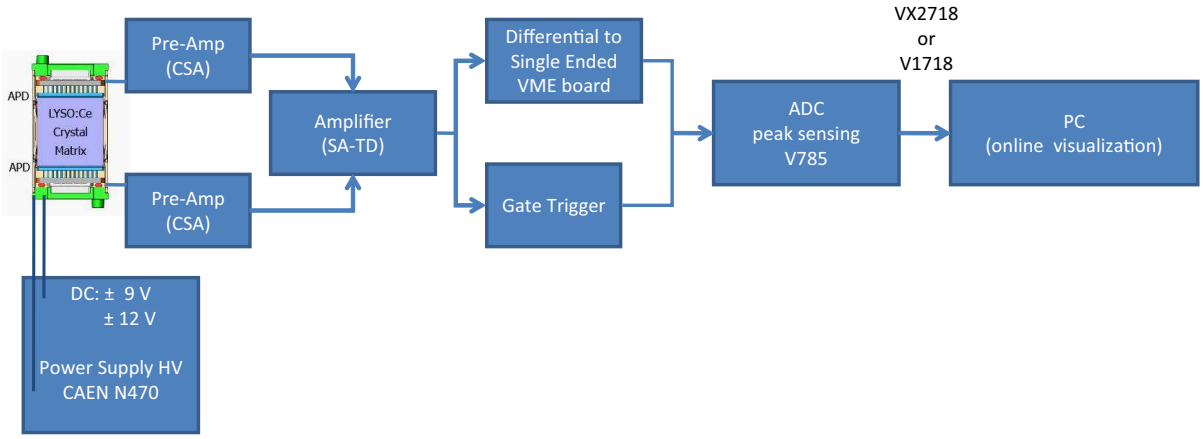


Figure 2.15: 32 channel discrete electronics for double readout scheme.

A schematic diagram of the setup for double readout using this electronic amplifier chain is shown in Fig. 2.15, as well as some illustrating photographs (Fig. 2.16). A detector module is placed in the discrete electronics chain to collect the signal from the radioactive source which can be positioned at one top of the detector module or at a side, for lateral incidence.

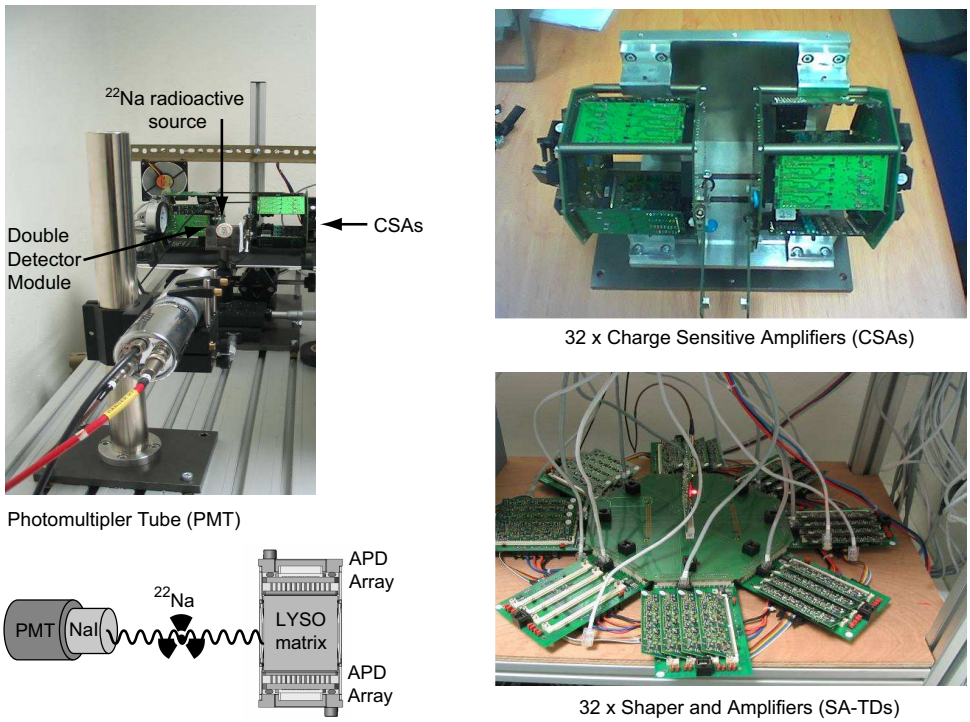


Figure 2.16: Photographs of the "Lausanne" electronic chain [Rodrigues2007].

Whenever a signal appears at any of the 32 channels it is compared with a common threshold. If one of the channels is higher than the amplitude threshold all 32 channels are readout and a digital trigger gate issued. When the amplified pulses are digitized by peak sensing ADCs, the trigger gate needs to reach the ADCs prior to the arrival of the amplified signals. This is accomplished by transporting the differential analogue signals in several meters of Cat5 cable, providing a 250 ns delay. The differential signals are converted to single-ended in a custom VME board, and then connected to the ADC. The "Lausanne" gate is fed, without delay, into a coincidence unit together with a CFD logic signal from the photomultiplier coupled to a NaI:Tl crystal for electronically collimated measurements with $^{22}$Na. The coincidence unit generates the ADC signal gate which is then used as trigger signal by the ADCs. For un-collimated and background measurements the NaI:Tl trigger is not used.

## 2.5.3 Discrete Electronics Commissioning

### 2.5.3.1 Single Readout Electronics

The commissioning of the single readout electronics consisted mainly on the injection of the controlled amounts of charge directly in each of the 32 CR-101D Cremat charge sensitive preamplifiers. A test signal, produced by a Tektronics AFG3252 function generator, was applied to a 2.2 pF capacitor. Synchronous to the test signal, a gate was generated and used to open the sensing gate of the peak sensing ADC V785. The analog output pulses after the final shaping stage were also routed to the V785 ADC.

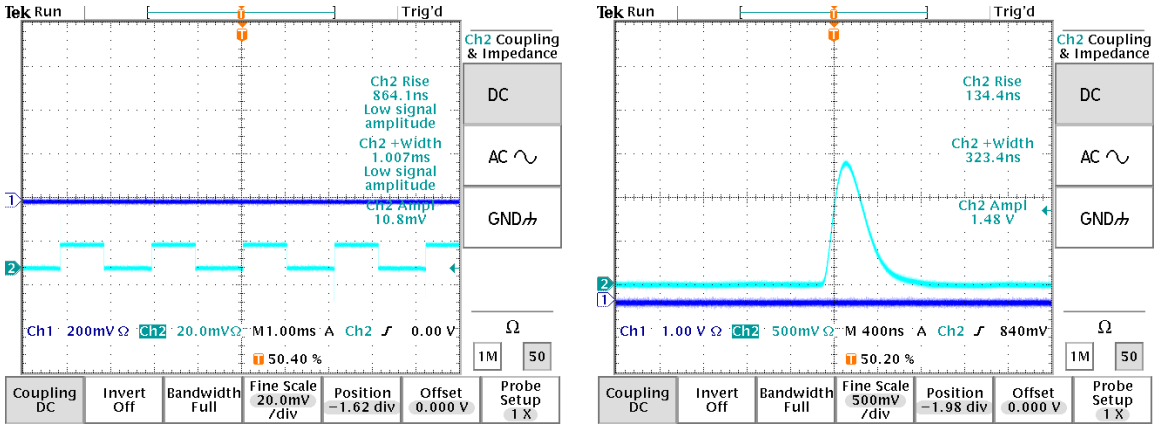


Figure 2.17: (*left*) Input test pulse with amplitude of 10.8 mV with 1.0 ms duration and (*right*) corresponding output pulse shape.

Six discrete values of voltage for the test pulse were selected: 6.85, 8.04, 9.3, 10.5, 11.6 and 12.8 mV. Fig. 2.17 (a) shows the applied test pulse (10.8 mV case) and the corresponding output pulse after the shapers (third board) (b). As can be observed in Fig. 2.18, the behaviour is rather linear, and a simple linear fit describes well the data. A similar plot, but for all channels is presented in Fig. 2.19. Is can be observed that the gain spread is low except channel 8, which has a low gain.

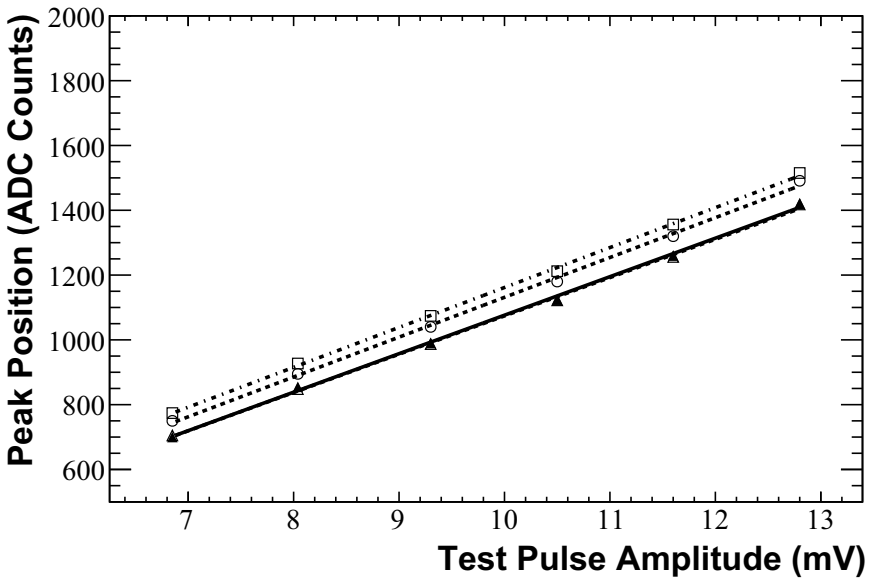


Figure 2.18: Variation of the pulse amplitude as function of the test pulse amplitude applied at a 2.2 pF capacitor for 4 typical channels.

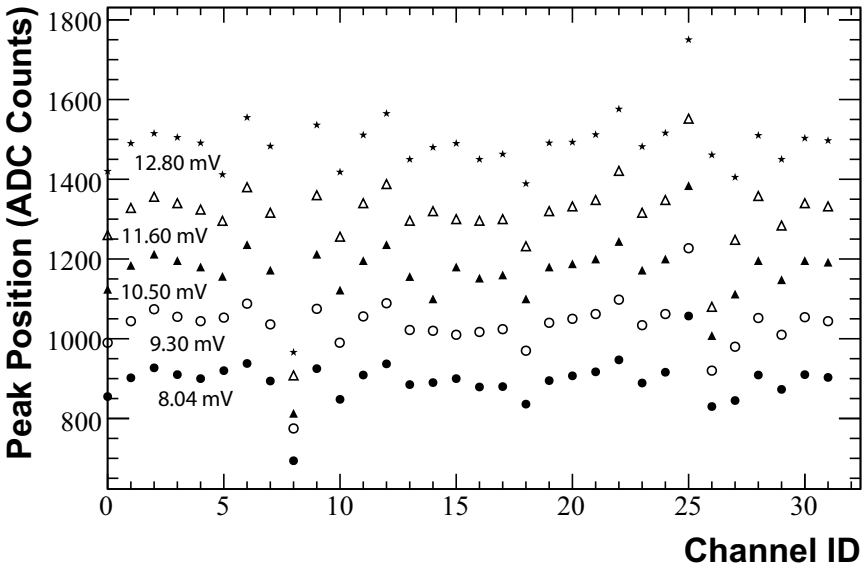


Figure 2.19: Scan of the variation of the pulse shape amplitude for all channels. Measurements corresponding to a test pulse of 6.8 mV not shown for clarity of the plot.

From the fits to the amplitude of the output pulse as function of the test pulse the slope or the combined gain of each channel was computed. Results are shown in Fig. 2.20. The mean relative gain is 122.9 ADC/mV with dispersion in relation to the mean value of about 2.8%. By taking into account the capacitor value of 2.2 pF, this yield a mean absolute gain of 55.8 mV/fC which correlates well with the expected value of 55 mV/fC.

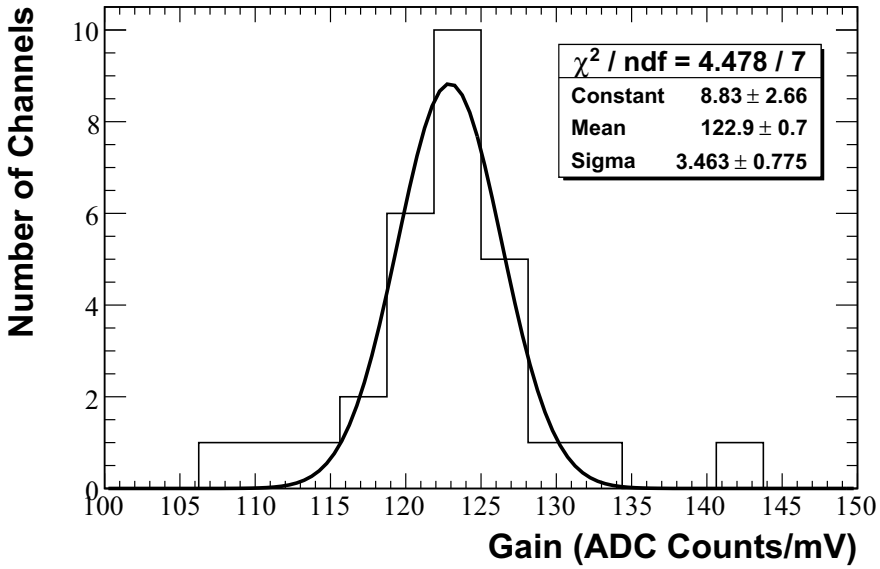


Figure 2.20: Absolute gain distribution of the single readout electronics.

The variability of the pedestal level (DC value from the Brussels electronics combined

with the DC value of the peak sensing ADC) was also evaluated. Results are shown in Fig. 2.21. The mean pedestal is of 156 ADC counts, with a dispersion of 15.9%. Two channels (13 and 27) show variations up to 260 ADC counts. This fact points out that a threshold common to all 32 channels should not be used in the ADC in order to avoid a decrease of the dynamic range of the remaining crystals.

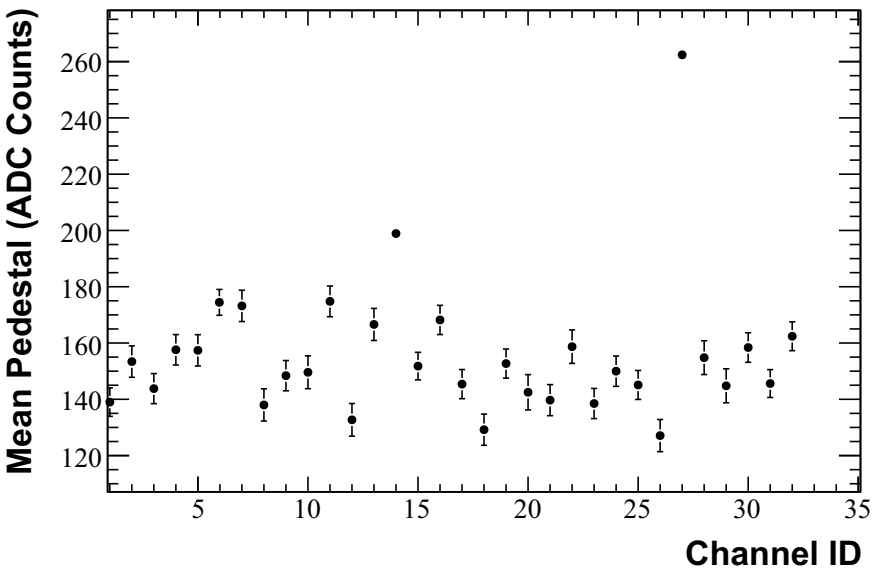


Figure 2.21: Measured pedestal as function of the channel identifier.

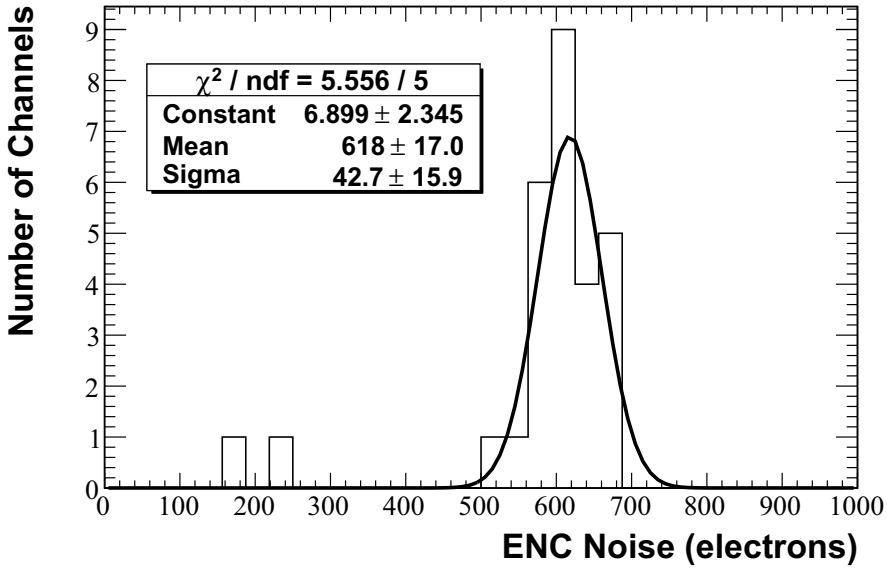


Figure 2.22: Equivalent noise charge (ENC) for the single readout electronic setup.

Combining the r.m.s. of each pedestal and the total absolute gain of each channel, the

total noise (without the contribution from the dark current produced by the APD) can be computed. Results are shown in Fig. 2.22. A mean ENC charge of 670 electrons with a dispersion less than 7% was obtained, which indicates that the developed electronics is well suitable for the evaluation of APD photodetectors.

#### 2.5.3.2 Double Readout Electronics

The commissioning of the double readout electronics was performed in a similar manner to the one employed for the single readout electronics, described in the prevision subsection. Briefly, it consists on the injection of electrical charge directly in each of the 32 CR–101D CREMAT charge sensitive preamplifiers, by means of a test signal produced by a Tektronics AFG3252 function generator at the terminals of a capacitor.

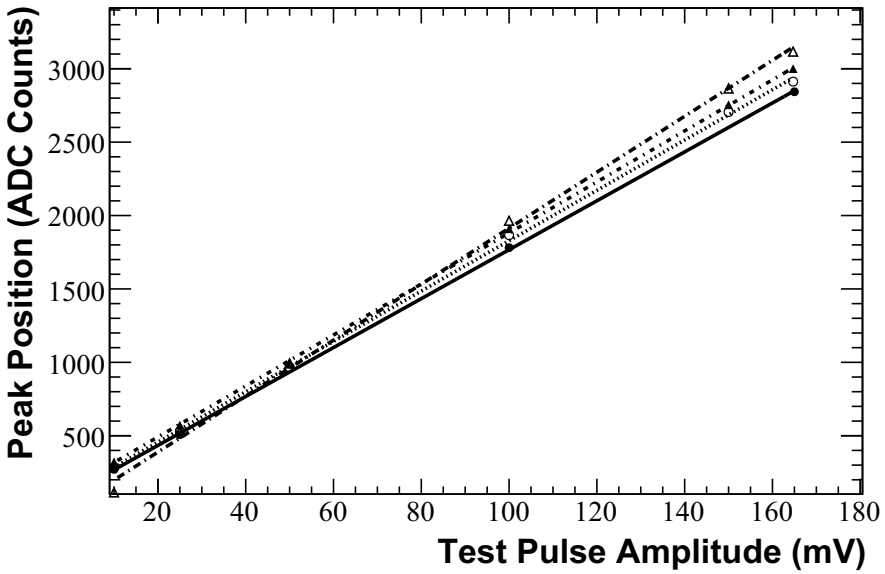


Figure 2.23: Variation of the pulse amplitude as a function of the test pulse amplitude applied for 4 typical channels.

In Fig. 2.23 the variation of the pulse amplitude for four typical readout channels is shown, where a good linearity can be inferred. For the scanned channels, the overall electronics gain expressed in terms of ADC counts, as recorded by the peak sensing ADC, in function of the test pulse amplitude was calculated. Results are shown in Fig. 2.24. A mean gain of 17.81 ADC Counts per mV was found. The inter-channel gain dispersion was of about 7%, slightly higher than the one obtained with the single readout electronics (2.8%). The mean gain is a factor of 7 lower than the one obtained with single readout version. This difference was traced back to the initial settings determined by the final amplification electronics, which is regulated by a turning knob.

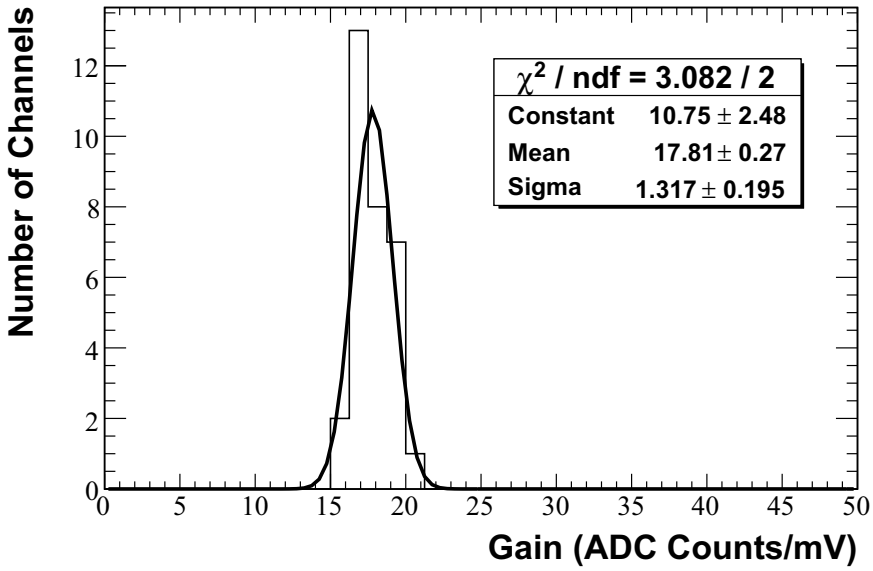


Figure 2.24: Absolute gain distribution of the double readout electronics.

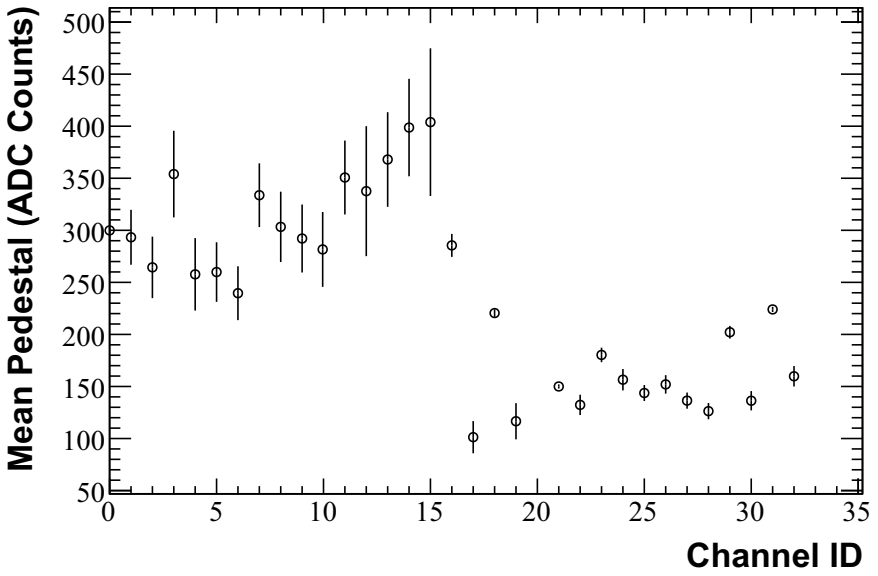


Figure 2.25: Measured pedestal as function of the channel identifier.

The variability of the pedestal, which reflects the combination of the DC value form the double readout electronics with the DC value from the ADC peak sensing module, was also assessed. Results are shown in Fig. 2.25. As can be observed two different behaviours were found for the channel pedestal and variability or noise r.m.s.. Channels with identifiers from 0 to 15, have a larger mean pedestal (320 ADC counts), with a noise r.m.s. of about 55 ADC counts. In contrast, the second group, corresponding to channels 16 up to 31, has a lower mean r.m.s. noise, down to less than 10 ADC. These

measurements are in good agreement with independent ones reported in [Rodrigues2007]. The different behaviour in terms of the mean and r.m.s. pedestal is expected to arise from the connectors that bridge the APD to the "Lausanne" frontend PCB.

### 2.5.4 ISEG High Voltage Supply Calibration

For an optimum performance of APD-type photosensors, precise, accurate and low-noise bias supplies mechanism need to be used. For example, the Hamamatsu S8550 multi-pixel array, which was adopted for the ClearPEM project (see Chapter 1), shows a gain variation of 3.6%/V at gain 50 rising up to 5.8%/V at gain 100. Therefore and in order to avoide the introduction of a bias in the gain response of the APD that would deteriorate the energy resolution, bias supplies should be stable at least at the 50 mV level.

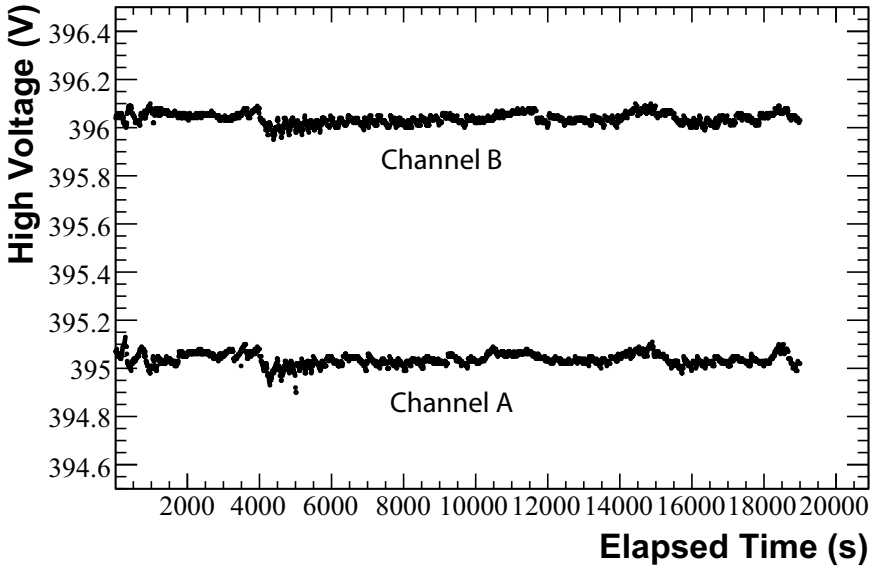


Figure 2.26: ISEG NHQ high voltage stability study. Values recorded along 5 hours. Input values: 395V (channel A) and 396V (channel B).

Characterization of the available HV modules at TagusLIP was performed by monitoring the HV voltage as function of time. Results for the NIM NHQ 224M ISEG module are shown in Figs. 2.26 and 2.27. Channel A was programmed with a target value of 395V while channel B was programmed to supply a value of 396 V. Values were recorded along a 5-hour interval. Results show that channel A actually delivers 395.036 V and channel B 396.039 V. The standard deviation is about 23.7 mV and 22.5 mV, respectively. The reported values are those obtained by the internal sensing circuit implemented in the NHQ module and correlate very well, within 50 mV, of the value measured with a Keithley 2000 multimeter at the end of the HV cables.

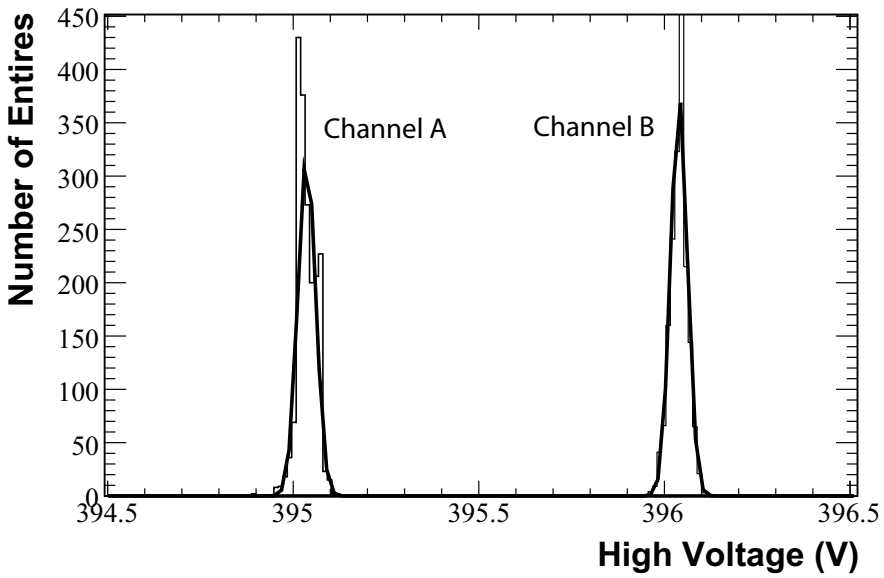


Figure 2.27: HV distribution of the two ISEG NHQ (VHR option) channels, monitored along 5 hours.

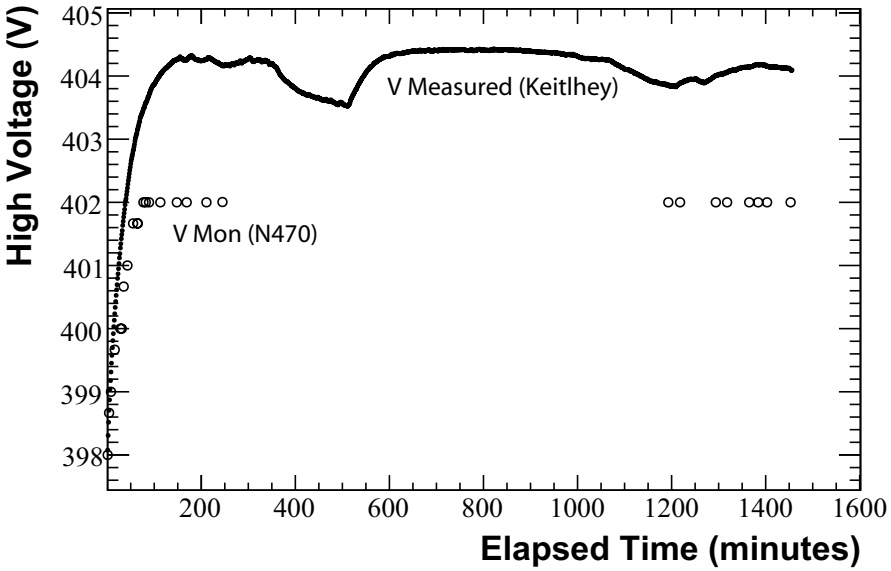


Figure 2.28: CAEN N470 high voltage stability study. Values were recorded along 25 hours. Only one channel, for clarity of the plot, is shown.

Results for the N470 module from CAEN are shown in Fig. 2.28. Only one channel is shown, which was programmed to deliver 403 V. As can be observed, the behaviour of this module in terms of accuracy and stability is significantly different from the NHQ module. During the first three hours, the module drifts from an initial value of 398 V up to about 404 V. After this warm-up time, the N470 module becomes more stable,

although differences in the 400 mV range can still be observed - Fig. 2.29. An interesting point with this module is that the internal sensing system of the N470 module (curve in Fig. 2.28 labeled as V MON) shows a systematic difference of about 2 V in relation to the stabilized value of 404 V ± 500 mV, measured with a Keithley 2000 multimeter at the end of the HV cable. Similar behaviour (not shown) was observed in the second channel of the N470 module.

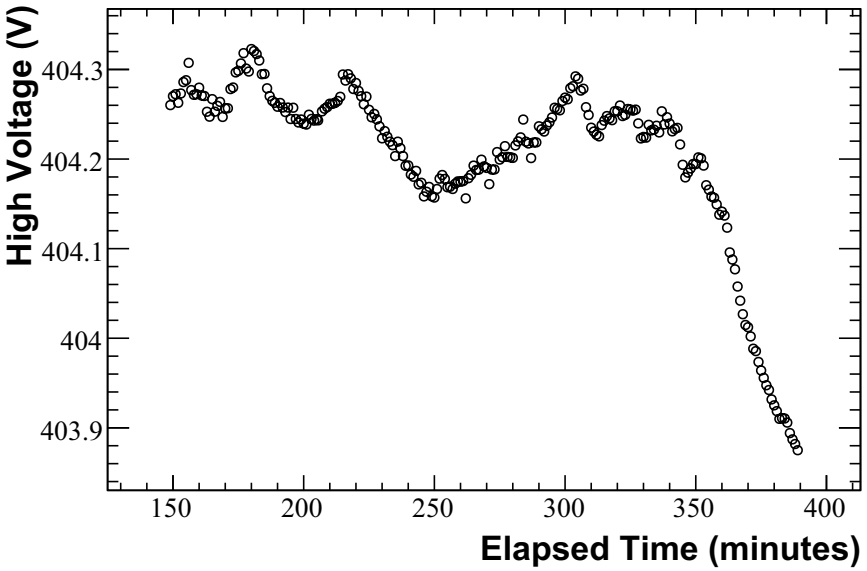


Figure 2.29: Behaviour of N470 high voltage in the stabilized operation region.

This study points out that for improved performance of the N470 module a settling time of roughly 3–4 hours should be adopted before measurements are made. In comparison, the ISEG NQH module can be used almost immediately after its power-on.

## 2.6 Summary and Discussion

The ClearPEM scanner was designed and developed during a timespan of several years that demanded a suitable working area, following radiological safety guidelines. Tagus-LIP was setup for R&D, experimental tests, integration and acquisition electronics. It currently has a working area of 300 $m^2$ with a hot bunker devoted to nuclear testing and radiological safety systems.

As part of this thesis, the evaluation of these radiological safety systems was carried out. Results indicate that the typical radiation dose is 2 $\mu$Sv per day. During the integration and commissioning phase of the scanner at IPO–Porto similar measurements were performed with a higher absorbed dose of 4 to 6 $\mu$Sv but still within the radiation limits established by International Commission on Radiological Protection.

Besides the radiological assessment, work was carried out on the commissioning of the discrete electronics setups available for the design an quality control phases of the ClearPEM detector modules. Both electronic setups, single and double readout modes, are characterizes by a good gain uniformity and low noise. Pedestal variations were found to be significant requiring individuals thresholds for the ADC modules. High voltage stability was also appraised for two independent modules and results have shown distinct behaviours. The ISEG NHQ module was found to be usable almost after power-up and is very stable in several hours but the CAEN N470 presented a significant drift that demanded a warm-up time of about 2 hours.

Chapter 3

# The Baseline ClearPEM Detector Module

## Contents

## 3.1 Introduction

Development of detectors for PET has often seen the migration of technologies, originally developed for high energy physics experiments, into prototype PET detectors. A key component of such imaging systems is the detector module, as its performance determines the overall functioning of the detector.

The design and construction of the ClearPEM detector module with depth of interaction (DOI) capability has been one of the most important and innovative aspects of the project and has required several developing iterations up to its final design. The process has involved the choice of the scintillator crystal and its polishing treatment, wrapping and optical coupling to the photodetector, in order to optimize both the light collection and the DOI measurement performance, and simultaneously solve electrical-mechanical connectivity questions, alignment constrains and the final mechanical packaging of the detector modules.

In this chapter, the ClearPEM detector module is fully characterized. The design principles and the mechanical assembly of the detector module are presented, as well as the performance evaluation results, obtained during the experimental work carried out in this thesis. Assessment of the long-term stability of the main performance parameters, namely light collection, energy and DOI resolution is also discussed.

## 3.2 Design Principles of the Detector Module

The ClearPEM prototype was initially intended to evaluate PET technology in the diagnosis of malign neoplasm in the breast and of ganglion loco-regional invasion. Relatively to whole body PET systems, a dedicated equipment has potentially better spatial resolution, obtained with fine-grain crystal segmentation, and allows a closer coverage of the region under analysis, leading to a better sensitivity. Moreover, whole body PET systems are expensive and massive and not adapted to a systematic breast screening. Because of their open geometry they are also very sensitive to the background from the chest which reduces the detectability of small lesions in the breast [Lecoq2002].

The ClearPEM scanner was developed considering three main guidelines: low background, minimizing the fraction of random coincidences under a high flux of single photons (up to 10 MHz); high sensitivity and spatial resolution down to 2 mm [Abreu2006]. Sensitivity is an important parameter on the design since when the sensitivity is increased it allows a lower injected dose and a shorter examination time. This is particularly important in determining the frequency of scans for women as well as the lower limit of their age for systematic screening. Sensitivity depends on geometrical and physical parameters of the detector. The detector geometry must cover the largest solid angle possible, although some limitations are imposed by image reconstruction considerations as well as by the specificity of human body anatomy and examination practice. The detector thickness and the crystal physical properties (density and composition) determine the photoelectric

interaction probability for the emitted photons and in consequence have a direct impact on ClearPEM sensitivity. On the other hand, the crystal length is responsible for the parallax effect in the image reconstruction process and the consequent degradation in spatial resolution [Moses2004]. Parallax effect in ClearPEM is an important issue especially for being a planar detector located close to the object under examination. In consequence, high-density crystals combined with a method that provides depth-of-interaction information were required for the detector.

The crystal transverse dimensions (about $2\times2$ mm$^2$) were determined by the desired position resolution, whereas the longitudinal dimension (20 mm) was dictated by the required detector sensitivity. The detector assembly is based on two detecting heads, each one formed by 96 detector modules of $8\times4$ crystal matrices. Depth-of-interaction information could be obtained by the "phoswich" technique using, instead of a single 20 mm long crystal, two 10 mm crystals with two different time constants [Ziemons2005, Mosset2006]. The analysis of the signal shape should allow distinguishing in which of the two longitudinal segments the interaction occurred. An alternative technique is to collect the crystal light in the front and back faces and to use the relative amplitude of the two signals to estimate the longitudinal coordinate of the interaction point [Shao2000]. This last technique was adopted for the ClearPEM prototype, as result of preliminary experimental work carried out in 2003, that falls outside of the scope of this thesis and will be only briefly discussed with the aim to better contextualize the work presented in this chapter.

### 3.2.1 Photosensors

As already discussed, one of the requirements for the ClearPEM scanner was to achieve spatial resolutions better than 2 mm without compromising the packing fraction (or the system sensitivity). To achieve this goal, the ability to obtain depth of interaction measurements on an event-by-event basis was mandatory as well as to readout the scintillation light without introducing ($b \approx 0$) light sharing effects. A solution based on a double readout scheme and an individual 1:1 coupling between the photodetector and the LYSO:Ce crystal was explored. However, to do this without putting large amount of non-active material in the patient port and without decreasing the packing fraction due to dead spaces usually introduced by the placement of several photodetectors side-by-side, it has required the adoption of a particular sensor. Position sensitive or multi-anode (PS-PMTs) photomultipliers could be used but only on one of the sides or when coupled to a crystal optical fiber readout. Due to its very compact assemblies, semiconductor photosensors are mandatory for the patient port, like in the implementation adopted for the LBNL PEM scanner [Wang2006]. Using multi-pixel silicon pin-diodes (Si PDs) together with photomultipliers has however downsides related to their very different gains [Shao2000, Shao2002, Wang2004]. This effect could be partial avoided with the multi-pixel avalanche photo-diodes (APDs) devices, currently available from different vendors such as Hamamatsu Photonics K.K., RMD – Radiation Monitoring Devices, Inc. and PerkinElmer Optoelectronics, Inc..

The traditional readout based on photomultipliers was thus replaced by APDs, allowing to implement a 1:1 readout type (b $\approx$ 0). APDs have higher quantum efficiency and less inter-channel cross-talk than standard PS-PMTs. The gain is between 50–1000, a clear improvement when compared with silicon photodiodes (Si PDs) which do not have internal gain, but still lower than the ones obtained in standard (PMT) and hybrid photon detectors (HPDs) [Braem2004]. The small dimensions of the APDs are compatible with a direct coupling to pixelized crystals. Due to its compactness, it is possible to read each single crystal with one APD pixel on each ends, and to use the relative amplitude of the two signals to estimate the longitudinal coordinate of the interaction point [Shao2000]. This solution named double readout cannot be easily implemented in conventional whole body ring and planar PET scanners, since the amount of non-active material (electronics and photomultipliers) placed between the anatomic region under examination and the crystals would lead to an unacceptable decrease of the solid angular coverage plus additional attenuation of the incoming photons. Optical fiber readout could be used to extract the scintillation signals to photomultipliers placed outside the detector heads but at the expense of energy and time resolution due to light losses inside the fibers and additional optical interfaces.

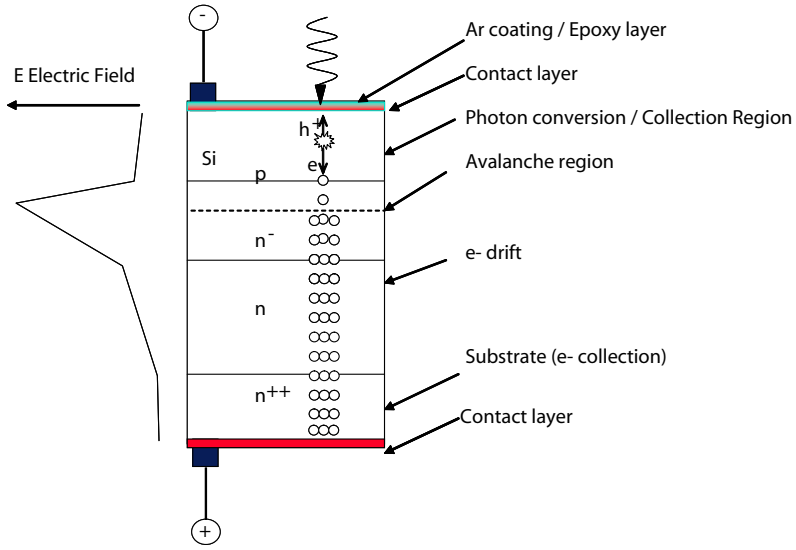


Figure 3.1: APD reverse structure scheme (adapted from [Rusack2003]).

In avalanche photodiodes, a reverse bias is applied to a p-n junction and a high-field is formed within the depletion layer. This leads to the acceleration by this field of the initial charge carrier (photo-electrons) which will collide with atoms in the field. After collision, secondary carriers are produced. The amount by which this process can be repeated, while maintaining the final charge proportional to the number of initial photo-electrons, is limited. Considering the schematic cross-section for a typical APD structure (Fig. 3.1), the basic structural elements provided by the APD include an absorption region "A", and a multiplication region "M". Present across region "A" is an electric field "E" that serves to separate the photo-generated holes and electrons, and sweeps one carrier toward the multiplication region. The multiplication region "M" is designed to ex-

hibit a high electric field so as to provide internal photo-current gain by impact ionization.

In spite of the low gain ($10^2$–$10^3$) when compared to photomultipliers, the light conversion quantum efficiency is significantly higher, by a factor of 2–3. The S8550 APD from Hamamatsu Photonics, K. K. with 32 pixels in a 8×4 configuration was evaluated by the Crystal Clear Collaboration in 2002–2003 [Mosset2003, Mosset2006]. Promising results led to its adoption for the ClearPEM scanner. The S8550 array is assembled from two distinct monolithic silicon wafer parts, of 2×8 "reverse" type structure pixel elements. The pixels are mounted on a 1 mm thick ceramic package with a 0.5 mm thick epoxy window [Hamamatsu2001, Kapusta2003]. Each Si pixel element has a 1.6×1.6 $mm^2$, compatible with an individual 1:1 readout of 2×2 $mm^2$ cross-section LYSO:Ce crystals (Fig. 3.2). The element pitch is 2.3 mm and all the pixels placed in the same sub-matrix share the same common bias. This particular APD is an upgrade of the original Hamamatsu 2×16 pixel APD, which was initially used in the small animal PET scanner MADPET [Pichler2001]. Most of its design layout is similar to the S8644–55 APD, developed by Hamamatsu for the CMS collaboration. The 4 × 8 version was also adopted for the MADPET–II upgrade [McElroy2005] with 1120 LSO:Ce crystals readout by 35 APD S8550 units and for the miniature PET scanner for in-vivo rat brain imaging (RatCAP) scanner with 384 LSO:Ce crystals (2.2×2.2×5 $mm^3$) arranged into 12 units [Vaska2005]. The specifications for the Hamamatsu S8550 APD are summarized in Tab. 3.1.

| Parameter | Value |
|---|---|
| Pixel size | 1.6 mm × 1.6 mm (× 32 pixels) |
| Pixel pitch | 2.3 mm |
| Window type | 0.5 mm thick epoxy resin |
| Peak sensitivity wavelength | 600 nm |
| Quantum efficiency @ 365 nm | 50–58% |
| Quantum efficiency @ 420 nm | 72–76% |
| Gain | 50–200 |
| Polarization bias | 400–500 V |
| Gain gradient @ M = 50 | 3.6%/V |
| Gain gradient @ M = 100 | 5.8%/V |
| Gain gradient @ M = 200 | 13.4%/V |
| Dark current | 2–4 nA (per pixel at gain M = 50) |
| Capacitance | 10 pF (per pixel at gain M = 50) |

Table 3.1: Hamamatsu S8550 APD electrical and optical characteristics.

The effective S8550 gain, the ratio of the total number of secondary avalanche electrons produced by the initial number of electron-hole pairs due to the scintillation light, can vary between 50 and 200, with a specified inter-pixel gain variation around 5% r.m.s. and a dark current of 2–4 nA per pixel. The terminal capacitance is 10 pF per pixel at gain 50. The S8550 APD operates at a bias voltage between 360-500 V, depending on the required gain. The gain varies by about -2.4%/°C at gain 50. This is due to lattice vibrations in the silicon structure of the APD which are enhanced as temperature increases making

more probable to interact with avalanche secondary electrons. Temperature drifts, if not controlled, may thus originate gain drifts contributing to a detioration of the energy resolution. The temperature gradient is also function of the bias voltage, which means that at higher gains the APDs show an increased susceptibility to temperature drifts. All this will impose the system to operate under very stable thermal conditions. The gain gradient as function of the polarizing bias increases as function of the gain itself. For higher gains, the bias polarization supplied must be very stable with controlled amounts of tension ripple.

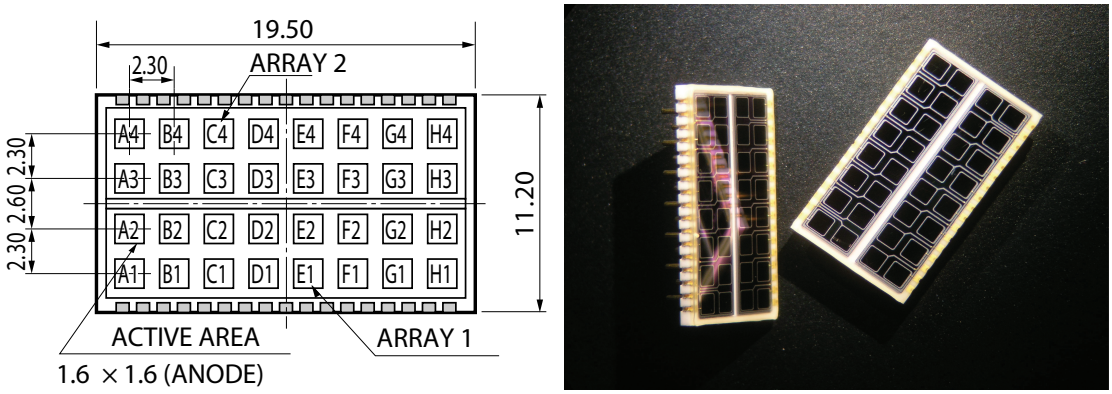


Figure 3.2: Hamamatsu S8550 APD: scheme and dimensions (*left*) and photograph (*right*).

The main features that dictated the adoption of the Hamamastu S8550 APD for the ClearPEM scanner were the following:

- Stable operation for gain between 50–150;
- Gain variation between pixels of the same subarray less than 20% (worst case);
- Reverse type design (Fig. 3.1), based on the S8664-55 APD, original developed for the CMS experiment at CERN. About $1.2\times10^5$ APDs were produced by Hamamatsu demonstrating the feasibility of its mass production;
- Availability in large quantities within a short lead-time (6 months for 400 units/ $1.4 \times 10^4$ pixel APDs).

The S8550 also presents an interesting aspect that is a low excess noise factor $F$ value, as will be shown latter, due to the thin depletion region, which makes it able to achieve energy resolutions comparable to a PMT based readout scheme. A quality control (QC) protocol and methodology for the 400 S8550 APDs were developed. Two independent setups were used in the QC: one setup based on the direct measurement of the APD array common cathode current when illuminated by a 420 nm blue LED light; the other, based on the measurement of light pulses induced on scintillating crystals by a $^{137}$Cs source. With the first setup each APD subarray was measured independently in terms of gain dependence on bias voltage, gain gradient at several voltages and dark current dependence on the bias voltage, while the second setup used dedicated amplification and

data acquisition electronics for the measurement of gain dispersion among individual APD pixels. The QC had very good results in terms of the performance of the Hamamatsu S8550 arrays: average bias voltage for gain 50, of 419 and 418 V for sub-array1 and 2 respectively, average dark current of 27.1 and 24.2 nA, for sub-array1 and 2, and average gain variation of 3.6%/V for both APD sub-arrays. Only 1 array was rejected by the QC procedure, due to a 22.7%/V gain variation in one of sub-array [Carriço2006, Abreu2007].

In parallel, several measurements were performed in the scope of this thesis to confirm performance observables of these arrays that were not originally included in the QC program. The following aspects were examined:

- Linearity and stability of the APD response to light in the optical region of the 420 nm which corresponds to the peak scintillation emission of the LYSO:Ce crystals [Pidol2004];
- Excess noise factor $F$;
- Linearity and stability of the APD response to direct ionization by low energy X–rays (5.9 keV) from $^{55}$Fe;
- Ratio of APD gain for 420 nm light versus direct ionization by low energy X–rays.

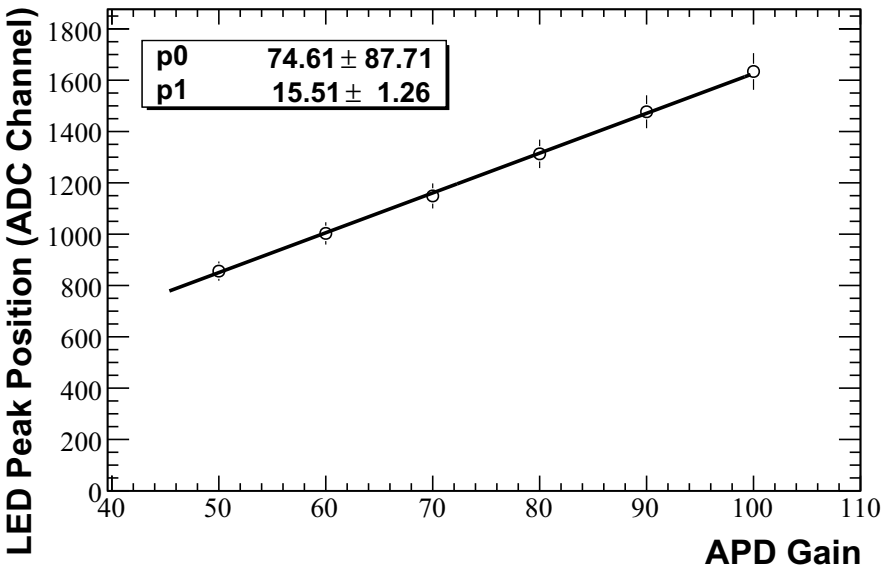


Figure 3.3: Mean variation, over 32 APD pixels of the same APD array, of the LED (420 nm) pulse height spectrum as function of the APD gain.

Linearity and stability of the S8550 APD were evaluated by pulsing a 420 nm LED with a Tektronics AFG3252 function generator. One S8550 APD array from the batch of 400 APDs delivered by Hamamatsu Photonics K.K. was chosen. The applied bias voltage to the APD was fixed in each measurement run. Gains of 50, 60, 70, 80, 90 and 100 were

explored. For each gain the appropriate high voltage was determined by measuring the total photo current when excited by a 420 nm LED. The photo current was measured with a Keithley picoamperimetre. Due to the required precision for the APD bias voltage, the ISEG NHQ 224M module, presented in Chapter 2, Section 2.5.4, was used. Results are shown in Fig. 3.3, indicating a good linearity in the gain working region from $M = 50$ up to 100. Superimposed to the data is a linear fit of the form $y = p_0 + p_1 x$.

Stability of the gain measurements was also assessed, by measuring with the same 420 nm LED, the pulse height spectra in three different runs. Each run was taken with a 48 hours apart. The same APD bias voltage correspondent to gain 50 was used. The APD bias voltage was kept the same while the LED polarization bias was varied from 2.4 V to 2.5 V. Results are shown in Fig. 3.4. While its known that the LED light output can strongly vary with the ambient temperature it is remarkable that the total amplified charge is constant at the 2% level, indicating a stable operation by the APD.

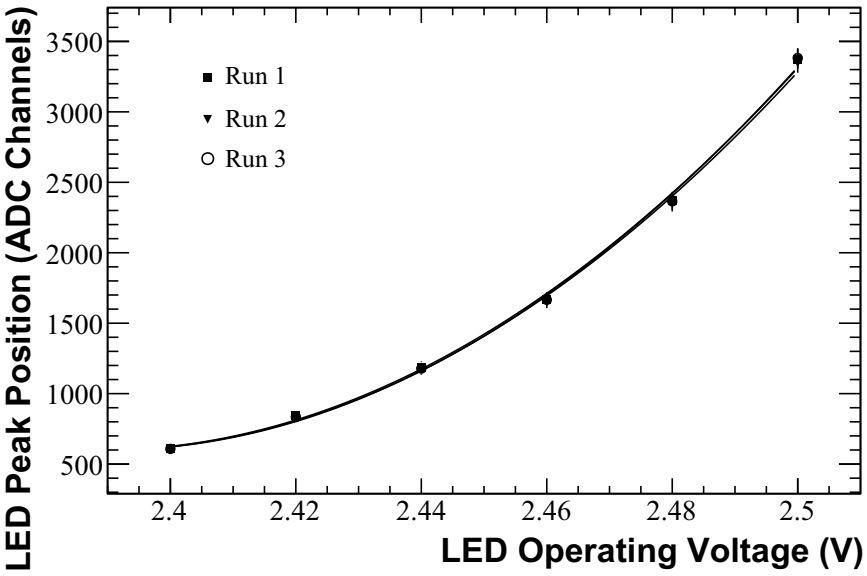


Figure 3.4: Variation of the LED pulse height spectrum peak position as function of the LED polarization bias (3 different runs are shown).

In addition to the APD linearity and stability, the excess noise factor of the S8550 was also determined. All avalanche photodiodes generate excess noise due to the statistical nature of the avalanche process. The Excess Noise Factor is generally denoted as $F$ and is given by:

$$F = \sigma_M^2 / M(M-1) \tag{3.1}$$

where $\sigma_M^2$ is the variance of the multiplication factor and $M$ is the average multiplication factor of the APD. $F$ is the factor by which the statistical noise on the APD current (equal to the sum of the multiplied photocurrent plus the multiplied APD bulk dark current) exceeds that which would be expected from a noiseless multiplier on the basis of Poisson statistics (shot noise) alone. The excess noise factor is a function of the carrier

ionization ratio, $k$, where $k$ is usually defined as the ratio of hole ($\beta$) to electron ($\alpha$) ionization probabilities (k $\leq$ 1). The excess noise factor may be calculated using the models developed by McIntyre [McIntyre1996] or Van Vliet [Van Vliet1979] which considers the statistical nature of avalanche multiplication. According to the McIntyre theory, the excess noise factor is given by:

$$\sigma_M^2 = kM + \left(2 - \frac{1}{M}\right)(1-k) \tag{3.2}$$

The theory of McIntyre cannot be applied because of the small size, of about 3–4 $\mu m$ of the avalanche region in the S8550 [Mosset2006]. In this conditions, the Van Vliet formula has to be used:

$$\sigma_M^2 = \frac{M(M-1)(1-k)}{(2+\beta+k\beta)}\left(-\beta + 2\left(\frac{(1-k\beta^2)}{(1+k\beta)}\right)\right)\left(Mk\frac{(1+\beta)}{(1-k)} + (1+\beta)^{-1}\right) \tag{3.3}$$

The excess noise factor of the S8550 was experimentally determined using the setup described earlier that employs a 420 nm LED pulsed at 500 Hz. The signal variance in the case of an APD illuminated with a LED is given as:

$$\sigma_{tot}^2 = \sigma_e^2 + N\sigma_M^2 + \sigma_N^2 M^2 + \left(\nu N_{LED} - \frac{1}{N_{LED}}N\right)NM^2 \tag{3.4}$$

Since experimentally, the behaviour of the $\sigma_{tot}^2$ is linear in respect to $NM^2$ it can be assumed that the contribution of fluctuations of the LED output is small. In that case, $\sigma_{tot}^2$ can be simplified:

$$\sigma_{tot}^2 = \sigma_e^2 + (F-1)NM^2 + NM^2 \equiv \sigma_{tot}^2 = \sigma_e^2 + FNM^2$$

where $\sigma_e$ is the electric noise of the readout chain (pre-amplifiers, amplifiers and ADCs), $\sigma_{tot}^2$ is the signal variance, $\sigma_e^2$ the electronic noise, $N$ is the average number of photoelectrons and $\sigma_N^2$ is the variance of the photoelectrons number. The APD was biased to a fixed gain of 70 and exposed to light pulses of various intensity. Results for $\sigma_{tot}^2$ versus $NM^2$ are shown in Fig. 3.5. To obtain the collected charge $NM^2$, the ADC channels are expressed in V units, which correspondence is done by knowing that the ADC range is 0–4 V and it is a 14 bit ADC (4096 channels). The ADC value has then to be corrected by the electronic chain gain (55 mV/fC), giving the total charge. To have the number of photoelectrons, $N$, the total charge is divided by the APD gain. Results are fitted with a linear model ($p_0 + p_1 x$) with the slope ($p_1$)giving $F$. The experimental value of 1.83 correlates well with published values for older versions of the S8550 APD ($F = 1.75 \pm 0.05$), by the former CCC – Lausanne Working Group [Mosset2003].

Finally, the performance of the S8550 APD arrays to detect 5.9 keV X-rays by direct ionization of the p-n junction was assessed. The device was irradiated by a $^{55}$Fe source. Spectra were acquired from gain 50 to gain 100. Results for the same APD pixel as function of the gain are shown in Fig. 3.6. The 5.9 keV $^{55}$Fe peak in the pulse height spectrum as function of the APD gain, averaged over 32 APD pixels of the same APD

array, is shown in Fig. 3.7. Similar to the variation of the collected charge by the APD as function of the gain for a fixed LED light output, the APD shows for direct ionization with $^{55}$Fe a very linear response. At gain 50, the energy resolution for the 5.9 keV X–ray is 12.1% with a dispersion of 9%.

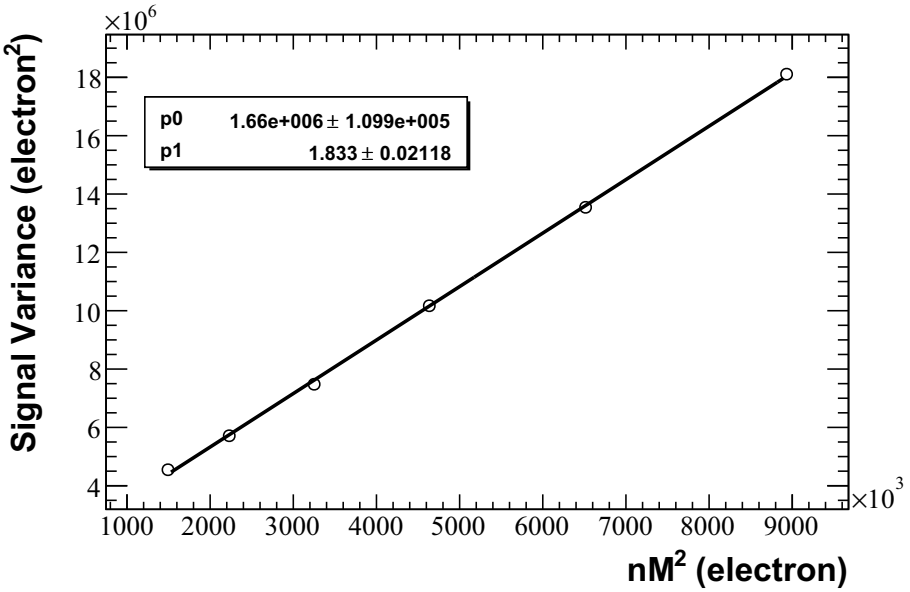


Figure 3.5: Signal variance $\sigma^2_{tot}$ as function of the S8550 collected charge $NM^2$ for gain $M = 50$.

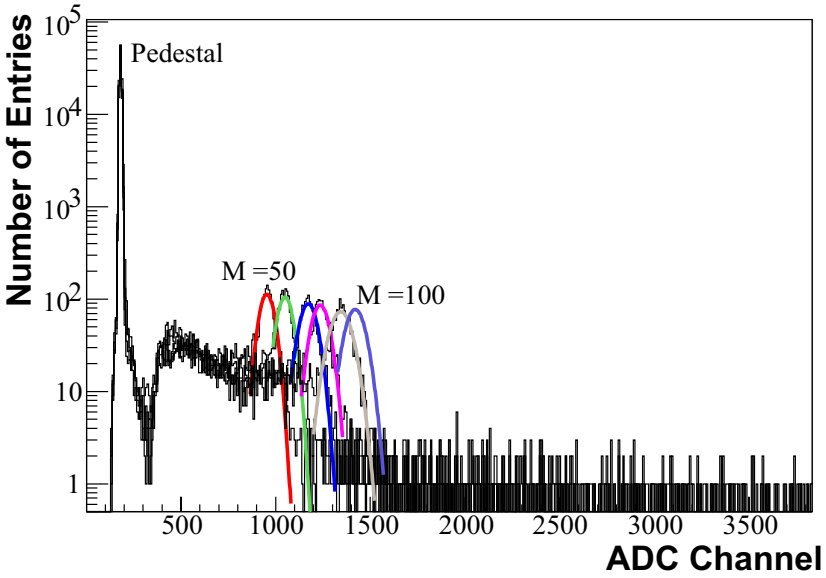


Figure 3.6: Superimposed spectra of the $^{55}$Fe (5.9 keV) for different gains ($M$ from 50 to 100, in steps of 10) for the same APD pixel.

In order to check the gain non-uniformity of the APD array from pixel to pixel, several spectra were acquired with a $^{55}$Fe source and with the same voltage, in two acquisition runs, 15 days apart. The position of the 5.9 keV $^{55}$Fe for each APD pixel taken in the two acquisition runs is shown in Fig. 3.8.

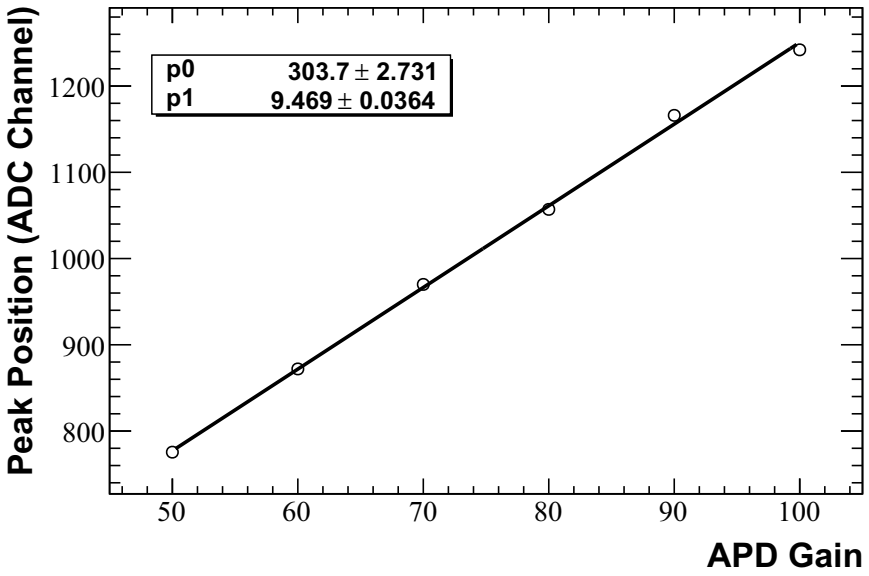


Figure 3.7: Amplitude of the 5.9 keV peak in the pulse height spectrum, averaged over 32 APD pixels of the same APD array, as function of the APD gain.

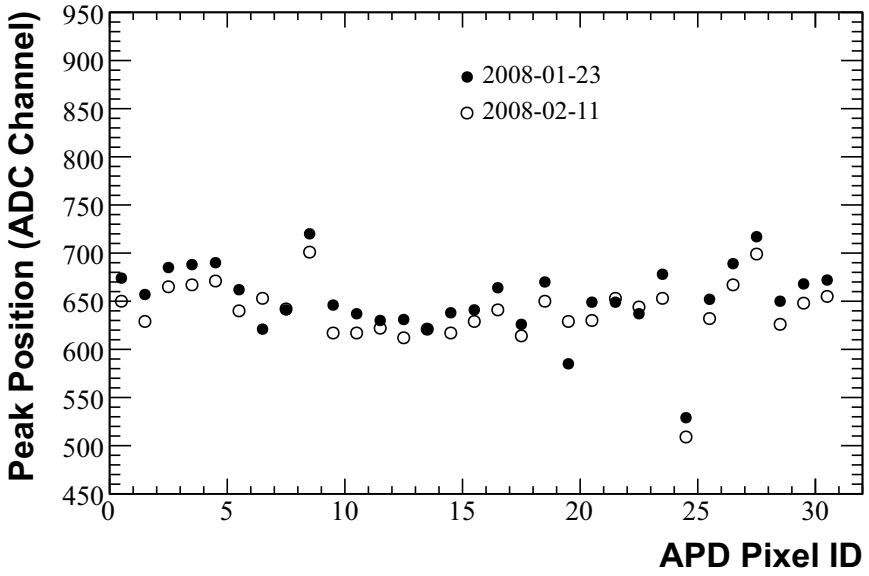


Figure 3.8: Position of the 5.9 keV $^{55}$Fe for each APD pixel taken in two acquisition runs, 15 days apart, at gain 50.

The mean position of the 5.9 keV line was in the first run 653 ADC counts with a dispersion of 5.6%. In the second the mean value of the 5.9 keV line for the 32 APD pixels was 639 ADC counts with a dispersion of 5.1%. While the overall trend between the different pixels of the array is similar in both runs, a 2% shift in the average value was observed. This shift can easly be accounted by differences in the room temperature of less than 1 °C, since APDs at gain 50 have a variation of gain with temperature of -2.4%/°C. The dispersion between APD pixels, when polarized to the same mean gain value is consistent with the device uniformity observed in the CMS APDs, supporting the good reproductibility of the Hamamatsu APD production process. For comparison purposes, the distribution of the relative inter-pixel gain for the 12 288 APD pixels of the ClearPEM scanner is shown in Fig. 3.9. The r.m.s. of the distribution is 4.6%.

It is interesting to note that the S8550, when is polarized to a fixed bias voltage, has different internal gains for pulsed light and X–rays. The difference, as referred in [Moszyński2001, Crespo2005], is due to the internal structure of the APD and the position of the p-n junction, optimized for the detection of light of short wavelength. According to the authors, the difference increases with the applied voltage due to the increasing extension of the avalanche region. Similar spectra acquired at different APD internal gains show a X-ray to light ratio that decreases as the gain increases. This behaviour was also verified in the ClearPEM APDs and is show in Fig. 3.10. This phenomena is due to a deeper penetration of the X–rays into the APD pixel, creating pairs of electron-holes inside the avalanche region. These electrons create a smaller signal in respect to those raised before the avalanche region as a consequence of their shorter path through the multiplication region.

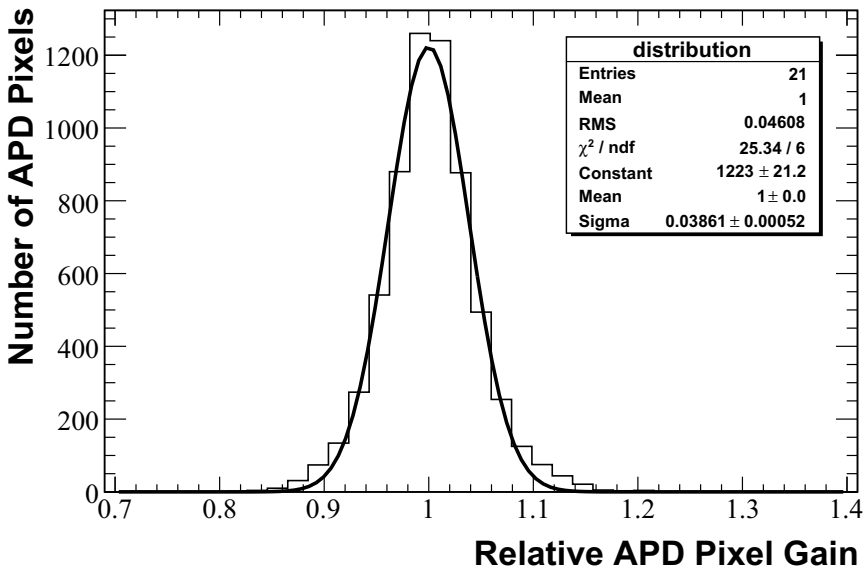


Figure 3.9: Distribution of the relative inter-pixel gain for the 12 288 pixels at M=50 (400 APD arrays).

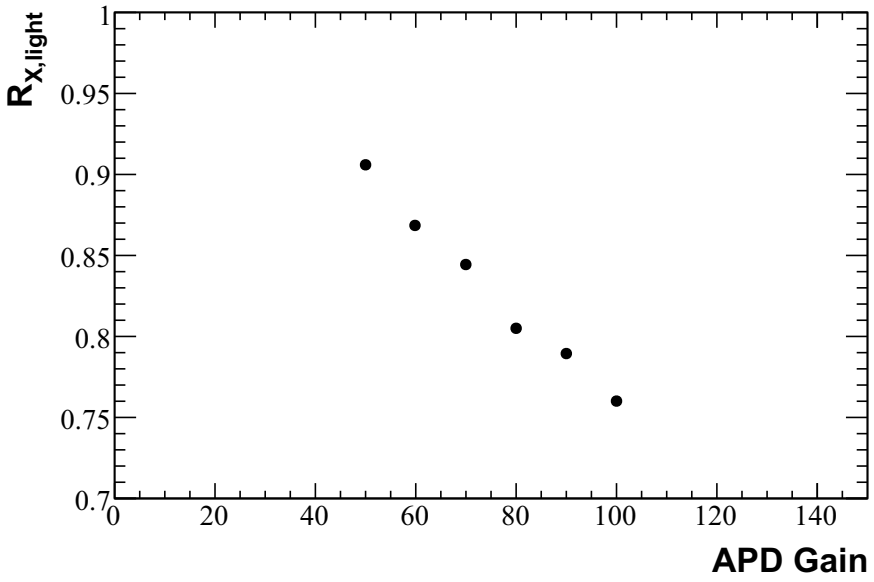


Figure 3.10: $R_{X,light}$ ratio between 5.9 keV $^{55}$Fe X-ray and 420 nm LED light gain for APD gains between 50 and 100.

### 3.2.2 Scintillation Crystals and Reflectors

In the vast majority of PET scanners, inorganic scintillator crystals are used to record the 511 keV photons produced by the annihilation of positrons emitted by injected tracers. The performance of the scanner is strongly tied to both the physical and scintillation properties of the crystals. For this reason, researchers have investigated virtually all known scintillator crystals for possible use in PET. Despite this massive research effort, only a few different scintillators have been found that have a suitable combination of characteristics, and only two, NaI:Tl (thallium-doped sodium iodide) and BGO (bismuth germanate), have found widespread use [Melcher2000]. Since late 90's, a new scintillator crystal was developed, LSO (cerium-doped lutetium oxyorthosilicate), that exceeded all previously used materials in most respects, becoming the scintillator crystal eligible for the new generation of PET scanners.

The desire scintillation crystal for PET has to have high stopping power so that a 511 keV gamma ray will be totally absorbed by the detector, to have very good energy resolution to be possible the rejection of the scatter events, to have fast time response for randoms' rejection and to be inexpensive to produce. The first ClearPEM detector module version proposed was based on the LuAP:Ce (cerium doped lutetium-ortho-aluminate) crystals developed by the Crystal Clear collaboration at CERN [Lecoq2002]. These crystals have high density when compared to LSO and to BGO but a lower light yield when compared to LSO - Tab. 3.2. At that time, LSO crystals were expensive and difficult to acquire but a similar one, LYSO:Ce had been developed with 2–10% of Ytrium content, having, for that reason lower density (7.1–7.3 g.cm$^{-3}$ against 7.4 g.cm$^{-3}$ for the LSO). LuAP:Ce has a density of 8.3 gcm$^{-3}$ but the main drawbacks of its use is the low light

yield, about 20% of LYSO:Ce and technical issues related to the growth process.

| | NaI | BGO | LSO | LYSO | LFS | LuAP |
|---|---|---|---|---|---|---|
| Effective atomic number (Z) | 51 | 74 | 66 | 60 | 63 | 65 |
| Linear Attenuation Coeff. ($cm^{-1}$) | 0.34 | 0.92 | 0.87 | 0.86 | 0.82 | 0.9 |
| Density (g $cm^{-3}$) | 3.67 | 7.13 | 7.4 | 7.1–7.3 | 7.3 | 8.34 |
| Index of refraction | 1.85 | 2.15 | 1.82 | 1.81 | 1.78 | 1.95 |
| Light Yield (% NaI(Tl)) | 100 | 15 | 75 | 80 | 77 | 16 |
| Peak wavelength (nm) | 410 | 480 | 420 | 420 | 430 | 365 |
| Decay constant (ns) | 230 | 300 | 40 | 41 | 35 | 18 |
| Hydroscopic | yes | no | no | no | no | no |

Table 3.2: Properties of some scintillators used in PET detectors (adapted from [Lewellen2008]).

Due to the adequate scintillation and mechanical properties for PET applications, LYSO:Ce became the natural choice for the ClearPEM detector. Among them are its high light output (27 photons/keV), high density (7.1 g.$cm^{-3}$ for 10% yttrium content), high effective atomic number ensuring a high photoelectric cross-section and a fast decay time (42 ns time constant). The LYSO:Ce is easy to machine into pixels and is not hygroscopic. As other scintillators based on lutetium oxide ($Lu_2O_3$), LYSO:Ce contains a natural activity background that arises from the decay of $^{176}$Lu. LYSO:Ce contains a 2.6% abundance of this long-life isotope (half-life $3.73\times10^{10}$ years [Melcher2000]). This radioisotope dacays through a $\beta^-$ decay followed by a gamma cascade from nuclear dexcitation (fig. 3.11). The decay rate is around 300 Bq/$cm^3$ and can be easily suppressed in coincidence measurements as required for PET.

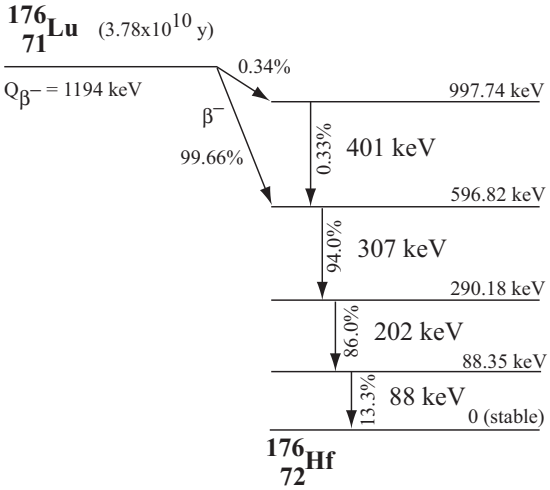


Figure 3.11: $^{176}$Lu decay scheme.

The presence of the $^{176}$Lu background also offers an interesting approach to calibrate double readout scanners, allowing to compute the inter-pixel gain calibration $k_{rel}$, that

equalizes the gain of both pixel APDs that read a given crystal, and the absolute gain calibration $K_{Abs}$ that translates the digit sum energy in a crystal into a physical value. The $^{176}$Lu decay is also used to compute the $C_{DOI}$ calibration constant that allows to translate the light collection asymmetry into the physical DOI constant, as will be shown.

In a double light collection readout approach, as the one implemented in the Clear-PEM scanner, the conversion of the digitized value of the amplified pulse to an energy value in keV requires the extraction of two calibration constants. The total deposited energy $\overline{E}$ in one crystal corresponds to the sum of top and bottom pixel APD pulse amplitudes that are proportional to the reconstructed energies:

$$\overline{E} = \overline{E_0} + \overline{E_1} \tag{3.5}$$

where $\overline{E_0}$ and $\overline{E_1}$ are the top and bottom in units of energy. Eq. 3.5 is formally equivalent to:

$$\overline{E} = K_0 E_0 + K_1 E_1 \tag{3.6}$$

in which $K_0$ and $K_1$ are the calibration constants for the top and bottom APD channel and $E_0$, $E_1$ the top and bottom reconstructed energies coded as ADC integers. The equation can be re-written as:

$$E = K_0 \left(E_0 + k_{rel} E_1\right) \tag{3.7}$$

where $k_{rel} = \frac{K_1}{K_0}$ is the relative inter–pixel calibration constant, with $K_0$ and $K_1$ in units of keV/ADC. Therefore, the energy calibration process can be taken as a two–step process. First, the relative inter–pixel calibration constant $k_{rel}$ is determined, which guarantees that the bottom APD provide a similar response in terms of ADC counts to the top APD. The second step consists in the determination of the absolute ADC counts to energy calibration constant $K_0$, also referred as $K_{Abs}$.

In Clear-PEM a method for the determination of the $k_{rel}$ inter–pixel calibration constant was developed by exploring the presence of the $^{176}$Lu background. It is based on the search of the $k_{rel}$ value that minimizes the differences between the top and bottom APDs, quantified as a $\chi^2/ndf$.

In the ClearPEM scanner, the measurement of the DOI coordinate for each photon allows for the determination of the $z$ coordinate of each interaction in the detector heads. The variation of the light collection as function of the depth of interaction was computed, through out this thesis, using the $^{176}$Lu background or, in alternative, a $^{137}$Cs flood irradiation. The $^{176}$Lu radioisotope decays through a $\beta^-$ decay followed by a gamma cascade from nuclear dexcitation. Due to the crystal production process it can be assumed that the $^{176}$Lu is uniformly distributed throughout the crystal. In this case the $\beta^-$ decays along the depth direction are distributed symmetrically and the light collection asymmetry distribution should be flat, with the exception of the far edges which correspond to the crystal extremities [Wang2004]. The interaction depth of a photon, $z$, is computed from the asymmetry of light collection between the two APDs that readout the light of a given crystal by:

$$z = C_{DOI} \frac{E_0 - k_{rel} E_1}{E_0 + k_{rel} E_1} \tag{3.8}$$

where the $C_{DOI}$ constant transforms the ratio of shared light into a physical distance unit and is obtained right after $k_{rel}$, also using the $^{176}$Lu background data. This constant is then determined by finding the edges of the light collection asymmetry, which is uniform due to the uniform concentration of the $^{176}$Lu decay along the crystal [Wang2004]. From this assumption, $C_{DOI}$ is estimated by:

$$C_{DOI} = \frac{20 \text{ mm}}{A_p - A_n} \tag{3.9}$$

where $A_p$ and $A_n$ are the asymmetry at the positive (+10 mm) and negative (-10 mm) edges of the distribution [Rodrigues2007, Pinheiro2008, Frade2009b].

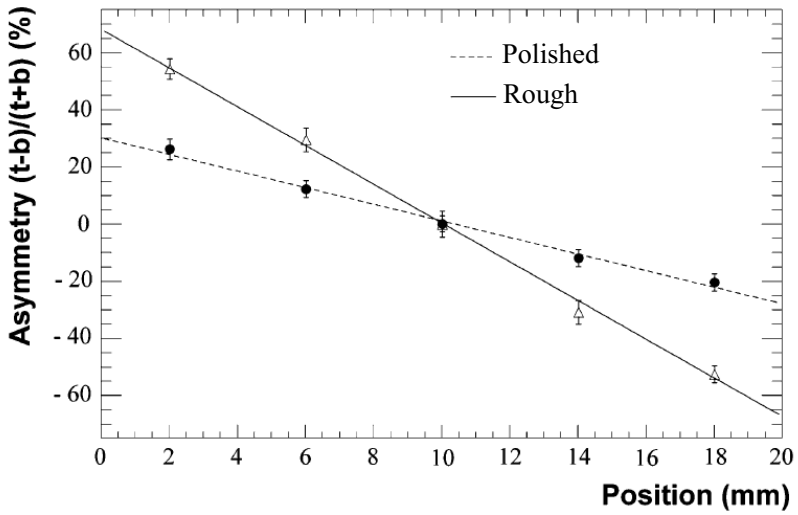


Figure 3.12: Asymmetry between light collected in the two crystal extremities for two LYSO:Ce crystals, one polished and the other very rough, wrapped in Tyvek (bars represent the FWHM of the asymmetry distributions) [Abreu2006, Moura2009].

2×2×20 mm$^3$ LYSO:Ce crystals with different surface roughness (polished, slightly polished and very rough, obtained with mechanical polishing) and wrappings (Tyvek and PTFE) were compared in terms of depth-of-interaction resolution. Each crystal under test was sandwiched between two photomultiplier (PM) tubes and irradiated at different depths with a 3.33 MBq (90 $\mu$Ci) $^{22}$Na radioactive source with 1 mm extension [Abreu2006, Moura2009]. A third PM tube coupled to a NaI:Tl scintillator of 3.8 cm diameter was aligned with the source and perpendicular to the crystal longest axis for electronic collimation coincidence purposes, such that a gamma spot with about 1 mm diameter was obtained on the LYSO:Ce crystal. The coincidence window between the three PM signals was 150 ns. Light collection asymmetry ($(E_0\text{-}E_1)/(E_0\text{+}E_1)$) was estimated on an event-by-event basis, and its dependence with the coordinate along the crystal axis where the photon interacts was studied. Results for the best configurations are shown in Fig. 3.12, which indicates that rough crystals wrapped with Tyvek have a large variation of asymmetry as function of interaction position which is a key feature for

a good DOI measurement. More on this topic can be found in the following references [Abreu2006, Moura2009].

Highly reflective materials are used to minimize light loss and maximize light output of scintillation material in calorimeter type detectors. The reflective characteristics of a material need to be coordinated with the wavelengths of scintillation light produced in the detector and with the transmission characteristics of any intermediate light collecting or guiding components [Stoll1996]. Thin, highly reflective, opaque separators are required to assemble compact arrays of small discrete scintillation crystals used in conjunction with photodiode array readouts in high-resolution imaging applications. Mechanical stability, individual detector performance, and ease of handling for wrapping crystals are the main factors to be considered in the choice of a suitable separator [Pepin2001]. In the first design version of the detector module, the crystals had dimensions $2 \times 2 \times 20$ mm$^3$ and were optically isolated by a Tyvek wrapping, assembled on a $4 \times 8$ crystal matrix (Fig. 3.13), following an assembly procedure already adopted for the first small animal Clear–PET scanners demonstrators [Ziemons2005].

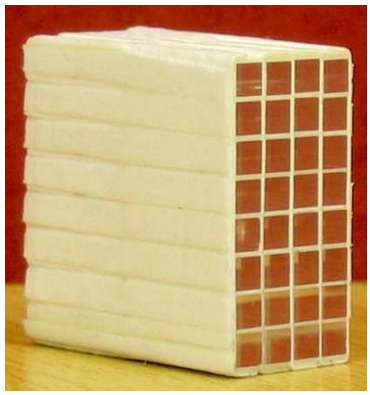

Figure 3.13: The first ClearPEM prototype Tyvek assembly.

Comparison studies of two Tyvek matrices with LYSO:Ce crystals were then performed, to verify the early measurements and to establish the final detector module configuration. Crystals with two different polishing treatment, referred in the following text as "light lap" (LL) and "rough lap" (RL), were compared in terms of light yield, DOI resolution and energy resolution. The difference between the LL and RL crystals is the roughness of the surface, that is usually described in the $R_a$ roughness parameter. For example, the lapping process which brings "rough from cut" crystals reduces the $R_a \approx 2$ $\mu$m down to lapped surfaces of $R_a \approx 0.5$ $\mu$m [Auffray2002]. The LL crystals have a $R_a$ of 175.88 $\pm$ 48.81 nm (slightly polished) and RL crystals have a $R_a$ of 735.98 $\pm$ 81.06 nm (rough polished). The matrices were measured using the same APDs and spectra of a $^{22}$Na (511 keV photopeak) source were obtained with a dedicated setup for double readout (described in section 2.5.2, chapter 2). On Fig. 3.14 it can be seen examples of spectra of a $^{22}$Na source (511 keV photopeak) for the two Tyvek grade matrices.

A gaussian with a linear background is fitted to the 511 keV photopeak to extract

photopeak position (light yield) and energy resolution. To determine DOI resolution, one inch NaI:Tl scintillator, coupled to a PMT, was used in coincidence for electronic collimation of 511 keV photopeak. To seek the centre of the matrix a profile of the coincidence trigger rates along the matrix was used. Finding the extremes of the crystal, the centre can be inferred. Three incident beam positions along the crystal were considered, one in the centre and two near the peripheries. At each beam position the light collection asymmetry was calculated and two reference parameters evaluated: 1) slope defined as the asymmetry variation per unit length; 2) DOI resolution estimated by the FHWM of the asymmetry peak over the slope. The adopted experimental procedure was similar to the first experimental measurements reported earlier [Abreu2006]. Light collection distributions at three excitation depths (-7.0, 0.0 and 7.0 mm) are presented on Fig. 3.15 (*left*, top and bottom) and the asymmetry average value as function of the excitation depth (3.15 *right*, top and bottom) for the two Tyvek matrices considered.

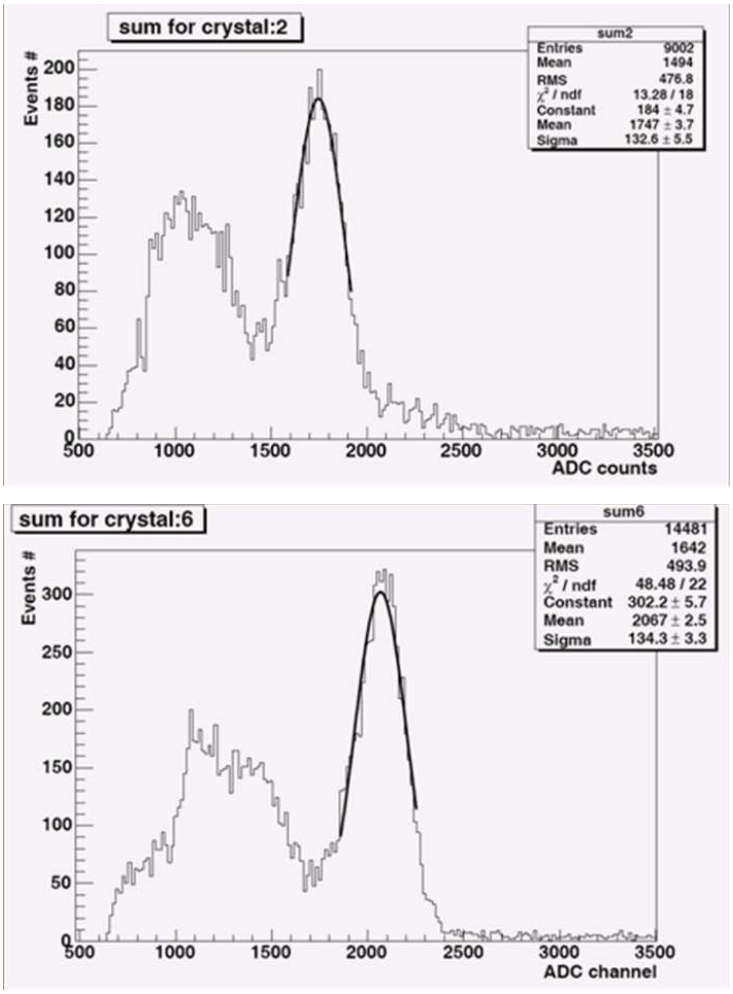


Figure 3.14: Typical $^{22}$Na (511 keV photopeak) spectra obtained from the online data acquisition software. *Top*: Tyvek-RL matrix; *Bottom*: Tyvek-LL matrix.

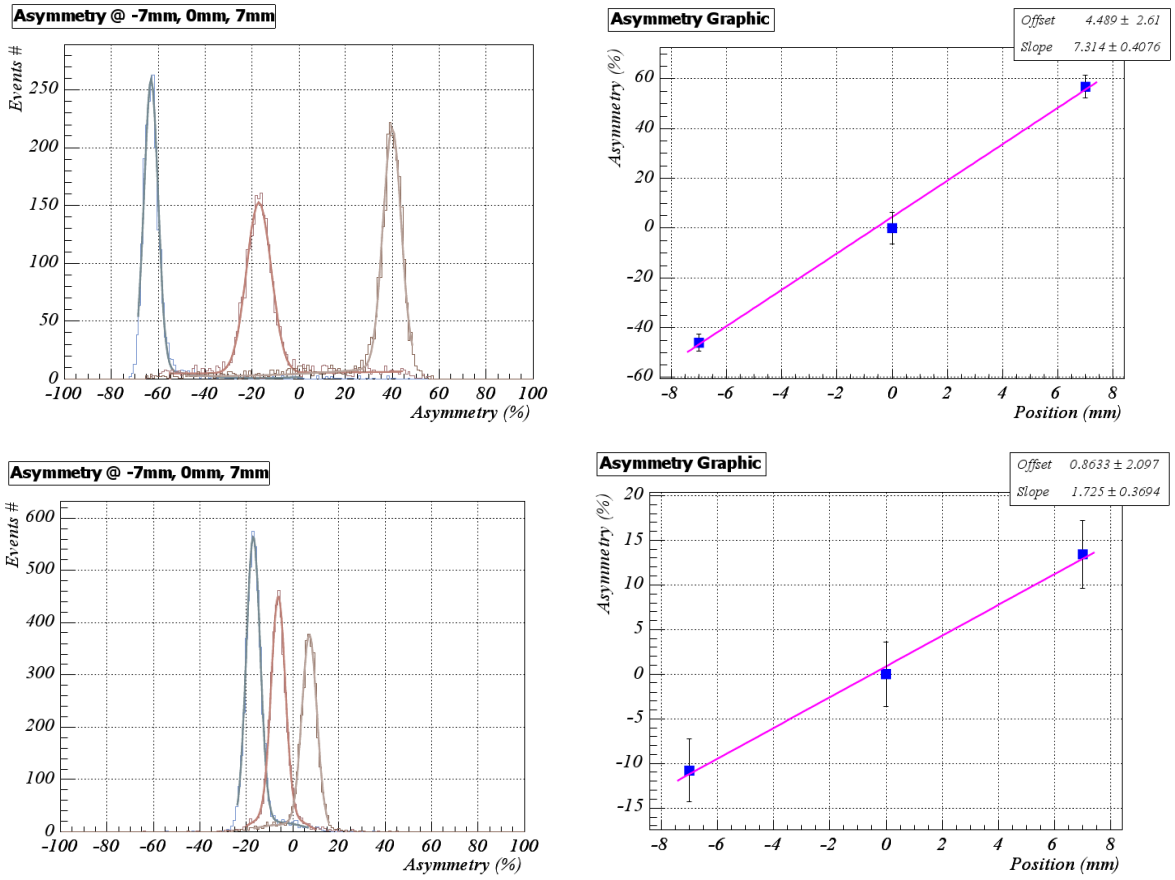


Figure 3.15: Typical plots of asymmetry distributions at three excitation depths (-7.0, 0.0 and 7.0 mm) and the asymmetry average value as function of the excitation depth. *Top*: Tyvek-RL matrix; *Bottom*: Tyvek-LL matrix.

Slightly polished crystals (LL) have better light collection and, consequently, also better energy resolution (15.5%) than the rough crystal (RL) matrix (16.2%). Rough crystals (RL) present an interesting DOI resolution (1.3 mm) but have a too low light collection to be used with an APD readout. Comparison results can be consulted in Tab. 3.3. The Tyvek matrix with LL crystals seemed to be the best compromised arrangement but the mechanical problems addressed to this configuration, like difficulty in inserting all 32 crystals without damaging the reflector, time consuming process without guaranties of homogeneous matrices and several waste tyvek matrix structures due to broken or folded inner walls, forced the scrutinize of other solutions and a new reflector was tested. In Fig. 3.16 the reflectance in terms of the incidence wavelength is shown for Tyvek, Teflon (PTFE) and barium sulfate, a white crystalline solid with the chemical formula $BaSO_4$. Barium sulfate is insoluble in water and other traditional solvents but is soluble in concentrated sulfuric acid. Barium sulfate ceramic is a superlative reflector and it was expected that used as a crystal separator it could enhance the light collection of the detector module due to is reflectance (97% at 420 nm). The production of $BaSO_4$ matrices (Fig. 3.17) was ordered to industry. Taking into account the results shown previously, the new matrix was assembled with slightly polished crystals. The typical spectra of a $^{22}$Na source (511

keV photopeak) for this matrix can be seen on Fig. 3.18. On Fig. 3.19 light collection distributions at three excitation depths (-7.0, 0.0 and 7.0 mm) and the asymmetry average value as function of the excitation depth for the $BaSO_4$ matrix are also presented.

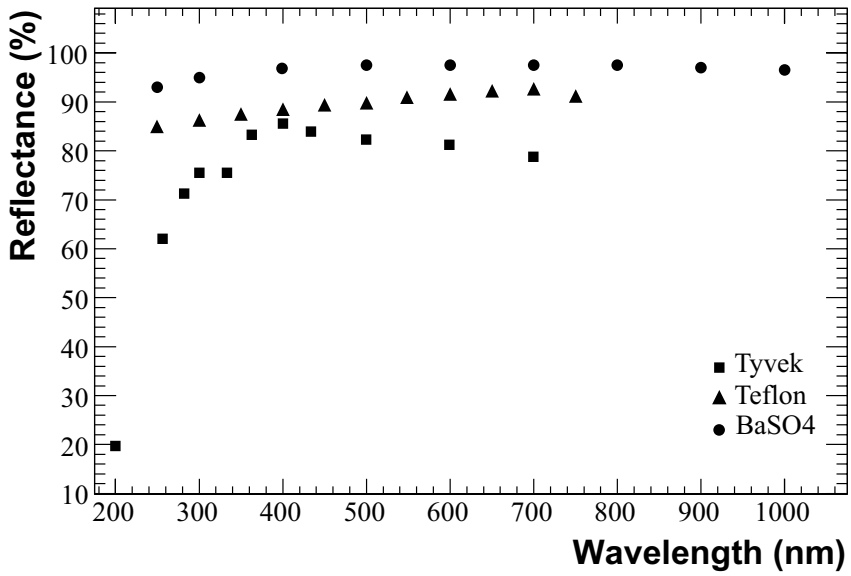


Figure 3.16: Reflectance of Tyvek, PTFE (teflon) and $BaSO_4$ in terms of the incidence wavelength [Pichler2000, Stoll1996, Labsphere2008].

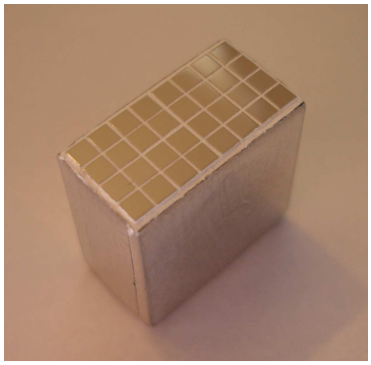

Figure 3.17: ClearPEM prototype $BaSO_4$ assembly.

The average values of the 32 crystals within each matrix were plotted in Fig. 3.20 for a better evaluation of light yield, energy and DOI resolution. Light yield for the different matrices was normalized to the mean photopeak position obtained with the $BaSO_4$ matrix. A resume with the comparison results is also presented in Tab. 3.3.

$BaSO_4$ matrix has shown the best behaviour, with the higher light collection, better energy resolution and a DOI resolution within the initial requirements for the ClearPEM scanner. Taking into account these results, the LL crystals assembled in $BaSO_4$ reflector

was considered the best configuration to the production of detector modules and a first batch of 24 matrices was order to industry to perform further studies.

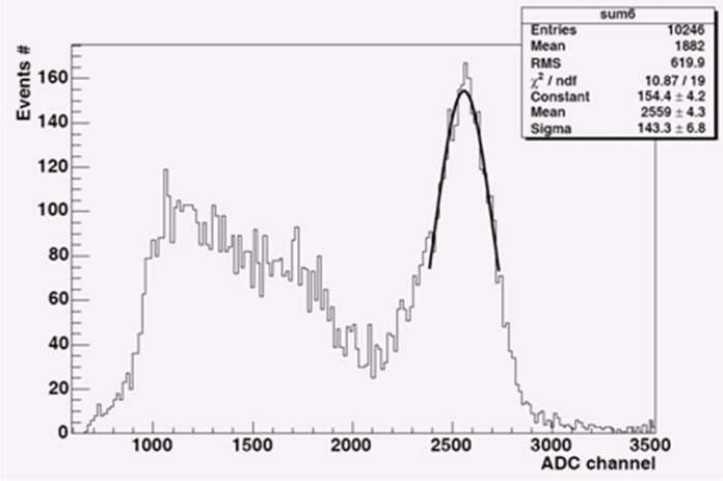


Figure 3.18: Typical $^{22}$Na (511 keV photopeak) spectra for the $BaSO_4$-LL matrix, obtained from the online data acquisition software.

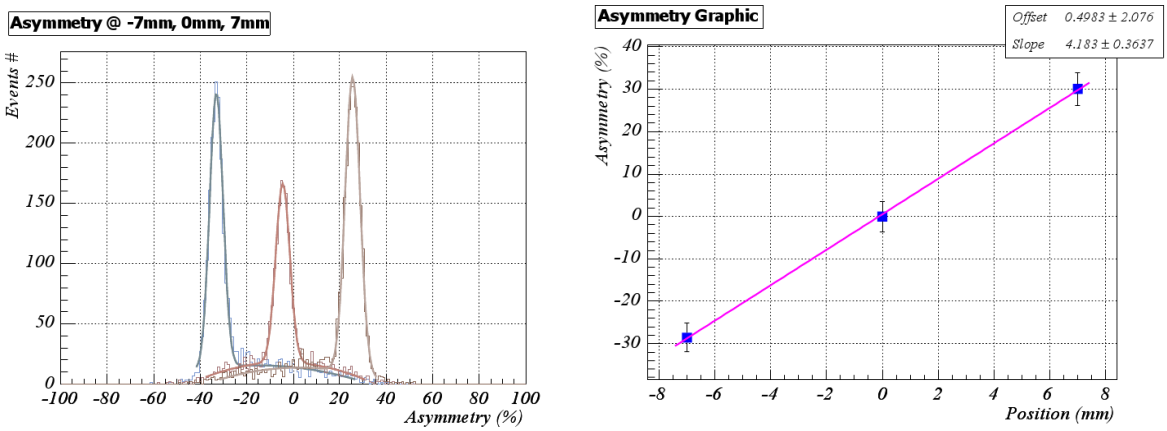


Figure 3.19: Typical plots of asymmetry distributions at three excitation depths (-7.0, 0.0 and 7.0 mm) and the asymmetry average value as function of the excitation depth for the new $BaSO_4$-LL matrix.

| Coating | Crystal Rough. $R_a$ (nm) | Light Yield (%) | Energy Resol. at 511 keV (%) | Asymmetry (%/mm) | DOI Resol. (mm) |
|---|---|---|---|---|---|
| Tyvek | 735.98 ± 81.06 | 66 | 16.2 ± 1.9 | 7.3 ± 0.8 | 1.3 ± 0.3 |
| Tyvek | 175.88 ± 48.81 | 80 | 15.5 ± 1.4 | 1.7 ± 0.2 | 4.2 ± 0.1 |
| $BaSO_4$ | 175.88 ± 48.81 | 100 | 13.5 ± 1.1 | 4.2 ± 0.1 | 1.7 ± 0.1 |

Table 3.3: Comparison results between the Tyvek and $BaSO_4$ matrices: Tyvek (LL and RL crystals) and $BaSO_4$ (LL crystals).

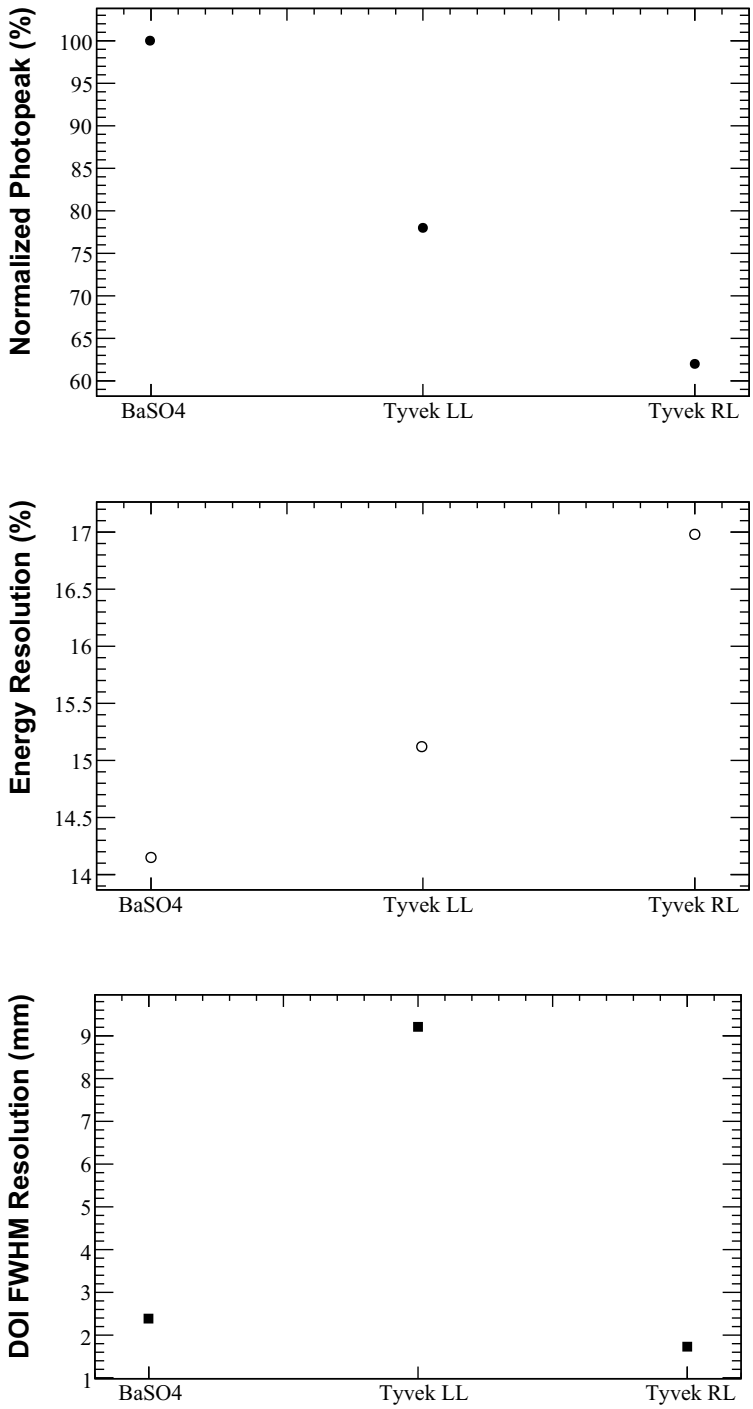


Figure 3.20: Light yield normalized, energy resolution and DOI resolution of 3 matrices.

## 3.3 Electromechanical Assembly

The design adopted for the ClearPEM detector module with DOI capability consists of 32 LYSO:Ce crystals with 2×2×20 mm$^3$ optically coupled, on both ends, to 32–pixel Hamamatsu S8550 APD arrays. In Fig. 3.21 *(a)* the schematic of a detector module with all its constituents is presented. The APD array is mounted in a small PCB with a low footprint KEL connector on the back side (Fig. 3.21 *(b)*), by a meticulous process of precise gluing with silver conductive epoxy glue. On the reverse side of this PCB a 40–pin connector allows a fast integration and un-mounting of the APDs in a detector module assembly. The components of a detector module are housed and sealed in a dedicated plastic assembly, developed by INEGI, with a mechanical precision of 0.1 mm in the placement of its components. The assembly has two empty slots in which two detector modules can be plug-in, defining a "double detector module" (Fig. 3.21 *(c)*), with external dimensions of 37.5 × 44 × 13 mm$^3$. 12 detector modules are mechanically fixed and electrically connected to a front and back Frontend Boards (FEBs) forming a supermodule. Each detector head has 8 of these supermodules in the final integration.

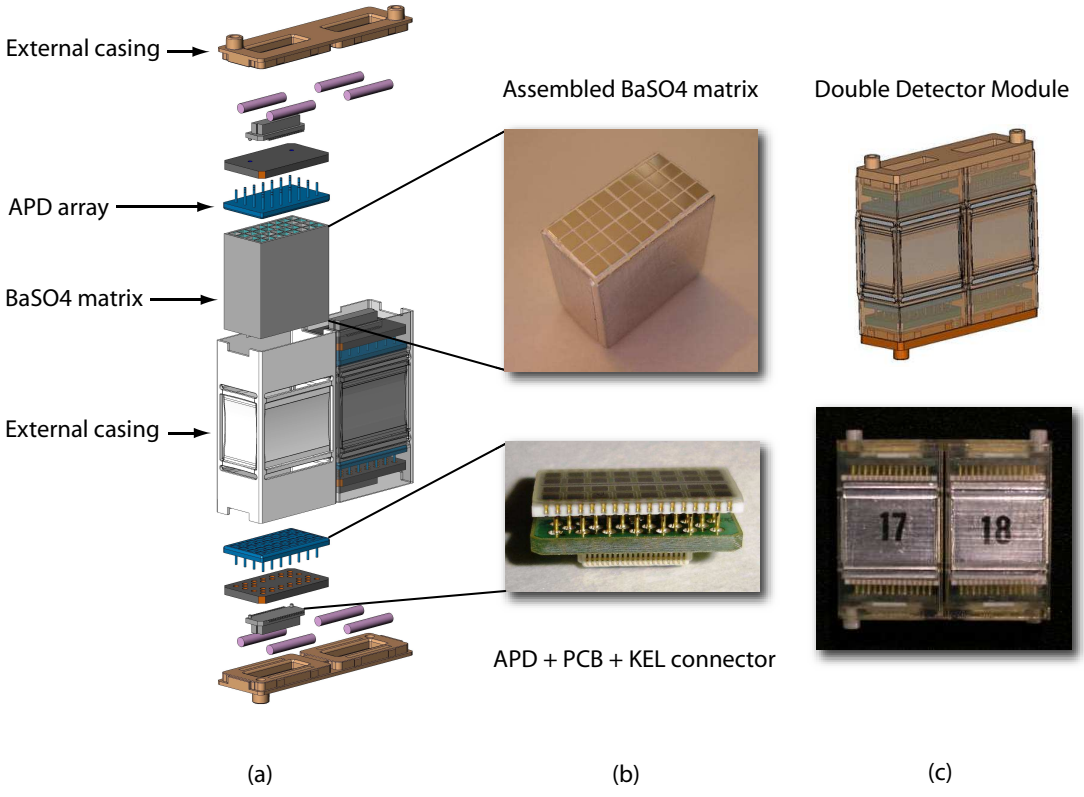


Figure 3.21: (a) Exploded detector module scheme; (b) APD mounted on a PCB (with KEL connector); (c) photograph of a double module assembled.

## 3.4 Performance of the ClearPEM Detector Modules

The detector modules were characterized by detailed experimental measurements. The performance results obtained for the first 24 detector modules worked also as proof-of-principle of the detector module design concepts. Light yield, energy resolution, depth-of-interaction resolution and inter-crystal crosstalk were measured in a dedicated setup of a discrete 32-channel electronic chain for double readout based on Cremat CR-101D pre-amplifiers and a VME-based data acquisition system with multichannel peak-sensing ADCs (described in detail in Chapter 2, Section 2.5.2). Inter-crystal crosstalk is discussed in the following chapter (Chapter 4). An analysis in the 511 keV photopeak region, corresponding to the sum of top and bottom APD pixel channels, was conducted. Relative gain, $k_{rel}$, and energy resolution, taking into account the contribution of light yield variation, light collection efficiency, APD quantum efficiency and gain were evaluated.

The relative dispersion of the $k_{rel}$ gain measured (r.m.s.) in 623 pixels is of the order of 18%, with a bias voltage set for APD gain M = 50. For this dispersion contributes the different crystal light yield, APD inter-pixel gain, differences in optical coupling and amplification electronics. Overall, the relative gain has a distribution centered at 1. The r.m.s. of less of 20% makes unnecessary gain compensation through bias voltage control, since dispersions of this magnitude can be compensated by calibration of the data acquisition electronics and software trigger. The low inter-pixel gain variation is also an indication that the application of the optical coupling does not introduces a significant varialibity on the total signal collected by each crystal. The average energy resolution is 18% with a r.m.s. dispersion of 3%. These results were obtained with a $^{22}$Na flood irradiation. In the flood irradiation, the electronic collimation is not used. Therefore, the 511 keV photopeak has the contribution of Compton events from the 1.2 MeV photopeak emitted during the $^{22}$Na desintegration. As result, the energy resolution is generally worse than the obtained with a 511 keV collimated beam.

The ability to measure the depth-of-interaction coordinate was also assessed in the first 24 detector modules, using a $^{22}$Na collimated beam. Light collection asymmetry was calculated and two reference parameters evaluated in a similar manner as in Section 3.2: 1) slope defined as the asymmetry variation per unit length ($C_{DOI}^{-1}$); 2) DOI resolution estimated by the FHWM of asymmetry peak over slope. The average value of the slope ($C_{DOI}^{-1}$) is 5%/mm and the relative dispersion is 12%. The average DOI resolution (FWHM) is 2 mm. This result is not corrected for the 1 mm beam width, which is originate from the finite size of the active medium (1 mm diameter) of the $^{22}$Na source. Results for the first 24 modules show that the major requirements for the ClearPEM scanner could be achieved, namely an energy resolution comparable to a PMT readout and a DOI resolution compatible with a spatial resolution suitable for early stage breast cancer imaging. As result of this study, the full production of the remaining modules was proceeded.

For the evaluation of the new batches of detector modules, the characterization procedure was modified in face of the large number of pixels to be measured. As $^{137}$Cs source

with an activity of 90 $\mu$Ci (3.33 MBq) was used and data acquisitions carried out in flood mode. The 60 detector modules of the second batch were assembled in two weeks and measurements were performed after that. Results of the 662 keV photopeak position for the 60 detector modules are shown in Fig. 3.22. The mean value is 1995 ADC channels with a dispersion between modules of 16.34%. The dispersion within the same matrix was 9% which is compatible to the early results obtain for set of 24 modules. It can be seen a considerable increase of the light yield on 6 detector modules (2693 ADC channels with a dispersion of 6%). These detector modules were the last to be assembled and point out a possible dependence of the light yield with the elapsed time after assembly. For that reason the long-term stablity of the detector modules were studied (see Section 3.5).

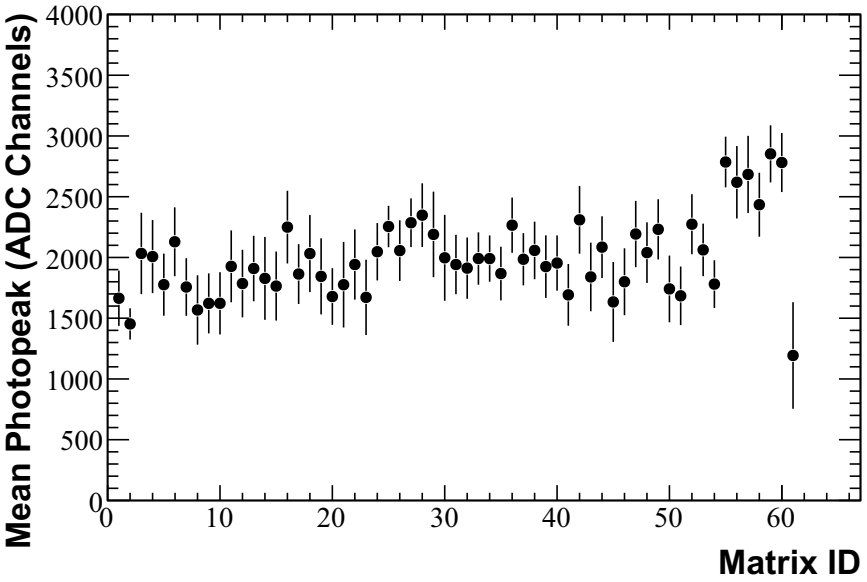


Figure 3.22: Mean (over all 32 crystals) 662 keV photopeak position for the first 60 matrices.

An interesting result was obtained for the correlation between the photopeak and the crystal positions in the matrix (Fig. 3.23). Typically, crystals placed in the inner lines of the matrix (A2–H2 and A3–H3) have larger mean photopeak positions. Average light yield and dispersions per set are: A1–H1, 1756 ADC channels with 2%; A2–H2, 2086 ADC channels with 5%; A3–H3, 2101 ADC channels with 4%; A4–H4, 1794 ADC channels with 3%. Pixels placed in mirror positions have shown to have similar behaviour with mean difference in photopeak position of 3% with a standard deviation of 2%, which is compatible with the assumption that the pixels of the same pair have similar gains. Therefore the two module sub-arrays are equivalent in terms of inter–pixel gain distribution. This systematic effect, observed over 60 different crystal matrices and APD arrays points out that the underlying mechanism should be related to the crystal matrices construction of differences between the inner and outer pixel APDs. The effect is, nevertheless, very small and can easily be corrected during system calibration (Chapter 6).

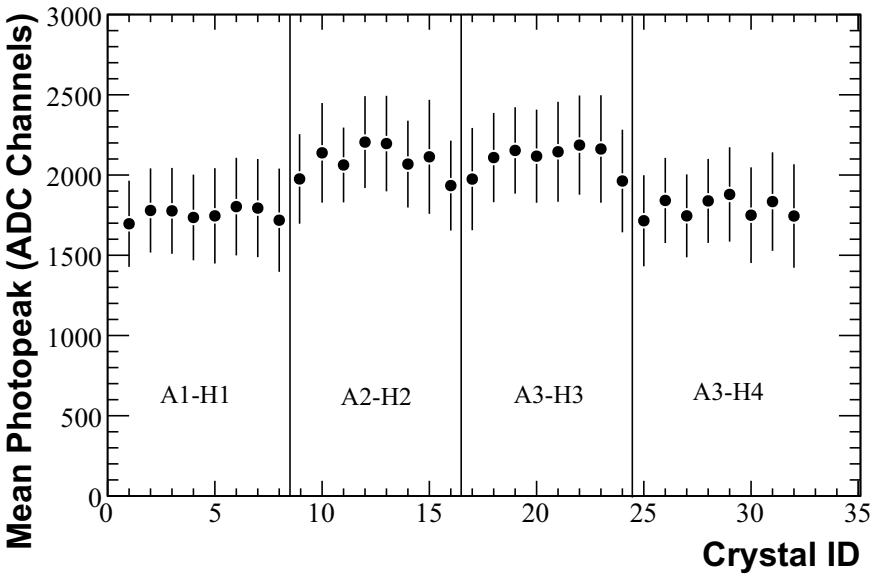


Figure 3.23: Mean (over 60 matrices) 662 keV photopeak position as function of the crystal identifier.

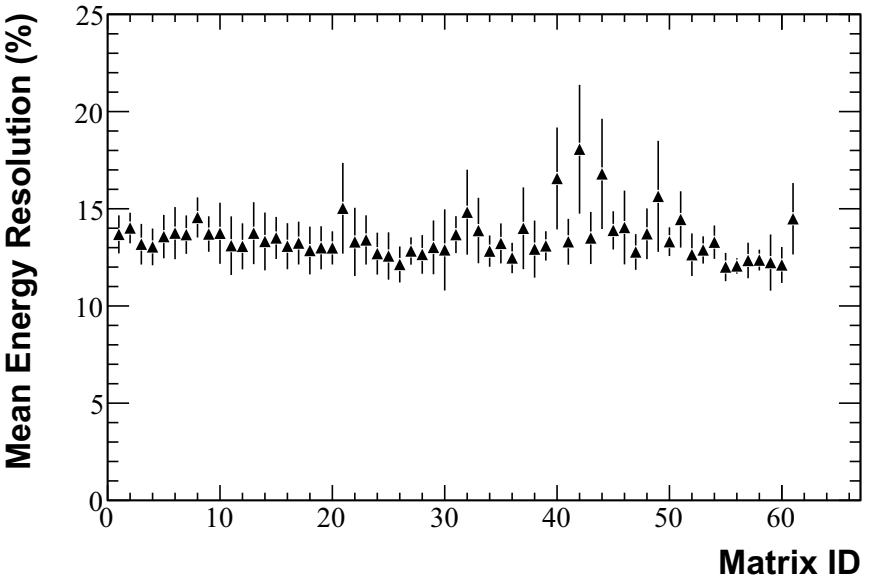


Figure 3.24: Average 662 keV energy resolution (over all 32 crystals) for the first 60 matrices.

The average energy resolution at 662 keV is shown in Fig. 3.24. The mean energy resolution is 13.6% with a 3% dispersion. The energy resolution is compatible with the 511 keV energy resolution of the first 24 modules batch (18 %) if a correction from the $1/\sqrt{E}$ is applied (15.5%). In Fig. 3.25 the mean energy resolution per crystal position is shown. No noticeable bias is observed.

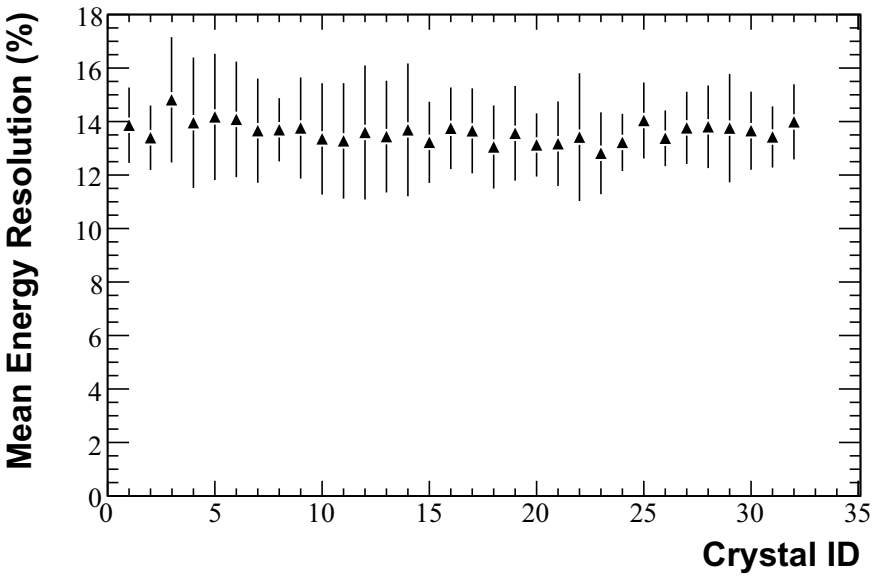


Figure 3.25: Average 662 keV energy resolution (over 60 matrices) as function of the crystal identifier.

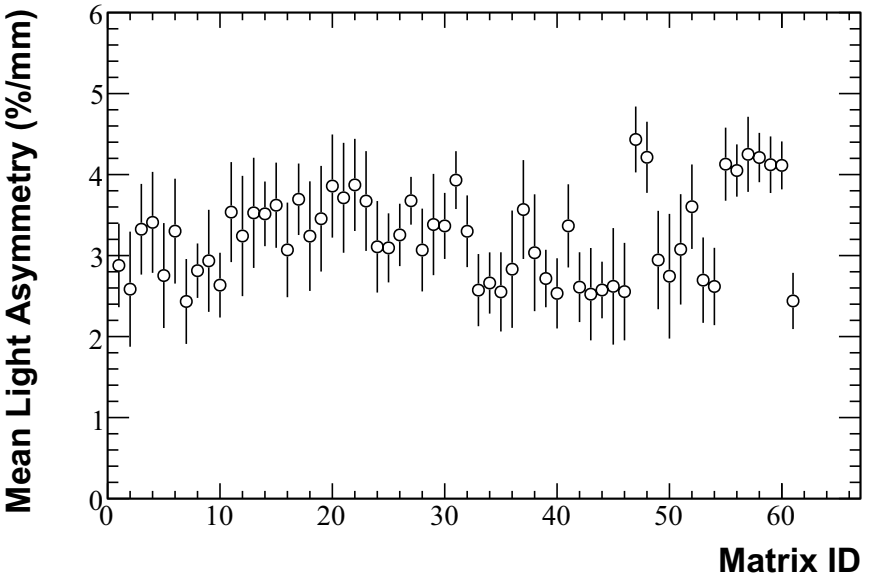


Figure 3.26: Average asymmetry (over all 32 crystals) for the first 60 matrices.

Results for the average asymmetry, which measures the capability of achieving a good DOI is shown in Figs. 3.26 and 3.27. The mean asymmetry is 3.2%/mm with a 3% dispersion. The same matrices that have shown higher light yield also have higher asymmetry. Since the asymmetry is a key parameter for achieving a good DOI measurement, this behaviour was further evaluated in the following section.

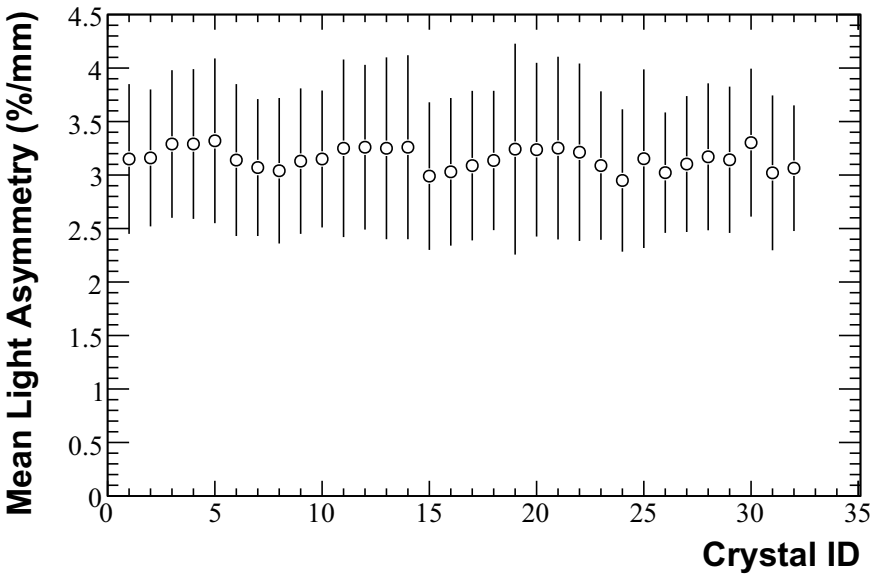


Figure 3.27: Average asymmetry (over 60 matrices) as function of the crystal identifier.

## 3.5 Long-term Stability Studies

Long-term stability studies of the ClearPEM detector modules were conducted in two ways. One ClearPEM module of the first batch of 60 had been chosen among the others and it was used as reference. It was established that the experimental setup would operate between 19 and 21°C to minimize temperature dependence deviations. This temperature was also adopted because it is close to the temperature at with the ClearPEM detector heads are kept by active cooling [Frade2009]. The bias voltage of the APDs was set to gain 50 and a $^{137}$Cs source was placed in front of the module for a flood irradiation. The total light yield, energy and the DOI asymmetry of the reference module along 20 measurements in different days were evaluated, and their time evolution was studied. Effects on the performance as a consequence of reassembling the module were also appraised.

The other procedure was to remeasure 5 detector modules one year after they had been assembled and compare the parameters.

### 3.5.1 Signal Yield

The total signal yield is measured by the photopeak position, corrected by the pedestal. The signal yield depends on the light yield of the crystals, light collection efficiency, APD and electronic chain gains. The average signal yield is 1580 ± 311 ADC counts, where the error is the standard deviation of all measurements made along this study. On the measurement 7, the reference module was reassembled and the effects on signal yield were studied. Fig. 3.28 shows an increase in signal yield after reassembling, followed by a decrease of its average value. This behaviour was a first indication of optical coupling aging and therefore results were object of further investigation.

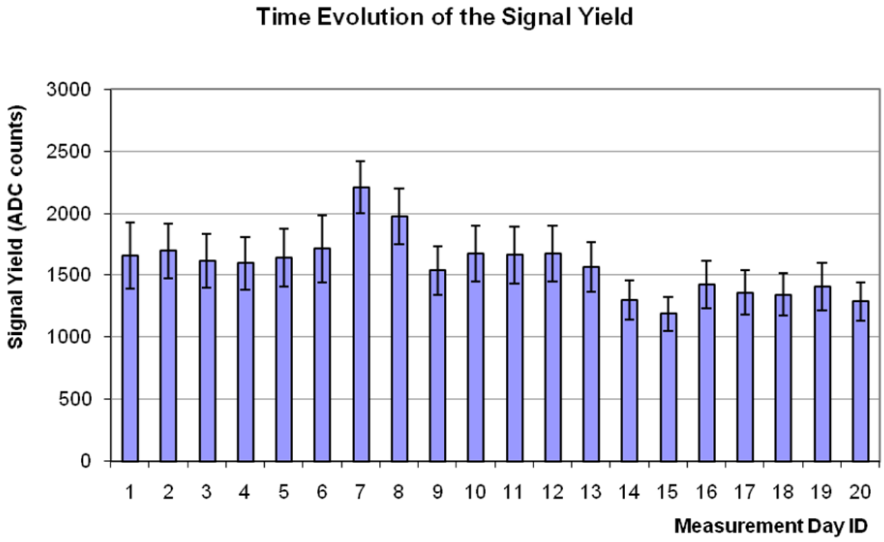


Figure 3.28: Time evolution of the 662 keV average signal yield of the reference matrix.

On Fig. 3.29 the variation of the signal yield is presented for the 5 detector modules measured twice with one year of difference. A systematic decrease was observed in all detector modules, resulting in average of a 11.5% degradation of this parameter. A summary is shown on Tab. 3.5. After this study some detector modules were openned for examination with a microscope. It was observed that the grease used as optical coupling had become opaque and brittle, which could justify the loss of light transmission.

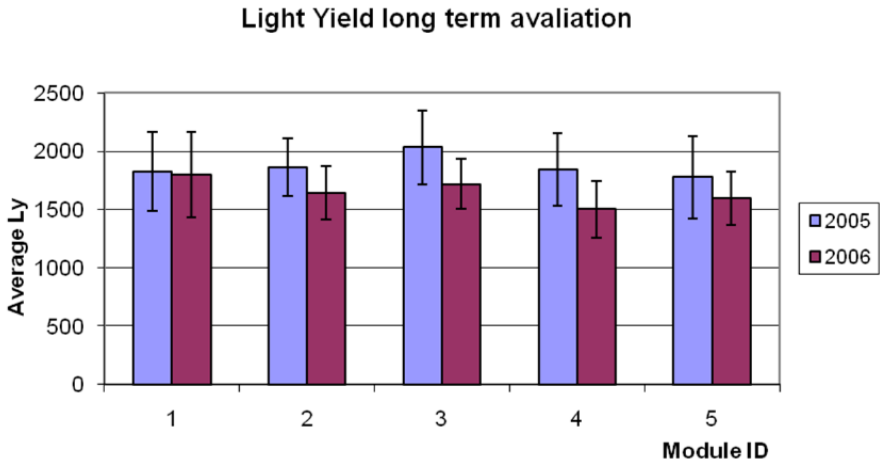


Figure 3.29: 662 keV average signal yield of 5 detector modules measured with 1 year difference.

### 3.5.2 Energy Resolution

The time evolution of the energy resolution at 662 keV is presented in Fig. 3.30. The average energy resolution for the reference matrix along the 20 measurements in a 5 month

interval is 13.77 ± 1.3%, where the error is the standard deviation of all measurements done during that period. Variations on this parameter were not found after reassembling the module on the measurement 7. The result is explained by the fact that in LYSO:Ce the energy resolution is dominated by a constant intrinsic term (9%) which offsets the photo-statistic term [Kuntner2002].

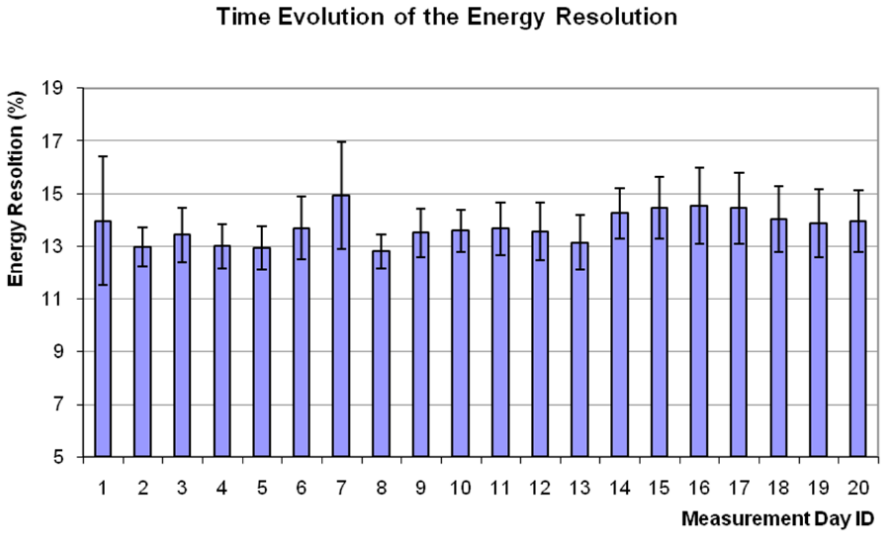


Figure 3.30: Time evolution of the average energy resolution at 662 keV of the reference matrix.

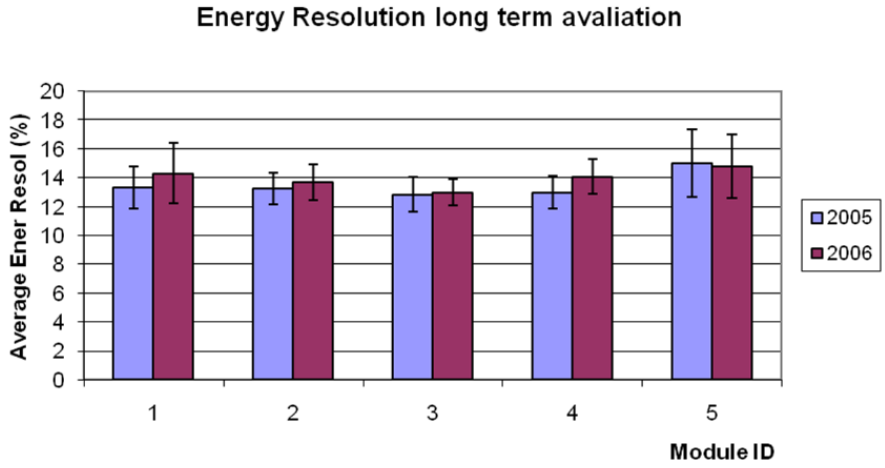


Figure 3.31: Average energy resolution of 5 detector modules measured with 1 year difference.

On Fig. 3.31 the variation of the energy resolution is presented for the 5 detector modules measured twice with one year of difference. In this case a residual degradation (3.8%) of the energy resolution was observed.

### 3.5.3 Depth of Interaction Resolution

Assessment of the stability of the depth of interaction resolution was done using the same flood $^{137}$Cs acquisition, making use of the asymmetry parameter for interactions that correspond to the 662 keV photopeak. Asymmetry was calculated on an event-by-event basis, from the interactions that correspond to the 662 keV photopeak. As discussed earlier, the width of the histogram obtained divided by the crystal length gives an estimation of the asymmetry per unit length, which provides an evaluation of the DOI performance. In Fig. 3.32, the time evolution of the average asymmetry is plotted by day of measurement. An increase of 75% in the asymmetry was observed after the module was reassembled. Four measuring days later the asymmetry parameter returns to its previous average value.

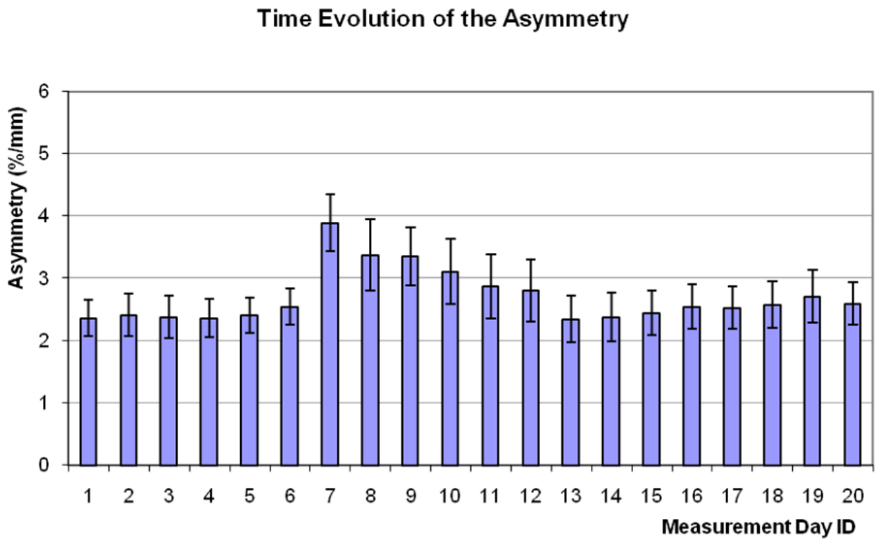


Figure 3.32: Time evolution of the average asymmetry of the reference matrix.

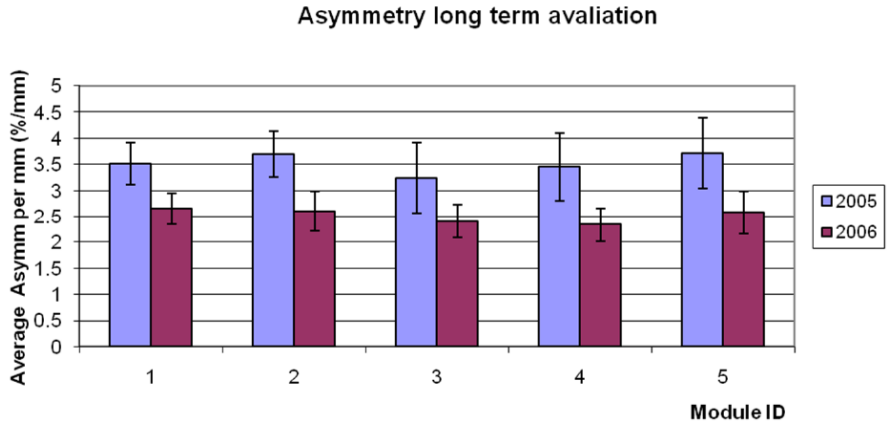


Figure 3.33: Average asymmetry of 5 detector modules measured with 1 year difference.

On Fig. 3.33 the variation of the asymmetry is presented for the 5 detector modules measured twice with one year of difference. It can be seen a degradation of this parameter of about 20–30% in each module.

| Module | Signal Yield (ADC ch) | | Energy Resol. (%) | | Asymmetry (%/mm) | |
|---|---|---|---|---|---|---|
| | 2005 | 2006 | 2005 | 2006 | 2005 | 2006 |
| 14 | 1828 ± 341 | 1798 ± 364 | 13.3 ± 1.5 | 14.3 ± 2.1 | 3.5 ± 0.4 | 2.7 ± 0.3 |
| 17 | 1864 ± 246 | 1642 ± 230 | 13.2 ± 1.1 | 13.7 ± 1.2 | 3.7 ± 0.4 | 2.6 ± 0.4 |
| 18 | 2032 ± 317 | 1720 ± 214 | 12.9 ± 1.2 | 13.0 ± 0.9 | 3.2 ± 0.7 | 2.4 ± 0.3 |
| 19 | 1844 ± 313 | 1504 ± 343 | 13.0 ± 1.1 | 14.1 ± 1.2 | 3.5 ± 0.7 | 2.3 ± 0.3 |
| 21 | 1776 ± 352 | 1599 ± 225 | 15.0 ± 2.3 | 14.8 ± 2.2 | 3.7 ± 0.7 | 2.6 ± 0.4 |

Table 3.4: Comparison results between 2005 and 2006 data.

| Module | Differences between measurements (%) | | |
|---|---|---|---|
| | Signal Yield | Ener Resol | Asymmetry |
| 14 | -1.66 | 7.52 | -24.70 |
| 17 | -11.88 | 3.34 | -29.59 |
| 18 | -15.37 | 1.15 | -25.67 |
| 19 | -18.43 | 8.40 | -32.27 |
| 21 | -9.96 | 1.45 | -30.70 |
| Average | -11.46 | 3.79 | -28.49 |
| rms | 6.37 | 4.18 | 3.27 |

Table 3.5: Percentage differences between measurements taken in 2005 and 2006.

A resume of the comparison results between 2005 and 2006 data is presented in Tab. 3.4. On Tab. 3.5 the differences between these measurements are shown. To corroborate these results that, at the time, were thought to be due to a degradation of the optical coupling transmission, a set of 20 detector modules from the last batch of 108 matrices was assembled and measured shortly after, with a settling time of 24 hours to prevent contamination from LYSO:Ce afterglow [Rogers2000]. Results are shown in Figs. 3.34. In this new set the average values are significantly better, with light yield of 2616 ADC channels (dispersion of 9%), energy resolution of 12.4% (5% dispersion) and asymmetry of 4.0 %/mm (dispersion of 7%).

This long-term study brought out a severe degradation on the light collection and DOI resolution, discovered to be a result of the aging of the optical coupling used and it has driven the search of new solutions. A detailed discussion of this process is described in Chapter 5.

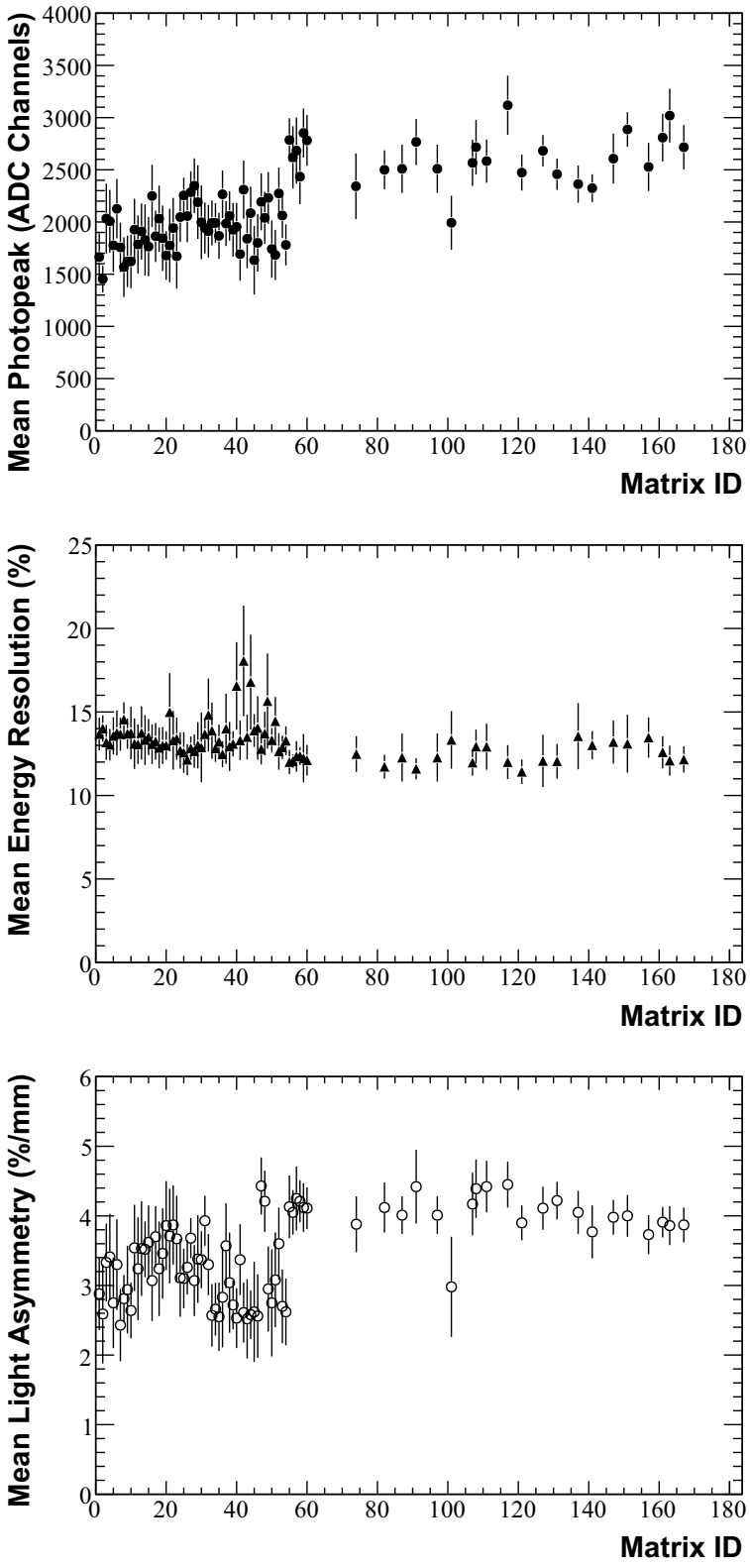


Figure 3.34: Comparison of the mean (over all 32 crystals) 662 keV photopeak position (*top*), energy resolution (*centre*) and asymmetry (*bottom*) between the first 60 matrices and the sample of the last batch of 108 matrices.

## 3.6 Summary and Discussion

The development of compact, small footprint solid state detectors allows the exploitation of readout approaches for PET scanners that when combined with fine pixelized crystals can provide an accurate 3D localization of the photon interaction coordinate in the detector active region. Two of the most successfully approaches were based on the double readout scheme either with a silicon photodiode plus a photomultiplier tube at the crystals ends or with two identical avalanche photodiode readout. The first has a significant disadvantage in terms of gain tuning due to the large difference between silicon photodiodes (unit gain) and classical photomultipliers (gain $10^6$–$10^7$). The ClearPEM design, with two Hamamatsu S8550 APDs at both ends of each array, should enable a higher performance since the use of identical photodetectors provide in theory a more uniform and symmetric detector performance.

In this chapter the evaluation of the ClearPEM detector module was presented, namely the characterization of some basic performance parameters of the S8550 APD as well as the optimization process of the crystal polish and wrappings that as led to the final configuration, based on a highly diffusive reflector build from $BaSO_4$ and slightly polished crystals. The initial Tyvek matrix with very rough crystals was abandoned due to its low light collection.The $BaSO_4$ matrix configuration yields an energy resolution of in the 14–17% range at 511 keV and a DOI resolution better than 2 mm. A key ingredient for these results is a stable operation of the APDs. Several S8550s were evaluated in the course of this work in relation to their linearity, excess noise and response to optical light in the UV long/blue short region as well as to direct ionization of $^{55}$Fe. A good long-term stability, at the 2% level was found. Independent measurements that the excess noise factor in the S8550 is low were confirmed. A mean excess noise factor, for 420 nm light, of 1.83 at gain 70 was found. As comparison, the RMD A1604 16 (4×4) multi-pixel shows an excess noise factor at gain 50–100 of 2, rising to 3 at gain 1000. For the quiet moderate excess noise of the S8550 contributes an avalanche layer no larger than 4 $\mu$m. APD inter-pixel, within same sub-array, gain variability (5.7% r.m.s.) was observed to be constant (2% level) over time. The different gain behaviour of the S8550 APD when subject to a blue light illumination (420 nm) or to direct ionization of 5.9 keV was examined. The decrease of the ratio R$x$,*light* is consistent with the small thickness of the avalanche region.

Results for the first batch of the adopted configuration (24 matrices) was also presented that shows that the good light collection, energy resolution and DOI resolution can be achieved without significant deterioration of one parameter in face of the other. These results are indicative that a good performance of the scanner, in terms of the quality of the information (energy, time, position) can be achieved for coincidence events, as a requisite for high-resolution PET. In summary:

- Good energy resolution, comparable to what is achieve with standard PMT readout, allows to reject the scatter events originated in the breast and outside the FOV.
- DOI resolution (longitudinal axis) is comparable to the crystal cross-section (2×2 mm$^2$), allowing to compute the 3D spatial coordinates of the interaction of the

photon in the scanner with a precision of about 2 mm.

- The dispersion of the relative light collection is small (less than 20%) and can be compensated at the hardware or software trigger, achieving an homogeneous energy response in the entire scanner.

As result, the final assembly of the remaining detector modules 168 was ordered. The modules were received during 2005 and 2006 and were subject to a quality control program. Results from this QC confirm the initial good performance in accordance to the initial requirements layout for the scanner.

An unexpected increase in the light collection and the DOI asymmetry distribution was found in some detector modules after the characterization of the first 60 matrices. This behaviour seemed to be correlated with the time elapsed after the detector modules were assembled in their plastic housing.

Long-term stability of the ClearPEM modules was appraised and the effects on the performance of a reassembled module was studied. Signal yield and asymmetry parameters suffer considerable variations when reassembling the module. To minimize inter-matrix variations for homogeneous response scanner, special care was taken when assembling the modules, in particular with the application of the optical grease.

Results show that one year after the detector modules were assembled a mean light collection reduction of about 12% and a decrease of the light collection asymmetry, which is fundamental for the DOI measurement, of almost 30% was observed. The degradation can be recovered by re-assembling the detector modules. Since the APD are very stable, when working in a stable temperature and the plastic housing boxes minimizes misalignments it was assumed that the behaviour was due to an aging of the optical grease. This was corroborated by visual inspection of the crystal-APD contact surfaces that have shown a loss of optical transmission of the grease. As result of this study, an improved revision of the optical coupling between the crystal and the APD was performed. A new optical coupling media was selected and successfully tested allowing to further improved the already good performance of the detector module. This part of the thesis work is described in Chapter 5.

Chapter 4

# Analysis of Electrical and Optical Crosstalk

## Contents

## 4.1 Introduction

Crosstalk is the leakage of a signal into adjacent channels or into another part of a system. Crosstalk may occur through optical, electrical, mechanical, magnetic, capacitive or other forms of coupling, for example, between adjacent wires on a printed circuit board that are close together or nearby pixelized photosensors.

High resolution and high sensitivity are the major requirements for dedicated PET scanners. A common solution to improve the resolution is to reduce the crystal cross-section, which usually implies a decrease of the system efficiency. The efforts to increase sensitivity normally are done at expense of data blurring due to DOI effect by increasing the crystal length [Rafecas2003]. Recalling Eq. 1.2 (Chapter 1), for the lowest spatial resolution possible, the 1:1 coupling between the scintillator and the readout element could scale the spatial resolution down to the size of individual crystals, but inter-crystal crosstalk has to be small as it has important implications in the data acquisition scheme, allowing to have $b \approx 0$. It is known that working with small cross-section crystals may lead to inter-crystal crosstalk contamination, which arises from Compton scattering from one crystal to another or possibly the escape of the photoelectron from the primary crystal following photoelectric absorption. Other reasons can induce crosstalk, like light sharing between two pixels due to position mismatch of the crystal pixel - APD pixel, inefficient optical isolation, namely air bubbles in the reflector walls between crystals, degradation or absence of the optical coupling interface crystal-APD.

The degree of crosstalk has particularly important implications for the design of the ClearPEM front-end electronics. If high enough, crosstalk can generate false triggering in channels adjacent to the actual event. Due to the architecture of the ClearPEM ASIC, 192 input channels, corresponding to 6 APDs, are multiplexed to 2 outputs. If 3 channels are higher than the common threshold, an error bit signals that part of the information was lost. In this case, the off-detector electronics, discard the entire event, leading to a loss of efficiency. On the other hand, it can be suppressed by sufficiently increasing the ASIC threshold, but on the other hand a threshold too high can already prevent valid events on the lower gain channels from being detected.

Thus, due to its possible impact on the system performance, this parameter was evaluated in a series of dedicated measurements to the study of the possible causes of crosstalk and the analysis is presented in this chapter.

## 4.2 Method and Materials

Several measurements were performed in order to study possible contributions for crosstalk along the ClearPEM detector module. To do that, it was defined a working plan, starting by the electronic crosstalk on S8550 APD and ending with the evaluation of the full assembled detector module.

### 4.2.1 Protocol of Measurements

The evaluation of the electrical and optical crosstalk on S8550 APD was performed by placing an APD in the socket of the 32 channel discrete electronics for single readout (see setup description on Chapter 2, Sub-Section 2.5.1) and polarized it to gain 50. A $^{55}$Fe was used for flood and collimated irradiations. An aluminum collimator was designed, with the same dimensions of the APD and 5 mm thickness that would be able to stop the 5.9 keV gamma rays - Fig. 4.1. One single hole was positioned in order to be possible to illuminate one of four different APD pixels, simply by rotation or inversion of the collimator - Fig. 4.2. All measurements were performed in the dark, at room temperature between 19°C and 21°C to minimize temperature dependence deviations.

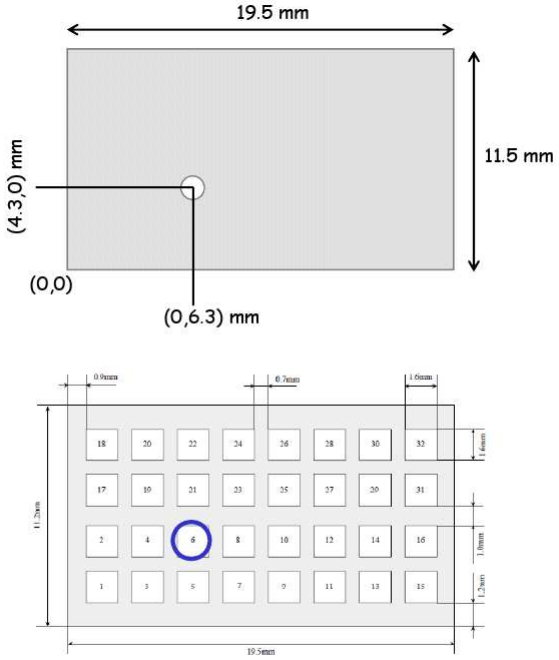


Figure 4.1: Collimator design scheme for measurements with the S8550 APD: dimensions and hole position of the collimator.

To study optical crosstalk on the APD epoxy and optical interface between APDs and the crystal matrices, another setup was developed. A blue LED (Light Emitting Diode) with 420 nm output peak (RLT420–3–30 from Roithner Lasertechnik), was optical coupled to a light guide, for pixel by pixel illumination. A dedicated black mask was used as support and as optical collimator for the fiber - Fig. 4.3. The intensity of the light was controlled by the signal generator (Tektronics AFG3252), as well as pulse width and frequency.

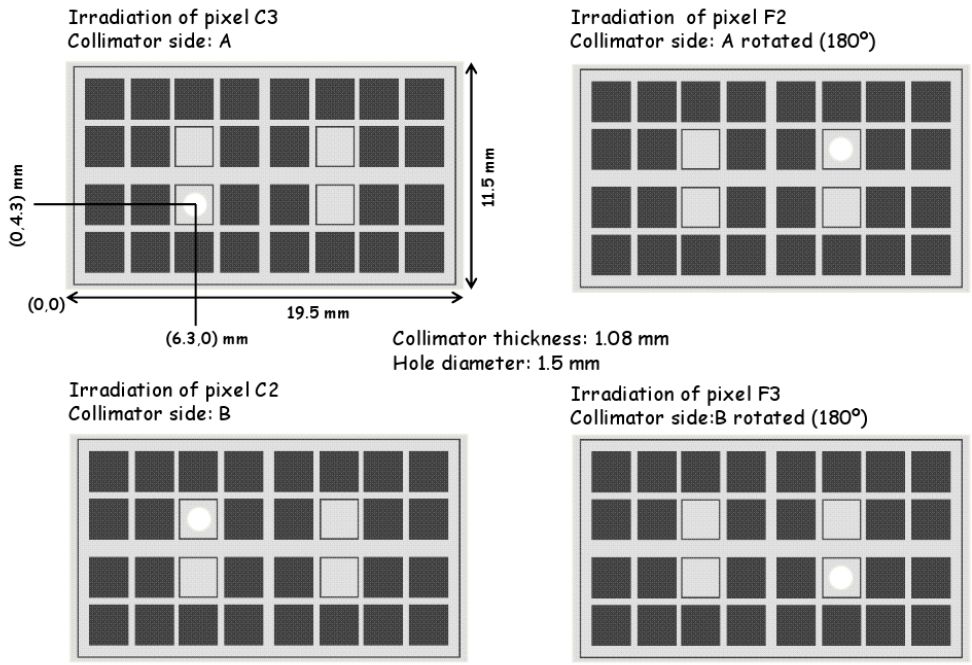


Figure 4.2: Collimator design scheme for measurements with the S8550 APD: representation of the possible irradiation pixels, by rotation and inversion of the collimator.

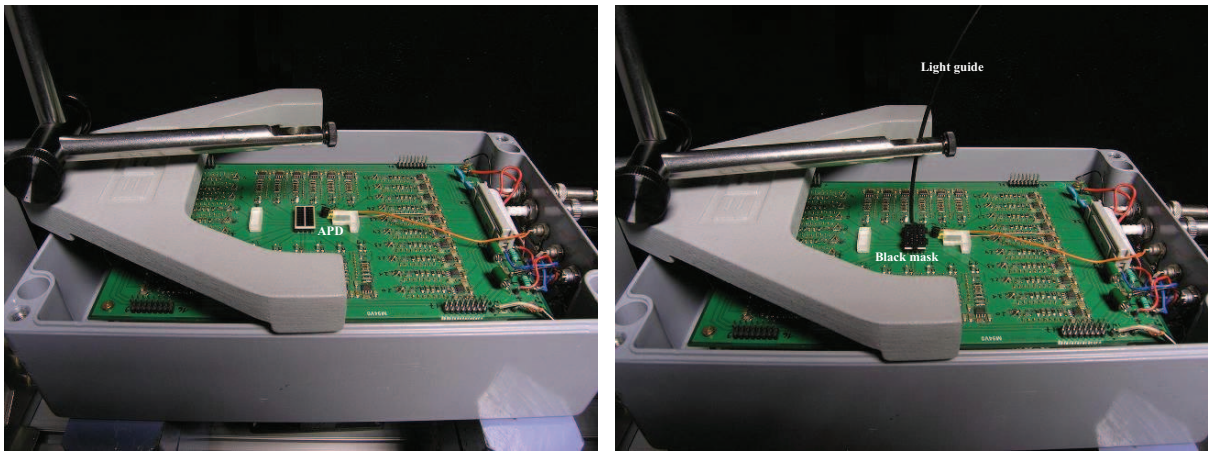


Figure 4.3: LED setup: S8550 APD placed on the PCB connector (*left*) and light guide with support and black mask (*right*).

Every time the LED was to be used, a quality measurement was conducted by varying the input voltage (2 to 3 V) and registering the signal on the same APD pixel (see Fig. 3.4 in Chapter 3). The characterization curve was then used to obtain the input voltage value that gave a peak signal at 1500 ADC channels, a typical value of the ADC output when operating with $^{22}$Na source (511 keV photopeak). This value is fixed and used to

illuminate all the pixels.

As for the crosstalk of the ClearPEM detector module, the evaluation was done with a single detector module placed in the 32 discrete electronics chain for double readout to collect the signal from the radioactive source ($^{22}$Na or $^{137}$Cs , which is positioned in lateral incidence (see setup description on Chapter 2, Sub-Section 2.5.2). The bias voltage of the APDs was set to gain 50 and a radioactive source is placed in front of the module for a flood irradiation. Data is collected on a dedicated computer for online visualization and analyzed shortly after.

### 4.2.2 Data Analysis

The principle of all analysis to evaluate crosstalk is to select the peak signal in one channel and seek for any leakage signal on the surrounded channels. Crosstalk contamination was analyzed by selecting events with a deposited energy in a central pixel or crystal (sum energy read from top and bottom APD, on double readout mode) and recording the energy distribution in the neighbour pixels or crystals.

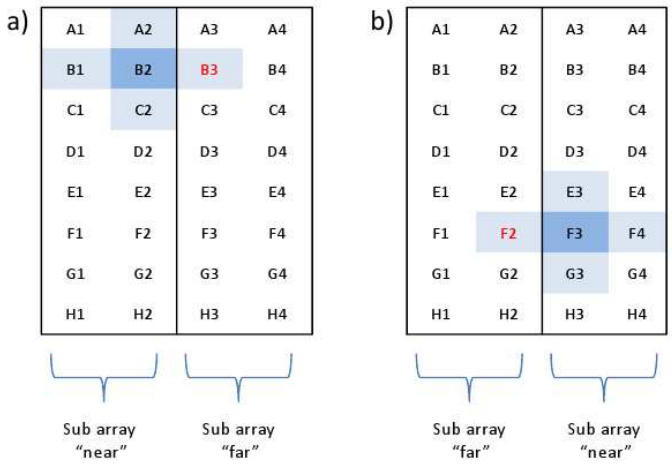


Figure 4.4: Definitions of neighbours on the APD: a) if pixel B2 is the central pixel, A2, B1 and C2 are first neighbours "near" and B3 is a first neighbour "far"; b) if pixel F3 is the central pixel, then E3, F4 and G3 are first neighbours "near" and F2 is a first neighbour "far".

As APDs have two sub arrays (the S8550 is built from $2 \times 8$ monolithic silicon wafers with a common HV bias), pixel neighbours were defined as "near", if in the same sub array, or "far", if in different sub arrays. Two cases are represented on Fig. 4.4. As it can be seen in the figure, if pixel B2 is selected (heavy blue), pixels A2, B1, B3 and C2 (light blue) are the first neighbours, but A2, B1 and C2 are in the same sub array of B2 - sub array near; but B3 is in the other - sub array far. In the same way, if pixel F3 is selected, E3, F4 and G3 are the first neighbours of the sub array "near" and F2 is the

first neighbour of the sub array "far".

For data analysis of the optical crosstalk on detector modules using the double readout electronic chain, each crystal was also assigned with a number, and equivalent walls of neighbours, according to the numbering scheme in Fig. 4.5. For example, if channel 2 is chosen as the central crystal then the walls 1, 2 and 9 are considered; if looking to channel 10 then walls 9, 16, 17 and 24 are considered. As the discrete electronic chain has 32 channels, for double readout only 16 crystals (corresponding to two APD sub-arrays) can be read at a time, meaning that walls on the frontier (23 to 30) are not evaluated, as can be seen in the result plots. Also, due to an inoperative electronic channel at the time of the measurements, walls 6 and 36 could not be assessed too.

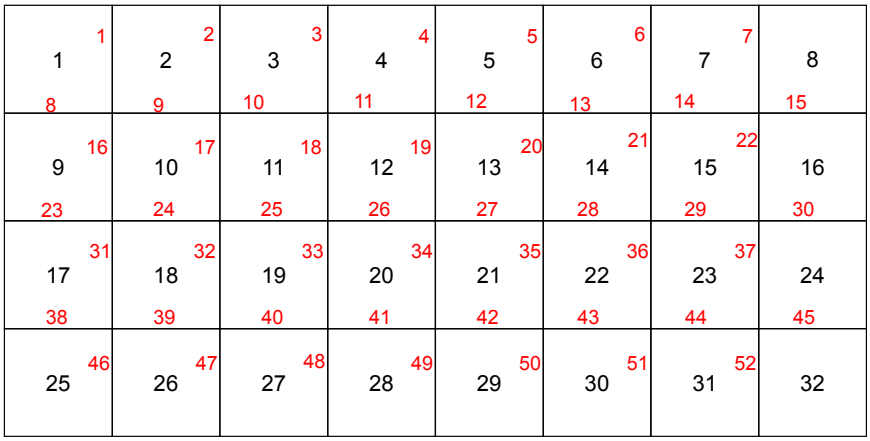


Figure 4.5: Numbering scheme for crosstalk analysis. Black: crystal number (energy sum of APDs bottom and top channels); Red: crosstalk walls.

The peak of the energy spectrum (511 keV or 662 keV) is found in the histogram of the central crystal considered by a dedicated peak finder ROOT script [Brun1997], and a fit with a Gaussian distribution and polynomial function of the first degree is performed to obtain the parameters for the energy cut per crystal. The average value of channel pedestal is then used to correct the peak position. For selected events, within the interval of interested [$\mu$-$\sigma$, $\mu$+3$\sigma$], the events of the neighbour crystal are plotted (Fig. 4.6), on an event-by-event basis. The position of crosstalk peak is found and also corrected by the correspondent pedestal value. The asymmetric interval os interest, [$\mu$-$\sigma$, $\mu$+3$\sigma$], was chosen to avoid Compton contamination. The crosstalk per wall is determined by the ratio of the peak positions:

$$\text{Crosstalk}[\%] = \frac{\text{peak of the leakage signal of the neighbour crystal}}{\text{photopeak position of central crystal}} \times 100 \qquad (4.1)$$

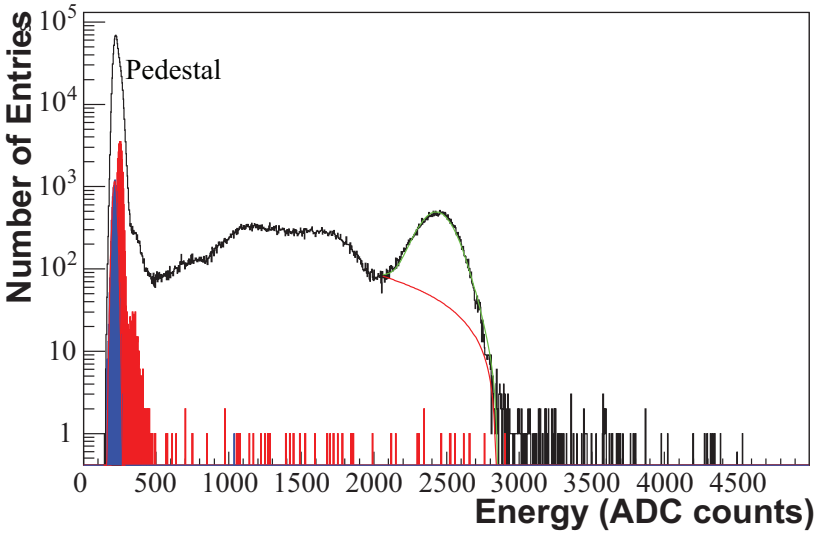


Figure 4.6: Example of the optical crosstalk analysis. In the plot, a $^{137}$Cs spectrum was fitted and, considering the events on the peak, spectra of the neighbouring crystals were superimposed (in red and blue).

## 4.3 Results

### 4.3.1 Electrical Crosstalk on the S8550 APD

Electrical crosstalk was evaluated using the $^{55}$Fe source and the designed aluminium collimator to irradiate pixels B3 and C3 of an APD. Results are shown in Fig. 4.7. Values were normalized to the fired pixel and two electronic channels, corresponding to pixels B7 and B8, were not working properly. It can be seen that electrical crosstalk is less than 0.3% in the first neighbouring pixels and negligible ($< 0.1\%$) on all the other. This result indicates a good electrical isolation between pixels and also of the channels of the electronic chain used, in this case, the discrete electronics for single readout.

### 4.3.2 Optical Crosstalk on the S8550 APD

The LED with light guide setup (Fig. 4.3) permitted to irradiate the APD pixel by pixel (Fig. 4.8). As can be observed, the optical crosstalk is mostly inexistent. On Tab. 4.1 it can be seen the average results for direct illumination on APD epoxy (0.23%) and with a layer of optical grease (0.31%). These results indicate that there are no significant signal propagation in the epoxy nor in the thin layer of optical grease (less than 20 $\mu$m).

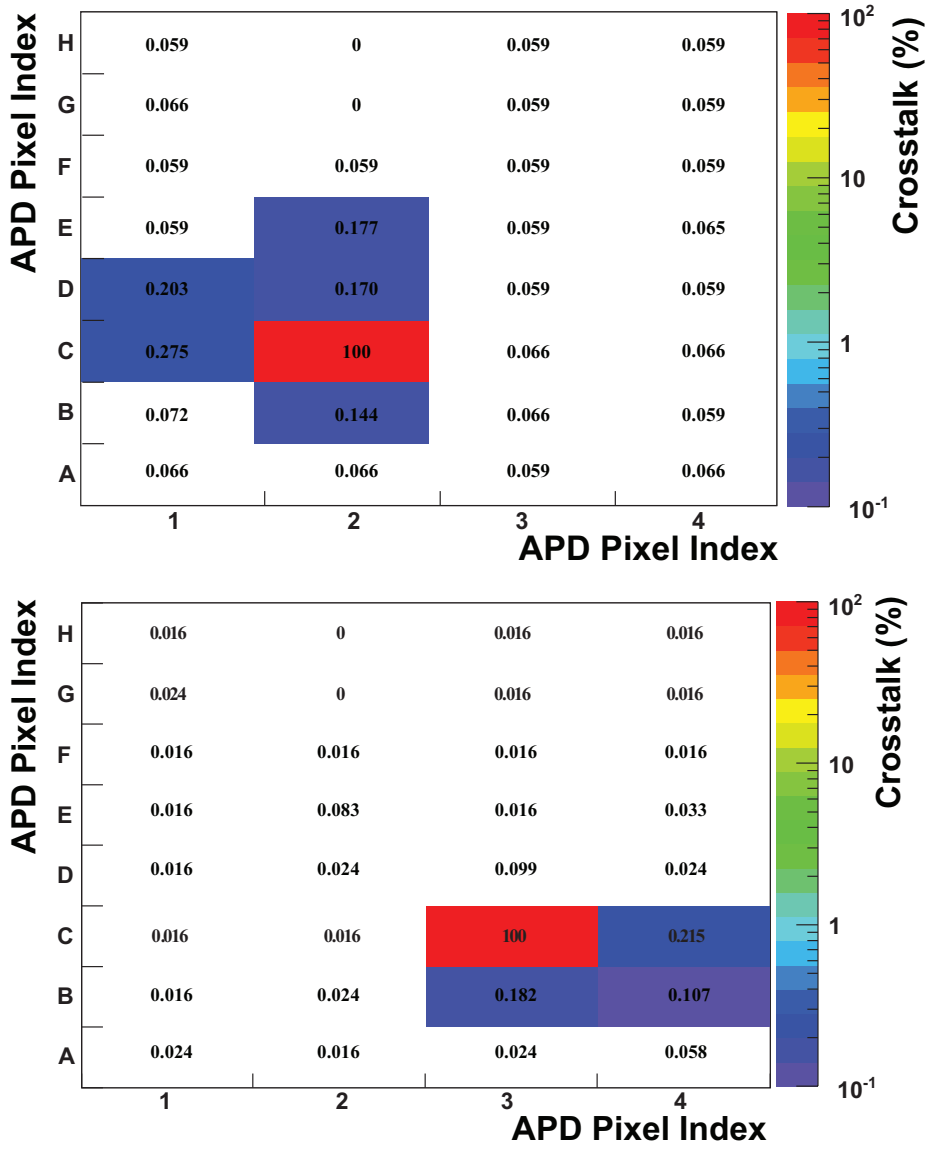


Figure 4.7: Electrical crosstalk evaluation with $^{55}$Fe irradiation on pixels B3 (*top*) and C3 (*bottom*).

| Coupling on APD | Without | Optical Grease |
|---|---|---|
| $1^{st}$ neighbours (near) | 0.23 ± 0.87% | 0.31 ± 0.94% |
| $1^{st}$ neighbours (far) | 0.00% | 0.00% |

Table 4.1: Average optical crosstalk on APD, using direct illumination on APD epoxy with and without optical grease.

Several pixels had no crosstalk at all, as can be seen in Fig. 4.9, which explains the larger variance in the average calculation.

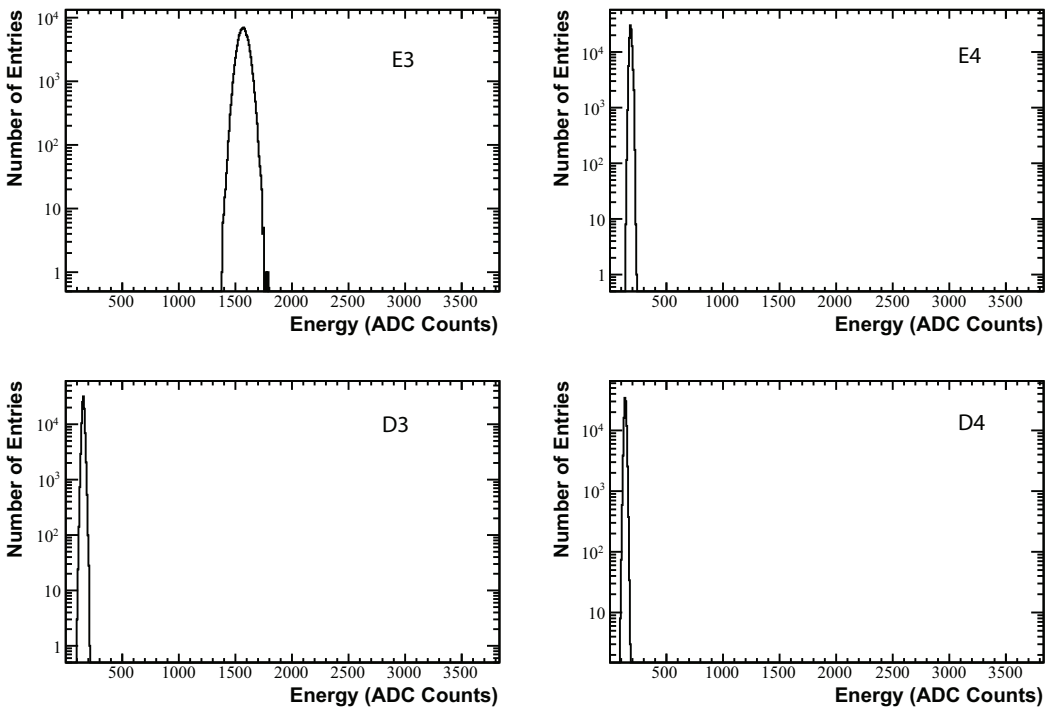


Figure 4.8: Optical crosstalk evaluation with a 420 nm LED: example of the output signal in the fired pixel (E3) and in the neighbouring pixels (E4, D3 and D4). The mean pedestal was subtracted.

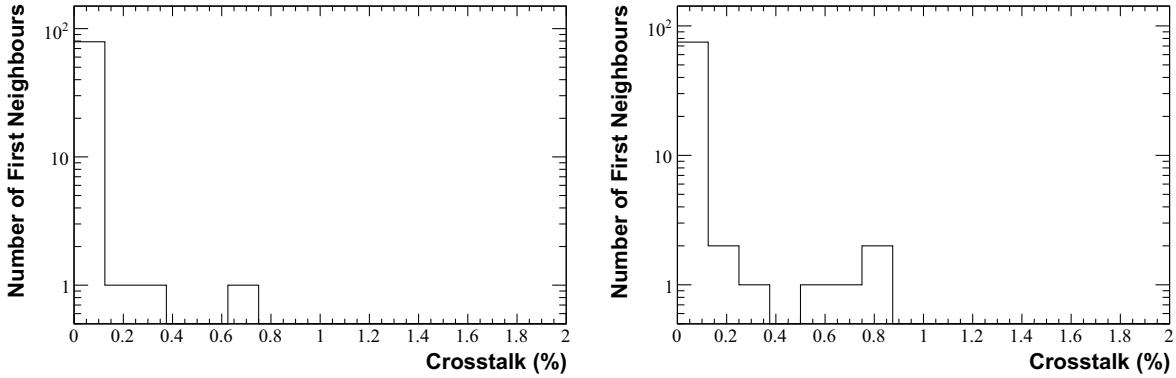


Figure 4.9: Optical crosstalk distributions on the S8850 APD.

### 4.3.3 Crosstalk on the ClearPEM Detector Module

On Fig. 4.10 it can be seen an example of the analysis performed to one channel, considering the 511 keV and the 1274 keV photo peaks from a $^{22}$Na source. On both spectra, it was superimposed the neighbours events when the event on the central crystal was within the interval of interest.

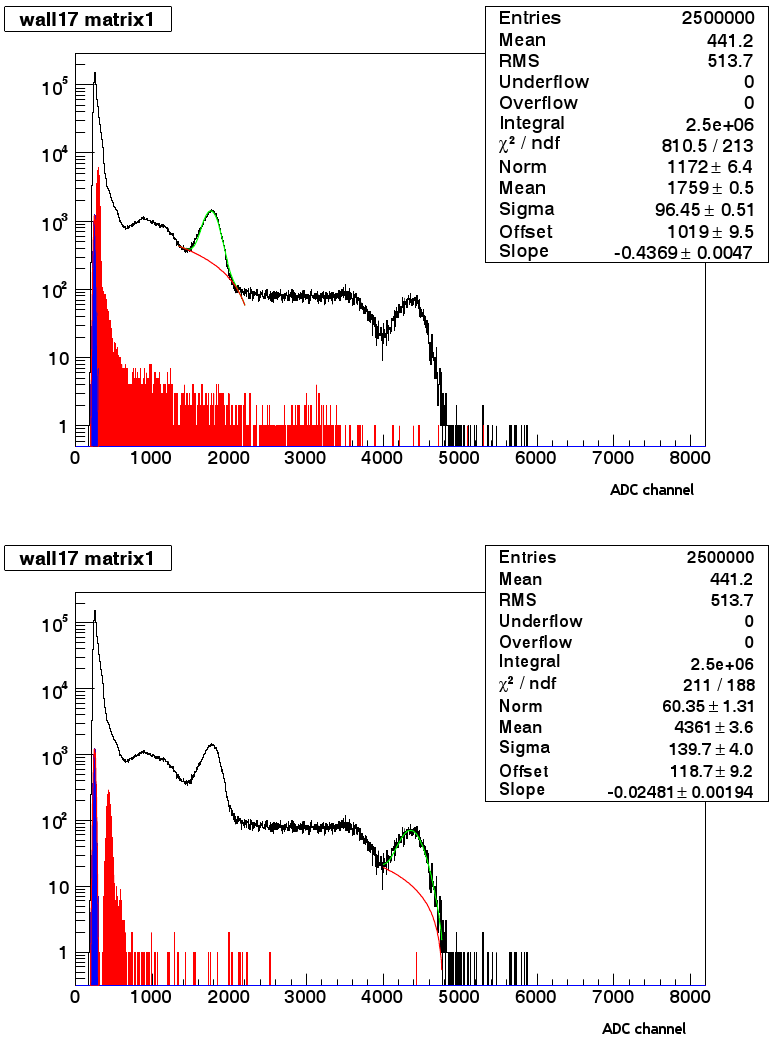


Figure 4.10: Spectrum and crosstalk evaluation for one channel, considering the 511 keV (*top*) and the 1274 keV peaks (*bottom*) from a $^{22}$Na source, obtained from the data analysis software. Spectra of neighbouring crystals were superimposed (in red and blue).

This primary analysis allowed the discrimination of optical crosstalk from Compton events. Choosing the events from the 1274 keV peak the contamination signal on the neighbouring crystal shifts to the right, considering the peak position resulting from the 511 keV photopeak. This shift is consistent to optical crosstalk and not to Compton events. In the case shown on Fig. 4.10, the fire crystal corresponds to the crystal 10 and wall 17 (that separates crystals 10 and 11 - recall Fig.4.5) was examined. The $^{22}$Na source was placed near crystal 9. Since the energy window in crystal 10 is 400–600 keV, forward Compton is excluded as it must deposit less than 100 keV in crystal 10 and about 400 keV in crystal 11 - Fig 4.11. Backward Compton is also excluded because it has to deposit about 300 keV in crystal 10 and 200 keV in crystal 11, which is below the energy window considered.

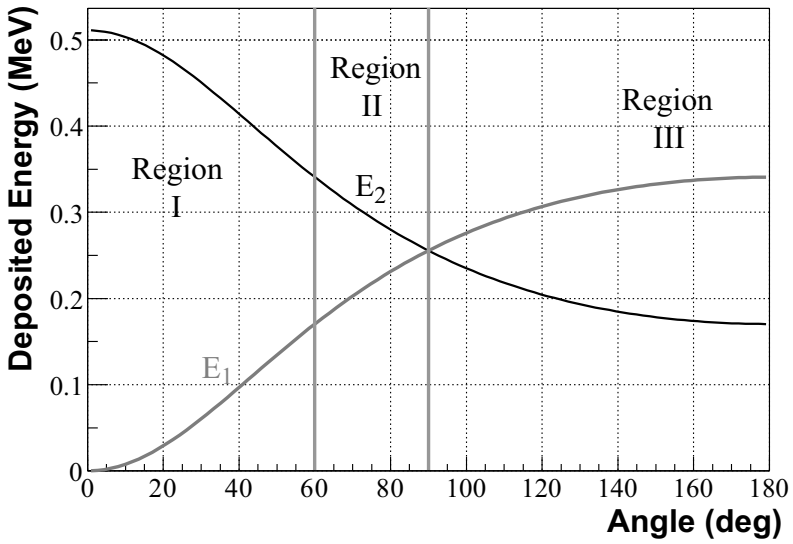


Figure 4.11: Energy deposited at the initial interaction point (E1) and energy deposited by the scattered photon (E2) as function of the Compton scatter angle ($\theta$), for 511 keV incident photons.

For analysis simplicity, the crosstalk evaluation was done with measurements with flood $^{137}$Cs acquisitions, since this allowed to re-use the earlier measurements performed for the characterization of the first batch of 24 detector modules as explained in Chapter 3. The most probable crosstalk of these 24 detector modules, corresponding to 1056 walls observed, was 3%, with 4.7% walls having a optical crosstalk larger than 5% - Figs. 4.12 and 4.13 [Abreu2005].

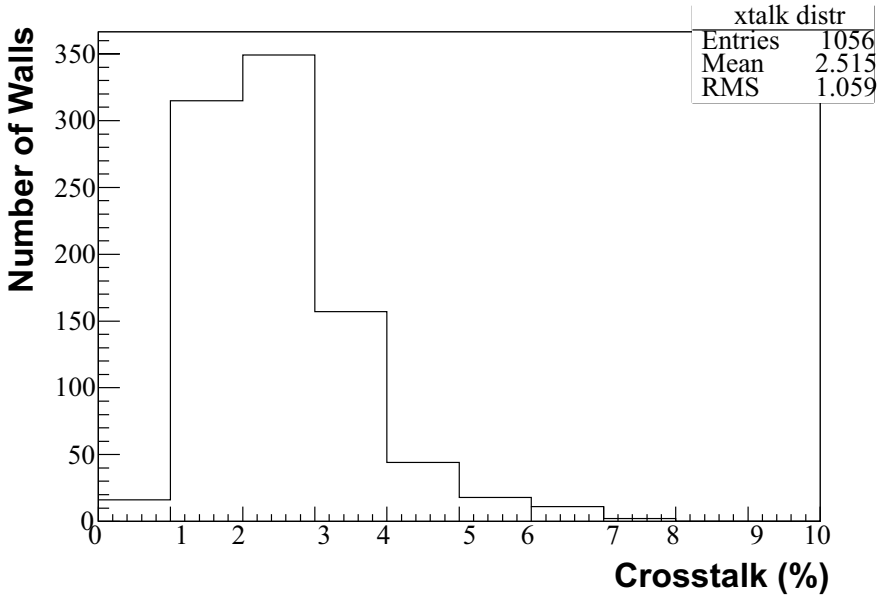


Figure 4.12: Crosstalk distribution per wall for the first 24 detector modules.

These results have indicated that the housing box developed to encase the detector module ensures a good match between crystals and APD pixels, minimizing the misalignment that could lead to a case in which one crystal is read by two different APD pixels.

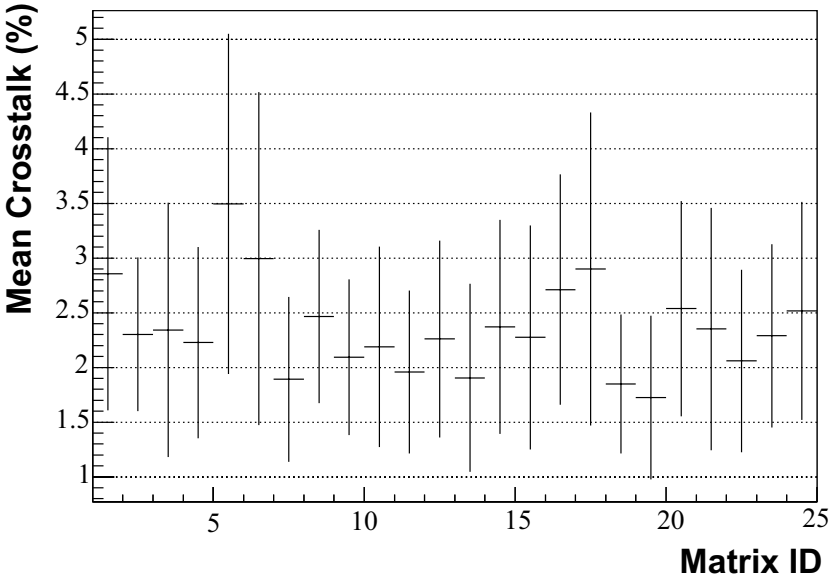


Figure 4.13: Average crosstalk per detector module.

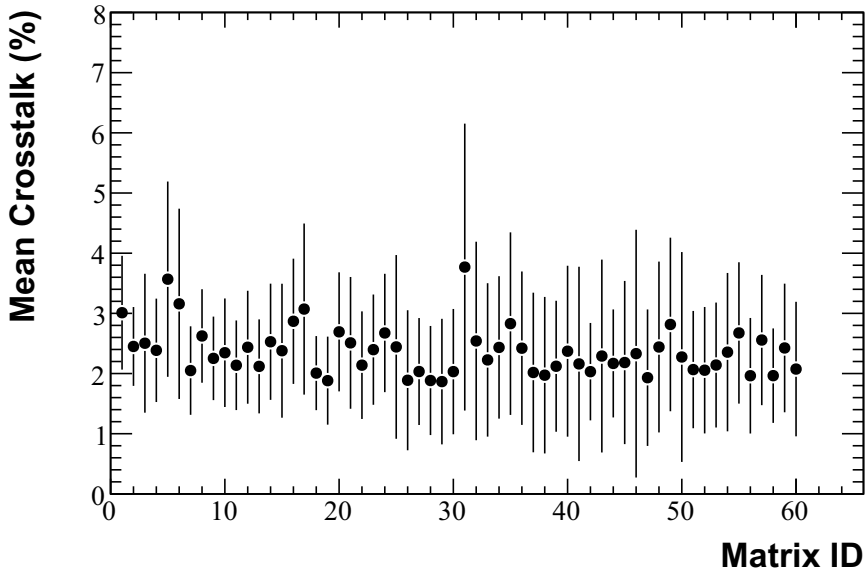


Figure 4.14: Average crosstalk found per matrix in the first batch of 60 detector modules.

After this assessment, crosstalk was included on the quality control protocol to reassure the good mechanical assembly of the detector modules, knowing that a considerable

mismatch between APDs and crystal matrices would lead to considerable crosstalk contamination. In Fig. 4.14 can be seen the average crosstalk for the 60 detector modules, were the error bars represent the r.m.s of each matrix. The average crosstalk found per matrix is 2.37 ± 0.39% (dispersion of 16.6%). The evaluation of the second bacth is not shown but the overall value of the 80 detector matrices remained small, 2.60 ± 0.89%. In Fig. 4.15 it is shown the maximum crosstalk contamination observed per matrix and in Fig. 4.16 the average crosstalk is presented per wall, to seek for correlations on matrix assembly, where error bars are the r.m.s per wall. As already reported, the wall 23 to 30 are not evaluated due to number of channels constrain of the discrete electronic chain.

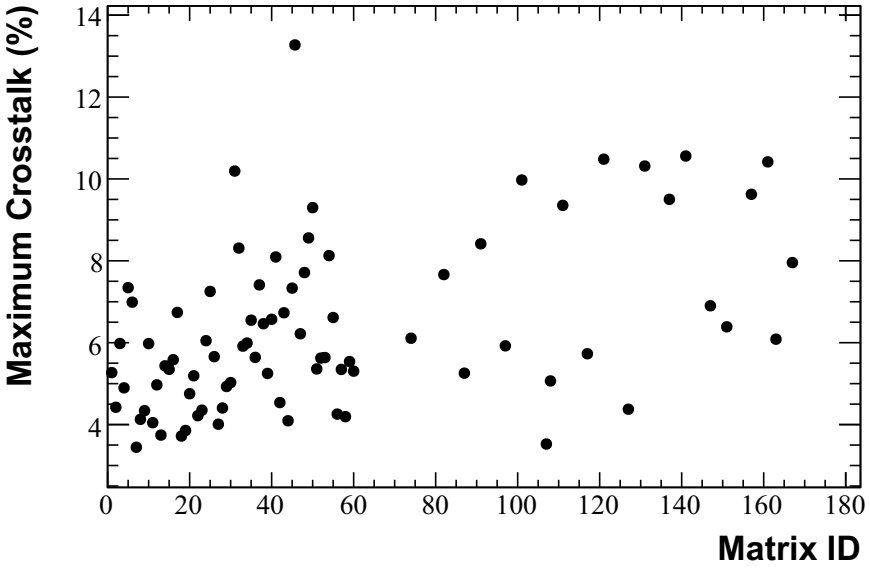


Figure 4.15: Maximum crosstalk found per matrix (80 detector modules).

The maximum crosstalk was found on the first batch of detector modules, with 13.25% (≈ 88 keV to 662 keV $^{137}$Cs photopeak, or ≈ 68 keV to 511 keV $^{22}$Na photopeak). The highest value on the second batch was 10.56% (≈ 54 keV to 511 keV $^{22}$Na photopeak). This means that only two values of the 3360 walls evaluated are above the threshold of the ASIC in the final ClearPEM system (Chapter 6). In a double readout scheme, the total energy deposited in a crystal is the energy collected by the two APD pixels. Therefore, two channels from different APDs and ASICs contribute to the total noise. Assuming that the two channels have similar noise and the total noise can be quadratically summed, the noise would be 7 keV which corresponds to a minimum threshold (7 × the noise RMS) of about 50 keV [Rodrigues2009]. Despite that, to avoid electronic noise problems like digital noise pick up, the common threshold was set to 1.55 V (equivalent to ≈ 120 keV), 56 mV above the chip baseline (1.49 V) so even the highest crosstalk values are not readout to the data acquisition electronics.

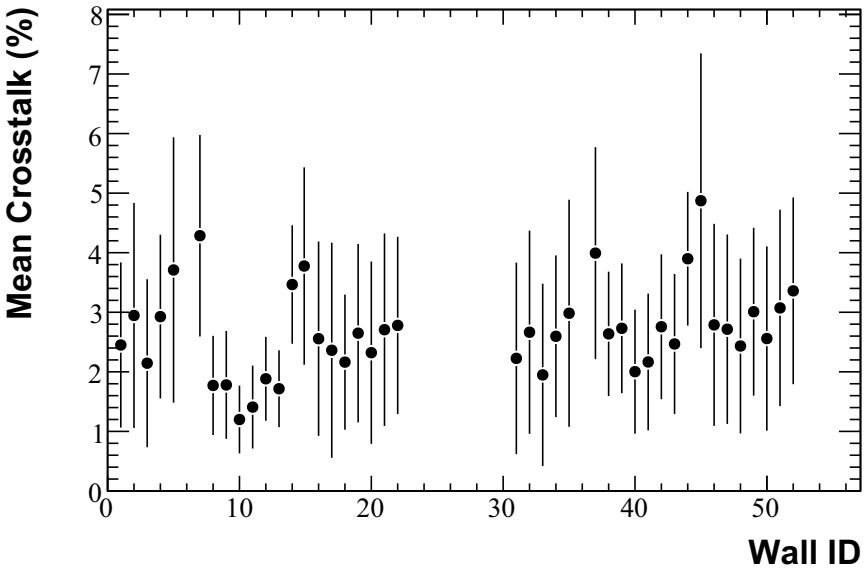


Figure 4.16: Average crosstalk per wall (80 detector modules).

A closer look to the Fig. 4.16 points out a similar behaviour from the first set (corresponding to walls 1 to 23) to the second set (walls 31 to 52), corresponding to the same electronic channels of the double readout electronic chain used. Although small, the average value is $2.69 \pm 0.76\%$. This behaviour could be attributed to a residual contamination of the adjacent channels of the double readout electronics chain.

## 4.4 Summary and Discussion

Working with small adjacent crystals may lead to inter-crystal crosstalk contamination, which arises from Compton scattering from one crystal to another or possibly the escape of the photoelectron from the primary crystal following photoelectric absorption. Light sharing between two pixels due to position mismatch of the crystal pixel - APD pixel, inefficient optical isolation, degradation or absence of the optical coupling interface crystal-APD may also induce crosstalk, which has particularly important implications for the design of the ClearPEM front-end electronics and on the system performance. This parameter was evaluated in a series of dedicated measurements to study the possible causes of crosstalk.

Electrical crosstalk was first evaluated by means of direct ionization of the silicon layer with a 5.9 keV $^{55}$Fe source. Results indicate a negligible level of electrical crosstalk ($<$0.3%). Optical crosstalk that can be introduced by the APD epoxy cover was assessed and it is mostly inexistent (average values: 0.31% and 0.23%, with and without optical grease respectively). As conclusions, it can be stated that there is no relevant electrical or optical crosstalk on APD. The major contribution to the detector module crosstalk from the small pixels separated by the 300 $\mu$m layer of $BaSO_4$. The contribution of crosstalk

on the ClearPEM detector modules, despite the pixelized matrix configuration, is low. The first 24 detector modules present average crosstalk of 3% and the overall evaluation of 80 detector modules reassures the small contamination.

Measurements in different conditions and with different discrete electronics did not disturbed the evaluation of the crosstalk, but permitted to infer a higher contamination on the double readout scheme electronics, probably due to current sharing between the PCB traces. Nevertheless, the average crosstalk value remained small, so this issue was not further investigated.

Several authors have presented similar studies of crosstalk. Reporting the Pichler et al [Pichler2001] study of the S8550 APD for a High-Resolution PET with 32-channel LSO matrix, it was found no electronic crosstalk on the S8550 APD and a optical crosstalk of 5.9%, when coupled to the LSO crystal matrix with 3M Vikuiti ESR reflector. This matrix was glued directly to the APD array, read by a 16–channel low-noise JFET–CMOS preamplifier chip specially developed. From the FZD group, working with LSO crystals readout by the S8550 APD as a possible detector for in-beam PET in hadron therapy, Crespo [Crespo2005] has shown inter-crystal crosstalk below 10%, with crystals wrapped in Tyvek reflector. Crosstalk on APD was also appraised by this author, with depreciate influence of electrical crosstalk (0.5% maximum) and an optical crosstalk of 3.6%, considered to be due to the epoxy window completely covering the sensitive area. The results regarding electrical and optical crosstalk on the APD are consistent with the ones obtained in this thesis. As for the ClearPEM detector module, optical crosstalk (less than 3%) was lower and, as it will be shown in Chapter 5, this can be attributed to the superior mechanical and optical isolation of the $BaSO_4$ relatively to the Tyvek based matrices.

These results are below of the final electronic threshold, that was set to 1.55 V (equivalent to $\approx$ 120 keV), so even the highest crosstalk values are not readout to the data acquisition electronics.

Chapter 5

# Optimization of the ClearPEM Detector Module

## Contents

## 5.1 Introduction

The ClearPEM detector module consists on 32 LYSO:Ce crystals with 2×2×20 $mm^3$ encased in a $BaSO_4$ matrix, readout at both ends by two Hamamatsu S8550 4×8 APD arrays. The evaluation of the detector module design was presented in Chapter 3 showing an energy resolution of 15% at 511 keV, DOI resolution better than 2 mm and light collection (photopeak position) variation better than 20%. Long-term stability was also appraised and detected that one year after the detector modules were assembled a mean light collection reduction of 12% and a decrease of the light collection asymmetry, fundamental for the DOI measurement, of almost 30% was observed. It was shown that the degradation can be recovered by re-assembling the detector modules and the behaviour traced back to an aging of the optical grease that acts as a coupling media between the LYSO crystals and the Si APD pixels.

As already described in Chapter 1, Section 1.3, the development of the ClearPEM detector module had explored the concept of having the intrinsic detector resolution as low as possible to achieve a good reconstructed image resolution. Sensitivity also played a central role on the design of the ClearPEM system. The detector heads close to the object provide a large angular coverage and the double readout for depths-of-interaction minimize the parallax effect. The position accuracy, characterized by the spatial resolution, was assured by the 2×2 $mm^2$ individual crystals. Inter-crystal crosstalk is small (Chapter 4) allowing to have $b \approx 0$ (recall Eq. 1.2, on Chapter 1).

In spite of the significant development and good performance already achieved (Chapters 3 and 4), optimization of the ClearPEM detector module design is a continuous work. In this chapter, the revision of the optical coupling is presented. Triggered by the aging problems detected with the optical grease, several optical coupling materials were studied, namely Meltmount 1.58, Histomount and RTV 3145, evolving for a permanent solution with better performance. To increase the sensitivity of the detector modules, efforts on improving the packing fraction of the ClearPEM detector module, which is 64% and is mainly constrained by the S8550 APD matrix layout and the thickness of the $BaSO_4$ walls, were explored with a new matrix with 2.2×2.2×30 $mm^3$ crystals and thinner specular reflector walls. More over, the low internal gain of the APD and the low ligh collection are currently the limiting factors in time resolution (5 ns FWHM measured with ClearPEM, as will be shown in Chapter 6). Further improvements on the timing information require an increase on the light collection which is limited by the 1.6×1.6 $mm^2$ APD pixel matching with the 2×2 $mm^2$ cross-section crystals. Possible solutions like the redesign of the S8550 APD were addressed. As a result of this work, a new APD, with 1.8×1.8 $mm^2$ pixels, quantum efficiency of 80–90% at 420 nm and gain 200, was developed by Radiation Monitoring Devices, under a frame contract with LIP.

## 5.2 Optical Coupling Optimization

A small amount of optical grease from Rhodorsil, designated as Paste 7, was used to provide a better refraction index matching in the crystal-APD interface, to increase the light transfer between crystals and the APD pixels. The optical grease is a silicone compound with refractive index of 1.47 for 420 nm, translucent and with a light grey colour, easy to handle which can be applied with a brush, a spatula or with a paste gun. When stored in its original unopened packaging at a temperature between 2°C and 50°C, Rhodorsil Paste 7 must be used within 36 months of the manufacture date shown on the packaging.

Long-term stability evaluation, shown on Chapter 3, has detected that one year after the detector modules were assembled a severe degradation on the performance could be observed. Some detector modules packages were disassembled for visual inspection. It was observed that the Paste 7 had lost the properties of a gel and had become solid (Fig. 5.1). The behaviour was assumed to be due to the aging of the optical coupling as the degradation on the light collection and asymmetry could be recovered by re-assembling the detector modules with a new application of fresh optical grease.

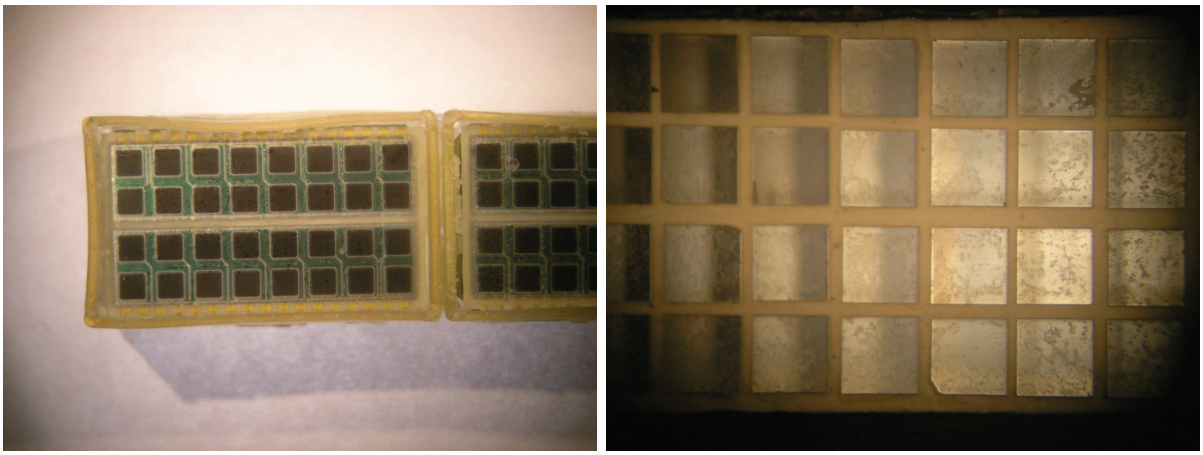

Figure 5.1: Photographs of a detector module open apart, 18 months after being assembled.

The choice of a new optical medium for ClearPEM detector modules was then mandatory and has taken into account some requirements, namely the refractive index for optimum light-transmission, aging effects, handling and curing processes. The number of photons detected by the APDs depends on the optical coupling medium between crystals and APD. The index of refraction, $n_{coupling}$, determines the angle of refraction and the reflection losses in the crystals interface to optical coupling medium and optical coupling medium to APD. Both effects influence the light collection efficiency with the optimum reached at $n_{coupling} \approx \sqrt{n_{crystal} \cdot n_{APD}}$ [Kirn1999]. In addition, the absorption length of the coupling medium should be large enough so the transmitted photons are not absorbed in the optical layer. The ideal optical coupling for the ClearPEM detector module should have an index of refraction of 1.63, between the indexes for the LYSO:Ce crystal (1.82 @ 420 nm) and the APD epoxy (1.53 @ 420 nm) layer that protect the Si pixels. Silicone

grease is a good option for temporary assembly but an epoxy based compound or resin type is preferable for a permanent construction. On Tab. 5.1 the optical couplings considered for the optimization of ClearPEM detector modules are listed and compared with the Rhodorsil Silicones Paste 7.

| Product | Vendor | n @ 420 nm | Curing time |
|---|---|---|---|
| Paste 7 | Rhodorsil Silicones | 1.47 | NA |
| Meltmount 1.58 | Cargille | 1.58 | $<$ 10s |
| RTV 3145 | Dow Corning | 1.50 | 2 to 72h @ RT |
| Histomount | National Diagnostics | 1.63 | 12h @ RT |

Table 5.1: Properties of the tested optical couplings for the optimization of the ClearPEM detector module.


Figure 5.2: Photograph of the tested optical couplings.

## Cargille Melmount 1.58

Cargille Melmount 1.58 (Meltmount) is a thermal plastic material. Its viscosity is inversely dependent on temperature. As the temperature increases the viscosity decreases. There is no sharp melting point. Being thermal plastic, it is capable of "cold flow". This means that Meltmount, the specimen, the slide and the cover slip can all move independently of each other given a mix of time, temperature, and lateral pressure or gravity. It is 100% usable, contains no solvents and it is thermally reversible for particle retrieval or reorientation. It is soluble in toluene for special techniques or clean-up. It becomes fluid at 65°C, a temperature chosen because it makes permanent mount and protects the majority of specimens from thermal changes. In Fig. 5.3 the refractive index of the Meltmount as a function of scintillation wavelength is shown. At 420 nm the refractive index is 1.58 and the absorption length is 10 cm, which is not a issue for ClearPEM detector module as a thin layer (10 to 20 $\mu$m) of optical material is sufficient to couple the crystal matrix to the APD arrays.

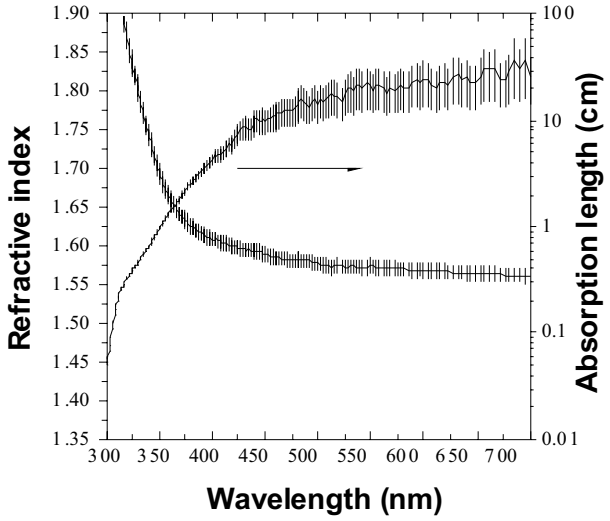


Figure 5.3: Meltmount refractive index and absorption length (extracted from [Montecchi2001]).

One detector module was assembled with Meltmount, which have implied the use of an oven (Fig. 2.11 *right*, Section 2.4, Chapter 2) to heat the optical coupling to the fluid state, completing all the process at the same temperature. The performance of this module was evaluated in terms of light yield, energy resolution and depth of interaction capability (asymmetry per millimetre) with the discrete electronic chain for double readout (see description on Chapter 2).

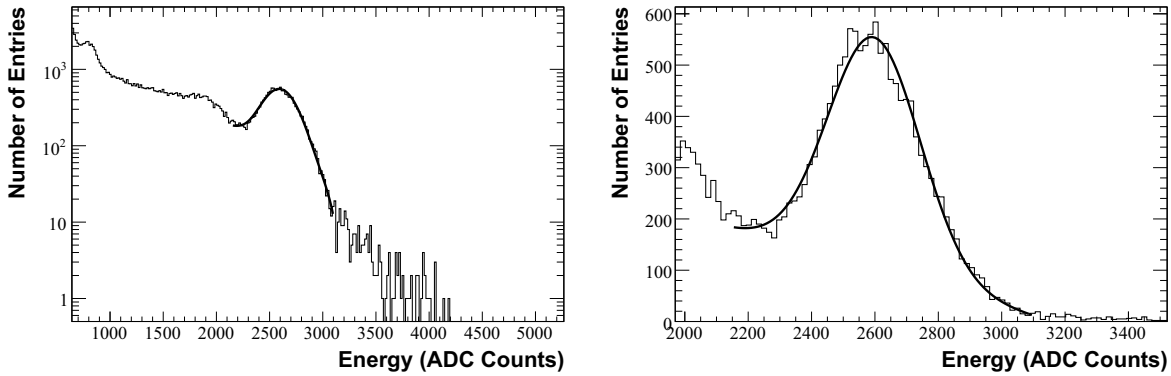


Figure 5.4: Typical pulse height spectra of a crystal glued with Meltmount (*left*) and close-up of the 662 keV photopeak region (*right*).

In Fig. 5.4 it can be seen a typical spectra of the $^{137}$Cs source. Mean light yield is 1974±306 ADC channels, the average energy resolution at 662 keV is 15.8±2.5% and the asymmetry per mm is 5.64±0.44 %/mm. Photopeak position variation of the Meltmount detector module along two months is shown in Fig. 5.5, presenting a stabler and higher light yield when compared with ClearPEM production detector module, assembled with Paste 7 (grease).

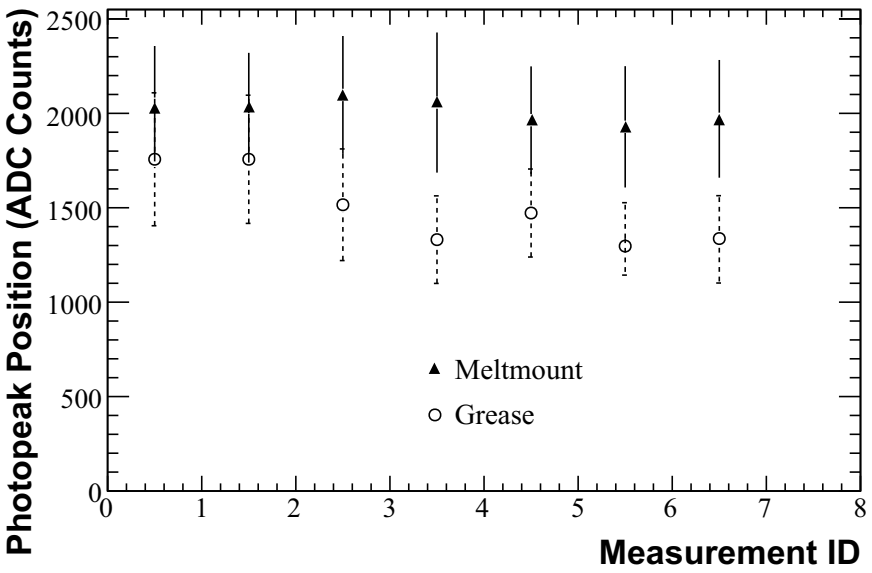


Figure 5.5: 662 keV ($^{137}$Cs) photopeak position variation of the Meltmount detector module along two months, compared with ClearPEM production detector module, assembled with Paste 7 (grease).

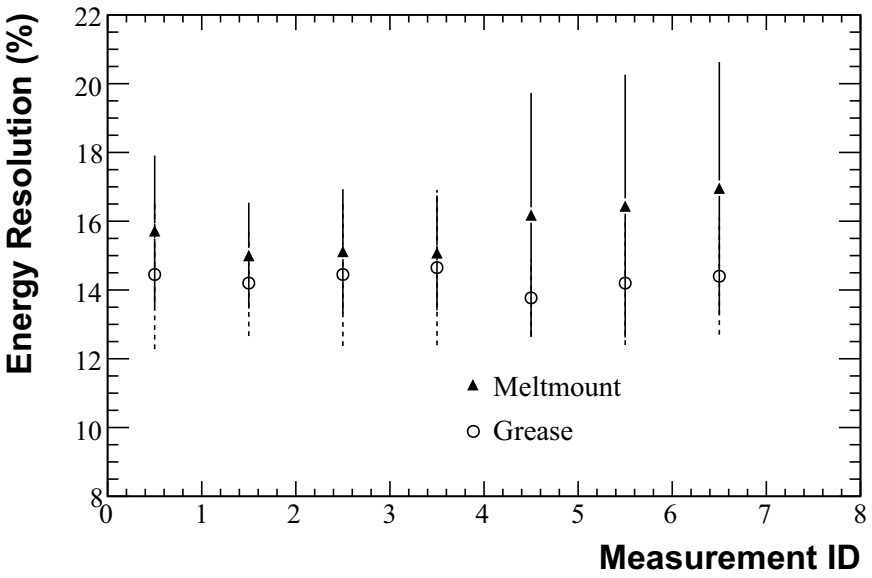


Figure 5.6: Energy resolution at 662 keV of the Meltmount detector module along two months compared with the ClearPEM production detector module, assembled with Paste 7 (grease).

Energy resolution variation at 662 keV of the Meltmount detector module along time is shown in Fig. 5.6, compared with a ClearPEM production detector module, assembled

with grease. It can be seen that the energy resolution achieved for the Meltmount detector module is higher when compared with the ClearPEM detector module, with larger dispersion, which is related to the difficulty of assembling the detector module with Meltmount. The action is performed at 65°C temperature as already referred, which makes the procedure difficult in the sense that the user has limited time for the gluing. As a consequence, air bubbles and inhomogeneous amount of optical coupling between crystals and APD pixels may be introduce. In result, one of APD pixels of the same crystal may collect more light than the other, enlarging the final sum photopeak in a double readout mode. An example of this behaviour is shown in Fig. 5.7, where the energy resolution of the photopeak grew up to 30%. Comparison of the top and bottom APD (Fig. 5.7, *left*) shows a significant difference in the light collection spectra, indicating different light collection efficiency between both APD pixels. As described in Chapter 3, in a double readout arrangement, the sum energy for a given crystal is given by:

$$E = K_{Abs}\left(E_{top} + k_{rel}E_{bottom}\right) \tag{5.1}$$

where $K_{Abs}$ is the absolute gain calibration constant that translate the energy in ADC counts to the physical value (in keV), and $k_{rel}$ is the inter-pixel calibration constant which guarantees that both APDs (top and bottom) provide a similar response in terms of ADC counts. With air bubbles in the optical coupling, it is expected that the top and bottom APDs collect different amounts of light. As a consequence, $k_{rel}$ can be much larger or smaller than 1. The miscalibration between two pixels, reading the same crystal, introduces an additional spread in the energy resolution. The effect was studied in dedicated Monte Carlo simulations ([Rodrigues2007]), where miscalibration higher than 20% can lead to a significant degradation of the energy resolution (Fig. 5.8). Below 20%, miscalibration does not affect the energy resolution. In measurements performed in Chapters 3, 4 and 5, the energy sum is computed assuming $k_{rel} = 1$, which implicitely assumes that miscalibabration is less than 20%.

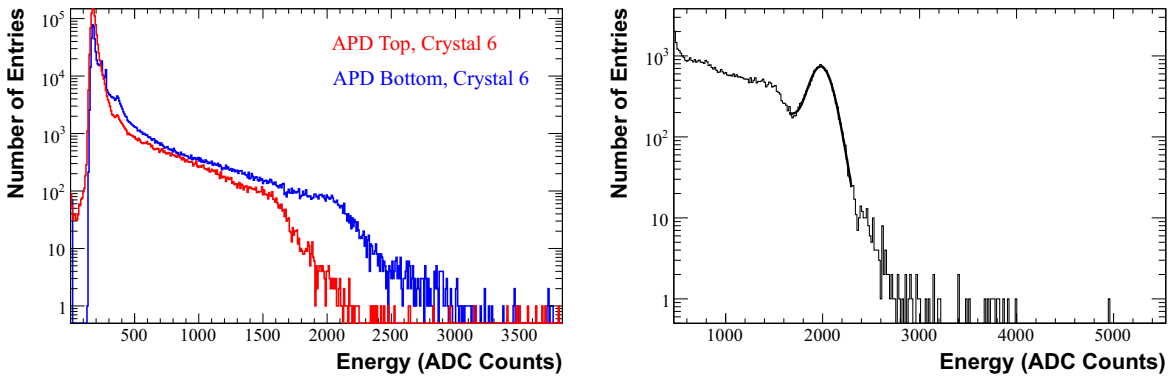


Figure 5.7: Top and bottom APD light collection for a crystal glued with Meltmount (*left*) and corresponding sum spetrum, with a 662 keV photopeak energy resolution of 30% (*right*).

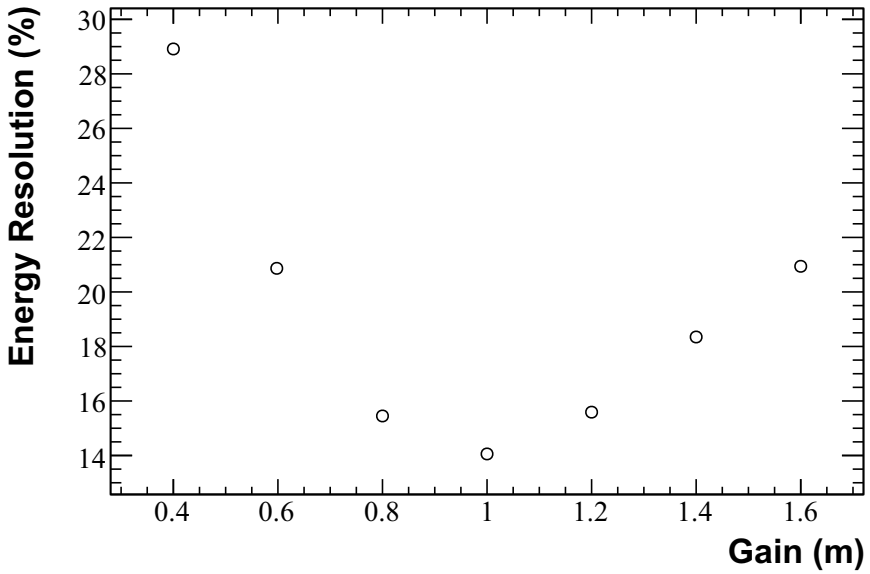


Figure 5.8: Energy resolution as function of the inter-pixel miscalibration ([Rodrigues2007]).

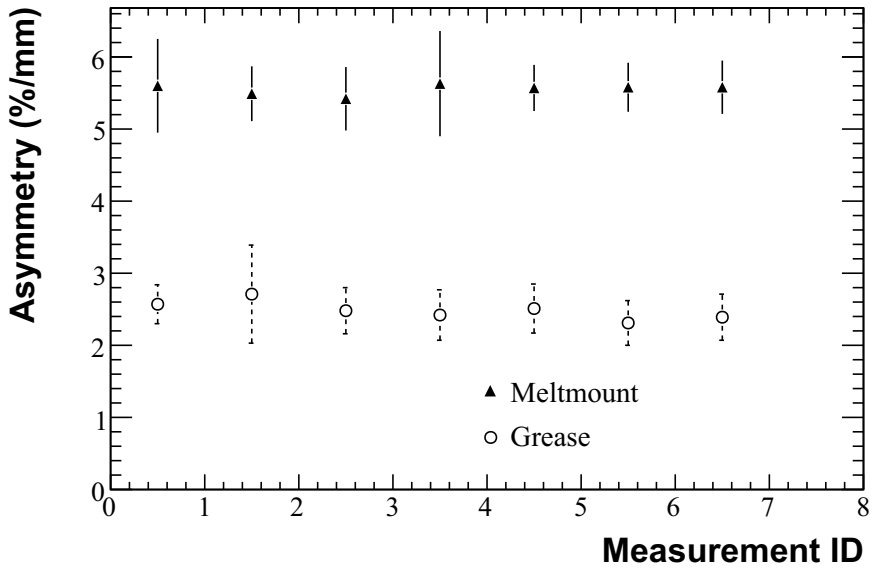


Figure 5.9: Light collection asymmetry variation of the Meltmount detector module along two months compared with the ClearPEM production detector module, assembled with Paste 7 (grease).

Light collection asymmetry variation of the Meltmount detector module along two months is presented in Fig. 5.9, where results were compared with a ClearPEM production detector module, assembled with Paste 7 (grease). The values presented for the ClearPEM detector module are lower than the average value presented on Chapter 3,

because these measurements were done 6 months after the detector module had been assembled, where the aging of the optical coupling affected the parameter performance. Despite that, even considering the best light collection asymmetry achieved with grease detector modules, the Meltmount detector module is considerable better.

In conclusion, the Meltmount detector module has shown to be more stable and with better performance in terms of light yield and asymmetry per mm (5.6%/mm) than modules assembled with grease (3.5%/mm, average value for ClearPEM). Energy resolution is marginally worse due to the asymmetrical light collection observed in some of the pixel APDs by the presence of air bubbles and inhomogeneities in the quantity of the Meltoumnt as result of the difficult gluing procedure. The performance of the assembled detector module along 2 months has shown no significant variation on the assessed parameters. This optical coupling was considered as a good candidate for ClearPEM but it is extremely difficult to assemble detector modules with Meltmount, to ensure good match between crystals and APD pixels and to avoid air bubbles, essentially by the need to heat and maintain the temperature at 65°C during the process. It is also crucial not to overcome this temperature to avoid damaging the APD epoxy. Therefore, for mechanical reasons, other solutions were considered.

## Dow Corning RTV 3145

Dow Corning 3145 RTV MIL-A-46146 Adhesive/Sealant (RTV) has a paste like consistency and can be applied directly from its collapsible tube or extruded from its cartridge. On exposure to moisture in the air, the surface of RTV will form a skin in about 25 minutes at room temperature with 50% relative humidity. Any tooling should be completed before this skin forms. After 90 minutes under these conditions, the RTV will become tack free, allowing limited handling until the cure is fully complete. Curing continues inward from the surface and it will be completed in 24 hours (at room temperature and 50% relative humidity) for a depth of 3 mm. Optimum physical properties are reached after curing for 7 days at room temperature. It resists to weight and pressure. In Fig. 5.10 it is shown the refractive index of RTV 3145 as a function of scintillation wavelength. At 430 nm the refractive index is 1.50, which is considerably lower than Meltmount and the absorption length is 2 cm, again not a problem when using a thin layer of optical coupling.

This optical coupling was rejected for the ClearPEM detector module due to identified problems with reassembly, since RTV can only be soften with acetone. However, to disassemble a detector module with RTV, acetone is not enough and an extra force is required which may damage the $BaSO_4$ walls of the crystal matrix and the APD epoxy cover (0.5 mm thickness). For this reason, the RTV 3145 option was abandoned and no further studies were carried out.

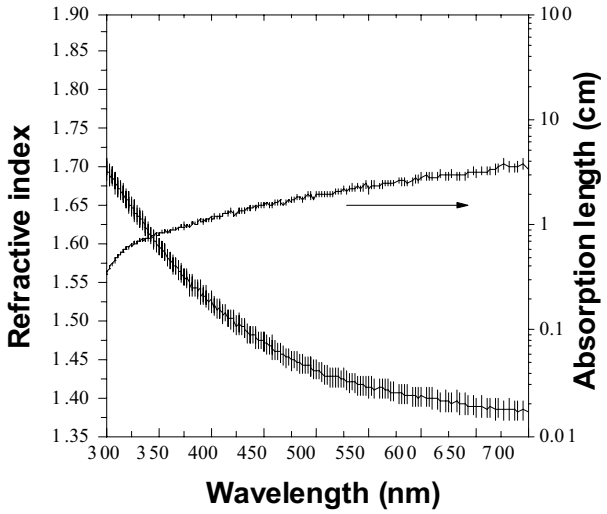


Figure 5.10: RTV 3145 refractive index and absorption length (extracted from [Montecchi2001]).

## National Diagnostics Histomount

Histomount, from National Diagnostics, is an organic based mounting medium for immunohistochemical procedures and is commonly used in archival slide preparation. It cures by the evaporation of xylene. High vapor concentrations are anesthetic and central nervous system depressants so it requires a fume hood during application to avoid inhalation of vapors irritating to the nose and throat. The optical coupling is viscous and forms a skim almost immediately. The refractive index and absorption length of Histomount as a function of scintillation wavelength is shown in Fig. 5.11.

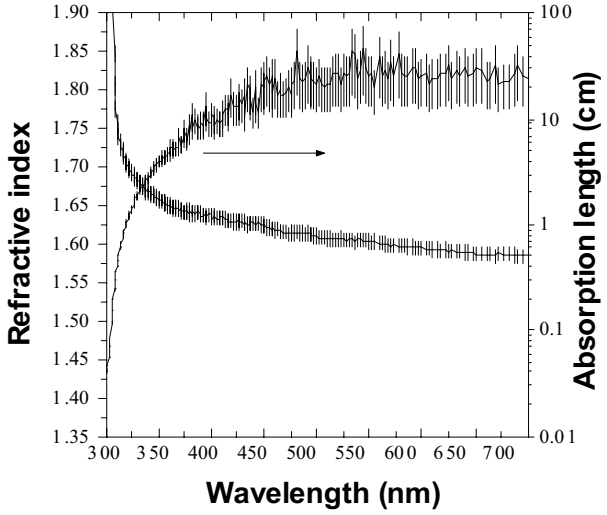


Figure 5.11: Histomount refractive index and absorption length (extracted from [Montecchi2001]).

At 420 nm the refractive index is 1.63, which is considered the best optimization in

terms of light collection efficiency for the ClearPEM scenario and the absorption length is 12 cm. As Histomount cures by the evaporation of xylene, whose refractive index (about 1.5) is lower than the constituent of Histomount (vinyl toluene), it can be seen in the curing process that the refractive index of this optical medium rises as the content of xylene falls (Fig. 5.12). This optical coupling were explored by the CMS collaboration at CERN, but has been abandoned because the long curing time for thick layers and toxicity when working with large quantities (120 000 APDs with a 5×5 $mm^2$ active area).

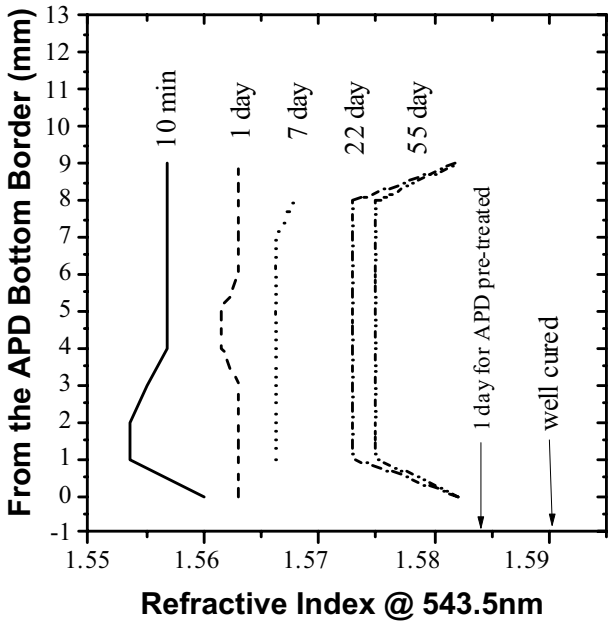


Figure 5.12: Histomount refractive index evolution with curing time (extracted from [Montecchi2001]).

For comparison purposes, one detector module was assembled with Histomount, using an organic mask (organic vapor half mask respirator, from 3M), to refrain the inhalation of xylene toxic vapors. Visual inspection with a microscope has shown no air bubbles or negligible by its dimensions. The thin layer used did not required long curing time and performance measurements were done 5 days after the detector module had been assembled. As the discrete electronic chain for double readout was inoperative for maintenance, light collection and energy resolution were assessed with the discrete electronic chain for single readout and compared with a ClearPEM detector module in the same measurement conditions. In Fig. 5.13 the photopeak positions of both modules are shown, where can be seen a consistent increase of the light collection in the Histomount module in all channels. The gain in terms of light yield obtained with the Histomout compared with the fresh Grease detector module, specifically assembled for this optical coupling comparison study, is presented in Fig. 5.14, having an average gain of 16%. Photopeak dispersion of the Histomount module is 14%, similar to the 15% value obtained with the Grease module.

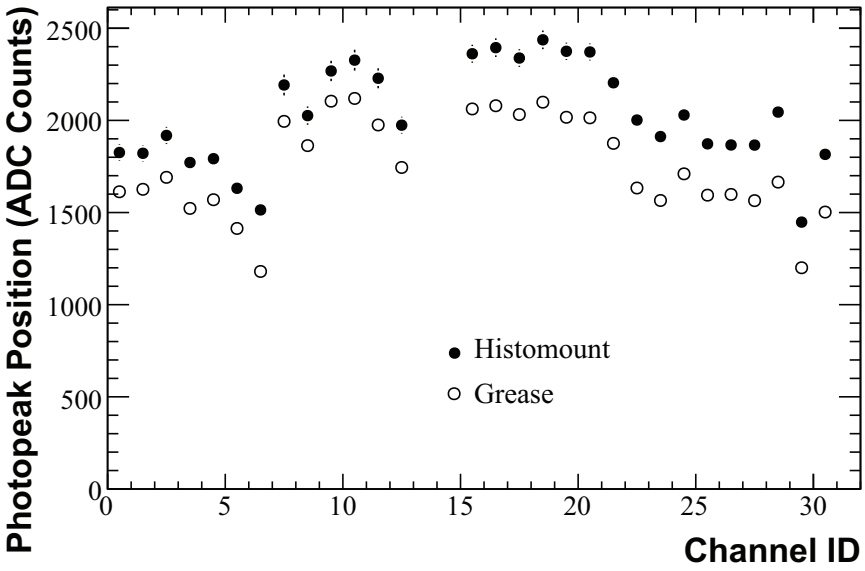


Figure 5.13: 662 keV ($^{137}$Cs) peak position of the Histomount detector module, compared with a ClearPEM production detector module.

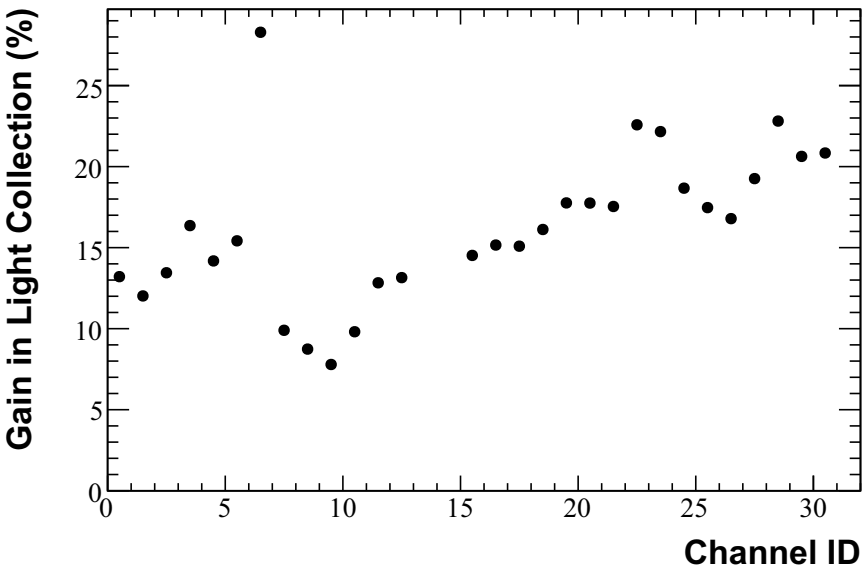


Figure 5.14: Light yield gain of the Histomount detector module relatively to the Grease detector module.

Long-term variation of the light yield for the Histomount detector module was evaluated along two months and compared with the Grease detector module. As can be seen in Fig. 5.15, there is no detectable degradation on the performance of this parameter.

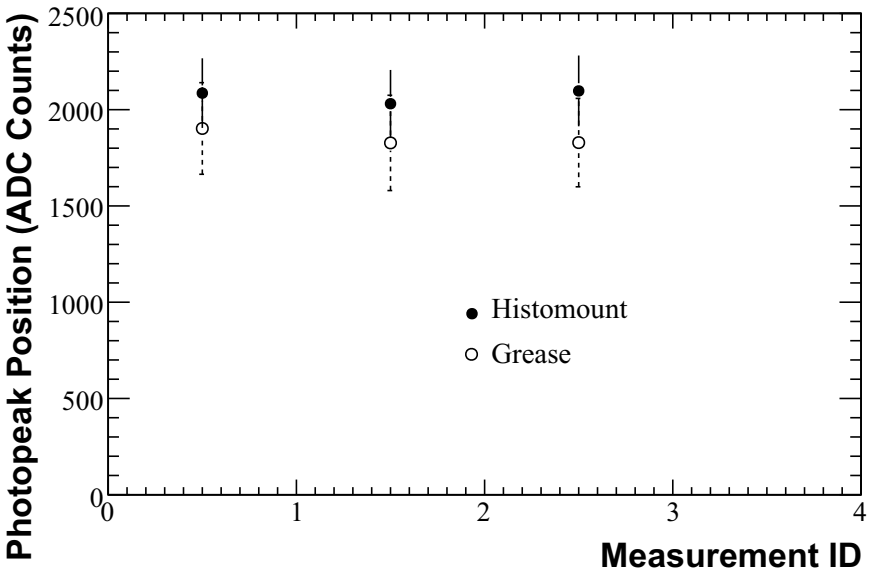


Figure 5.15: Long-term variation of the light yield for the Histomount detector module along two months, compared with the ClearPEM production detector module, measured in the same experimental conditions.

In agreement with this result, a better energy resolution is achieved for the Histomount detector module, in comparison with the Grease detector module (Fig. 5.16). The average energy resolution at 662 keV for the Histomount detector module, measured in the single readout electronics, is 13.36 $\pm$ 0.57% and 14.23 $\pm$ 0.73% for the Grease detector module.

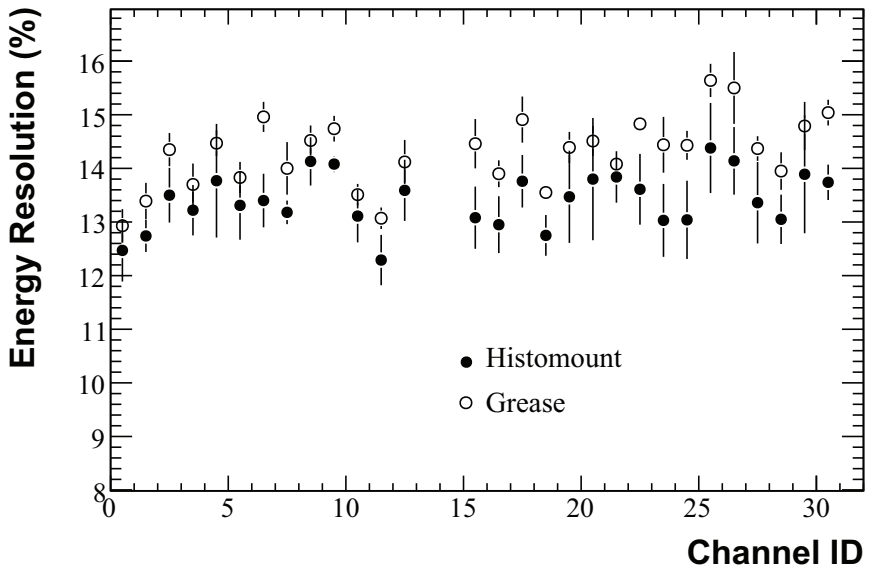


Figure 5.16: Energy resolution at 662 keV of the Histomount detector module, compared with a ClearPEM production detector module.

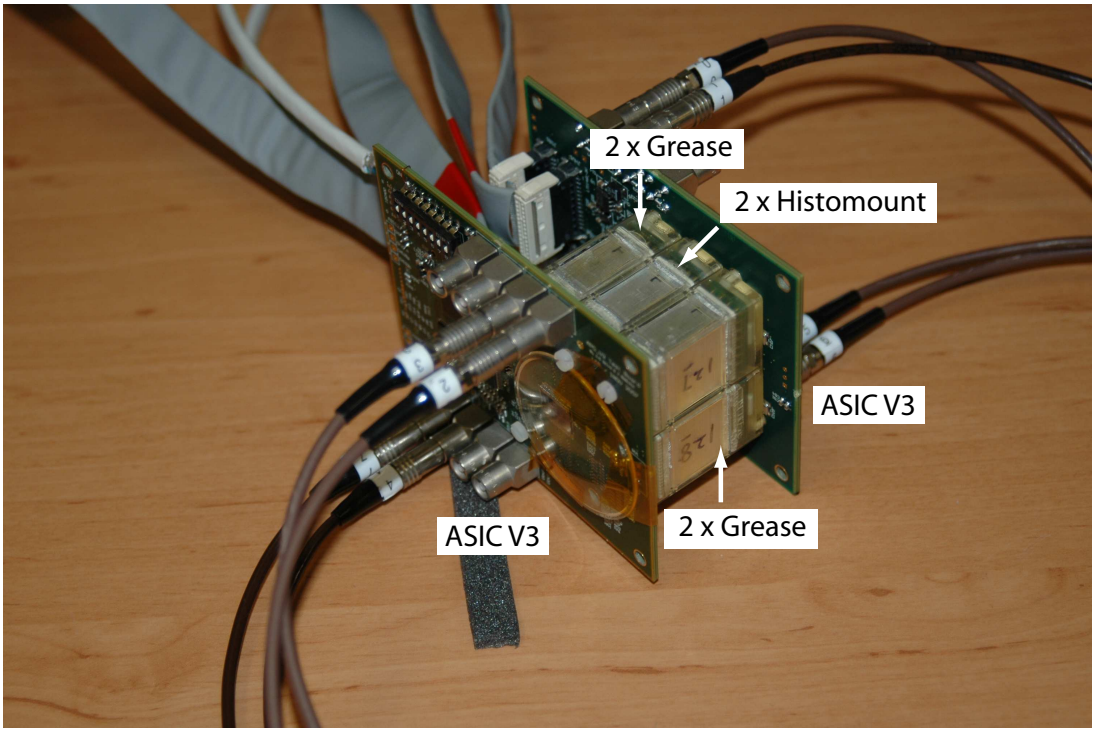


Figure 5.17: Photograph of the "Trigger Cell" setup, with two ASIC test boards reading 6 Hamamatsu S8550 APDs coupled to detector modules assembled with Grease and Histomount.

To assess the impact of this optical medium in DOI, measurements in double readout scheme were performed with the Trigger Cell setup (Fig. 5.17) as replacement for the discrete double readout electronics. This setup manage to read 6 detector modules at the same time in double readout by the two ASIC test boards. Each test board has a ClearPEM frontend ASIC allowing to readout up to 6 Hamamatsu S8550 APDs [Rodrigues2009]. In these tests, the ASICs dies were covered by a temporary glass since the thermally conductive epoxy adhesive (glob-top) covering step had not been performed. This prevents the usage of a suitable cooling system. Instead cold air was directed to the board avoiding the uncontrolled heating of the APDs. Using this approach the temperature measured under the PCB region underlying the APDs was 24–26°C. The trigger mode was operated in single photon mode, which means that all accepted events above the energy threshold (set at 200 keV) are readout to the data acquisition server. Measurements were performed with 2 detector modules assembled with Histomount, 2 detector modules with fresh Grease and 2 other detector modules already assembled months before, considered, for that reason, that were assembled with old Grease.

In Figs. 5.18 and 5.19 examples of the 662 keV spectra and asymmetry plot for the Histomount detector module are shown, in comparison with the ClearPEM detector module. As expected, an increase light yield is observed with better asymmetry per millimetre is achieved with the Histomount optical coupling.

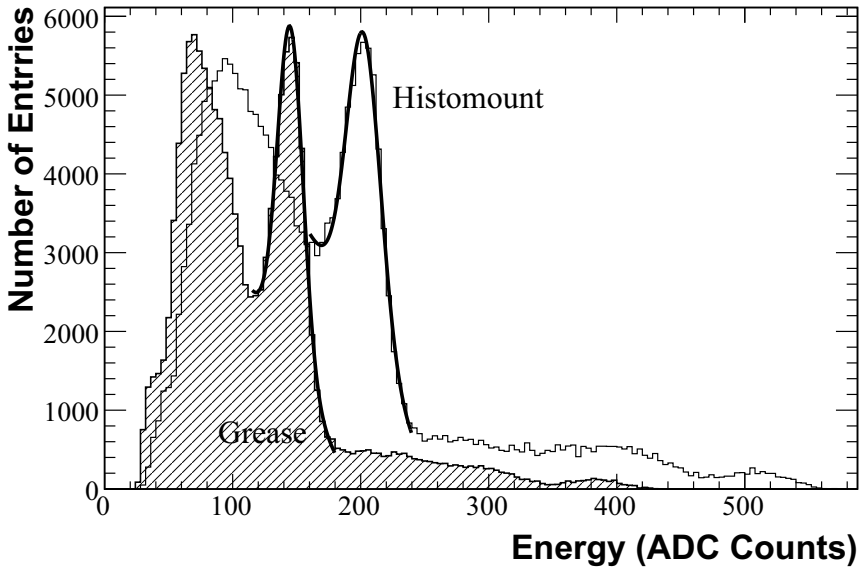


Figure 5.18: Example of a $^{137}$Cs spectra (662 keV photopeak) for a crystal from the Histomount detector module readout with the Trigger Cell setup, compared with a crystal from the ClearPEM production detector module (2 months mounting time).

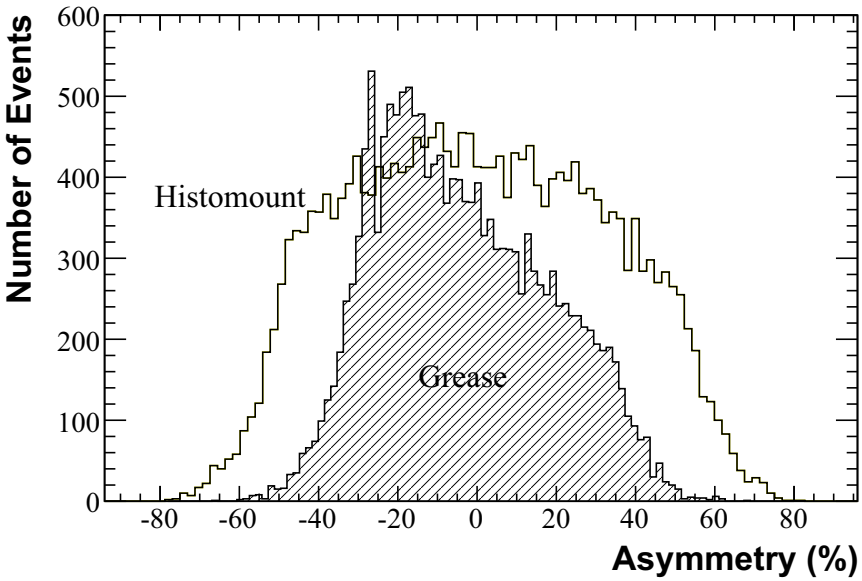


Figure 5.19: Example of a light collection asymmetry plot for the Histomount detector module, compared with the ClearPEM production detector module.

For a better picture of the impact of the optical coupling on the detector performance, in Fig. 5.20 values for the asymmetry per millimetre are shown for Histomount and Grease detector modules. It can be seen the aging effect of the optical glue, with average asymmetry of 3.5%/mm for the old grease (grease results on the left, for channel

IDs inferior to 1600), compatible with results already presented in the characterization of the ClearPEM baseline detector modules (Chapter 3) and a better performance when reassembled with fresh Grease (grease results on the right, for channel IDs superior to 1664), with 4.5%/mm average asymmetry. Despite that, Histomount coupling can achieve more favourable performance, with a mean asymmetry of 5.4%/mm.

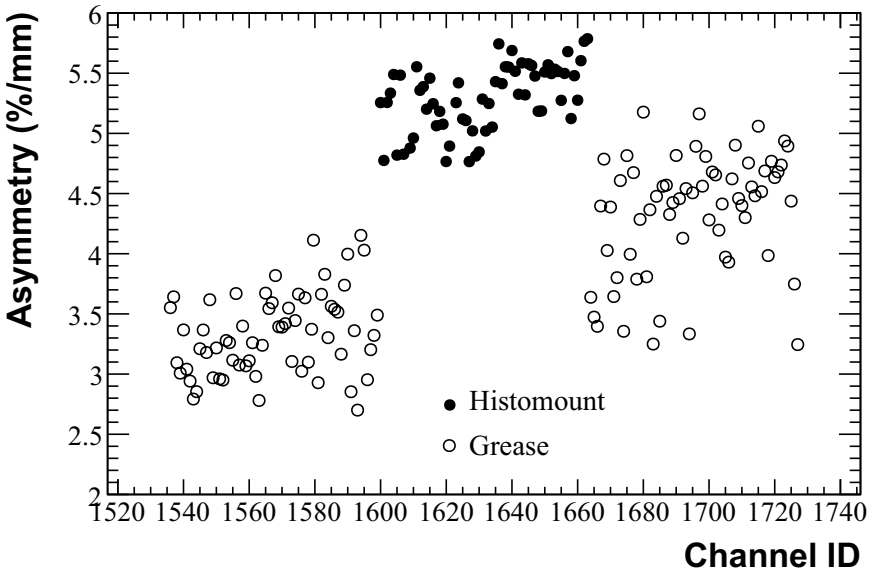


Figure 5.20: Light collection asymmetry comparison results obtained with detector modules assembled with Histomount (centre), old Grease (left) and fresh Grease(right).

Proving to be the best optical coupling for the ClearPEM, regarding the long-term stability of the light collection, energy and DOI resolution, all detector modules were reassembled with Histomount, an action performed in 8 working days.

## 5.3 High Packing Fraction Matrices

The ClearPEM scanner was developed with a high sensitivity requirement to intend less injected dose or faster exams. For that reason, the ClearPEM detector module has high-Z scintillation crystals to improve the detection efficiency of the 511 keV photons and exploits both photoelectric and Compton interactions in the detector improving substantially the detection sensitivity. To be able to detect small lesion dimensions, the system has to have large sensitivity and high resolution, with the aim to increase the signal over background significance. The point source sensitivity of a PET scanner, defined in Chapter 1, depends on three main factors: the subtended solid angle at the symmetry center of the system, the scintillator sensitivity for 511 keV photons and the packing fraction, which is defined as the active crystal area over the total surface of the module. The baseline ClearPEM detector module consists on 32 LYSO:Ce crystals with 2×2×20 $mm^3$ (0.82 interaction probability for 511 keV incident photons) encased in a $BaSO_4$ ($Z_{eff}$ = 56, $\rho$ = 4.5 $g/cm^3$) matrix, readout at both ends by two Hamamatsu S8550-01 4×8 APD pixel

for depth-of-interaction measurement of the incoming photons, in order to achieve the required 2 mm spatial resolution after reconstruction. The packing fraction is 64% and is mainly constrained by the S8550 APD matrix layout and the thickness of the $BaSO_4$ walls.

To increase the detection and light collection efficiencies keeping, as a first approach, the same scintillator type and photodetector, preserving the depth-of-interaction capability, one crystal matrix from Proteus Inc. (Fig. 5.21), with 2.2×2.2×30 $mm^3$ LYSO:Ce pixels (0.92 interaction probability for 511 keV photons) optically isolated by a 3M Vikuiti$^{TM}$ ($Z_{eff} = 10$, $\rho \leq 2$ g/$cm^3$) ESR film specular reflector with 61–68 $\mu$m thickness and 98% reflectivity was evaluated. The packing fraction is 78% which represents an increase in detection sensitivity, which scales with the square of the packing fraction, by about 1.48.

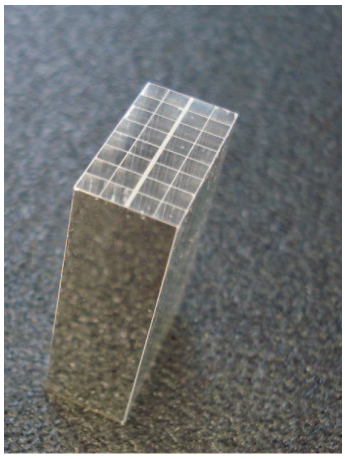

Figure 5.21: Photograph of a Proteus crystal matrix with 2.2×2.2×30 $mm^3$ LYSO:Ce pixels optically isolated by a 3M Vikuiti$^{TM}$ ESR film specular reflector.

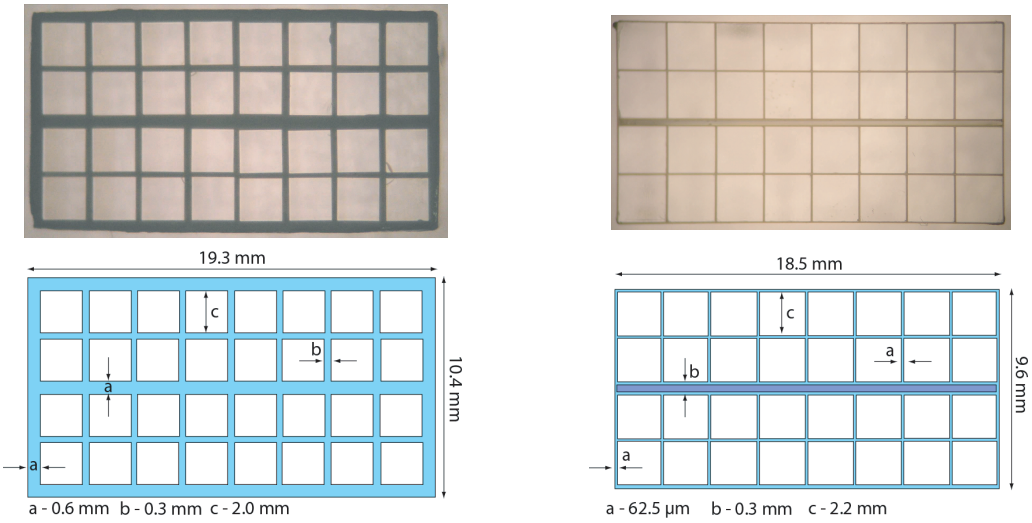


Figure 5.22: (left) End-view of a production-type ClearPEM crystal matrix with 2×2 $mm^2$ cross-section pixels. (right) End-view of a Proteus crystal matrix with 2.2×2.2 $mm^2$ cross-section pixels.

In Fig. 5.22, end-views of a ClearPEM production matrix and the Proteus matrix (also named Vikuiti matrix) are shown, with corresponding dimensons schema.

Vikuiti$^{TM}$ is made of a multilayer polymeric film giving it a very high specular reflectivity for visible and infra-red light. It is suitable for LYSO emission spectra but transparent for shorter wave lengths, as the bandwidth is 415 to 1020 nm. In Fig. 5.23 the spectral response of Vikuiti$^{TM}$ and emission spectra of LSO and LuAP is shown.

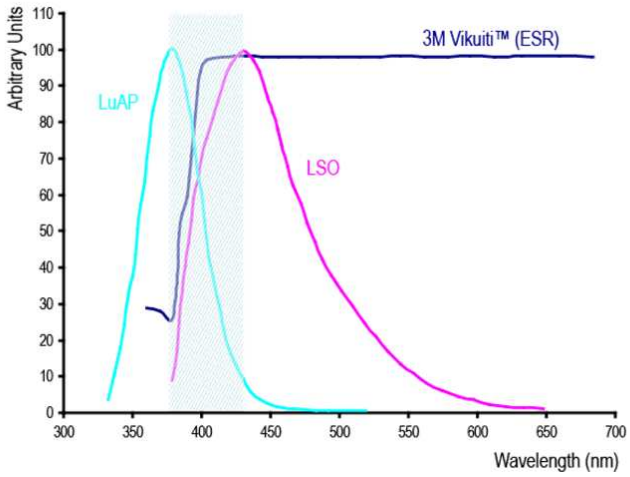


Figure 5.23: Spectral response of Vikuiti$^{TM}$ and emission spectra of LSO:Ce and LuAP:Ce.

The first available Vikuiti matrix had all crystals polished and its performance, in terms of scintillation linearity, energy resolution, light yield and inter-pixel crosstalk, was assessed in dedicated testbenchs using the single readout electronics. Results were compared with the other crystal matrices proposed for the ClearPEM detector module, 32 2×2×20 mm$^3$ crystals wrapped in Tyvek (first matrix version) and encased in $BaSO_4$ (production matrix), measured in the same experimental conditions.

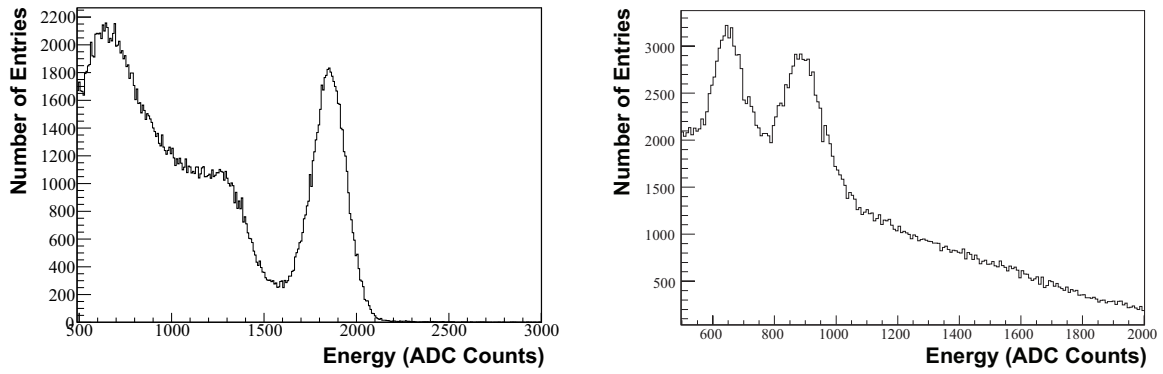


Figure 5.24: Typical spectra for the Vikuiti matrix: $^{137}$Cs (662 keV) spectrum (*reft*) and $^{176}$Lu peaks (202 and 307 keV) (*right*).

In Fig. 5.24, typical spectra for the Vikuiti matrix are shown. It can be seen a well defined photopeak for the $^{137}$Cs (662 keV) source and good resolution to discriminate the two peaks (202 and 307 keV) emitted during the $^{176}$Lu decay.

In Fig.5.25, light yield as a function of the photopeak energy (202 and 307 keV from $^{176}$Lu; 511 and 1274 keV from $^{22}$Na; 662 keV from $^{137}$Cs) for the Vikuiti and ClearPEM production matrices is presented, where can be seen that both matrices have good scintillation linearity. Variation on slope between the two matrices is due to the different light collection. For the Vikuiti matrix, due to the superior energy resolution, photopeak positions at 202 and 307 keV are easily observed. Moreover, for the Vikuiti matrix, a good linearity was found in the 200–1200 keV energy range.

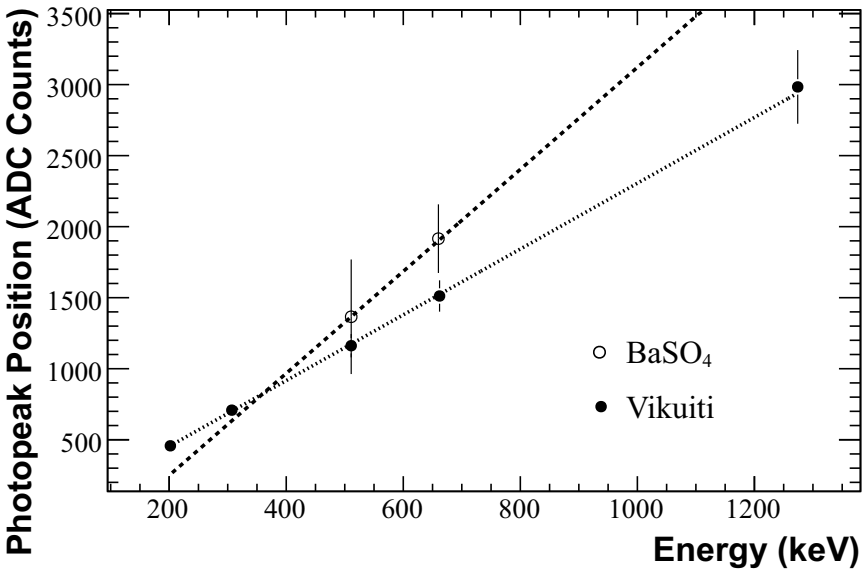


Figure 5.25: Photopeak position as a function of the photon energy for the $BaSO_4$ and Vikuiti matrices.

Photopeak position per pixel, per matrix, are shown in Fig. 5.26. The 2D maps representation enables to realize the homogeneity of the matrices, where results were calibrated in terms of electronic channel gain variation. Mean light yields of the Vikuiti and Tyvek matrices were compared with the ClearPEM production matrix ($BaSO_4$). Vikuiti (1588 $\pm$ 99 ADC channels) presents 20% less light than $BaSO_4$ (1907 $\pm$ 242 ADC channels) but smaller inter pixel dispersion. Tyvek (848 $\pm$ 295 ADC channels) presents 56% less light than $BaSO_4$ and higher inter pixel dispersion.

Energy resolution per pixel, presented per matrix in a 2D map, is shown in Fig. 5.27. Vikuiti matrix (mean value of 12.51 $\pm$ 0.80% at 662 keV) presents an improvement of 11% in energy resolution and Tyvek matrix (mean value of 17.76 $\pm$ 4.62% at 662 keV) presents the highest energy resolution values, 23% worse than $BaSO_4$ matrix (mean value of 14.48 $\pm$ 1.90% at 662 keV).

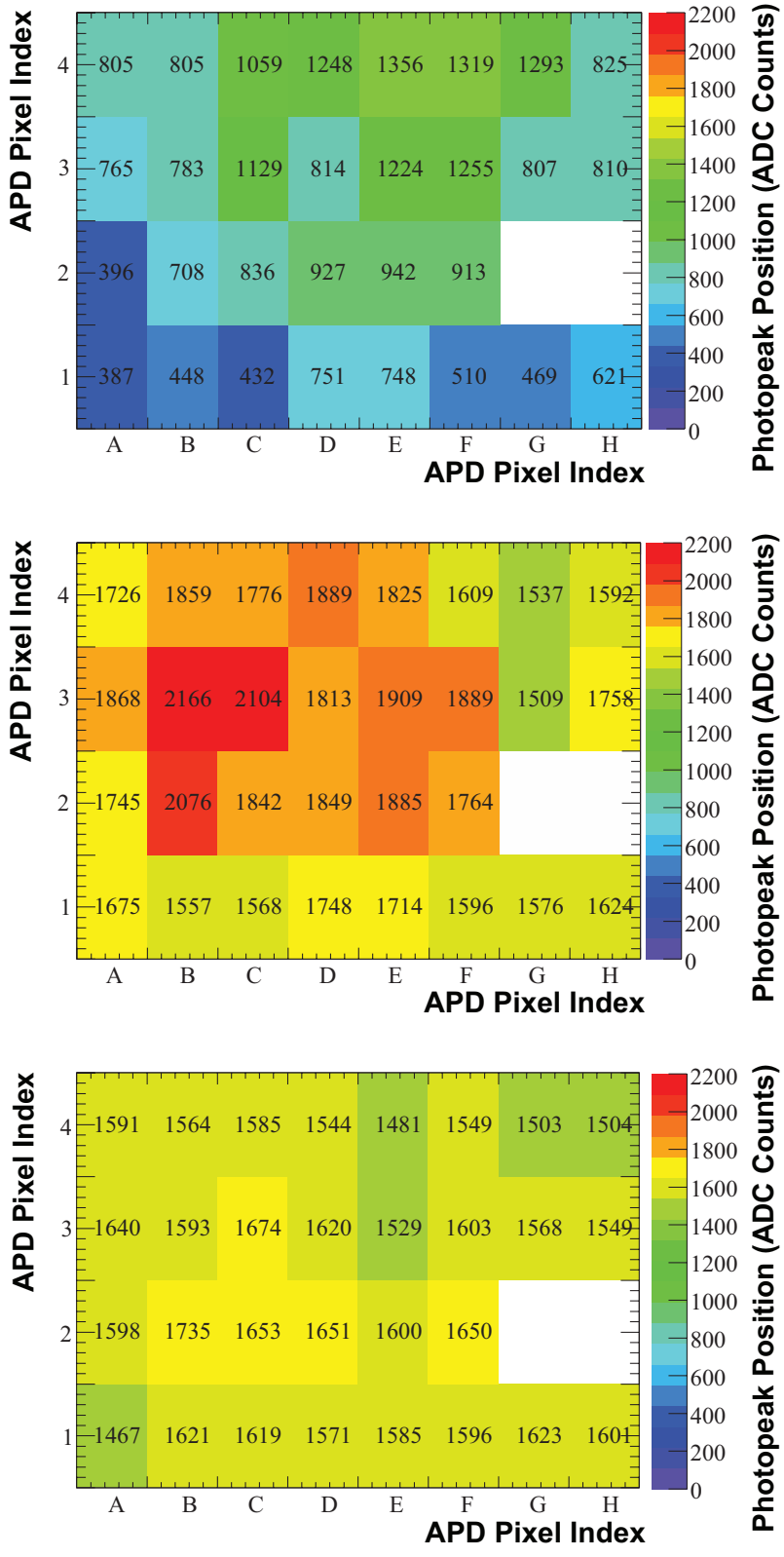


Figure 5.26: Light yield for the 3 matrices: Tyvek (*top*); $BaSO_4$ (*centre*) and Vikuiti (*bottom*) in single readout (two dead channels, corresponding to G2 and H2).

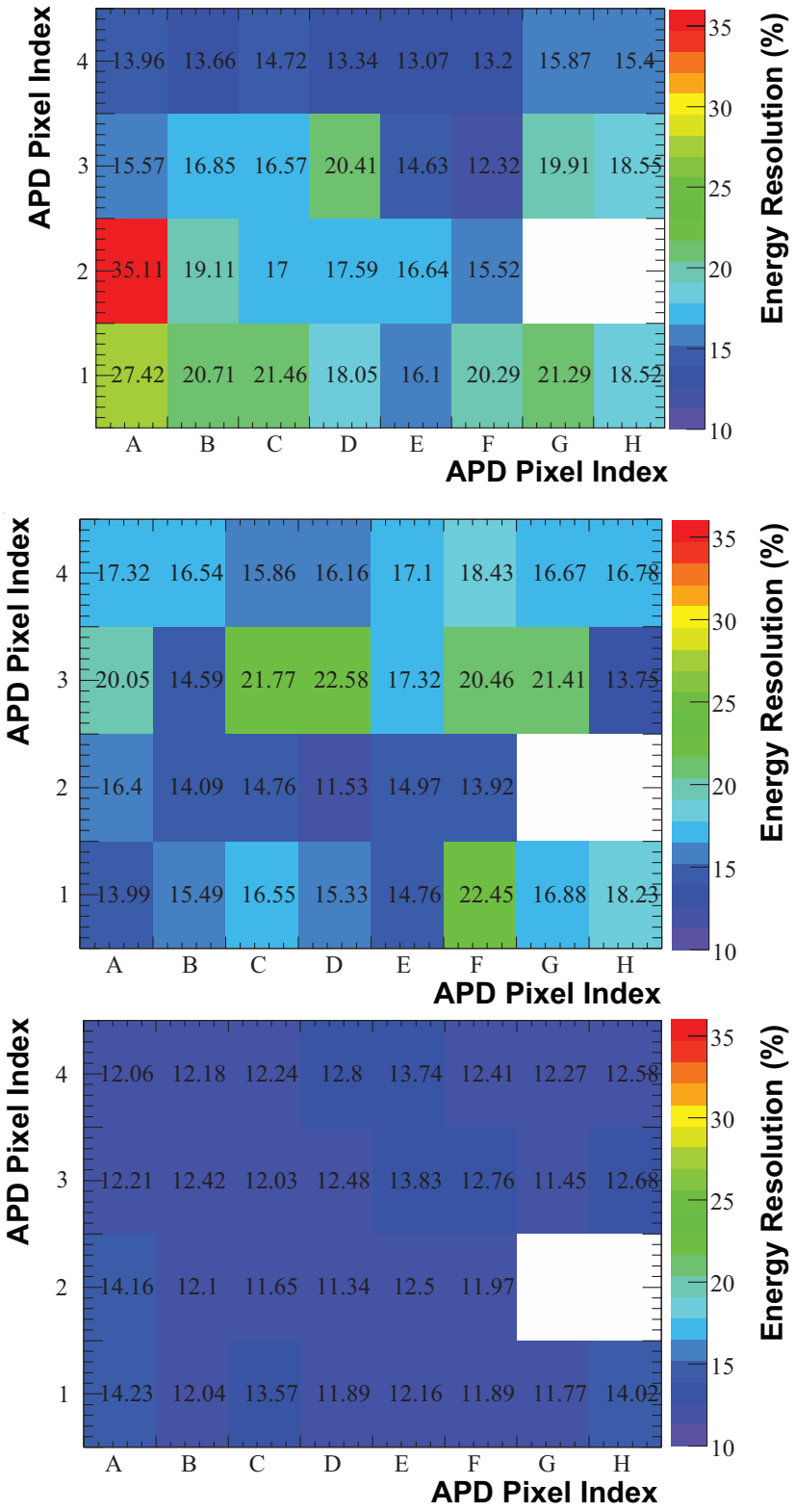


Figure 5.27: Energy resolution for the 3 matrices: Tyvek (*top*); $BaSO_4$ (*centre*) and Vikuiti (*bottom*) in single readout (two dead channels, corresponding to G2 and H2).

In Figs. 5.28 and 5.29, the study of the energy resolution for the Vikuiti matrix is presented. First, it is shown the average energy resolution as a function of the photopeak energy (Fig. 5.28) and secondly, the validation of the previous results by a linear fit (Fig. 5.29) to the energy resolution expression: $(2.35\ \sigma/E) = a/\sqrt{E} + b$. As can be seen, the Vikuiti matrix follows very well the expected behaviour of energy resolution with energy.

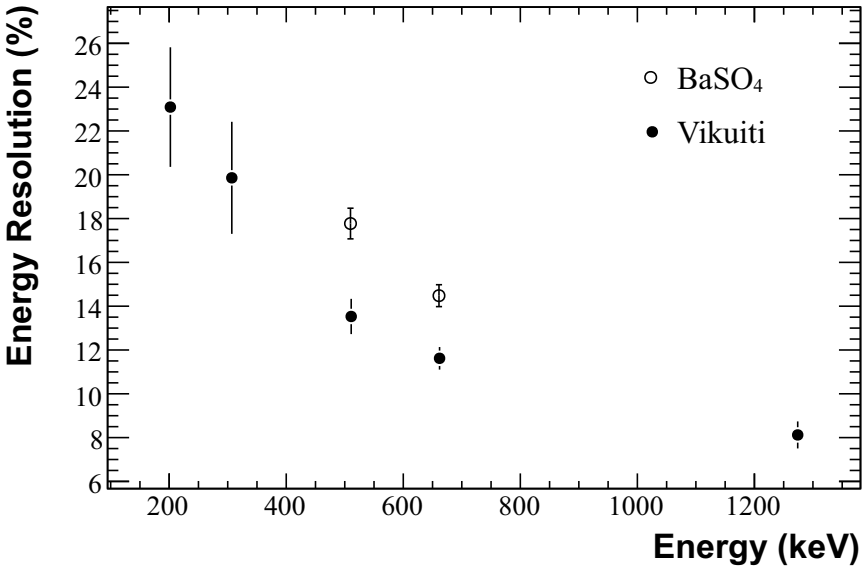


Figure 5.28: Average energy resolution for the Vikuiti and $BaSO_4$ matrices as a function of the photon energy.

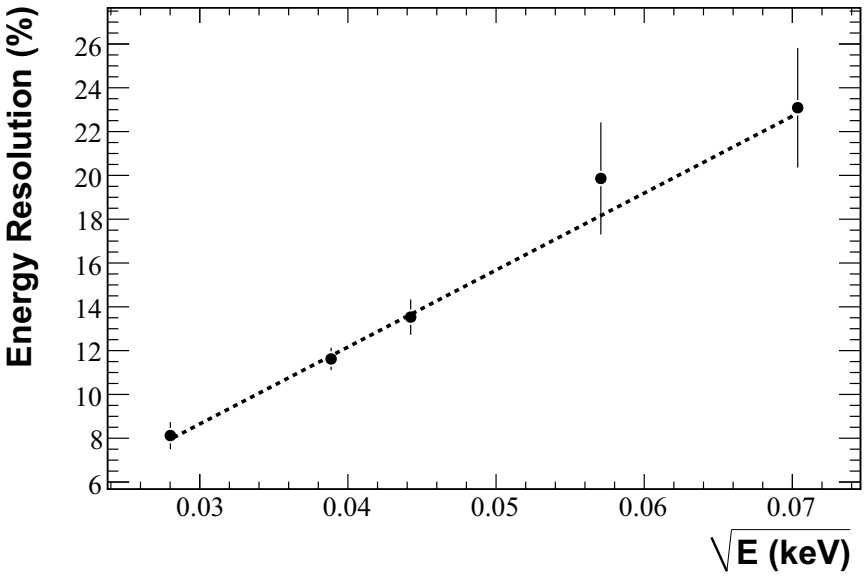


Figure 5.29: Energy resolution for the Vikuiti matrix as a function of $\sqrt{E}$.

Inter-pixel crosstalk is a parameter of concern for the Vikuiti matrix as it has larger crystals (2.2×2.2 $mm^2$) and thinner reflector walls (62.5 $\mu$m). Mismatch with APD, due to pixel size (1.6 × 1.6 $mm^2$), may be more likely. Crosstalk was evaluated for the Vikuiti, $BaSO_4$ and Tyvek matrices in the same conditions and results compared. Data analysis followed the method already described for the single readout mode in Chapter 4, where neighbouring crystals were discriminated as near, if in the same APD sub-array, and far, if in the other APD sub-array. In Fig. 5.30, a schematic 2D view of the crosstalk found for some pixels of the three matrices is shown. Average values are presented in Tab. 5.2, per sub-array and per matrix. Differences in sub-arrays can be seen in all matrices, which is consistent with the APD layout. Similar values of crosstalk between the Proteus (11.93 ± 4.86%) and the $BaSO_4$ (10.73 ± 6.40%) matrices were found. The Tyvek matrix has shown a unfavourable performance in terms of crosstalk (24.10 ± 18.86%). The larger crosstalk value in the Tyvek matrix is consistent to the higher light collection dispersion and worse energy resolution, which may to be introduced by the manual assembly process of the Tyvek detector module where incomplete optical isolation of the crystal pixels may prevail. In this study, crosstalk results are higher than the presented in Chapter 4 for the ClearPEM detector module, where measurements were perfomed in a double readout mode. In the single readout mode, alignment of the matrix crystals with the APD pixels is a manual trial-and-error process, which can induce more crosstalk. This situation does not happen in the final detector module, insured by the double readout configuration and dedicated design cover box in which is assembled.

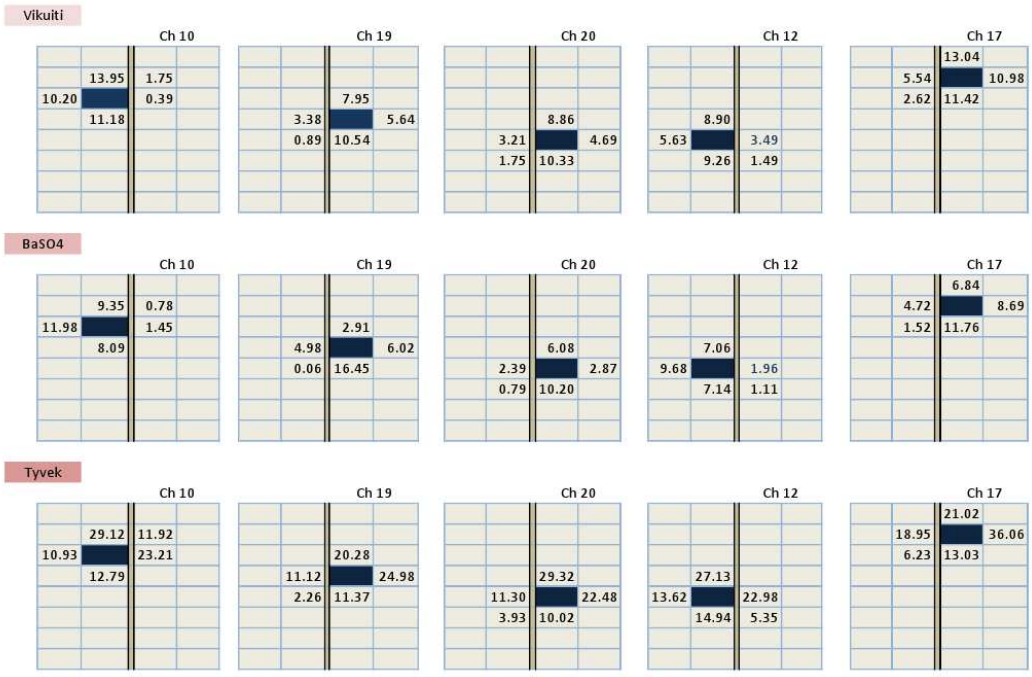


Figure 5.30: Typical 2D crosstalk distributions for the Vikuiti, $BaSO_4$ and Tyvek matrices in single readout. Fired channel marked as blue.

| crosstalk on: | Vikuiti | $BaSO_4$ | Tyvek |
|---|---|---|---|
| $1^{st}$ neighbours near | 12.72 ± 4.34% | 11.49 ± 6.28% | 24.42 ± 19.11% |
| $1^{st}$ neighbours far | 4.77 ± 3.17% | 3.96 ± 1.97% | 21.21 ± 17.18% |
| $2^{nd}$ neighbours near | 3.47 ± 3.47% | 2.73 ± 3.14% | 9.58 ± 9.48% |
| $2^{nd}$ neighbours far | 1.43 ± 1.43% | 0.74 ± 3.15% | 9.02 ± 8.27% |
| $1^{st}$ neighbours | 11.93 ± 4.86% | 10.73 ± 6.40% | 24.10 ± 18.86% |
| $2^{nd}$ neighbours | 2.76 ± 3.24% | 2.06 ± 2.77% | 9.39 ± 9.03% |

Table 5.2: Average crosstalk per sub-array and per matrix.

In overall, the Vikuiti design allows to achieve significant better results that the $BaSO_4$ design in a single readout option. In the double readout configuration, and due to the use polished LYSO crystals together with a specular reflector, DOI information cannot be extracted since there is no mechanism that creates a light collection asymmetry as function of the interaction depth of the photon in the crystal. To overcome this difficulty and as result of the study, other Proteus matrices were manufactured using crystals in which the lateral 30 mm surfaces had different polishing treatments [Rodrigues2008]. In matrices with as-cut crystals, DOI information can be extracted, with a DOI resolution of about 1.7 mm, at the expense of a degradation in the light collection and the energy resolution. Further studies, outside the scope of this thesis, with crystals having a mixture of polished and saw-cut surfaces were carried out. In matrices with two sides polished, DOI resolutions in the 2.3 mm range, with energy resolutions of 16% at 511 keV were achieved, opening the possibility to use this type of detector module design for scanners with double readout schemes.

## 5.4 Prospects for an Improved Multi-pixel APD

Currently, the design of the S8550 APD introduces several design limitations to the detector matrices, namely on the mismatch between the crystal cross section of 2×2 $mm^2$ and the APD active pixel size of 1.6×1.6 $mm^2$. Due to this mismatch, up to 30-35% of the light may be lost, in the interface between the crystal and the APD. This fact and the low gain of the S8550 places an intrinsic limit on the achievable time resolution as well as loss on the total collected charge by the APD, requiring the use of a very low noise, high bandwith and high gain frontend electronics. Due to the crystal size–APD pixel mismatch, the usefulness of crystal matrices with high packing fractions (by instance by using crystals with 2.2×2.2 $mm^2$ cross section) is impaired.

Therefore, a limited redesign of the basic S8550 APD layout was carried out in collaboration with Radiation Monitoring Devices Inc. (RMD) for the development of a improved APD by means of a R&D contract. The new device, called A3220, is a S8550-pinout compatible APD array which incorporates some changes in order to improve its performance in respect to the original Hamamatsu S8550 APD. The most significant technical specifications of this new device is presented in Table 5.3. A photograph of one of the first A3220 samples, delivered in the second half of 2009, is shown in Fig. 5.31.

| Parameter | Value |
|---|---|
| Pixel size | 1.8 mm×1.8 mm (× 32 pixels) |
| Pixel pitch | 2.3 mm |
| Window type | Windowless (bare silicon) |
| Peak sensitivity wavelength | 650 nm |
| Quantum efficiency @ 420 nm | 80–90% |
| Bias voltage operating range | -1750 V up to -1850 V |
| Breakdown voltage | -1860 V |
| Gain regime | 200–1000 (function of bias) |
| Typical bias voltage for gain $M$=200 | -1750 V |
| Maximum gain (requires cooling) | 10 000 |
| Gain gradient @ $M = 100$ | 2%/V |
| Temperature gradient @ $M = 100$ | -3%/°C |
| Dark current (room temperature) | 30 nA (per pixel at $M = 200$) |
| Capacitance | 2.4 pF (per pixel at $M = 200$) |

Table 5.3: Preliminary RMD A3220 APD 32 channel electrical and optical characteristics.

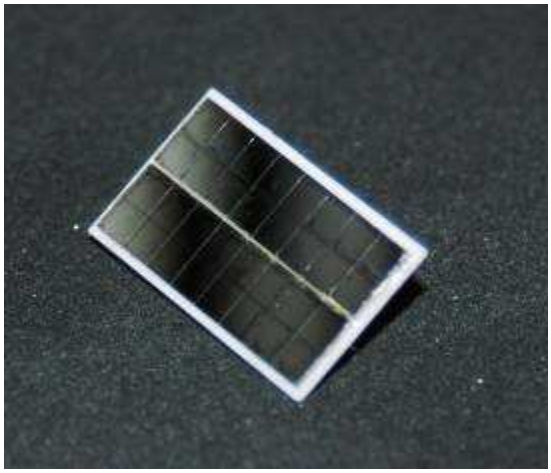

Figure 5.31: Photograph of the new multi-pixel RMD APD A3220.

The new A3220 multi-pixel APD, operates at a higher voltage bias, from -1750V to -1850V, allowing to achieve typical gains from 200 to 1000. Higher gains (theoretical 10 000) are possible according the manufacturer by cooling the APD down to negative temperatures (-22°C). The active pixel die was increased from the original size of 1.6×1.6 $mm^2$ to an extended size of 1.8×1.8 $mm^2$ in order to reduce the pixel-crystal mismatch from the original 36% value to 19%. The overal quantum efficiency was also increased, by means of abandoning the protective epoxy layer used in the S8550. With this windowless approach, quantum efficiency at 420 nm can go up, according to RMD internal measurements, up to 80–90%. Another improvement was the reduction of the pixel capacitance from 10 pF to 2.4 pF, which will allow a theoretical faster response of the frontend electronics, contributing to an improvement of the overall time resolution. Due to the large thickness of the avalanche layer, the excess noise at gain 200 reported by RMD is 2.2 (at

gain 50, the S8550 has an excess noise factor of 1.85, as shown in Chapter 3).

The major drawback of the A3220 is the high HV (typically -1800V) that is required to polarize the APD. Such characteristic demands a re-design of the original ClearPEM high-voltage system, due to the need of larger PCB traces clearances, both in the frontend boards and HV supply system. A second factor that must be taken into account is the probability of breakdown of the dielectric air medium between the APD HV and signal pins. In order to reduce the probability of such occurence, the APDs must be operated in a controlled humidity. This can be easily achieved by pressuring the detector housing with $N_2$ gas.

While the 16 pixels of one sub-array of the S8550 APD have a common cathode, the A3220 is built in a common anode configuration. This means that the obtained pulses have negative polarity, being incompatible with the current ClearPEM frontend ASIC. This has motivated the design of a new ASIC, which can accommodate both polarities. The gain of this new ASIC may also be programmed in order to fit the different typical gains of the S8550 and the A3220 APD. The ASIC development is currently being performed by INESC–ID and INFN–Torino and the first 32 channel ASIC demonstrator is expected to be received from foundry in early 2010.

## 5.5 Summary and Discussion

The ClearPEM scanner was designed with the goal to optimize both the detection sensitivity of 511 keV photons as well as the spatial resolution along the entire FOV. Such requirements have led to the adoption of a basic sensitive volume comprehended by 2×2 $mm^2$ fine pitch LYSO:Ce crystals coupled to a double readout based on 1.6×1.6 $mm^2$ multi-pixel APD array.

On this type of readout, light collection can be impaired by the long path that the optical photons need to travel before can exit the crystal, due to the reduced crystal cross-section (2×2 $mm^2$) in comparison with the crystal length (20 mm), which increases the cumulative probability of being attenuated inside the crystal, the optical coupling media used to create an appropriate intermediate layer with a refractive index that maximize the probability of the photon and the photosensor pixel sensitive area in relation to the crystal cross section.

Besides the light collection aspect, the detection sensitivity of the scanner is also a parameter of concern. In crystal pixel-based modules, the packing fraction is generally reduced due to the compromise between reflector thickness and light collection isolation. Since the detection sensitivity of 511 keV photon pairs follows the square of the packing fraction, marginally improvements in the packing fraction may introduce significant gains on the scanner performance, allow to achieve higher values lesion detectability in shorter time exams. The crystal length is also a parameter that can be optimized. Usually, in scanners without DOI interaction capability, the length of the crystal is sub-optimal to

avoid the introduction of the parallax effect. In the ClearPEM case, 20 mm crystals can be used since the double readout scheme allows to extract the DOI coordinate with a resolution better than 2 mm, minimizing the effect of the parallax effect while offering a moderate detection efficiency for 511 keV photons.

In this chapter, the optimization studies on several of these aspects were reported. Triggered by the long-term stability issues of the optical coupling initially selected, based on a silicon grease (Paste 7), permanent optical glues were explored in terms of the light collection, energy resolution and DOI resolution. Three options were explored: Meltmount, RTV 3145 and Histomount. Initial tests with Meltmount shown a superior light collection capability over grease, with a gain up to 30% and a significant improvement in the light collection asymmetry (from 4%/mm up to 5.5%/mm). Long-term stability measurements did not shown for any decrease of light collection with time. The main issue with this optical glue was the need to perform the modules mounting and un-mounting at high temperature, slightly above 65°C. At this temperature, manual manipulation of the detector module is more difficult leading to the formation of air bubbles in the application phase. These bubbles can introduce a systematic asymmetry in the light collection between the top and bottom APDs, which in turn lead to a degradation of the energy resolution. RTV 3145 glue was explored in order to circumvent some of these difficulties. While this glue is routinely used to mount detector matrices to PMT glasses, it was found that the un-mounting procedure requires some mechanical force after 24 hours embedding in acetone. This procedure can be a hazard to delicate surfaces such as the APD epoxy and therefore the RTV 3145 was discarded. Histomount mounting media was then explored. This medium was one of the best choices initially explored for the CMS ECAL subdetector, for the gluing of 5×5 $mm^2$ APDs to PWO crystals. It was rejected due to curing problems. Histomount relies on the evaporation of a organic solvent, named xylene. In large areas, like the 5×5 $mm^2$ APD pixel for CMS, curing would only be completed after 55 days after initial application. The toxic nature of xylene was also a problem since the application of large quantities of the compound (around 120 000 APDs) requires the use of a controlled-air chamber. These problems have a very different magnitude in the ClearPEM case since the application area is small. Tests with Histomount have shown a similar performance to Meltmount in terms of the light yield (20–30% improvement) and DOI resolution (5.5–6%/mm). Energy resolution was systematic better than grease, largely out-performing the Meltmount module energy resolution. As result of this work, it was decided to re-assemble all ClearPEM matrices with Histomount. Currently, a second ClearPEM scanner, named ClearPEM–Sonic, which combines the Clear-PEM technology with an Ultrasound imaging device, is being built. The camera will be used for evaluation of correlations between different radiotracer uptakes and nodule elastometric parameters for breast cancer. Performance results of the ClearPEM detector using the Histomount modules will be shown in detail in Chapter 6.

While the optimization of the optical coupling media led to a good stability in the light collection, with direct consequences in the obtained energy, DOI and time resolution, optimization studies of the detector module packing fraction and detection efficiency were also carried out. The initial approach consisted on the exploration of a novel matrices

design, manufactured by Proteus Inc, composed by LYSO crystals with cross-sections of 2.2×2.2 mm2, with 30 mm length, optically isolated by a layer of Vikuiti$^{TM}$ specular reflector with 61–68 micron thick. The reduction on the optical layer thickness from 300 $\mu$m in $BaSO_4$ to 70 $\mu$m with the Vikuiti$^{TM}$ reflector, together with the larger crystal cross-section, allows increasing the packing fraction up to 90%, a gain in detection sensitivity of about a factor of 1.48. When the crystal length of 30 mm is taken into consideration, the overall detection sensitivity gain goes from 1.48 to 2.1. Characterization results have shown that matrices with this design, using polished crystal, in a single readout, achieve better energy resolutions (12.5% at 662 keV) in comparison with the mean energy resolution of the standard ClearPEM $BaSO_4$ modules (14.5% at 662 keV) and Tyvek based modules (17.8% at 662 keV). A smaller light collection dispersion between different pixels was also found (6.2%) in comparison with the $BaSO_4$ (12.7%) and Tyvek (34.8%) matrices. With the use of crystals with larger cross-section, there was a concern on the increase of the crosstalk, since the larger crystal dimension make more prone a given crystal being readout by two different pixel APD. Crosstalk was evaluated for the Proteus, $BaSO_4$ and Tyvek matrices. Similar values of crosstalk between the Proteus and the standard $BaSO_4$ matrices were found. The Tyvek matrix has shown a sub-optimum performance in terms of crosstalk (24.1%). In overall, the Proteus design allow to achieve significant better results that the $BaSO_4$ design in a single readout option. In the double readout option, and due to the use polished LYSO crystals together with a specular reflector, DOI information cannot be extracted since there is no mechanism that creates a light collection asymmetry as function of the interaction depth of the photon in the crystal. To bypass this difficulty, matrices, following the Proteus design, were manufactured using crystals in which the lateral 30 mm surfaces were leaved as-cut. In this approach, DOI information can be extracted, with a DOI resolution of about 1.7 mm, at the expense of a degradation in the light collection and the energy resolution. Further studies, carried out outside of the scope of this thesis, were conducted with crystals having a mixture of polished and saw-cut surfaces coupled to Vikuiti$^{TM}$. In matrices with two sides polished, DOI resolutions in the 2.3 mm range, with energy resolutions of 16% at 511 keV were achieved, opening the possibility to use this type of detector module design for scanners with double readout schemes.

Chapter 6

# ClearPEM Detector Head Validation

## Contents

## 6.1 Introduction

Before the final integration of the ClearPEM scanner was completed, several partial integration and engineering runs were carried out at TagusLIP (Chapter 2). One of the most important activities consisted on the validation of the supermodules, each unit comprehending a set of twelve detector modules, whose individual performance was measured in dedicated discrete electronics setup described in the previous chapters, to characterize its performance before the final assembly of the supermodules inside the ClearPEM detector heads could took place. The tests of the supermodules allowed to assess the performance of the detector modules in their final working environment, combining instrumentation effects introduced by the frontend electronics readout and the processing of the data flow by the data acquisition electronics and trigger system, allowing a direct comparison with the previous results obtained in limited discrete electronics test benches as reported in Chapter 3 and in [Moura2005]. After the validation of each individual supermodule, the final assembly of the ClearPEM detector heads was carried out.

The present chapter is organized as follows: First, the spatial organization of the individual detector modules in the larger logical structures called supermodules, carried out in the scope of this thesis, is presented. This organization was performed by taking into account the compromise between the different high voltages required to operate each one of the 384 Hamamatsu S8550 APDs at gain 150 and the fact that each detector head has 384 HV lines than can be grouped in 32 independent sets. Second, the assembly and test of the supermodules in a stand-alone test bench is reported. Results were compared with the expected values from the initial characterization phase. The supermodules were inserted in the ClearPEM detector heads and its behaviour characterized in terms of energy resolution, DOI resolution, light collection, linearity and time resolution. The spatial resolution of the system was then measured with a $^{22}$Na source. A preliminary evaluation of the system sensitivity was also performed. Finally, these results are discussed in terms of the initial performance requirements layout for the scanner, at the light of early stage breast cancer detection, as discussed in Chapter 1.

## 6.2 Detector Modules Organization in Supermodules

The organization of the each detector module in the ClearPEM detector heads was conducted by exploring the modularity of the architectural design of the detector. Crystals are grouped in a set of 192 matrices and groups of two matrices are assembled in a detector module (Chapters 2 and 3). Since the detector modules are assembled in two detector heads in a planar arrangement, a mechanical structure called supermodule, grouping 12 detector modules placed between a top and a bottom Frontend board, was conceptualized [Trindade2008].

The Frontend boards corresponds to the first level of signal processing performed by a low noise and high gain ASICs that carry out the readout, amplification, sampling and storage in analogue memories of the APD output channels signals. Analogue Digital Con-

verters (ADCs) digitize the output analogue sampled pulses and Low Voltage Differential Signaling (LVDS) Channel Link transmitters serialize the data to the off–detector system over a 2.5 Gbps link [Albuquerque2006]. Each ClearPEM detector head has 16 independent supermodules in a total of 96 detector modules - Fig. 6.1. The Frontend system is physically located on the detector heads as close as possible to the detector modules in order to minimize noise and keep the compactness of the full system. For that reason, it is one of the most challenging and innovative sub-system of the ClearPEM detector. It is composed by the Frontend Boards (FEBs) interfacing directly with the APDs assembled in the detector modules and one Service Board in each detector head, for clock and power supply distribution, bias voltage regulation and temperature monitoring surrounding the APDs inside the detector heads. Two FEBs, each one with two 192 channels ASICs, are used to mount one supermodule structure with a total of 768 electronic channels, as illustrated in Fig. 6.2.

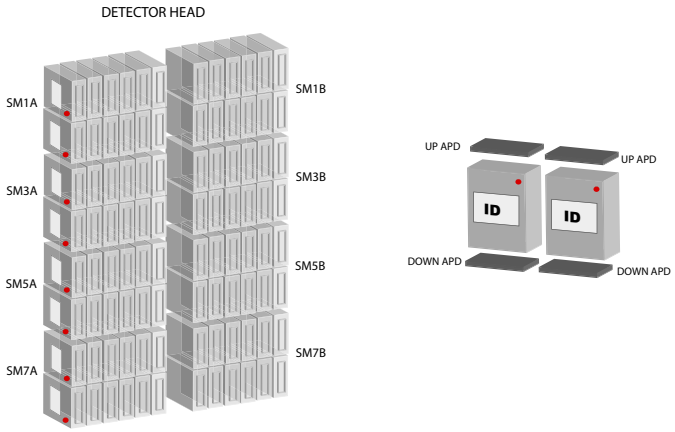


Figure 6.1: Scheme of the structure of one detector head (*left*). Double detector modules (*right*) are grouped in a total of 8 supermodules.

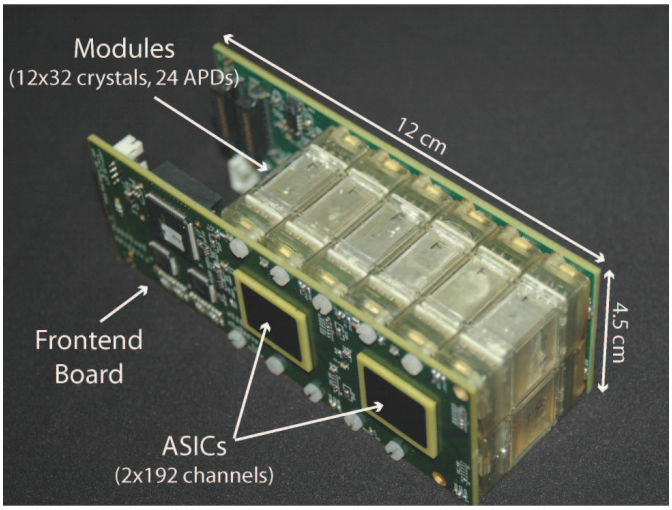


Figure 6.2: Photograph of a fully assembled supermodule.

In each detector head, 8 supermodules needs to be supplied with 3.3V low voltage lines for the frontend ASIC, ADCs and Channel Link chips. In addition, each APD sub-matrix needs to be polarized. The regulation of the required high voltage is performed in the Service Boards (one per detector head). Each Service Board is placed on the backside of the detector head, and integrates 32 HV independent regulation channels to supply the APDs (Chapter 1, Section 1.3), with a range regulation between 350 to 500 V and stability better than 0.1% r.m.s [Pinheiro2008].

Due to space limitation in the Service Board PCB, only 32 independent HV regulation channels were implemented. However, a total of 384 HV lines per detector head (192 APDs) are needed. Since the S8550 is composed of two independent sub–matrices that need to be biased, a connection matrix placed above the Service Board provides inter–connections between the 32 independent HV channels and the 384 HV output lines – Fig. 6.3. The 32 independent HV channels have therefore to cover a range that includes all APD HV values for a given gain. The APD HV values were binned per independent HV channel and the HV connection matrix is programmed by soldering establishing a direct correspondence between the APD HV and the HV bin.

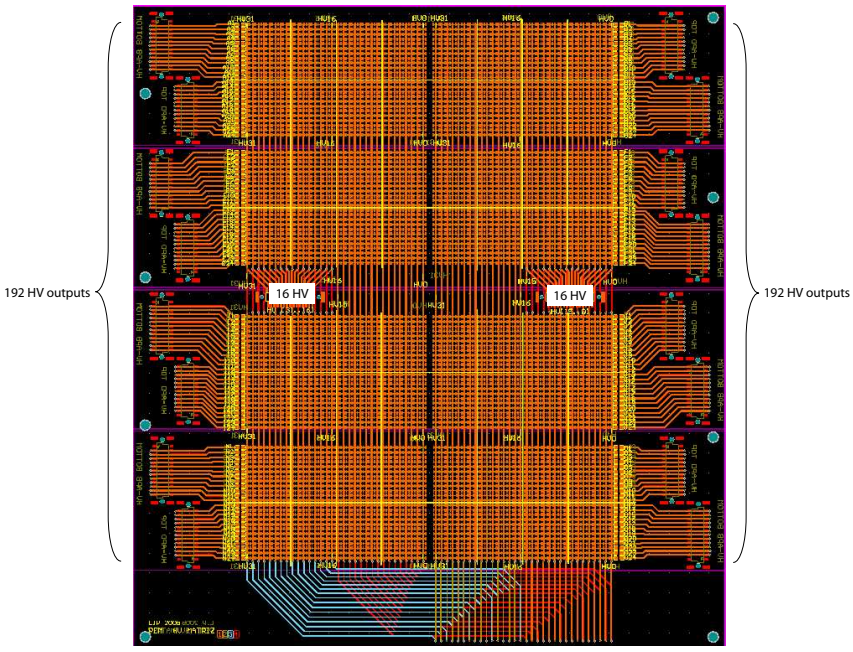


Figure 6.3: CAD overview of the HV interconector matrix.

To carry out the programing of the HV connection matrix the values of the HV required to polarized each APD sub-matrix for gain 150 were examined. Tab. 6.1 shows the main characterization parameters, obtained during the APD QC phase, for the 384 APDs used in the ClearPEM scanner [Carriço2006].

| Bias Voltage | Sub–Array 1 (V) | Sub–Array 2 (V) |
|---|---|---|
| Average ± r.m.s. | 434 ± 22 | 434 ± 21 |
| Minimum | 375 | 379 |
| Maximum | 473 | 474 |
| Gain Variation | Sub-array 1 (%/V) | Sub-array 2(%/V) |
| Average ± r.m.s. | 6.3 ± 1.8 | 6.0 ± 0.8 |
| Minimum | 5.4 | 5.4 |
| Maximum | 26.5 | 19.4 |

Table 6.1: ClearPEM Hamamatsu S8550 APDs HV and gain gradient distribution range for gain 150.

As it can be observed, at gain 150, the maximum variation in the polarization HV can amount up to 98 V. If the APDs were placed randomly in each detector head, then each independent HV channel in the Service Board would have a bin width of about 3.2 V. Since the mean gain gradient ($dM/dV$), or variation of the APD gain per Volt, at gain 150 is of about 6%/V this would mean that APDs connected to the same HV bin could have gain differences over 20%. To reduce this effect the APDs were splitted in two classes, denoted as "Low" and "High". The "Low" class is characterized by 32 HV bins ranging from 375 V to 437 V – Fig. 6.4. The "High" class is characterized by 32 HV bins ranging from 411 V to 473 V – Fig. 6.5. This yields a bin size of 1.93 V, for both classes. In this case, the mean gain variation for two APDs atributed to the same bin would be less than 12%. At gain 150, about 5% of the 384 APDs have a $dM/dV$ above 10% (Fig. 6.6. This indicates that in the some cases, 20% differences in gain are expected. As a consequence the broadning of the inter–pixel calibration, $k_{rel}$, (Chapter 3) will be higher. Nevertheless, they can be compensated both on the hardware and software trigger by means of a suitable calibration procedure [Frade2009].

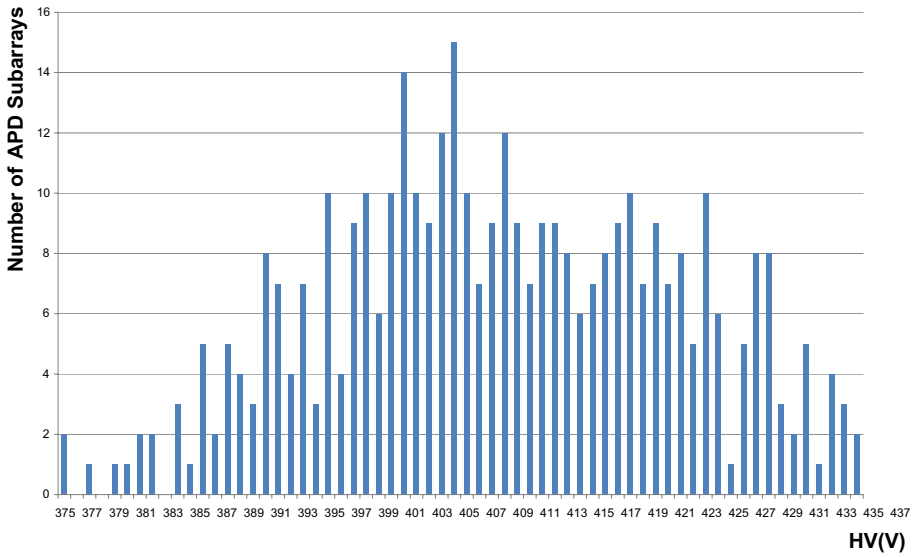


Figure 6.4: HV distribution (gain 150) for the "Low" class detector head.

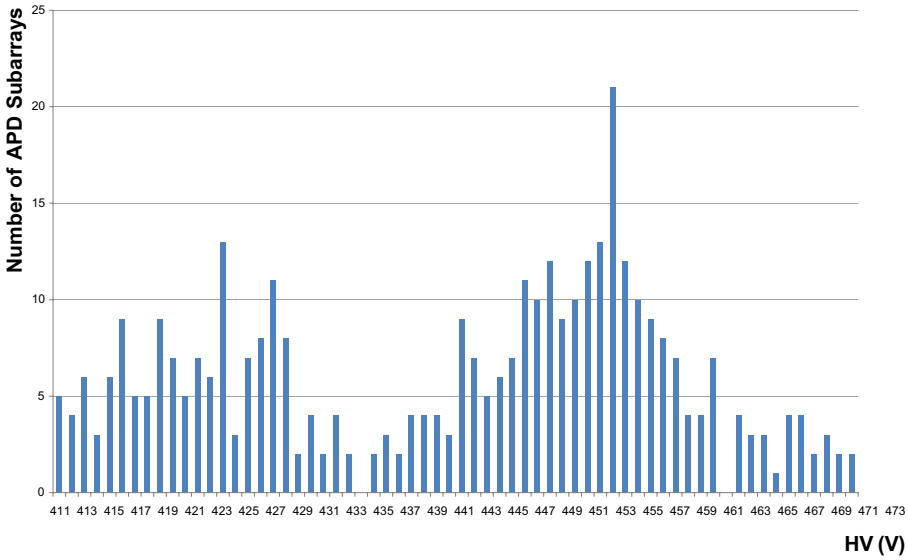


Figure 6.5: HV distribution (gain 150) for the "High" class detector head.

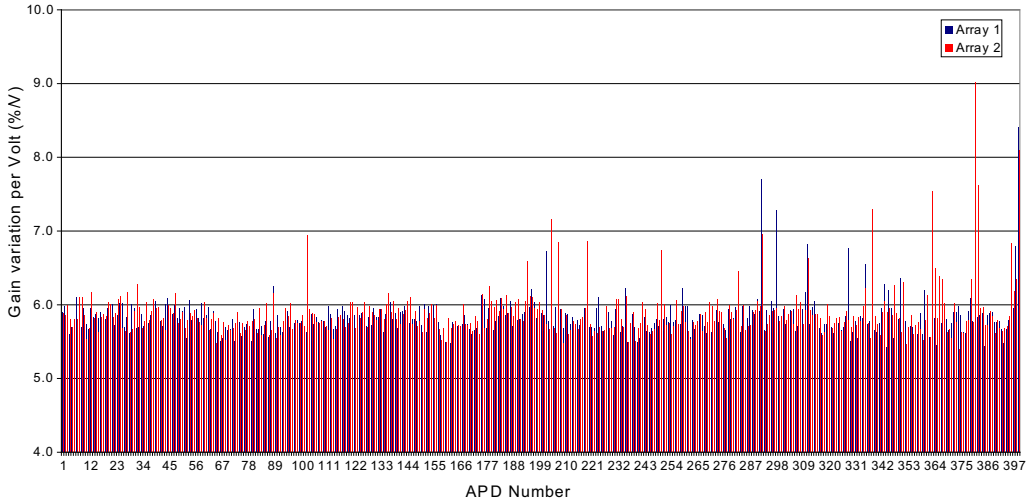


Figure 6.6: Distribution of the $dM/dV$ at gain 150 for each measured APD. Both subarrays are shown.

## 6.3 Experimental Measurements of Individual Supermodules

The validation of the ClearPEM supermodules is an important quality control step that guarantees that the desired performance of the ClearPEM detector can be obtained. It should be noted that all the LYSO:Ce crystal matrices were glued to the APDs using the National Diagnostics Histomount media, replacing the Rhodorsil Paste 7 silicon grease that has shown signs of accelerated aging (Chapters 3 and 5). The individual calibration of

the supermodules can be a good indicator of its performance, providing a first indication of the relative gain between top and bottom APDs, the absolute gain and the energy resolution and the DOI light collection asymmetry constant. Pulse shape parameters for each APD-ASIC readout channel were also determined, but will not be present since they fall outside the scope of this thesis (see [Pinheiro2008, Frade2009]).

The supermodules were tested in a setup that integrates the electronics and data acquisition sub-systems as it will operate in the fully assembled detector. The cooling system was a small version of the final system and is capable of cooling one supermodule. In the ClearPEM scanner, heat dissipated by the ASICs, ADC and serializers is removed by means of water-cooled dissipation plates in thermal contact with the FEBs. A similar approach was used in this testbench, were the FEBs are in thermal contact via a gap filler with two alumminium plates (Fig. 6.7). These plates are cooled by running water at 20°C. This setup can be taken as a small scale ClearPEM demonstrator as the experimental testbench that was setup to characterize the supermodules uses all the different electronic sub-systems developed for the ClearPEM scanner. The input clock, for the tests described in this work was set to 50 MHz. The system clock is generated in the L1 data acquisition electronics TGR/DCC board and fanout by a dedicated board, before arrival to the supermodule FEBs (Fig. 6.8).

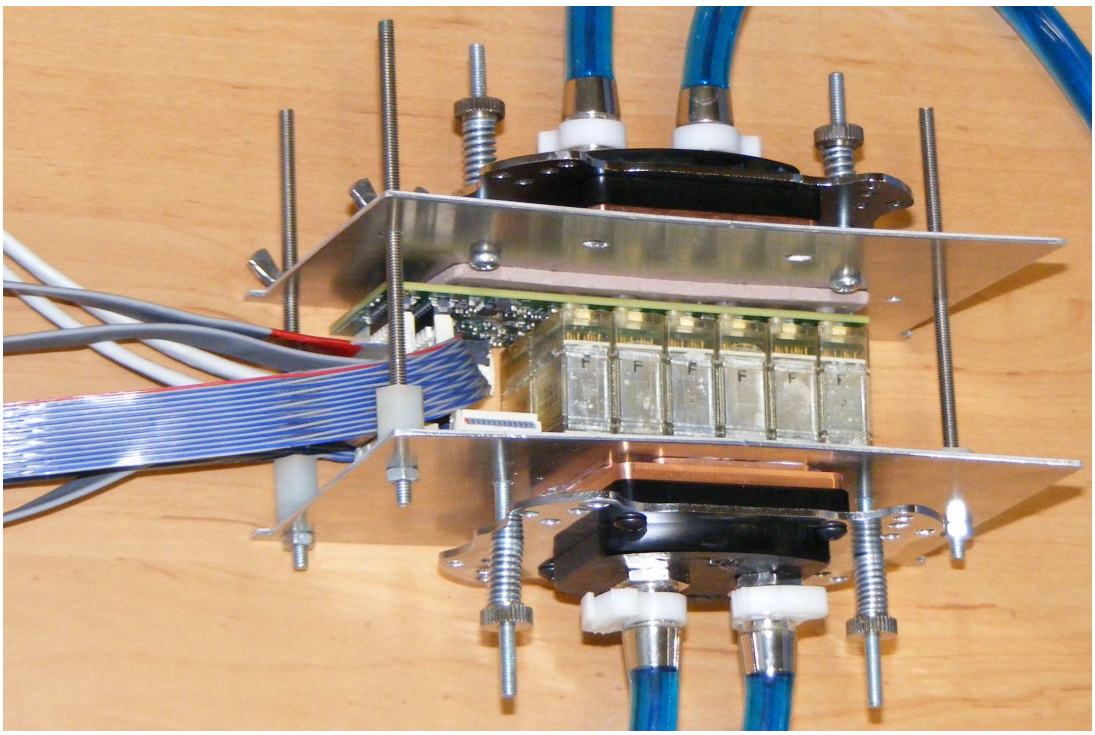

Figure 6.7: Photograph of the supermodules characterization testbench.

The serialized output of the supermodule FEB boards was connected to one of the DAQ Boards of the L1 trigger (Chapter 1, Section 1.3). The trigger was operated in single photon mode, which means that all accepted events above the L1 energy threshold (set at 200 keV) are readout to the data acquisition server.

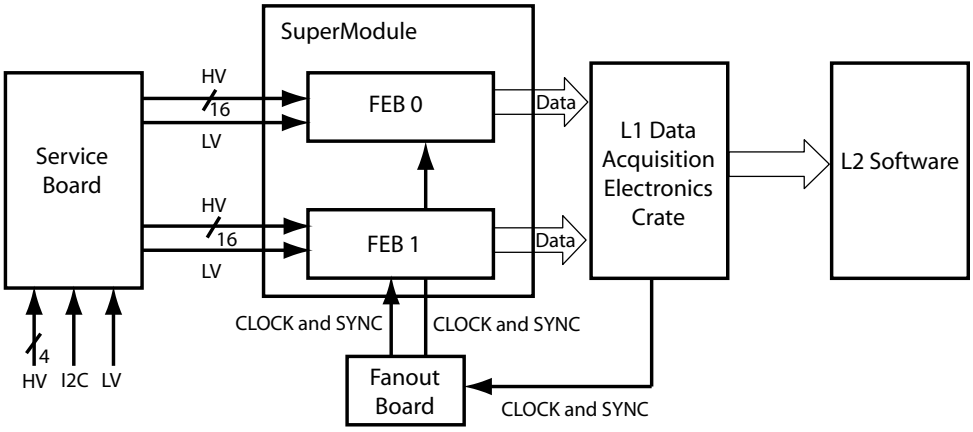


Figure 6.8: Scheme of the supermodules characterization testbench.

For the validation of each supermodule, $^{176}$Lu background decay, $^{22}$Na and $^{137}$Cs (Chapter 3) data acquisitions were performed. The validation takes into account the values of the calibration constants (if they are within an expected range) and the quality control parameters (for example, energy resolution).

From the set of 16 supermodules that were individually measured, 3 typical supermodules are shown (SM2B, SM4B and SM6A) and results compared with the previous measurements reported in Chapter 3 with the aim to detect a possible performance degradation due to the adopted binning HV scheme and readout electronics. As mentioned earlier, APDs have a lower gain (less than 200), in comparison with standard PMTs, that demanded the design of a specific frontend ASIC [Rodrigues2009]. The ASIC must be low noise and has high gain. These requirements pose a very specific challenge, aggravated by the fact the ASIC itself must be mounted on high density frontend boards which require a careful layout for electromagnetic compatibility with the ASIC to avoid noise pickup from, for example, the digital activity from the ADCs or the Channel Link serializer. If the PCB layout is not able to cancel this noise contribution, the physics performance of the SM could be affected, which stresses the importance of this QC phase. The analysis of the remaining supermodules is currently undergoing. The physical observables that characterize the mentioned supermodules were:

- Inter–pixel gain variation
- Photopeak position at 511 keV and linearity
- Energy resolution at 511 keV
- DOI asymmetry

### 6.3.1 Inter–pixel Gain Variation

The results obtained for the relative gain ($k_{rel}$) for the SM2B, SM4B and SM6A supermodules are summarized in Tab. 6.2 and shown in Fig. 6.9. The relative gains of the 3

supermodules have a dispersion comprehended between 14 and 17%, which is consistent with the reported value of 13%, when using a discrete electronics testbench (Chapter 3).

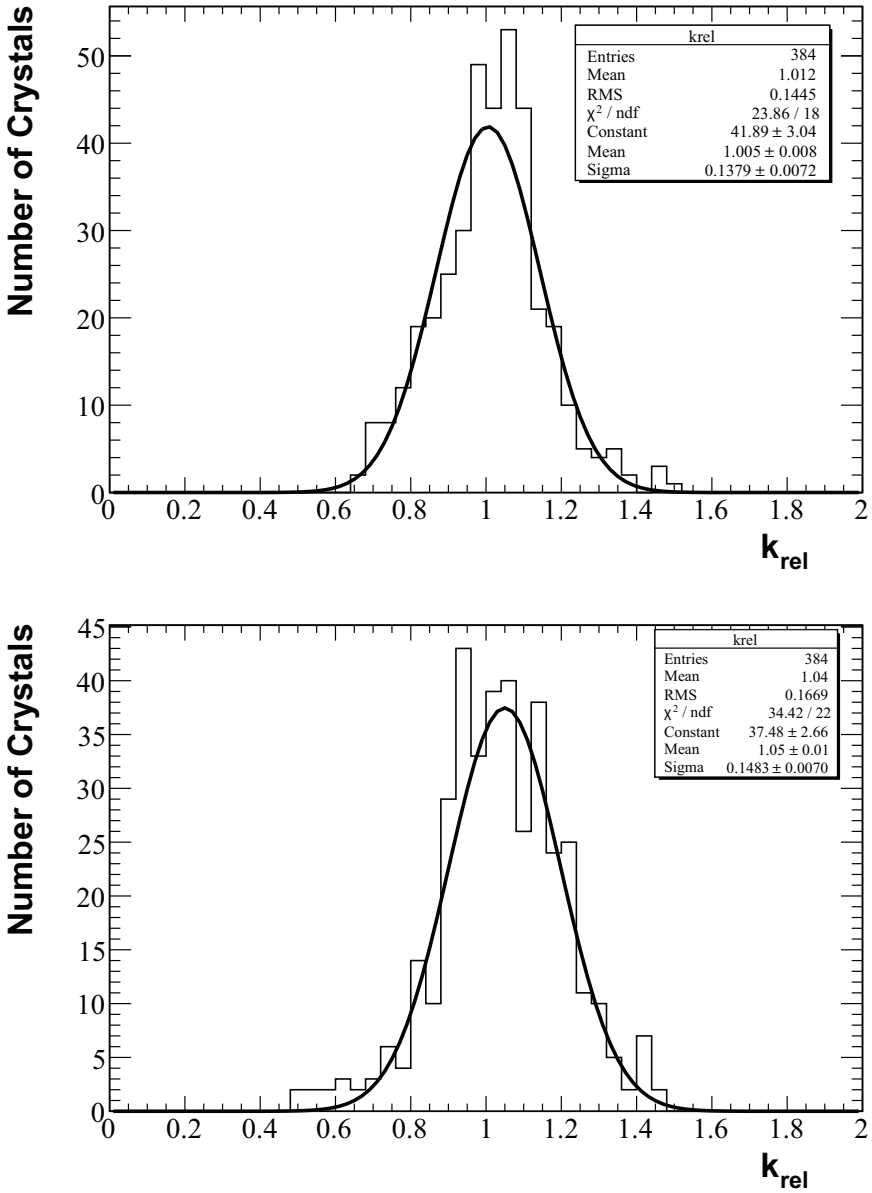


Figure 6.9: Distribution of the inter-pixel $k_{rel}$ gain for SM2B and SM4B.

| Supermodules | Mean $k_{rel}$ | Dispersion |
|---|---|---|
| SM2B | 1.012 | 14.3% |
| SM4B | 1.040 | 16.0% |
| SM6A | 1.099 | 16.9% |

Table 6.2: Results (mean and dispersion) for the inter-pixel $k_{rel}$ for supermodules 2B, 4B and 6A.

### 6.3.2 Photopeak Position at 511 keV and Linearity

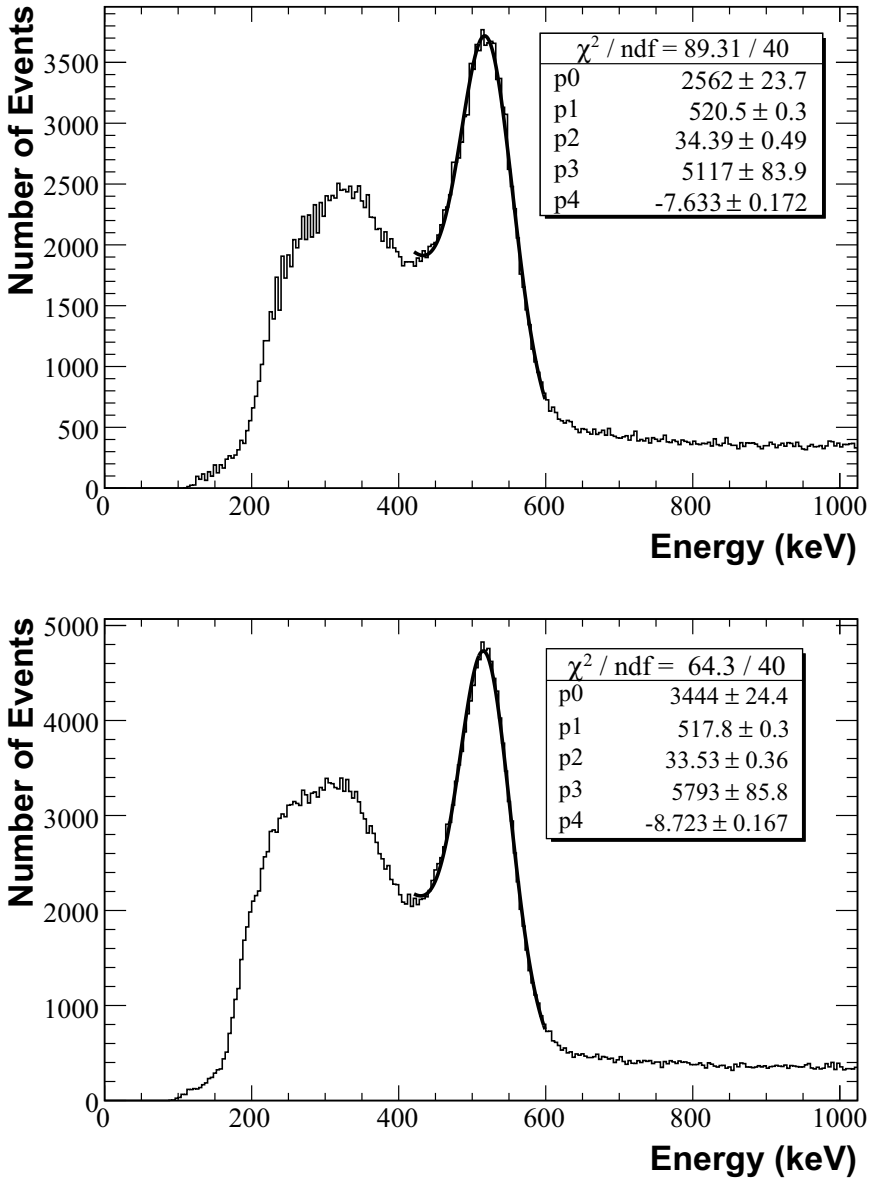


Figure 6.10: Typical calibrated pulse height spectra obtained with the $^{22}$Na source, from a crystal of the SM2B.

Fig. 6.10 shows typical pulse height spectra obtained with the $^{22}$Na source. A well defined 511 keV photopeak is observed with energy resolutions of 15.5% (Fig. 6.10 (a)) and 15.2% (Fig. 6.10 (b)). In this plot set, the 511 keV photopeak position in ADC counts was converted to a physical energy value in keV through the application of a calibration constant $K_{Abs}$. This constant provides an absolute gain calibration, compensating for the different light yield between crystals. Typical distributions for the three supermodules (SM2B, SM4B and SM6A) are shown in Fig. 6.11 and Tab. 6.3.

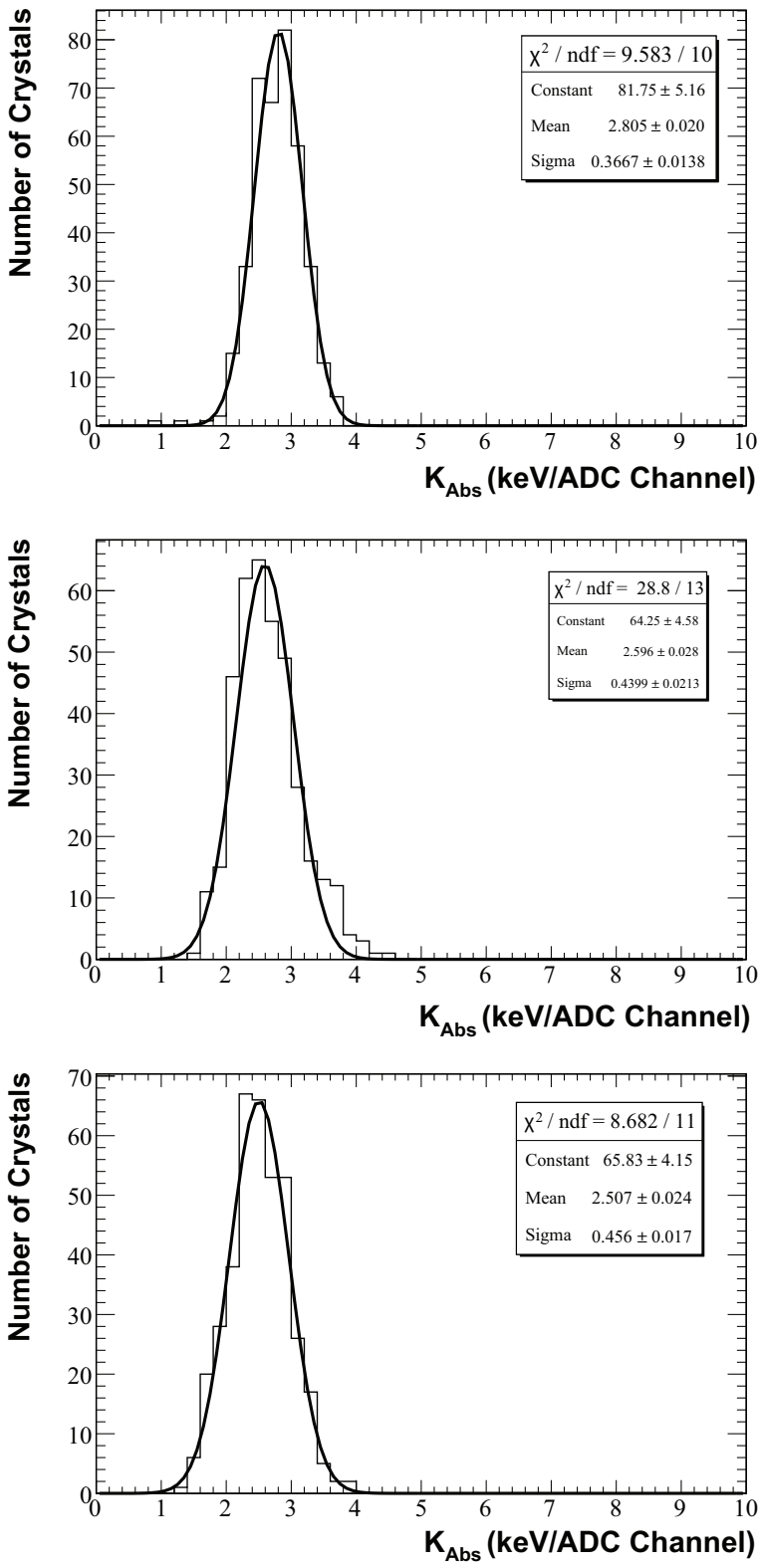


Figure 6.11: Distribution of the absolute gain, $K_{Abs}$ for three supermodules: SM2B (*top*), SM4B(*centre*), SM6A (*bottom*).

The $K_{Abs}$ dispersion (r.m.s. over the mean value) for the three supermodules vary between 13% and 18%. These results are in good agreement with the photopeak variability (16.34% dispersion) measured in individual detector matrices (Chapter 3, Section 3.4).

Energy linearity, or variation of the photopeak position in ADC counts as function of the energy of photon was also assessed. Four distinct photopeak positions were used for this analysis: 303 keV from the $^{176}$Lu background decay (Fig. 6.13, *top*), 511 keV from the $^{22}$Na decay (Fig. 6.13, *centre*), 662 keV from the $^{137}$Cs decay (Fig. 6.13, *bottom*) and finally the 1.2 MeV line from the $^{22}$Na decay. A typical plot is shown in Fig. 6.12. As can be observed, a good linearity was found over the entire energy range.

| Supermodules | Mean $K_{Abs}$ (keV/ADC) | Dispersion |
|---|---|---|
| SM2B | 2.80 | 13.1% |
| SM4B | 2.60 | 16.9% |
| SM6A | 2.51 | 18.1% |

Table 6.3: Results (mean and dispersion) for the absolute gain calibration.

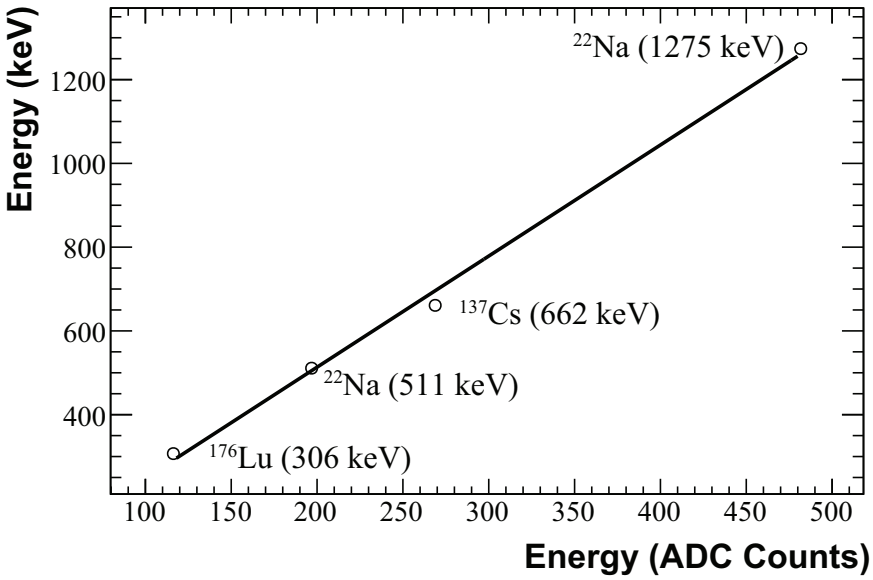


Figure 6.12: Reconstructed energy as a function of the photopeak position.

### 6.3.3 Energy Resolution at 511 keV

Energy resolution at 511 keV was extracted from a Gaussian fit, over a linear background, of each crystal in a supermodule. Distributions for the three supermodules are shown in Figs. 6.14 and the respective dispersions presented in Tab. 6.4. The mean energy resolution was 15.35% with 8.4% dispersion. The results are in very good agreement with

the ones discussed in Chapter 3, where a set of 80 matrices were readout by discrete electronics based on CREMAT 110 charge sensitive preamplifiers, in which the mean energy resolution and the standard deviation were, respectively, 15.6% and 1.3% (8.3% dispersion). This result is explained by the fact that in the LYSO:Ce, the intrinsic term dominates largely the energy resolution, and therefore, in spite of the light collection increase when using the Histomount coupling media when compared with the Paste 7 grease, small improvement is observed in the energy resolution.

| Supermodules | Energy resolution (%) | Dispersion (%) |
|---|---|---|
| SM2B | 15.55 | 7.72 |
| SM4B | 14.62 | 8.21 |
| SM6A | 15.89 | 9.19 |

Table 6.4: Results (mean and dispersion) for the energy resolution at 511 keV.

### 6.3.4 DOI Resolution

For the three analyzed supermodules, the inverse of the $C_{DOI}$ was computed since it relates directly to the asymmetry per millimetre values shown earlier in Chapter 3 and 5. Results are shown in Table 6.5 and Fig. 6.15. The mean value is 5.8%/mm, with dispersions in the 6–8% range. The larger asymmetry per milimiter in comparison with the ones obtained in Chapter 3 (3–4%/mm) are expected if one takes in consideration the work carried out regarding the optimization of light collection. As shown in Chapter 5, Section 5.2, the replacement of the Rodorshil Pate 7 grease by the Histomount glue leads to an increase in the light collection of up to 40% and as a consequence a broadening of the light asymmetry distribution. Altough $^{22}$Na collimated measurements where not made with the supermodules, the expected DOI resolution should be better than 2.2 mm FWHM, since the measurements that establish this DOI resolution value, in Chapter 3, were made with a Paste 7 optical grease where light collection asymmetry is in the 4% range.

| **Supermodules** | **Mean $C_{DOI}^{-1}$ (%/mm)** | **Dispersion** |
|---|---|---|
| SM2B | 5.70 | 6.3% |
| SM4B | 5.63 | 8.6% |
| SM6A | 6.21 | 6.1% |

Table 6.5: Results (mean and dispersion) for the $C_{DOI}^{-1}$ constant.

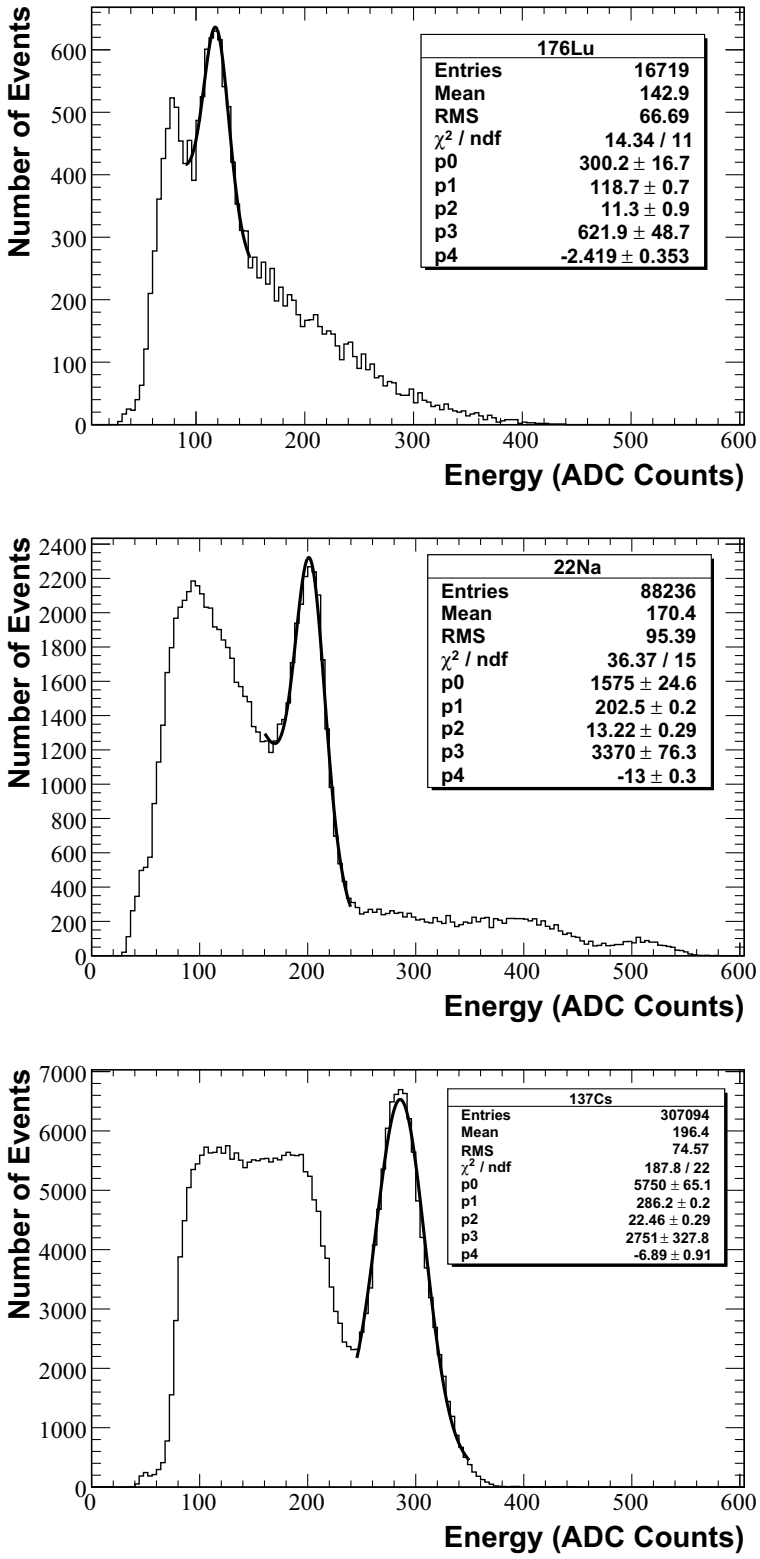


Figure 6.13: Typical energy spectra for a given crystal: $^{176}$Lu (*top*), $^{22}$Na (*centre*), $^{137}$Cs (*bottom*).

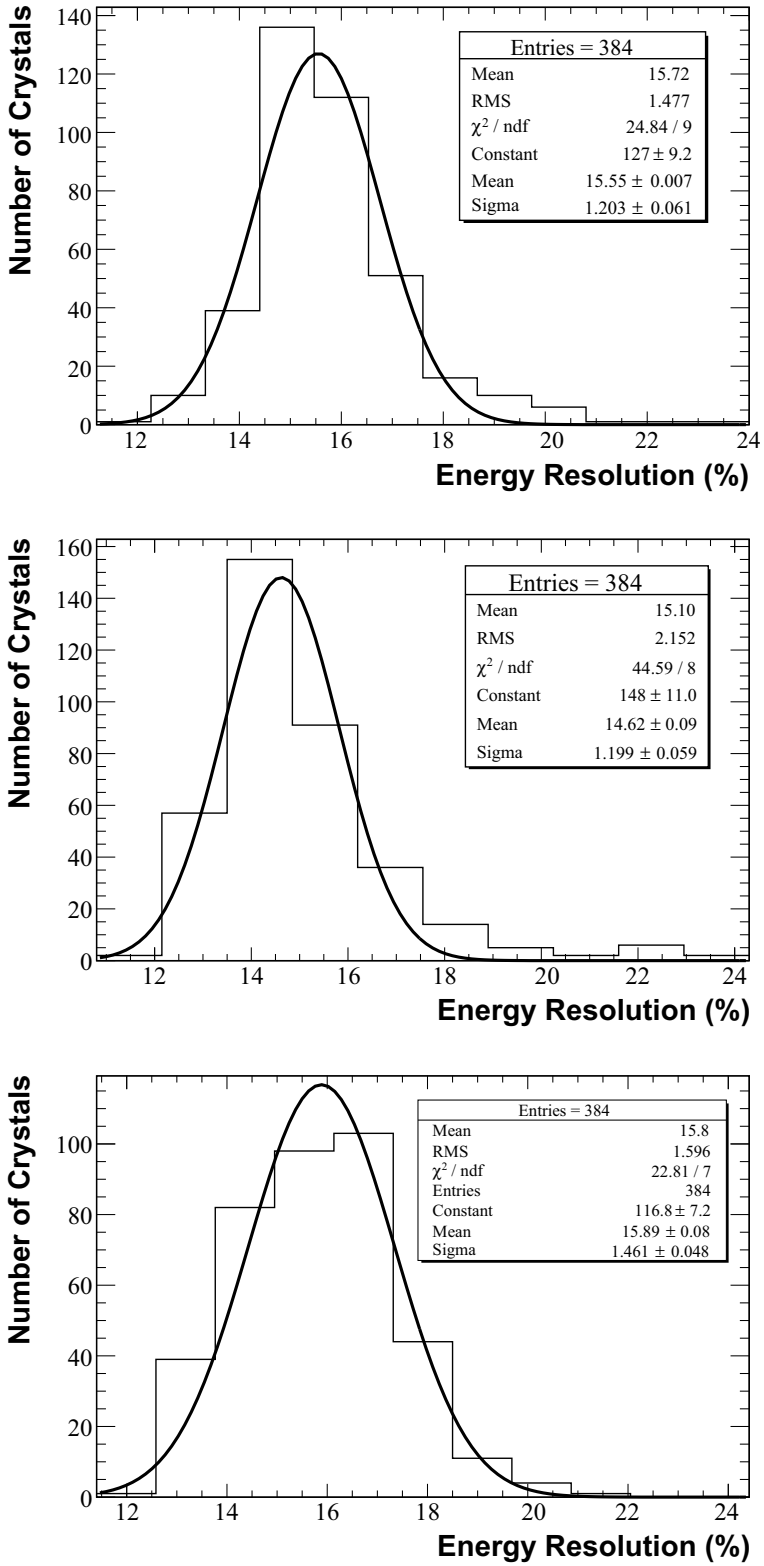


Figure 6.14: Distribution of the energy resolution for three supermodules: SM2B (*top*), SM4B(*centre*), SM6A (*bottom*).

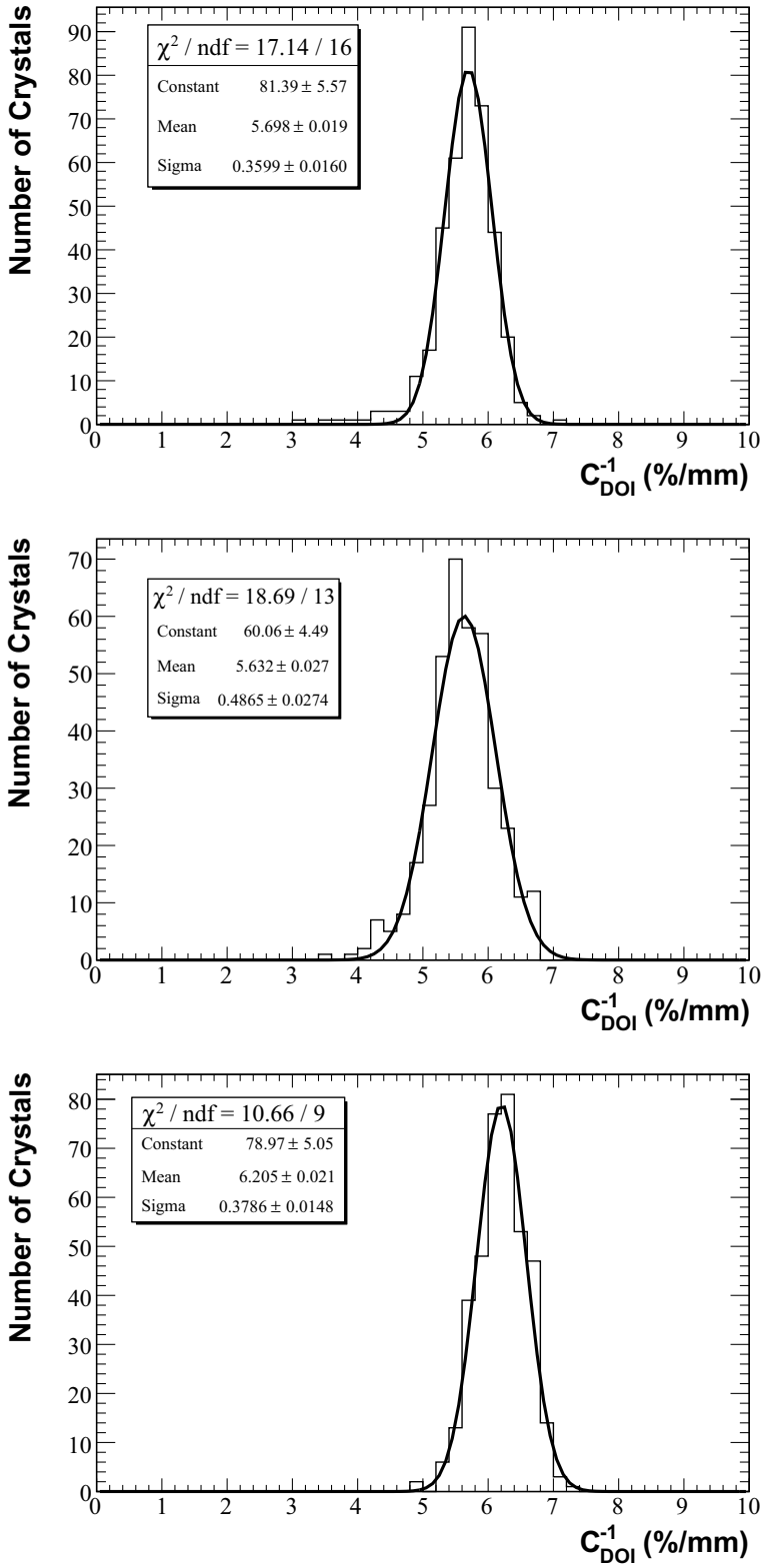


Figure 6.15: Light collection asymmetry $C_{DOI}^{-1}$ distributions for supermodules SM2B (*top*), SM4B (*centre*) and SM6A(*bottom*).

## 6.4 Experimental Measurements with the ClearPEM Detector Heads

During Fall 2008 the ClearPEM detector was on its final assembling phase at TagusLIP, where all the electronic sub-systems, computing, power suppliers and software components were tested in combined runs. Due to logistics-related time constraints, only 75% of the total number of crystal matrices were assembled. Fig. 6.16 shows the first test of one of the detector heads operating in single mode trigger. Latter, the two detector heads were placed in the robotic structure and combined tests, both in single mode and coincidence photon trigger, performed. Fig. 6.17 shows the occupancy plots, e.g. number of hits per crystal, obtained with a 0.5 mCi planar $^{68}$Ge radioactive source in single photon trigger mode. 99.7% of all channels were found to be active.

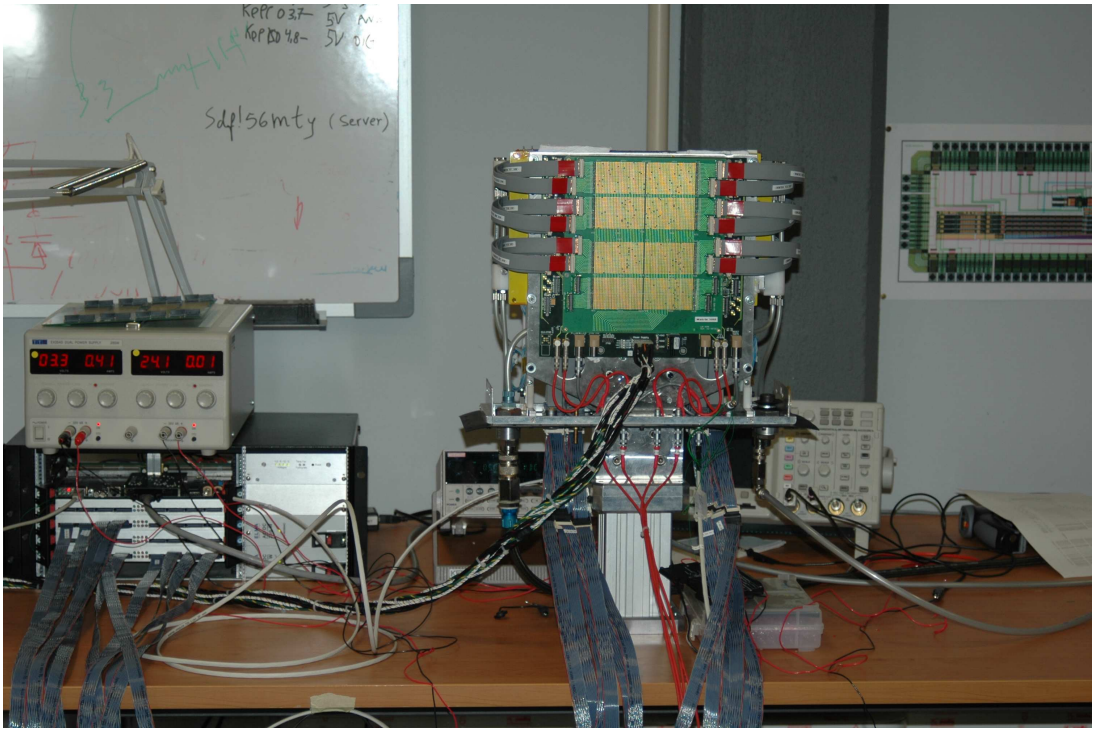


Figure 6.16: Photograph of integration tests at TagusLIP of one ClearPEM detector heads.

The occupancy map of a $^{22}$Na point-source in coincidence trigger is also shown in Fig. 6.18. In parallel with this functional tests, acquisitions both with $^{176}$Lu background and $^{68}$Ge were obtained. The scanner was calibrated and results compared with the obtained with the discrete electronics as well also the supermodules quality control [Frade2009].

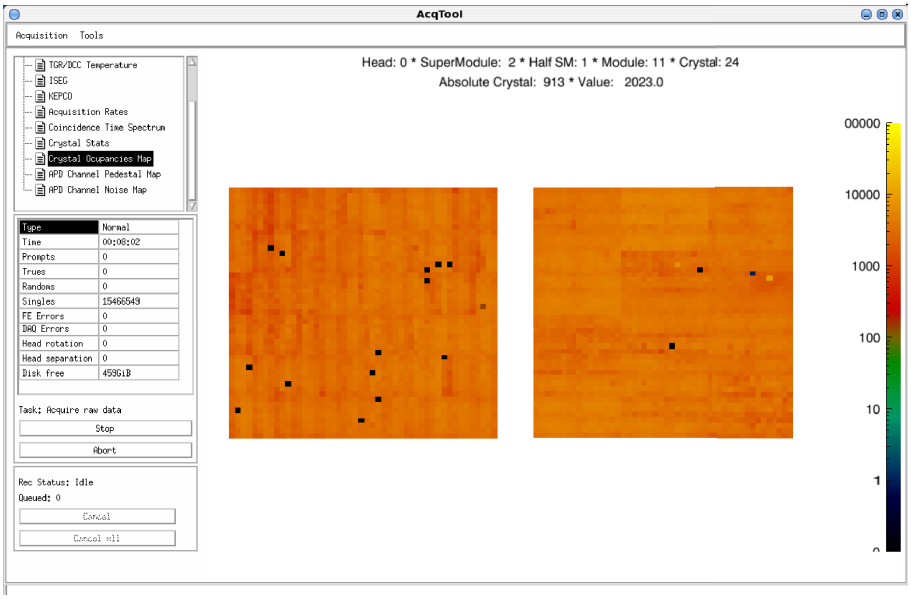


Figure 6.17: On-line monitoring of a $^{68}$Ge acquisition run on single-photon trigger.

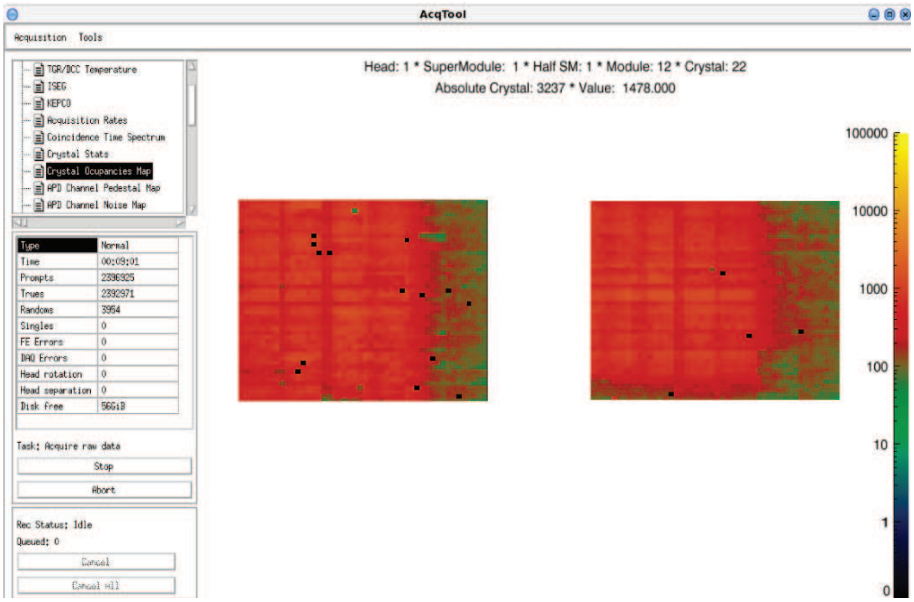


Figure 6.18: On-line monitoring of a $^{22}$Na point source acquisition run on coincidence trigger.

### 6.4.1 Inter–pixel Gain Variation

Fig. 6.19 shows the $k_{rel}$ inter–pixel calibration constant distribution obtained with the assembled scanner. The distribution has a mean value of 1.02 and a dispersion of 12%. This dispersion is in good agreement with the the 13% value obtained earlier with the discrete electronics and slightly better than the one obtained in individual supermodules

(16%). The improvement can be attributed to the fact that the temperature inside the detector heads is kept much more controlled (18±0.1°C) in comparison with the simpler approach envised for the supermodules testing.

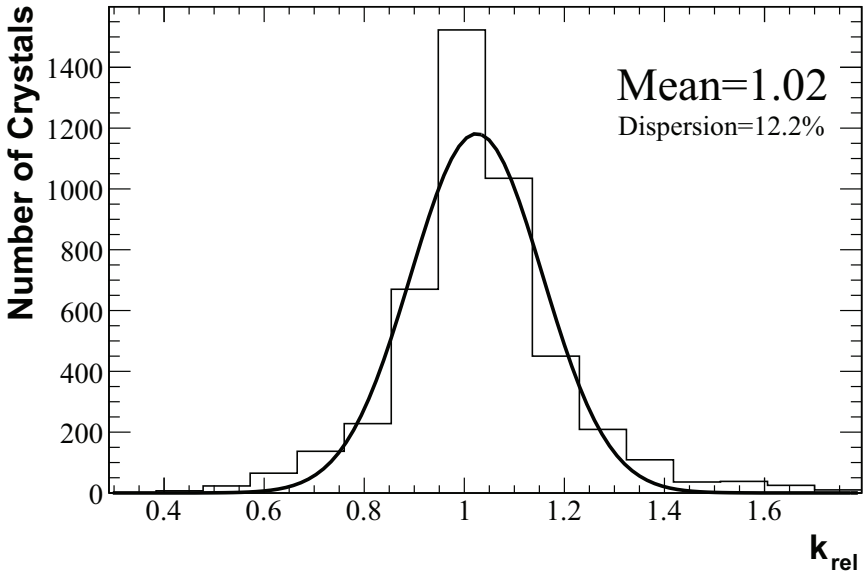


Figure 6.19: Distribution of the ClearPEM scanner $k_{rel}$ inter-pixel gain.

### 6.4.2 Photopeak Position at 511 keV and Linearity

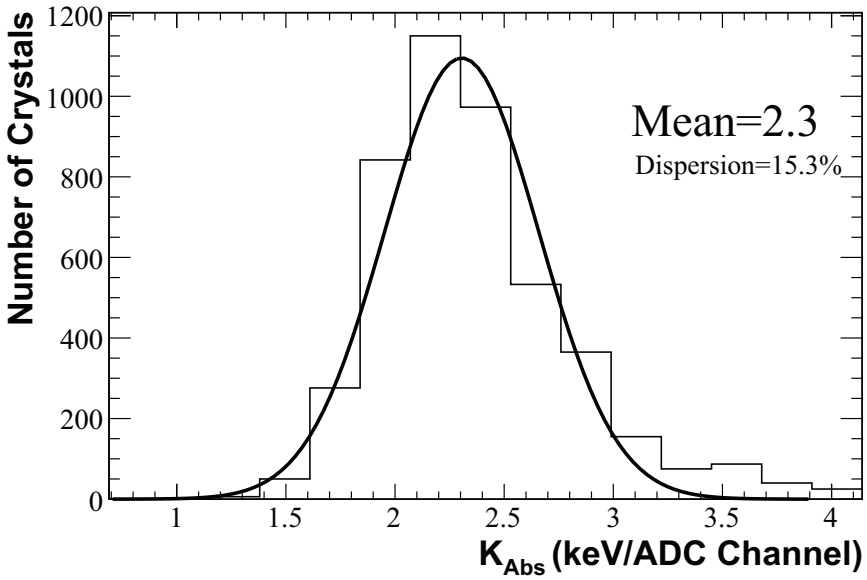


Figure 6.20: Distribution of the ClearPEM scanner absolute gain.

The absolute gain distribution, shown in Fig. 6.20, shows a mean value and dispersion, of, respectively, 2.3 keV/ADC and 15.1%. The mean gain has, in these measurements, an improvement from 2.6 to 2.3 keV/ADC. This means that the absolute gain is higher by roughly 12%. This can be explained by the lower temperatures at which the ClearPEM detector heads were operated in the lab (18°C) in relation to the supermodules characterization setup (20°C). At gain 150, the $dM/dT$ for the Hamamatsu S8550 APD is ≈4%/°C [Mosset2002], which correlates well with the observed difference in the absolute gain.

### 6.4.3 Energy and Time Resolution at 511 keV

The distribution of the energy resolution at 511 keV for all crystals is shown in Fig. 6.21, with a mean value of 15.9% and 9.1% dispersion, extracted from a gaussian fit. These results are in order with those obtained with the supermodules quality control phase as well as with the individual measurements carry out earlier.

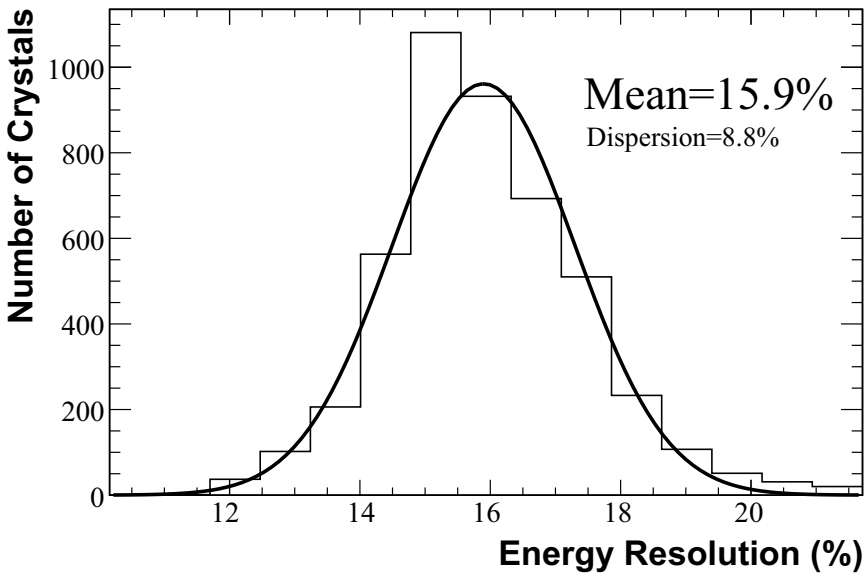


Figure 6.21: Energy resolution at 511 keV for the ClearPEM scanner.

The sum of the energy spectra for all crystal in the same plot is shown in Fig. 6.22. The calibrated plot of the entire ClearPEM scanner shows a well defined 511 keV photopeak, above the Compton continuum. The energy resolution is 16%, very close the mean value of 15.9% of the individual energy resolutions, confirming the correctness of the energy calibration procedure as well as the excelent energy response of the detector [Frade2009].

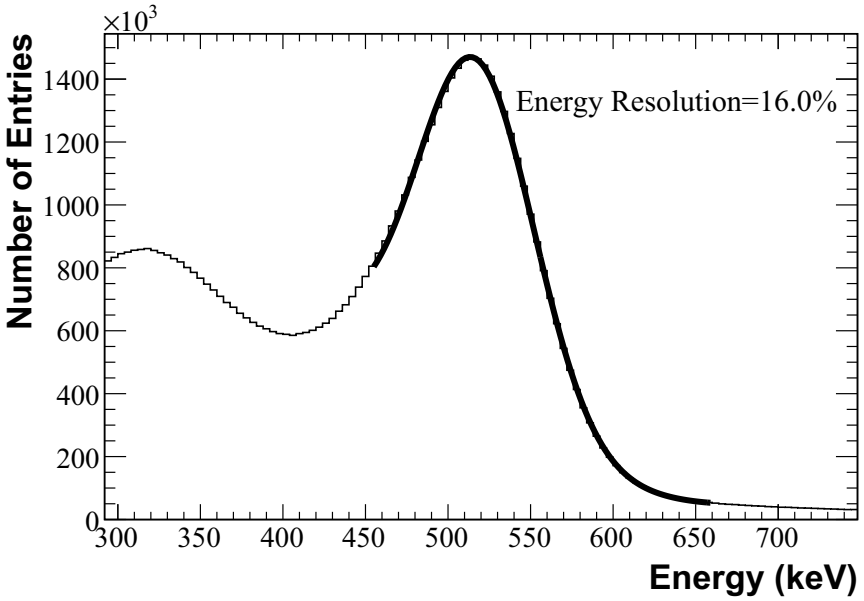


Figure 6.22: Energy sum plot of ClearPEM scanner.

The coincidence time resolution for 511 keV photons, defined as the FWHM of the gaussian fit of the distribution of the time difference between 2 photons originated from the same positron decay, using a 400–600 keV energy window, is of 5.2 ns, as shown in Fig. 6.23. For this measurement a $^{22}$Na source (100 $\mu$Ci) was placed between the detector heads. The distribution was obtained by subtracting a linear background that arises from the presence of random coincidences (less than 5%).

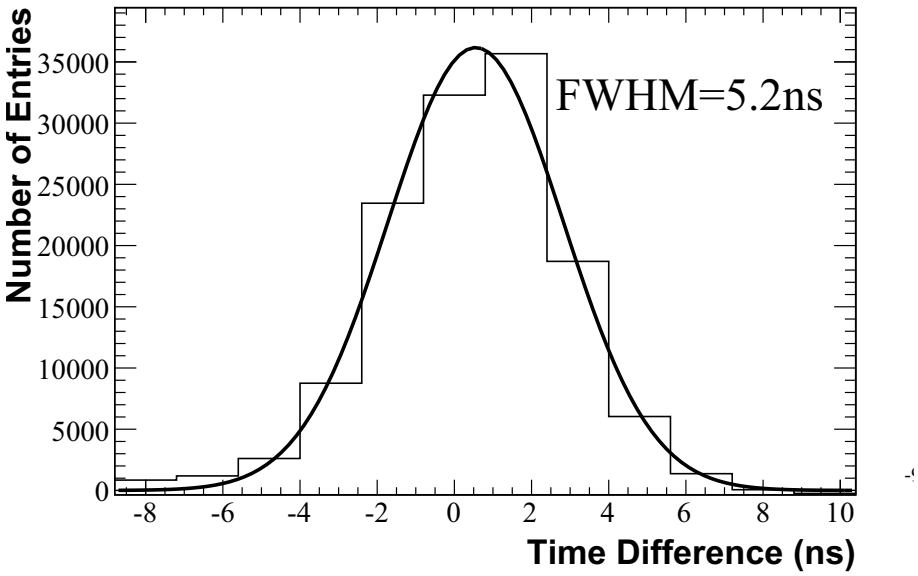


Figure 6.23: Time difference distribution for coincidence photon events in the energy range 400–600 keV.

### 6.4.4 DOI Resolution

The light collection asymmetry $C_{DOI}^{-1}$ distribution is presented in Fig. 6.24, having a mean value of 5.9%/mm and a dispersion of 7.8%, obtained from a gaussian fit. Results are in very good agreement with the obtained in the supermodules characterization phase (5.8%/mm with 6–8% dispersion), confirmimg the improvement in the light collection asymmetry obtained after the Rhodorsil Paste 7 grease was replaced by the Histomount coupling, presented in Chapter 5.

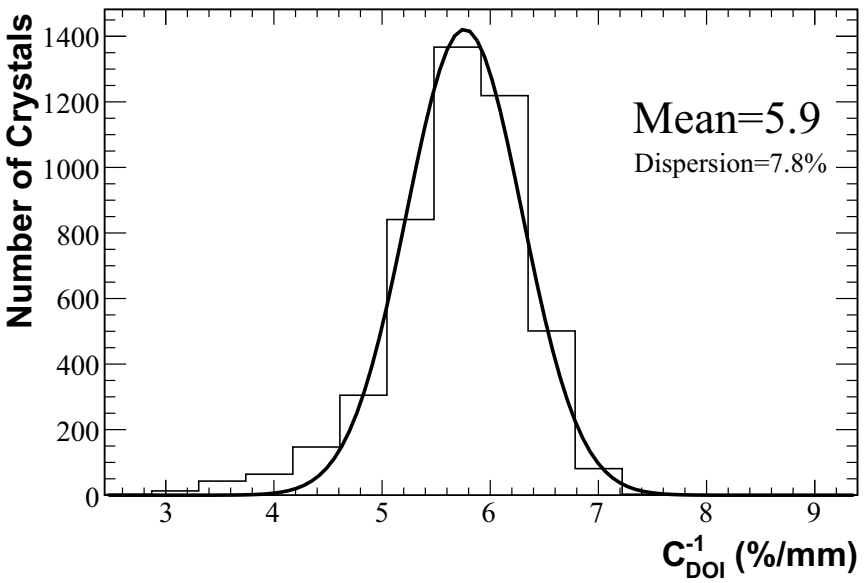


Figure 6.24: Light collection asymmetry width ($C_{DOI}^{-1}$) for the ClearPEM scanner.

### 6.4.5 Preliminary Image Performance

For a direct estimation of the spatial resolution, a 1 mm diameter $^{22}$Na radioactive source was placed between the detector heads and displaced in 5 mm steps with a $xy$ translation stage. A total of 16 displacements were performed. Data was acquired in two angular projections. Two–photon coincidence events in the 400–600 keV energy range inside an 20 ns time window were selected. A list mode file (LMF) that includes the spatial coordinates of each photon was produced and images reconstructed using a OSEM–3D algorithm. The OSEM algorithm for the ClearPEM scanner relies on the Software for Tomographic Image Reconstruction (STIR) toolkit, an object–oriented open source software for 3D PET image reconstruction [Thielemans2004, Martins2005]. This software implements different image reconstruction algorithms and scanner geometries including both cylindrical and dual–planar scanners. The maximum likelihood estimation reconstruction method available in STIR is called OSMAPOSL, an implementation of the OS–EM One Step Late algorithm [Thielemans2004]. This algorithm was tunned to reconstruct data from the ClearPEM scanner, acquired at two orthogonal detector positions but it is also capable to reconstruct data acquired with only one angular orientation. No normalization of other image corrections, namely for random coincidences, were used.

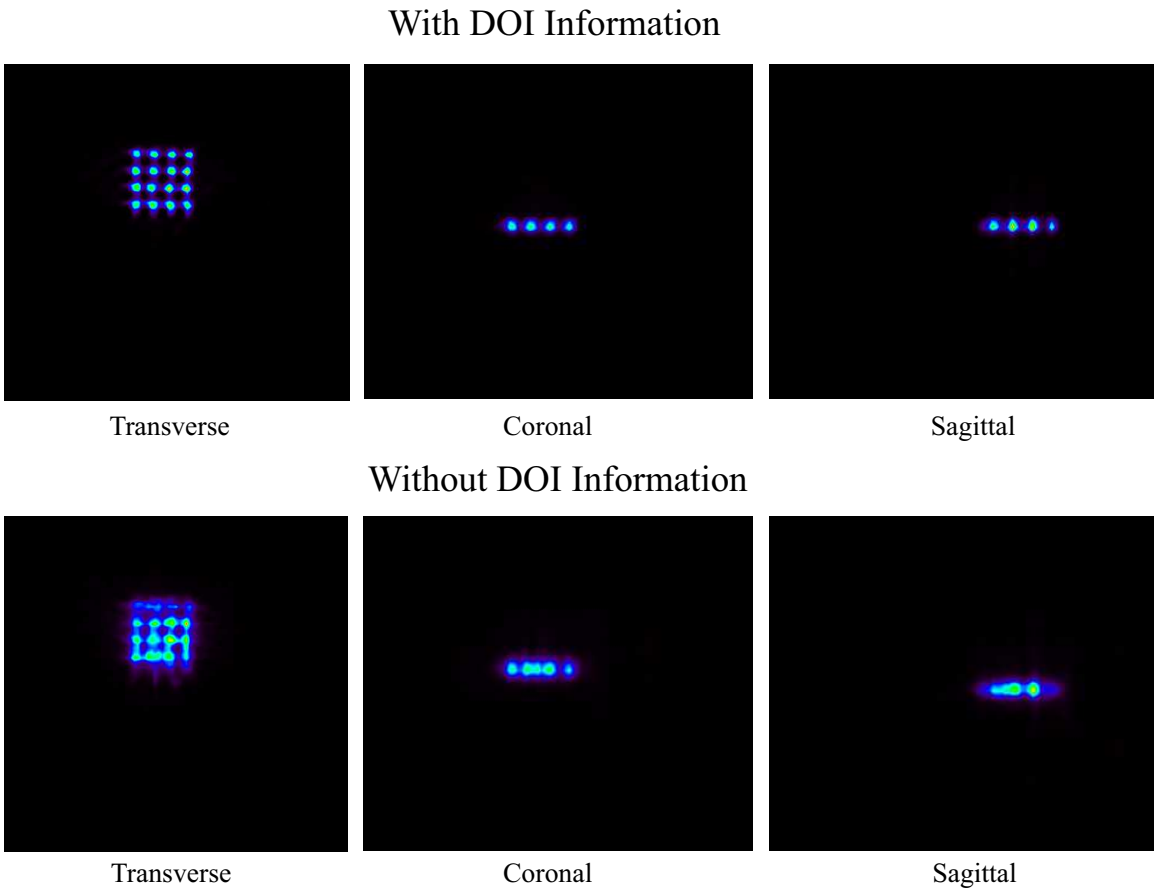


Figure 6.25: $^{22}$Na point source image reconstructed with and without DOI information.

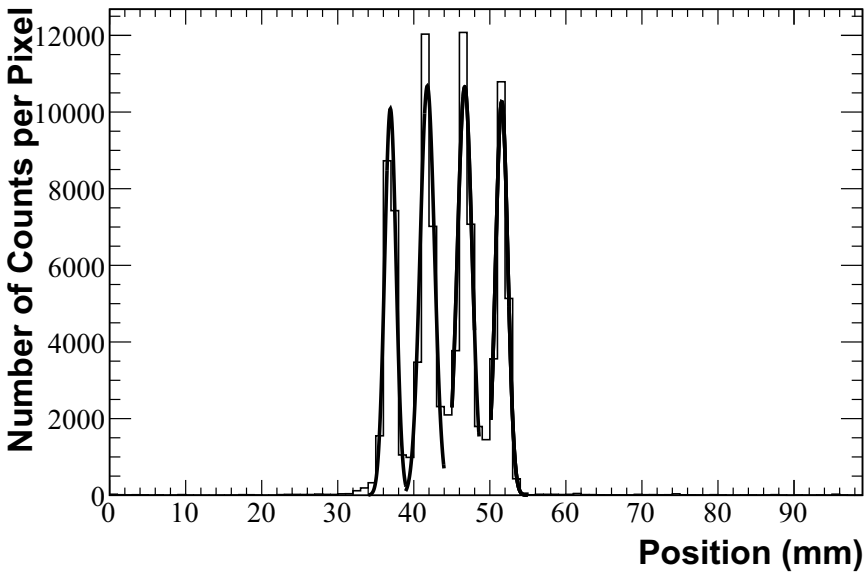


Figure 6.26: Profile of $^{22}$Na point source image reconstructions with DOI information.

For comparison purposes, the original data was re-processed and the $z$ coordinate discarded. Instead of the DOI information, the $z$ coordinate was attributed to the crystal face closer to the patient port, as in conventional PET scanners. Results are shown in Fig. 6.25. As can be observed, the use of the DOI coordinate has a drastic impact in the image quality of these small radioactive sources. A FWHM spatial resolution of 1.3–1.6 mm was obtained - Fig. 6.26.

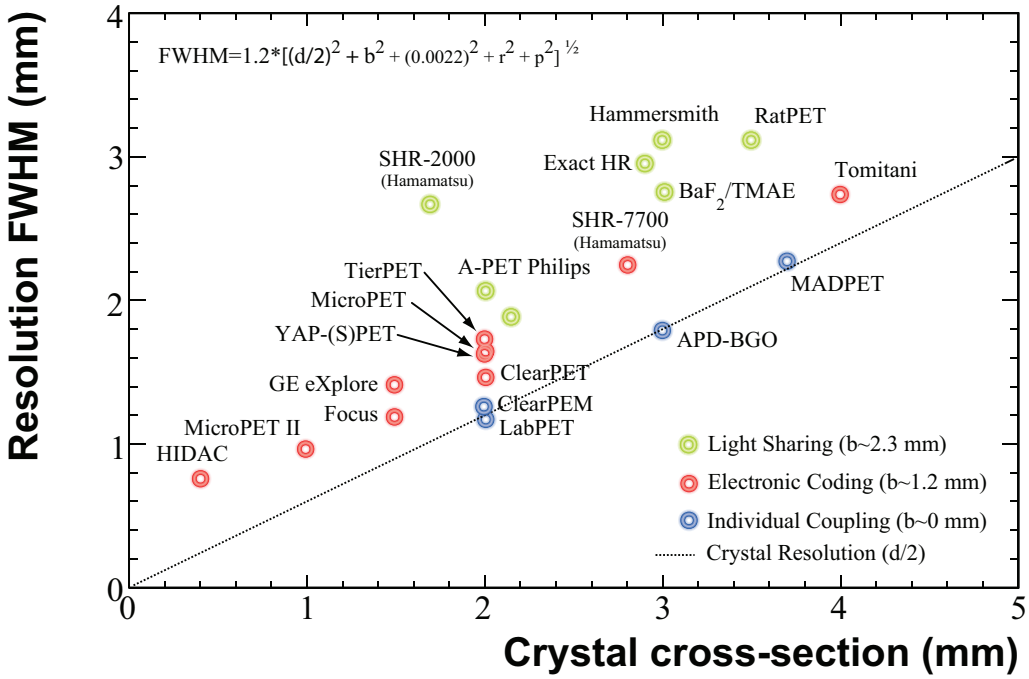


Figure 6.27: Spatial resolution as a function of the crystal cross-section.

To conclude this topic of discussion, it is important to compare the experimental ClearPEM spatial resolution with other dedicated PET scanners. Lecomte has published in [Lecomte2004] the intrinsic spatial resolution of several existing small-animal PET scanners as a function of the crystal pixel size. The effects of non-collinearity, positron range or in some cases the effective source size used to measure the detector resolutions were de-convoluted from the data. The scanners were organized according to the type of coupling scheme ($b$ in Eq. 1.2 shown in Chapter 1) of each scanner and compared with the crystal resolution theoretical limit as shown in Fig. 6.27. The ClearPEM spatial resolution obtained with this first set of images was plotted over the survey. It is clear that ClearPEM follows the trend of remaining scanners with individual coupling schemes, in which the spatial resolution is limited by the size of the crystal pixel ($d$). Small deviations from the theoretical limit can be attributed either to the performance of the image reconstruction algorithm or to the adopted event reconstruction method, when in the presence of in-detector Compton scattering. The comparison suggests that ClearPEM currently represents one of the most promising dedicated human PET scanner developed so far, combining pixelized detector modules with an individual coupling between the crystal pixels and the photodetector, making the spatial resolution only limited by the crystal pixel size.

### 6.4.6 Preliminary Sensitivity Assessment

For the sensitivity assessment of the ClearPEM scanner, a $^{22}$Na source was previously calibrated at TagusLIP. Several activity measurements with dose calibrator in different days with background subtraction using the Atom100 Dose Calibrator (described earlier in Chapter 2) were performed. The measured activity for the 1 mm diameter $^{22}$Na source was 2.73 $\mu$Curie (101 kBq), with a 0.3% uncertainty. The $^{22}$Na source was placed on a metallic holder structure and was fixed to the robotized examination bed (Fig. 6.28), which has 3 degrees of freedom (XYZ).

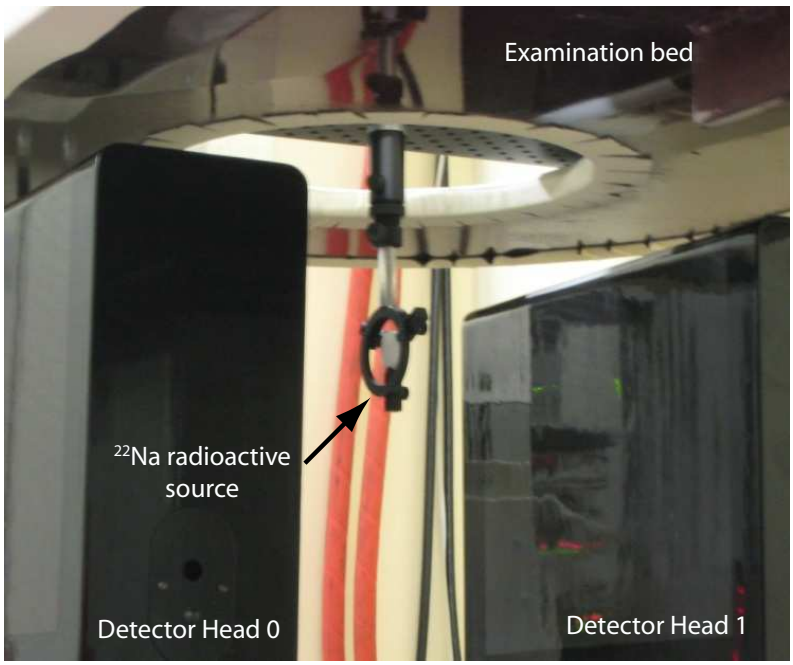


Figure 6.28: Photograph of ClearPEM scanner with a $^{22}$Na source for sensitivity assessment.

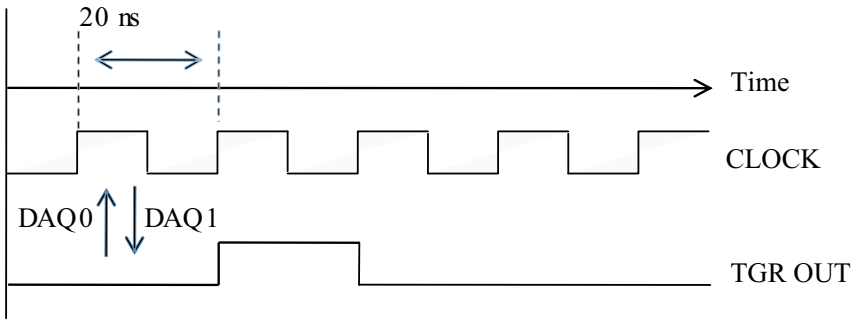


Figure 6.29: Trigger scheme for ClearPEM sensitivity assessment.

The TGR OUT output of the TGR/DCC board which is set HIGH during a clock period when two photon hits inside the selected time window are detected (Fig. 6.29) was feed into a CAEN N470 NIM scaler. For the sensitivity measurements reported in

this section, the energy windows was set to 350–700 keV and a time window of 20 ns was selected because of the 101 kBq activity of the $^{22}$Na source (since random coincidences are suppressed due to the low activity of the source).

In order to search for the peak sensitivity of the system, a XYZ scan was performed in steps of 0.5 mm. After the peak sensitivity has been found in a given axis, the following axis was scanned starting from that point until the point that maximizes the detector sensitivity in the new axis. The two photon system sensitivity as function of the rotation axis of the scanner, defined as the fraction of detected two photon events over the total number of decays, was corrected by the branching ratio of the $^{22}$Na decay to a single 1.2 MeV photon and by the presence of random coincidences when the $^{22}$Na was removed from the field-of-view. Without the $^{22}$Na, coincidences arise either due to random single photons or from background coincidences of the $^{176}$Lu. The measured random rate was 24 Hz, in good agreement with the Monte Carlo simulations that yield a random rate of 20 Hz [Trindade2007]. The system sensitivity profile, along the rotation axis for a separation distance between the external carbon fiber detector housing of 70 mm, equivalent to a separation distance between the crystal top face of 132 mm, is shown in Fig. 6.30. After correction by the $^{176}$Lu contribution and $^{22}$Na branching ration, the peak sensitivity amounts to 1.33%.

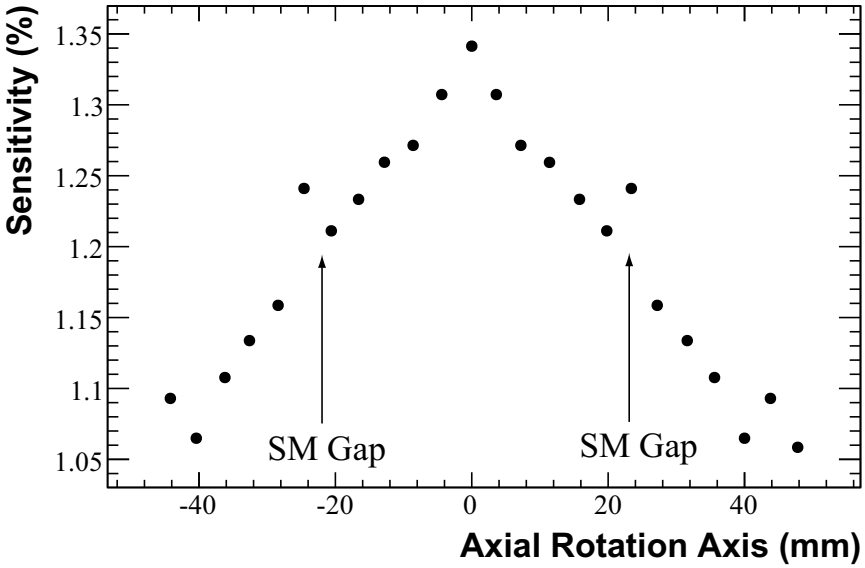


Figure 6.30: ClearPEM sensitivity with axial distance.

Two larger irregularities on the sensitivity profile can be found at roughly -20 and +20 mm and these, according to Monte Carlo simulations, are due to dead spaces between the detector supermodules. The region comprehended between -25 and +25 mm corresponds to the central SM, which is consistent with the fact that each SM has a width of about 4.5 cm.

According to the Monte Carlo simulation, the system sensitivity for a separation distance of 70 mm (equivalent to a crystal separation distance of 132 mm) should be 4.1%. This value has to be corrected by the following factors:

1. The Geant4 Monte Carlo simulation assumed a detector module with a packing fraction of 0.52. However the plastic assembly, described in Chapter 3, introduces additional dead spaces leading to a decrease down to 0.47. The sensitivity is proportional to the square of the packing fraction and, therefore, the Monte Carlo simulations have to be corrected by a factor of $(0.46/0.52)^2$, or 0.78.

2. The Geant4 Monte Carlo simulations assumed Tyvek reflector walls, since those were made before the adoption of the $BaSO_4$ solution. Due to higher density and effective atomic number of the $BaSO_4$, photons have a larger probability of being absorbed in the 300–600 $\mu$m thickness walls. Monte Carlo simulations in which Tyvek was replaced by $BaSO_4$ were done, indicating that the original Tyvek simulations need to be corrected by an additional term of 0.85 (15% additional attenuation).

When these two factors are taken into account, the original Monte Carlo sensitivity estimation decreases from 4.1% to 2.7% (also assuming an energy window of 350–700 keV). A third factor, which will need additional Monte Carlo simulations and therefore was not taken into account, is that the experimental measurements of the ClearPEM scanner were made with only 75% of the SMs assembled. This contributes to a decrease of the solid angle coverage. As explained earlier, the system sensitivity scales also quadratically with the solid angle coverage.

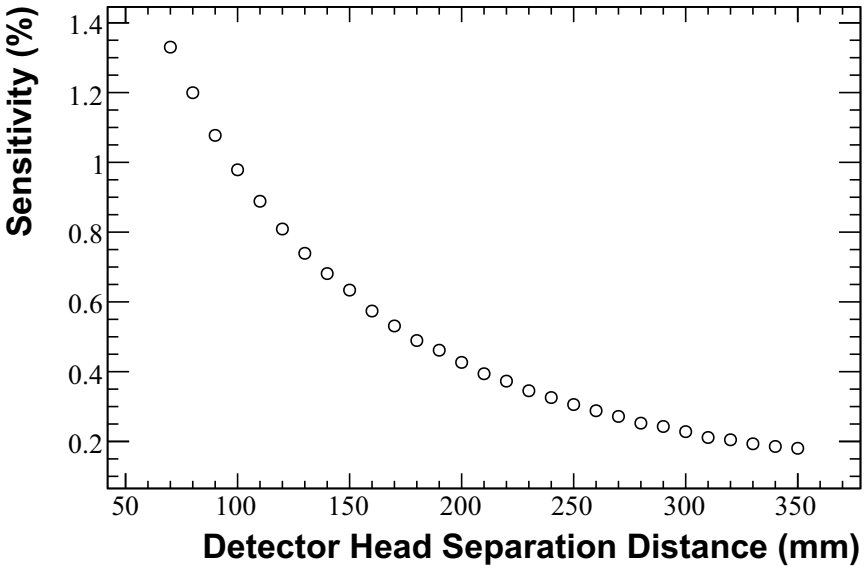


Figure 6.31: ClearPEM sensitivity with detector heads distance.

The peak system sensitivity as function of the distance between the detector heads external housing is shown in Fig. 6.31, decreasing from the 1.33% at 70 mm down to 0.18% for a detector heads distance of 350 mm. Further sensitivity assessment will be carried out when the remain SM are assembled, during the final detector upgrade.

## 6.5 Summary and Discussion

The measurements shown in this chapter confirm the good performance of the ClearPEM supermodules, indicating that the integration of a large number of channels in a very compact readout system does not lead to a degradation on the basic spectrometric performances of the developed detector modules, namely its energy and DOI measurement capability. All modules were re–mounted with the National Diagnostics Histomount media, following the results described in Chapter 5. The main consequence of this change was a consistent improvement in the light collection and the light collection asymmetry (5.85%/mm ± 8%) in comparison with the individual detector matrices modules measurements (3.26%/mm ± 22%). The higher the $C_{DOI}^{-1}$ means that the light asymmetry between top and bottom APDs is higher, therefore allowing a better determination of the $z$ coordinate where the photon interaction occurs, improving the scanner performance. Regarding the energy resolution and photopeak variability, results are consistent with the first measurements but with a significant difference: while in the first measurements, only 32 crystals (2 HV lines) were readout, with the supermodules each aquisition measurement allows to process 384 crystals (48 HV lines) in the same run. The small dispersion in the $k_{rel}$ inter–pixel calibration constant indicates that the HV multiplexing scheme, introduced in the ClearPEM scanner to bias a total of 768 APD sub-matrices, does not lead to a degradation on the system performance. The dispersion of the absolute gain (or photopeak position) is less than 15% which indicates that the change in the optical medium does not introduce additional variability in the light collection. In fact, the energy resolution and photopeak variability is systematic better than most multi–pixel APD animal PET systems [Wang2006, Roldan2007, Lecomte2009, Ziegler2005], in spite of the fact that the double-readout configuration decreases the ammount of collected light. Measurements with the assembled ClearPEM scanner have confirm the excelent performance that reflects in a spatial resolution between 1.3–1.6 mm FWHM very close to theoretical limit for the 1:1 individual crystal–photosensor coupling.

In the end of December of 2008, the scanner was re-assembled in the nuclear department of IPO–Porto where commissioning work was carried out to confirm the earlier measurements at TagusLIP. Sensitivity assessment of 75% assembled ClearPEM scanner was performed with a $^{22}$Na source and the peak sensitivity is 1.33%. Further assessement of the system sensitivity of the fully assembled scanner is foreseen after the upgrade phase, scheduled to the end of 2009. The commissioning phase was concluded in April 2009 and the detector was considered to be ready for the pre-clinical trials phase.

# Summary and Conclusions

The ClearPEM detector was developed by the Portuguese PET Consortium under the framework of the Crystal Clear Collaboration for early stage breast cancer detection. The scanner was developed based on three main guidelines: low background, minimizing the fraction of random coincidences under a high flux of single photons (up to 10 MHz); high sensitivity; and spatial resolution down to 2 mm. Due to the small lesion dimensions in the early stage of the disease, detection techniques require a large sensitivity and high resolution, with the aim to increase the signal over background significance. Sensitivity is an important parameter on the design as it allows a lower injected dose and a shorter examination time. This is particularly important in determining the frequency of scans for women as well as the lower limit of their age for systematic screening. Sensitivity depends on geometrical and physical parameters of the detector. The detector geometry must cover the largest solid angle possible, although some limitations are imposed by image reconstruction considerations as well as by the specificity of human body anatomy and examination practice. The detector thickness and the crystal physical properties (density and composition) determine the photoelectric interaction probability for the emitted photons and in consequence have a direct impact on ClearPEM sensitivity. On the other hand, the crystal length is responsible for the parallax effect in the image reconstruction process and the consequent degradation in spatial resolution. Parallax effect in ClearPEM is an important issue since the planar detector heads are located close to the object under examination. In consequence, high-density crystals combined with depth-of-interaction information were required for the detector. The crystal transverse dimensions (about 2 $\times$ 2 $mm^2$) were determined by the desired position resolution, whereas the longitudinal dimension (20 mm) was dictated by the required detector sensitivity. Depth-of-interaction information in the ClearPEM detector is obtained by collecting the crystal light in the front and back faces and using the relative amplitude of the two signals to estimate the longitudinal coordinate of the interaction point.

This thesis presents the evaluation of the ClearPEM detector module design, namely the characterization of basic performance parameters of the S8550 APD as well as the optimization process of the crystal polish and wrappings that as led to the final configuration, based on a highly diffusive reflector build from $BaSO_4$ and slightly polished crystals. The ClearPEM detector module consists on 32 LYSO:Ce crystals with 2×2×20 $mm^3$ encased in a $BaSO_4$ matrix, readout at both ends by two Hamamatsu S8550 4×8

APD arrays, showing an energy resolution of 15% at 511 keV, DOI resolution better than 2 mm and light collection (photopeak position) dispersion better than 20%. A key ingredient for these results is a stable operation by the APDs. Several S8550s were evaluated in the course of this work in relation to their linearity, excess noise and response to optical light in the UV long/blue short region as well as to direct ionization of $^{55}$Fe. A good long-term stability, at the 2% level was found. Independent measurements confirmed that the excess noise factor in the S8550 is low. A mean excess noise factor, for 420 nm light, of 1.83 at gain 70 was found. As comparison, the RMD A1604 16 (4×4) multi-pixel shows an excess noise factor at gain 50–100 of 2, rising to 3 at gain 1000. For the quiet moderate excess noise of the S8550 contributes an avalanche layer no larger than 4 $\mu$m. Inter-pixel gain variability (5.7% r.m.s.) was observed to be constant (2% level) over time. The different gain behaviour of the S8550 APD when subject to a blue light illumination (420 nm) or to direct ionization of 5.9 keV from $^{55}$Fe was examined. The decrease of the ratio R$x,light$ is consistent with the small thickness of the avalanche region.

Long-term stability of the ClearPEM modules was appraised and the effects on the performance of a reassembled module was studied. Signal yield and asymmetry parameters suffer considerable variations when reassembling the module. To minimize inter-matrix variations for homogeneous response scanner, special care must be taken when assembling the modules, in particular with the application of the optical grease. Results show that one year after the detector modules were assembled a mean light collection reduction of about 12% and a decrease of the light collection asymmetry, which is fundamental for the DOI measurement, of almost 30% was observed. The degradation can be recovered by re-assembling the detector modules. As result of this study, a revision of the optical coupling between the crystal and the APD was performed and a new optical coupling media was selected.

The degree of crosstalk has particularly important implications for the design of the ClearPEM front-end electronics. If high enough, crosstalk can generate false triggering in channels adjacent to the actual event. Due to architecture of the Clear PEM ASIC, 192 input channels, corresponding to 6 APDs, are multiplexed to 2 outputs. If 3 channels are higher than the common threshold, an error bit signals that part of the information was lost. In this case, the off-detector electronics discard the entire event, leading to a loss of efficiency. On the other hand, it can be suppressed by sufficiently increasing the ASIC threshold, but on the other hand a threshold too high can already prevent valid events on the lower gain channels from being detected. Working with small adjacent crystal may lead to inter-crystal crosstalk contamination, which arises from Compton scattering from one crystal to another or possibly the escape of the photoelectron from the primary crystal following photoelectric absorption. Light sharing between two pixels due to position mismatch of the crystal pixel - APD pixel, inefficient optical isolation, degradation or absence of the optical coupling interface crystal-APD may also induce crosstalk. This parameter was evaluated in a series of measurements dedicated to the study of the possible causes of crosstalk. It was found that there is no relevant electrical or optical crosstalk on the S8550 APD, being the major contribution to the detector module crosstalk from the small pixels separated by a 300 $\mu$m layer of $BaSO_4$. The contribution of crosstalk

on the ClearPEM detector modules, despite the pixelized matrix configuration, is small. The first 24 detector modules present average crosstalk of 3% and the overall evaluation of 80 detector modules reassures the small contamination. Measurements in different conditions and with different discrete electronics did not disturbed the evaluation of the crosstalk, but permitted to inferred a higher contamination on the double readout scheme electronics, probably due to current sharing between the PCB traces. Nevertheless, the average crosstalk value remained small, so this issue was not further investigated.

In spite of the significant development and good performance achieved, optimization the ClearPEM detector module design is a continuous work. Triggered by the aging problems detected with the optical grease, several optical coupling materials were studied, evolving for a permanent solution with better performance. To increase the sensibility of the detector modules, efforts on improving the packing fraction of the ClearPEM detector module, which is 64% and is mainly constrained by the S8550 APD matrix layout and the thickness of the $BaSO_4$ walls, were explored with a new matrix with 2.2×2.2×30 $mm^3$ crystals and thinner specular reflector walls. More over, the low internal gain of the APD and the low ligh collection are currently the limiting factors in time resolution (5 ns FWHM measured with ClearPEM). Further improvements on the timing information require an increase on the light collection which is limited by the 1.6×1.6 $mm^2$ APD pixel matching with the 2×2 $mm^2$ cross-section crystals. Possible solutions like the redesign of the S8550 APD were addressed. As a result of this work, a new APD, with 1.8×1.8 $mm^2$ pixels, quantum efficiency of 90% at 420 nm and gain 200, was developed by Radiation Monitoring Devices, under a frame contract with LIP.

Besides the light collection aspect, the detection sensitivity of the scanner was also a parameter of concern. In crystal pixel-based modules, the packing fraction is generally reduced due to the compromise between reflector thickness and light collection isolation. Since the detection sensitivity of 511 keV photon pairs follows the square of the packing fraction, marginally improvements in the packing fraction may introduce significant gains on the scanner performance, allowing to achieve higher values of lesion detectability in shorter time exams. The crystal length is also a parameter that can be optimized. Usually, in scanners without DOI interaction capability, the length of the crystal is sub-optimal to avoid the introduction of the parallax effect. In the ClearPEM case, 20 mm crystals can be used since the double readout scheme allows to extract the DOI coordinate with a resolution better than 2 mm, minimizing the effect of the parallax effect while offering a moderate detection efficiency for 511 keV photons.

Permanent optical glues were explored in terms of the light collection, energy resolution and DOI resolution. Three options were explored: Meltmount, RTV 3145 and Histomount. Initial tests with Meltmount shown a superior light collection capability over grease, with a gain up to 30% and a significant improvement in the light collection asymmetry (from 4%/mm up to 5.6%/mm). Long-term stability measurements did not show any decrease of light collection with time. The main issue with this optical glue was the need to perform the modules mounting and un-mounting at high temperature, slightly above 65 degree Celsius. At this temperature, manual manipulation of the detector mod-

ule is more difficult leading to the formation of air bubbles in the application phase. These bubbles can introduce a systematic asymmetry in the light collection between the top and bottom APDs, which in turn lead to a degradation of the energy resolution. Tests with Histomount have shown a similar performance to Meltmount in terms of the light yield (20–30% improvement) and DOI resolution (5.5–6%/mm). Energy resolution was systematic better than grease, largely out-performing the Meltmount module energy resolution. As result of this work, it was decided to re-assemble all ClearPEM matrices with Histomount. The scanner spectrometric results obtained with this optical medium are well within the initial requirements, which has led the adoption of the Histomount mounting coupling also for the detector modules of the second ClearPEM scanner, named ClearPEM–Sonic, which combines the ClearPEM technology with an Ultrasound imaging device.

While the optimization of the optical coupling media led to a good stability in the light collection, with direct consequences in the obtained energy, DOI and time resolution, optimization studies of the detector module packing fraction and detection efficiency were also carried out. The initial approach consisted on the exploration of a novel matrices design, manufactured by Proteus Inc, composed by LYSO crystals with cross-sections of 2.2×2.2 $mm^2$, with 30 mm length, optically isolated by a layer of Vikuiti$^{TM}$ specular reflector with 61–68 micron thick. The reduction on the optical layer thickness from 300 $\mu$m in $BaSO_4$ to 70 $\mu$m with the Vikuiti$^{TM}$ reflector, together with the larger crystal cross-section, allows increasing the packing fraction up to 90%, a gain in detection sensitivity of about a factor of 1.48. When the crystal length of 30 mm is taken into consideration, the overall detection sensitivity gain goes from 1.48 to 2.1. Characterization results have shown that matrices with this design, using polished crystal, in a single readout, achieve better energy resolutions (12.5% at 662 keV) in comparison with the mean energy resolution of the standard ClearPEM $BaSO_4$ modules (14.5% at 662 keV) and Tyvek based modules (17.8% at 662 keV). A smaller light collection dispersion between different pixels was also found (6.2%) in comparison with the $BaSO_4$ (12.7%) and Tyvek (34.8%) matrices. With the use of crystals with larger cross-section, there was a concern on the increase of the crosstalk, since the larger crystal dimension make more prone a given crystal being readout by two different pixel APD. Crosstalk was evaluated for the Proteus, $BaSO_4$ and Tyvek matrices. Similar values of crosstalk between the Proteus (11.9%) and the standard $BaSO_4$ (10.7%) matrices were found. The Tyvek matrix has shown a sub-optimum performance in terms of crosstalk (24.1%). In overall, the Proteus design allows to achieve significant better results than the $BaSO_4$ design in a single readout option. In the double readout option, and due to the use polished LYSO crystals together with a specular reflector, DOI information cannot be extracted since there is no mechanism that creates a light collection asymmetry as function of the interaction depth of the photon in the crystal. To bypass this difficulty, matrices, following the Proteus design, were manufactured using crystals in which the lateral 30 mm surfaces were leaved as-cut. In this approach, DOI information can be extracted, with a DOI resolution of about 1.7 mm, at the expense of a degradation in the light collection and the energy resolution. Further studies, outside the scope of this thesis, were carried out in which crystals having a mixture of polished and saw-cut surfaces were coupled to Vikuiti$^{TM}$. In matrices with two sides polished, DOI resolutions in the 2.3

mm range, with energy resolutions of 16% at 511 keV were achieved, opening the possibility to use this type of detector module design for scanners with double readout schemes.

Before the final integration of the ClearPEM scanner was completed, several partial integration and engineering runs were carried out at TagusLIP. One of the most important activities consisted on the validation of the supermodules, each unit comprehending a set of twelve detector modules, whose individual performance was measured in dedicated discrete electronics setup, to characterize its performance before the final assembly of the supermodules inside the ClearPEM detector heads could took place. The tests of the supermodules allowed to assess the performance of the detector modules in their final working environment, combining instrumentation effects introduced by the frontend electronics readout and the processing of the data flow by the data acquisition electronics and trigger system, allowing a direct comparison with the previous results obtained in discrete electronics test benches. Measurements have confirmed the good performance of the ClearPEM supermodules, indicating that the integration of a large number of channels in a very compact readout system does not lead to a degradation on the basic spectrometric performances of the developed detector modules, namely its energy and DOI measurement capability. The main consequence of changing the optical coupling media was a consistent improvement in the light collection and the light collection asymmetry (5.85%/mm $\pm$ 8%) in comparison with the individual detector matrices modules measurements (3.26%/mm $\pm$ 22%). The small dispersion in the $k_{rel}$ inter-pixel calibration constant indicates that the HV multiplexing scheme adopted for the ClearPEM scanner to bias a total of 768 APD sub-matrices does not lead to a degradation on the system performance. The dispersion of the absolute gain (or photopeak position) is less than 15% which indicates that the change in the optical medium has not introduced additional variability in the light collection.

In the end of December of 2008, the scanner was re-assembled in the Nuclear Medicine department of IPO–Porto where commissioning work was carried out to confirm the earlier measurements at TagusLIP. This phase was concluded in April 2009 and the detector was considered to be ready for the pre-clinical trials phase, which has started in June 2009. The first commissioning results have shown 99.7% active channels, which, after calibration, have inter-pixel and absolute gain distributions with dispersions of, respectively, 12.2% and 15.3%, demonstrating that, despite the large number of channels, the system is uniform. The average energy resolution at 511 keV is 15.9% (8.8% dispersion) and a DOI resolution better than 2 mm FWHM. The coincidence time resolution, at 511 keV, for an energy window between 400 and 600 keV, is 5.2 ns FWHM. The first images have demonstrated a spatial resolution of 1.3 mm at the centre of the field of view (FOV), close to the theoretical limit for crystals with 2×2 mm$^2$ cross-section.

**Prospects of Future Work**

Animal models of human disease are an important and widely used research tool in understanding disease processes and evaluating potential therapies. Among the several imaging technologies applied to *in vivo* studies of research animals, positron emission

tomography (PET) is a nuclear imaging technique that permits the spatial and temporal distribution of compounds labeled with a positron-emitting radionuclide to be determined noninvasively. Many different positron-labeled compounds have been synthesized as tracers that target a range of specific markers or pathways. These tracers permit the measurement of quantities of biological interest, ranging from glucose metabolism to gene expression. PET has been extensively used in imaging studies of larger research animals such as dogs and nonhuman primates. Using high-resolution dedicated animal PET scanners, these types of studies can be performed in small laboratory animals such as mice and rats.

The mouse is the experimental model of choice in many situations due to a range of factors including relatively high genetic homology with man and widespread expertise and well developed methodology for genetic manipulation. PET enables repeat studies in a single subject and significant data can be obtained from a handful of animals without the need to euthanize hundreds of animals that might be required for a similar study with other imaging techniques.

In Portugal, there is a well established and active community on biomedical research, namely in the genetic basis of development and evolution of complex systems, like mice and rats, and on the genetics of complex human diseases, like cancer. In this context, the design and installation in Portugal of a PET scanner specially tailored for Small Animal (PET-SA) imaging could extend the imaging spectrum available for study of genetic regulated processes and pharmaceutical kinetics studies.

The performance shown by the Clear-PEM scanner is suitable for small animal imaging, which have motivated the redesign of the baseline ClearPEM technology for this application, in order to be fully competitive with other small animal PET scanners in the market. This new scanner will be assembled on a fixed planar configuration, with a FOV of about $9\times14$ cm$^2$, having a total of 6144 APD pixels.

Characterization in terms of light collection, energy resolution, DOI resolution, interpixel crosstalk and long-term stability, evolving from performance evaluation of the baseline detector module, passing by electrical and mechanical assembly validation to the integration phase of the full PET-SA scanner, will be carried out.

In order to perform exams with small animals, legal conditions on the judgments required in the management of animal facilities and radiation protection have to be fulfilled and certified in terms of animal welfare. The small animal PET-SA scanner will be physical installed at the TagusLIP. For that, the existing hot area needs a major overhaul. Protocols for animal care and use and corresponding certification processes will be conduced. Support will be provided in animal PET images logistics, ensuring institutional policies and responsibilities on animal environment, husbandry, management and veterinary care. Participation in exam trials aimed at demonstrating the performance of the PET-SA/CT scanner in high resolution animal PET and CT images will be carried out.

Many different types of radiation have been exploited to provide images of the structure and function of tissues inside a living subject. Each imaging modality is characterized by different resolutions on the spatial and temporal scales, and by a different sensitivity for measuring properties related to morphology or function. Combinations that integrate the strengths of two imaging modalities and, at the same time, eliminate one or more weaknesses of an individual modality, thus offer the prospect of improved diagnostics, therapeutic monitoring, and preclinical research using imaging approaches. In this context, the PET - Consortium in collaboration with the CERIMED organization and CERN has started the development of the ClearPEM-Sonic scanner. The ClearPEM-Sonic is a dual modality scanner (PET and Ultrasound) dedicated breast imaging camera for evaluation of correlations between different radiotracer uptakes and nodule elastomeric parameters for breast cancer.

The PET-SA scanner with its CT extension as well as the ClearPEM-Sonic scanner will correspond to a significant landmark in terms of multimodality imaging in relation to the current commercial solutions. However, both scanners rely on the integration of different apparatus (PET/CT/US) in the same machine, which increases the overall system complexity and cost. Further improvements to this approach are thus desirable. One of the most promising research lines will be the development of a single detector module that is able to detect not only the 511 keV photons relevant to PET imaging but also low-energy X-ray photons (20–50 keV) for CT imaging and intermediate energy photons (100–150 keV) for Single Photon Emission Computerized Tomography (SPECT). This development would then be used as a starting point for the design of a new scanner that is able to acquire using the same electronics, images in PET, SPECT mode and CT mode. The addition of SPECT capabilities will allow carrying simultaneous imaging studies with different radiopharmaceuticals in order to obtain images of the different biochemical pathways involved, for example, in gene expression and regulation.

The initial phase of the work will consist on the development, in collaboration with a leading APD manufacturer, of an APD multi-pixel array with higher gain (200–1000). This APD will be used for light collection using LYSO:Ce crystal matrices or other scintillation crystals (like $LaBr_3$:Ce). The use of an APD with higher gains (current APDs are limited to gains 100–150) will enable the detection of X-rays, opening a new window in the small animal studies, combining anatomical information from X-ray images with metabolic images from PET/SPECT detectors. The development of a high gain APD, with a large active region, and exploration of Silicon Photomultiplier photo detectors (gains of $10^4$–$10^5$) is expected also to reduce some of the factors that limit the time resolution obtainable with the current Clear-PEM scanner technology (low internal gain of the APD S8550 from Hamamatsu and the low light collection due to the $1.6\times1.6$ mm$^2$ APD pixel matching with the $2\times2$ mm$^2$ cross-section crystals). Experimental characterization of the developed APDs will be performed and results will be used to select the best APDs or SiPM for this multimodality application.

In parallel with the work to develop an enhanced APD, investigation will be carried out on the optimization of the detector module crystal array and reflector wrapping, with

the aim to increase the total light collected, enabling the detection of photons from 20 keV to 511 keV covering the energy range of interest for multimodality PET/SPECT/CT. Possible solutions like the exploration of the new bright scintillator such as LaBr3:Ce (60 000 optical photons per MeV in comparison with the 27 000 optical photons per MeV with LYSO:Ce), and specular reflector materials with thickness of the order of 70 $\mu$m will be performed.

# Bibliography


[Abreu2005] M.C. Abreu, J.D. Aguiar, E. Albuquerque, F.G. Almeida, P. Almeida, P. Amaral, P. Bento, R. Bugallho, B. Carriço, H. Cordeiro, M. Ferreira, N.C. Ferreira, F. Gonçalves, C. Leong, F. Lopes, P. Lousã, M.V. Martins, N. Matela, P.R. Mendes, R. Moura, J. Nobre, N. Oliveira, C. Ortigão, L. Peralta, J. Rego, R. Ribeiro, P. Rodrigues, A.I. Santos, J.C. Silva, M.M. Silva, I.C. Teixeira, J.P. Teixeira, A. Trindade and J. Varela, *First experimental results with the Clear–PEM detector*. IEEE Nuclear Science Symposium Conference Record 2005, pp. 2785–2789.

[Abreu2006] M.C. Abreu, J.D. Aguiar, E. Albuquerque, F.G. Almeida, P. Almeida, P. Amaral, P. Bento, R. Bugallho, B. Carriço, H. Cordeiro, M. Ferreira, N.C. Ferreira, F. Gonçalves, C. Leong, F. Lopes, P. Lousã, M.V. Martins, N. Matela, P.R. Mendes, R. Moura, J. Nobre, N. Oliveira, C. Ortigão, L. Peralta, J. Rego, R. Ribeiro, P. Rodrigues, J. Sampaio, A.I. Santos, J.C. Silva, P. Sousa, I.C. Teixeira, J.P. Teixeira, A. Trindade and J. Varela, *Design and evaluation of the Clear–PEM scanner for positron emission mammography*. IEEE Trans. Nuc. Sci. 53 (2006) pp. 71–77.

[Abreu2007] M.C. Abreu, P. Amaral, B. Carriço, M. Ferreira, J. Luyten, R. Moura, C. Ortigão, P. Rato Mendes and J. Varela, *Characterization and quality control of avalanche photodiode arrays for the Clear–PEM detector modules.* Nucl. Instr. and Method. in Phys. Res. A 576 (2007), pp. 19–22.

[Amsler2008] C. Amsler et al. (Particle Data Group), Physics Letters B667, 1 (2008)

[Auffray2002] E. Auffray, F. Cavallari, M. Lebeau, P. Lecoq, M. Schneegans and P. Sempere-Roldan, *Crystal conditioning for high-energy physics detectors*, Nucl. Instr. and Methods in Phys. Res. A 486 (2002), pp. 22–34.

[Albuquerque2006] E. Albuquerque, P. Bento, C. Leong, F. Gonçalves, J. Nobre, J. Rego, P. Relvas, P. Lousã, P. Rodrigues, I. C. Teixeira, J. P. Teixeira, L. Silva, M. M. Silva, A. Trindade and J. Varela, *The Clear–PEM electronics system*, IEEE Trans. Nuc. Sci. 53 (2006) pp. 2704–2711.

[Braem2004] A. Braem, E. Chesi, C. Joram, J. Séguinot, P. Weilhammer, M. Giunta, N. Malakhov, A. Menzione, R. Pegnad, A. Picciolid, F. Raffaelli and G. Sartori, *Design, fabrication and performance of the 10-in. TOM HPD*, Nucl. Instr. and Method. in Phys. Res. A 518 (2004), pp. 574–578.

[Brun1997] Rene Brun and Fons Rademakers, *ROOT - An Object Oriented Data Analysis Framework*, Proceedings AIHENP'96 Workshop, Lausanne, Sep. 1996, Nucl. Inst. and Methods in Phys. Res. A 389 (1997) pp. 81–86. See also http://root.cern.ch/.

[Bugalho2008] V. Bexiga, R. Bugalho, B. Carriço, C. S. Ferreira, M. Ferreira, C. Leong, P. Lousã, P. Machado, R. Moura, P. Neves, C. Ortigão, F. Piedade, J. F. Pinheiro, J. Rego, P. Rodrigues, I. C. Teixeira, J. P. Teixeira, J. C. Silva, A. Trindade and J. Varela, *Experimental Validation and Performance Analysis of the Clear–PEM Data Acquisition Electronics*, IEEE Medical Imaging Conference and 16th Room Temperature Semiconductor Detector Workshop, 2008, pp. 4065–4067.

[Carriço2006] B.Carriço, *Quality Control of Avalanche Photodiode Arrays for the project "PET - Development of PET technology for Mammography"*, Master Thesis, Faculdade de Ciências e Tecnologia, Universidade do Algarve.

[Caen2008] Caen, Nuclear Physics Division, http://www.caen.it/. Online, 2008.

[Crespo2005] P. Crespo, *Optimization of in-beam Positron Emission Tomography for monitoring heavy ion tumor therapy*, PhD thesis, 2005, Technischen Universität Darmstadt.

[Degenhardt2007] C. Degenhardt, K. Fiedler, T. Frach, W. Rutten, T. Solf and A. Thon, *Impact of Intercrystal Crosstalk on Depth-of-Interaction Information in PET Detectors*, IEEE Trans. Nuc. Sci. 54 (2007) pp. 427–432.

[Dezenzo1993] S. E. Derenzo, W. W. Moses, R. H. Huesman and T. F. Budinger, *Critical instrumentation issues for <2 mm resolution, high sensitivity brain PET*, published in the book "Quantification of Brain Function", Elsevier Science Publishers, 1993, pp. 25–37.

[Ferreira2009] R. Bugalho, B. Carriço, C. S. Ferreira, M. Frade, M. Ferreira, R. Moura, C. Ortigão, J. F. Pinheiro, P. Rodrigues, I. Rolo, J. C. Silva, R. Silva , A. Trindade and J. Varela, *The Clear–PEM Imaging Scanner for Positron Emission Mammography*, 14th International Conference on Emerging Nuclear Energy Systems, Conference record, 2009.

[Frade2009] R. Bugalho, B. Carriço, C. S. Ferreira, M. Frade, M. Ferreira, R. Moura, C. Ortigão, J. F. Pinheiro, P. Rodrigues, I. Rolo, J. C. Silva, R. Silva , A. Trindade and J. Varela, *Experimental Characterization of the Clear–PEM Scanner Spectrometric Performance*, accepted for publication on JINST, Expected online publication: October 2009.

[Frade2009b] M. Frade, *Evaluation of the Clear-PEM scanner in Clinical Environment*, Master thesis, 2009, Instituto Superior Técnico, Universidade Técnica de Lisboa.

[HSVU2008] Health Systems of Virginia University, based in Charlottesville since 1825, http://www.healthsystem.virginia.edu/. Online, 2008.

[Hamamatsu2001] I. Hamamatsu Photonics, *Si APD array S8550*, Technical data sheet (2001).

[Hoagland2004] T. Hoagland, *A Brief Discussion of NIM, CAMAC and VME Standards*, documentation of the National Superconducting Cyclotron Laboratory, 2004, http://www.nscl.msu.edu/, online in 2008.

[Imaginis2008] Imaginis The Breast Cancer Resource, http://www.imaginis.com/, Online in 2008.

[Iseg2008] Iseg, High Voltage, http://www.iseg-hv.de/. Online, 2008.

[Jiangui2004] L. Jiangui, *Amplifier for the 32 channel Hamamatsu APD array*, Technical report of IIHE/VUB, 2004, Crystal Clear Collaboration.

[Kapusta2003] M. Kapusta, P. Crespo, M. Moszyńsk, W. Enghardt and D. Wolski, *Hamamatsu S8550 APD Arrays for High-Resolution Scintillator Matrices Readout*, Nucl. Inst. and Methods in Phys. Res. A 504 (2003) pp. 139–142.

[Kataoka2005] J. Kataoka, T. Saito, Y. Kuramoto, T. Ikagawa, Y. Yatsu, J. Kotoku, M. Arimoto, N. Kawai, Y. Ishikawa and N. Kawabata, *Recent progress of avalanche photodiodes in high-resolution X-rays and Gamma-rays detection*, Nucl. Inst. and Methods in Phys. Res. A 541 (2005) pp. 398.

[Kirn1999] T. Kirn, M. Häring, D. Schmitz, W. Schulz, *Absorption length, radiation hardness and ageing of different optical glues*, CMS NOTE 1999/003, January 1999.

[Knoll2000] G. F. Knoll, *Radiation Detection and Measurement*, Third Edition, Wiley, 2000.

[Kuntner2002] C. Kuntner, E. Auffray, P. Lecoq, C. Pizzolotto and M. Schneegans, *Intrinsic energy resolution and light output of the $Lu_{0.7}Y_{0.3}AP$:Ce scintillator*, Nucl. Instr. and Method. A 493 (2002), pp. 131–136.

[Labsphere2008] Labsphere, global distributor, White reflectance coating datasheet, http://www.labsphere.com/. Online, 2008.

[Lecomte2004] R. Lecomte, *Technology challenges in small animal PET imaging*, Nucl. Inst. and Methods in Phys. Res. A527 (2004), pp 157–165.

[Lecomte2009] M. Bergeron, J. Cadorette, J. F. Beaudoin, M. D. Lepage, G. Robert, V. Selivanov, M. A. Tetrault, N. Viscogliosi, J. P. Norenberg, R. Fontaine, R. Lecomte, *Performance evaluation of the LabPET APD-based digital PET scanner*, IEEE Trans. Nuc. Sci. 56 (2009) pp. 10–16.

[Lecoq2002] P Lecoq and J. Varela, *Clear–PEM, a dedicated PET camera for mammograghy*, Nucl. Inst. and Methods in Phys. Res. A 486 (2002) pp. 1–6.

[Leo1994] W. R. Leo, *Techniques for Nuclear and Particle Physics Experiments: A How-to Approach*, Second Revised Edition, Springer–Verlag, 1994.

[Leong2005] C. Leong, P. Bento, P. Rodrigues, J.C. Silva, A. Trindade, P. Lousa, J. Rego, J. Nobre, J. Varela, J.P. Teixeira, C. Teixeira, *Design and test issues of a FPGA based data acquisition system for medical imaging using PEM*, in Conference Records of the 14th IEEE–NPSS RT2005, Stockholm, Sweden.

[Levin1997] C. S. Levin, M. P. Tornai, S. R. Cherry, L. R. MacDonald and E. J. Hoffman, *Compton Scatter and X-ray Crosstalk and the Use of Very Thin Intercrystal Septa in High-Resolution PET Detectors*, IEEE Trans. Nuc. Sci. 44 (1997) pp. 218–224.

[Levine2003] E. A. Levine, R.I. Freimanis, N. D. Perrier, K. Morton, N. M. Lesko, S. Bergman, K. R. Geisinger, R. C. Williams, C. Sharpe, V. Zavarzin, I. N. Weinberg, P. Y. Stepanov, D. Beylin, K. Lauckner, M. Doss, J. Lovelace, L. P. Adler, *Positron Emission Mammography: Initial Clinical Results*, Annals of Surgical Oncology 10 (2003) pp. 86–91.

[Lewellen2008] T. K. Lewellen, *Recent Developments in PET detector technology*, Phy. Med. Biol. 53 (2008) pp. R287–R317.

[Martins2005] M. V. Martins, N. Matela, P. Rodrigues, A. Trindade, N. Oliveira, H. Correia, N. C. Ferreira, J. Varela, and P. Almeida (2005), *Reconstruction of Clear–PEM Data with STIR*, In Nuclear Science Symposium Conference Record, 2005 IEEE, volume 4, pp. 2098–2102.

[McElroy2005] D. P. McElroy, M. Hoose, W. Pimp, V. Spanoudaki, V. T. Schüler and S. I. Ziegler, *A true singles list-mode data acquisition system for a small animal PET scanner with independent crystal readout*, Phys. Med. Biol. 50 (2005), pp. 3323–3335.

[McIntyre1996] R. J. McIntyre, *Multiplication noise in uniform avalanche diodes*, IEEE Trans. Electron Devices, vol. ED–13 (1996), pp. 164–168.

[Melcher2000] C. L. Melcher, *Scintillation Crystals for PET*, The Journal of Nuclear Medicine, Vol 41 (2000) No. 6, pp. 1051–1055.

[Miyaoka2000] R. S. Miyaoka and T. K. Lewellen, *Effect of detector scatter on the decoding accuracy of a DOI detector module*, IEEE Trans. Nuc. Sci. 47 (2000) pp. 1614–1619.

[Moses2003] W. Moses and J. Qi, *Fundamental limits of Positron Emission Mammography*, Nucl. Inst. and Methods in Phys. Res. A 497 (2003) pp. 82–89.

[Moses2004] W. Moses, *Positron Emission Mammography imaging*, Nucl. Instr. and Methods in Phys. Res. A 525 (2004) pp. 1–2.

[Mosset2002] J. B. Mosset, S. Saladino, J. F. Loude, and C. Morel, *Characterisation of arrays of avalanche photodiodes*, Internal Report of the ClearPET Project, Universite de Lausanne, 2002.

[Mosset2003] J. B. Mosset, S. Saladino, J. F. Loude, and C. Morel, *Characterisation of arrays of avalanche photodiodes for small animal positron emission tomography*, Nucl. Instr. and Method. in Phys. Res. A 504 (2003), pp. 325–330.

[Mosset2006] J. B. Mosset, *Développement d'un module de détection phoswich LSO–LuYAP pour le prototype de caméra à positrons ClearPET*. PhD thesis, 2006, Faculté des Sciences de base de l'Ecole Polytechnique Féderale de Lausanne.

[Montecchi2001] M. Montecchi and Q. Ingram, *Study of some optical glues for the Compact Muon Solenoid at the large hadron collider of CERN*, Nucl. Inst. and Methods in Phys. Res. A 465 (2005) pp. 329–345.

[Moura2005] P. Amaral, B. Carriço, M. Ferreira, R. Moura, C. Ortigão, P. Rodrigues, J.C. da Silva, A. Trindade and J. Varela, *Performance and Quality–Control of Clear–PEM Detector Modules*, Nucl. Inst. and Methods in Phys. Res. A 580 (2005) pp. 1123–6.

[Moura2009] R. Moura, *Depth-of-Interaction Determination and Spatial Resolution in the ClearPEM Detector*, PhD Thesis, 2009, Instituto Superior Técnico, Universidade Técnica de Lisboa.

[Moszyński2001] M. Moszyński, M. Kapusta, M. Balcerzyk, M. Szawlowski, D. Wolski, I. Węgrzecka and M. Wegrzecki, *Comparative Study of Avalanche Photodiodes With Different Structures in Scintillation Detection*, IEEE Trans. Nuc. Sci. 48 (2001) pp. 1205–1210.

[Muehllehner2006] G. Muehllehner and J. S. Karp.,*Positron Emission Tomography*, Phys. Med. Biol. 51 (2006) pp. R117–R137.

[NRC2008] The U.S. Nuclear Regulatory Commission, http://www.nrc.gov/. Online, 2008.

[Ogasawara2005] K. Ogasawara, K. Asamura, T. Mukai and Y. Saito, *Avalanche photodiode for measurement of low-energy electrons*, Nucl. Inst. and Methods in Phys. Res. A 545 (2005) pp. 744–752.

[Ortigao2007] P. Amaral, P. Bruyndonckx, B. Carriço, M. Ferreira, R. Moura, C. Ortigão, P. Rodrigues, J.C. da Silva, A. Trindade and J. Varela, *Long-term Stability of Clear–PEM Detector Modules*, Nucl. Inst. and Methods in Phys. Res. A 571 (2007) pp. 488–492.

[Pepin2001] C. M. Pepin, P. Bérard and R. Lecomte, *Assessment of Reflective Separator Films for Small Crystal Arrays*, Nuclear Science Symposium Conference Record, 2001 IEEE, Vol. 2 (2001), pp. 879–883.

[Pichler1998] B. Pichler, G. Boning, E. Lorenz, R. Mirzoyan, W. Pimp, M. Schwaiger and S. I. Ziegler, *Studies with a Prototype High Resolution PET Scanner based on LSO–APD Modules*, IEEE Trans. Nuc. Sci. 45 (1998) pp. 1298–1302.

[Pichler2000] B. J. Pichler, E. Lorenz, R. Mirzoyan, L. Weiss and S. I. Ziegler, Production of a diffuse very high reflectivity material for light collection in nuclear detectors, Nucl. Inst. and Meth. in Phys. Res. A 442 (2000), pp. 333–336.

[Pichler2001] B. Pichler, F. Bernecker, G. Böning, M. Rafecas, W. Pimpl, M. Schwaiger, E. Lorenz and S. I. Ziegler, *A 4 × 8 APD array, consisting of two monoloithic silicon wafers coupled to a 32-channel LSO matrix for high-resolution PET*, IEEE Trans. Nuc. Sci. 48(2001), pp. 1391–1396.

[Pidol2004] L. Pidol, K. Kahn-Harari, B. Viana, E. Virey, B. Ferrand, P. Dorenbos, J. T. M. de Haas and C. W. E. van Eijk, *High efficiency of lutetium silicate scintillators Ce-dopped LPS, and LYSO crystals*, IEEE Trans. Nuc. Sci. 51(2004), pp. 1084–1087.

[Pinheiro2008] J. F. Pinheiro, *Control System and Calibration Software for the Clear-PEM Scanner*, Master Thesis, 2008, Instituto Superior Técnico, Universidade Técnica de Lisboa.

[Rafecas2003] M. Rafecas, G. Boning, J.B. Pichler, E. Lorentz and M. Schwaiger, *Inter-crystal scatter in a dual layer, high resolution LSO-APD positron emission tomograph*, Phys. Med. Biol. 48 (2003) pp. 821–848.

[Renker2002] D. Renker, *Properties of avalanche photodiodes for applications in high energy physics, astrophysics and medical imaging*, Nucl. Inst. and Methods in Phys. Res. A 486 (2002) pp. 164–169.

[Roldan2007] P. S. Roldan, M. Cañadas, O. Dietzel, C. Pautrot, I. Sarasola and A. Wagner, *Performance evaluation of Raytest ClearPET, a PET scanner for small and medium size animals*, IEEE Nuclear Science Symposium Conference Record, 2007, pp. 2859–2864.

[Rodrigues2007] P. Rodrigues, *Study and Development of the Clear–PEM Trigger and Data Acquisition System*, PhD thesis, 2007, Instituto Superior Técnico, Universidade Técnica de Lisboa.

[Rodrigues2008] F.G Almeida, S. Augusto, J. Barbosa, R. Bugalho, B. Carriço, C. S. Ferreira, M. Ferreira, M. Frade, R. Moura, P. Parkhust, C. Ortigão, J. F. Pinheiro, P. Rodrigues, I. Rolo, D. N. Sá, J. C. Santos, J.C. Silva, R. Silva, A. Trindade and J. Varela, *Development of a High Packing Fraction Detector Module with DOI Measurement Capability for High–Resolution PET*, IEEE Nuclear Science Symposium Conference Record, 2008, pp. 3797–3800.

[Rodrigues2009] E. Albuquerque, V. Bexiga, R. Bugalho, B. Carriço, C. S. Ferreira, M. Ferreira, J. Godinho, F. Goncalves, C. Leong, P. Lousã, P. Machado, R. Moura, P. Neves, C. Ortigão, F. Piedade, J. F. Pinheiro, J. Rego, A. Rivetti, P. Rodrigues, J.C. Silva, M. M. Silva, I. C. Teixeira, J. P. Teixeira, A. Trindade and J. Varela, *Experimental Characterization of the 192 Channel Clear–PEM Frontend ASIC Coupled to a Multi–Pixel APD readout of LYSO:Ce crystals*, Nucl. Inst. and Methods in Phys. Res. A 598 (2009) pp. 802–814.

[Rogers2000] J. G. Rogers and C. J. Batty, *Afterglow in LSO and its possible effect on energy resolution*, IEEE Trans. Nuc. Sci., 47(2000), pp. 438–445.

[Rusack2003] R Rusack, *Avalanche Photodiodes: Readout options for a very large scintillator detector*, Oral presentation on $23^{rd}$ Off–Axis Detector Workshop at Fermi National Accelerator Laboratory, July 2003.

[Schilling2008] K. Schilling, MD, *The role of positron emission mammography in breast cancer imaging and management*, Applied Radiology. 37(2008) pp. 26–36.

[Shao2000] Y. Shao, R. W. Silverman, R. Farrell, L. Cirignamo, R. Grazioso, K. S. Shah, G. Visser, M. Clajus, T. O. Tümer and S. R. Cherry, *Design studies of a high resolution PET detector using APD arrays*, IEEE Trans. Nuc. Sci. 47(2000), pp. 1051–1057.

[Shao2002] Y. Shao, K. Meadors, R. W. Silverman, R. Farrell, L. Cirignamo, R. Grazioso, K. S. Shah and S. R. Cherry, *Dual APD readout of LSO crystals: optimization of crystal surface treatment*, IEEE Trans. Nuc. Sci. 49 (2002), pp. 649–654.

[Smith1999] I. C. Smith and F. J. Gilbert., *Role of Positron Emission Tomography in the management of breast cancer*, The Breast Journal 8 (1999) pp. 303–10.

[Song2003] T. Y. Song, J. B. Mosset, J. F. Loude, Y. Choi and C. Morel, *Characterization of New Avalanche Photodiode Array Prototypes*, Nucl. Instr. and Methods in Phys. Res. A 504 (2003) 325–330.

[Stoll1996] S. P. Stoll, *An Investigation of the Reflective Properties of Tyvek Papers and Tetratex PTFE Film*, Phenix note 245, Brookhaven National Laboratory, 1996.

[Streun2005] M. Streun, D. Christ, A. Hollendgung, H. Larue, K. Ziemons and H. Halling, *Effects of crosstalk and gain nonuniformity using multichannel PMTs in the ClearPET scanner*, Nucl. Instr. and Method. in Phys. Res. A 537 (2005) pp. 402–405.

[Thielemans2004] K. Thielemans, D. Sauge, C. Labbé, C. Morel, M. Jacobson and A. Zverovich (2004). Software for Tomography Image Reconstruction (STIR).

[Thompson1994] C. J. Thompson, K. Murthy, I. N. Weinberg and F. Mako. *Feasibility study for Positron Emission Mammography*, Med. Phys. 21(1994) pp. 529–38.

[Thompson2005] C. J. Thompson, S. St. James, and N. Tomic, *Under-sampling in PET scanners as a source of image blurring*, Nucl. Instr. and Methods in Phys. Res. A 545 (2005), pp 436–445.

[Trindade2004] A. I. Santos, P. Almeida, M. V. Martins, N. Matela, N. Oliveira, N. C. Ferreira, J. D. Aguiar, F. G. Almeida, F. Lopes, J. Sampaio, P. Bento, F. Gonçalves, C. Leong, P. Lousã, L. Silva, I. C. Teixeira, J. P. Teixeira, M. C. Abreu, B. Carriço, P. R. Mendes, R. Pereira, P. Sousa, M. Ferreira, R. Moura, C. Ortigao, L. Peralta, R. Ribeiro, P. Rodrigues, J. C. Silva, A. Trindade, J. Varela, *Design and evaluation of the Clear-PEM detector for positron emission mammography*, 2004 IEEE Nuclear Science Symposium Conference Record, pp. 2785–2789.

[Trindade2007] A. Trindade, *Design and Evaluation of a Positron Emission Tomograph for Breast Cancer Imaging*, PhD thesis, 2007, Instituto Superior Técnico, Universidade Técnica de Lisboa.

[Trindade2008] E. Albuquerque, F. G. Almeida, P. Almeida, S. Augusto, V. Bexiga, R. Bugalho, S. Carmona, B. Carriço, C. S. Ferreira, N. C. Ferreira, M. Ferreira, J. Godinho, F. Gonçalves, C. Guerreiro, C. Leong, P. Lousã, P. Machado, M. V. Martins, N. Matela, R. Moura, P. Neves, N. Oliveira, C. Ortigão, F. Piedade, J. F. Pinheiro, J. Rego, P. Relvas, A. Rivetti, P. Rodrigues, D. N. Sá, J. Sampaio, A. I. Santos, M. M. Silva, I. C. Teixeira, J. P. Teixeira, J. C. Silva, A. Trindade and J. Varela, *Performance Evaluation of a Highly Integrated APD/ASIC Double–Readout Supermodule with 768 channels for Clear–PEM*, 2008 IEEE Nuclear Science Symposium Conference Record, pp. 3022–3025 .

[Turner2007] J. E. Turner, *Atoms, Radiation, and Radiation Protection*, Third, Revised and Enlarged editon, Wiley-VCH, 2007.

[Van Vliet1979] K. M. Van Vliet, A. Friedmann and L. M. Rucker, *Theory of carrier multiplication and noise in photo-avalanche devices – Part II: Two carrier processes*, IEEE Trans. Electron Devices, vol. ED–26 (1979), pp. 751–764.

[Varela2004] J. Varela,*Electronics anda Data Acquisition in Radiation Detectors in Medical Imaging*, Nucl. Instr. and Method. in Phys. Res. A 527 (2004) pp. 21–26.

[Varela2007] J. Varela, *A PET imaging system dedicated to mammography*, Radiation Physics and Chemistry 76 (2007) pp. 347–350.

[Varela et al.2007] M. C. Abreu, D. Aguiar, E. Albuquerque, F. G. Almeida, P. Almeida, P. Amaral, E. Auffray, P. Bento, P. Bruyndonckx, R. Bugalho, B. Carriço, H. Cordeiro, M. Ferreira, N. C. Ferreira, F. Goncalves, P. Lecoq, C. Leong, F. Lopes, P. Lousã, J. Luyten, M. V. Martins, N. Matela, P. R. Mendes, R. Moura, J. Nobre, N. Oliveira, C. Ortigão, L. Peralta, J. Rego, R. Ribeiro, P. Rodrigues, A. I. Santos, J. C. Silva, M. M. Silva, S. Tavernier, I. C. Teixeira, J. P. Teixeira, A. Trindade, J. Trummer and J. Varela, *Clear–PEM: a PET imaging system dedicated to breast cancer diagnostics.* Nucl. Inst. and Methods in Phys. Res. A 571 (2007) pp. 81–84.

[Vaska2003] P. Vaska, S. P. Stoll, L. Woody, D. J. Schlyer and S. Shokouhi, *Effects of Intercrystal Crosstalk on Multielement LSO/APD PET Detectors*, IEEE Trans. Nuc. Sci. 50 (2003) pp. 362–366.

[Vaska2005] P. Vaska, C. L. Woody, D. J. Schlyer, V. Radeka, P. O'Connor, J. F. Pratte, S. Shokouhi, S. P. Stoll, S. S. Junnarkar, M. Purschke, S. J. Park, S. Southekal, V. Dzhordzhadze, W. Schiffer, J. Neill, M. Murphy, T. Aubele, R. Kristiansen, A. Villanueva, S. Boose, A. Kandasamy, B. Yu, A. Kriplani, S. Krishnamoorthy, R. Lecomte, and R. Fontaine, *Initial performance of the RatCAP, a PET camera for conscious rat brain imaging*, In 2005 IEEE Nuclear Science Symposium Conference Record, pp. 3040–3044.

[Wang2004] G. C. Wang, J. S. Hubber, W. W. Moses, W. S. Choong and J. S. Maltz, *Calibration of a PEM detector with depth-of-interaction measurement*, IEEE Trans. Nuc. Sci. 51 (2004), pp. 775–781.

[Wang2006] G. C. Wang, J. S. Hubber, W. W. Moses, W. S. Choong and J. S. Maltz, *Characterization of the LBNL PEM camera*, IEEE Trans. Nuc. Sci. 53 (2006), pp. 1129–1135.

[WHO2008] World Health Organization, http://www.who.int/. Online, 2008.

[Wrixon2008] A. D. Wrixon, *New ICRP recommendations*, J. Radiol. Prot. 28 (2008) pp. 161–168.

[Zhang2007] J. Zhang, A. M. K. Foudray, P. D. Olcott, R. Farrell, K. Shah and C. S. Levin, *Performance Characterization of a Novel Thin Position-Sensitive Avalanche Photodiode for 1 mm Resolution Positron Emission Tomography*, IEEE Trans. Nuc. Sci. 54 (2007), pp. 415–421.

[Ziemons2005] K. Ziemons, E. Auffray, R. Barbier, G. Brandenburg, P. Bruyndonckx, Y. Choi, D. Christ, N. Costes, Y. Declais, O. Devroede, C. Dujardin, A. Fedorovd, U. Heinrichs, M. Korjik, M. Krieguer, C. Kuntner, G. Largeron, C. Lartizien, H. Larue, P. Lecoq, S. Leonard, J. Marteau, C. Morel, J. Mosset, C. Parl, C. Pedrini, A. Petrosyan, U. Pietrzyk, M. Rey, S. Saladino, D. Sappey-Marinier, L. Simon, M. Streun, S. Tavernier and J. Vieira, *The ClearPET $^{TM}$ project: development of a 2nd generation high-performance small animal PET scanner*. Nucl. Instr. and Method., A 537 (2005) 307–311.

[Ziegler2005] D. P. McElroy, W. Pimpl, B. J. Pichler, M. Rafecas, T. Schuler, S. I. Ziegler, *Characterization and readout of MADPET–II detector modules: validation of a unique design concept for high resolution Small Animal PET*, IEEE Trans. Nucl. Sci. 52 (2005) pp. 199–204.